



Mathieson, Jennifer Sharon (2011) *Probing the self assembly, reactivity and structure of supramolecular architectures using high resolution mass spectrometry*. PhD thesis..

<http://theses.gla.ac.uk/2693/>

Copyright and moral rights for this thesis are retained by the author

A copy can be downloaded for personal non-commercial research or study, without prior permission or charge

This thesis cannot be reproduced or quoted extensively from without first obtaining permission in writing from the Author

The content must not be changed in any way or sold commercially in any format or medium without the formal permission of the Author

When referring to this work, full bibliographic details including the author, title, awarding institution and date of the thesis must be given

Probing the Self Assembly, Reactivity and Structure of
Supramolecular Architectures Using High Resolution Electrospray
Mass Spectrometry



University
of Glasgow

Jennifer Sharon Mathieson

A thesis submitted to the University of Glasgow for the degree of
Doctor of Philosophy

School of Chemistry

May 2011

This thesis is dedicated to Bryan and to my family. Without you I wouldn't be the person I am today. Thankyou for all your support.

ACKNOWLEDGMENTS

This project was carried out between October 2007 and March 2011 in the Department of Chemistry in the University of Glasgow. Throughout the course of the research I was lucky to meet and be helped by many people, some I would like to acknowledge in particular:

Professor Leroy Cronin, for giving me the opportunity to work on a project that has been extremely interesting, for his ideas and for his constant encouragement throughout.

Dr De-Liang Long, for his help with crystallography in this thesis.

Dr Geoffrey J. T. Cooper and Dr Graham Newton for their research into *trans*-tach which gave me a great basis to start working from and for their help with the *tach* synthesis.

Dr Carsten Streb, Dr Phil Kitson and Dr Scott Mitchell, for their constant support and random conversations in the upstairs office. Thankyou for all the help and answering my daft questions.

Dr Haralampos N. Miras and Dr Elizabeth Wilson, for their help with the maintenance of the mass spectrometer.

Dr Thomas McGlone, for his friendship throughout the years and listening to me complain when things went wrong.

Mali Husby Rosnes for being my running companion on all those cold winter mornings.

Roslyn Eadie for being a great flatmate and constant source of hilarious comments: “are there grapes in this wine?”

Claire Lydon for our chats in the lab and comparison of who had the worst asthma..

Neus Corella Ochoa for bringing some Spanish flare into my life.

Jim McIver for his constant help with anything I tried to throw at him and for phoning Bruker whenever the mass spectrometer decided not to work.

The technical staff of the University of Glasgow School of Chemistry in particular **Dr David Adam** for help with NMR.

All the members of the Cronin group past and present who made the three years of my PhD an enjoyable experience. In addition to those above I would also like to mention **Johannes Thiel, Dr Craig Richmond, David Gabb, Feng Xu, Dr Christoph Busche, Dr Jun Yan, Dr. Pradeep C. Parameswaran, Dr Marie Hutin and Pedro Molina Sanchez**.

I would finally like to thank my family and Bryan Boyle for their constant love and support throughout the years. Words cannot explain how grateful I am.

TABLE OF CONTENTS

ACKNOWLEDGMENTS	I
TABLE OF CONTENTS	II
PUBLICATIONS	V
ABBREVIATIONS	VI
INSTRUMENTATION	VIII
1.1 Materials	ix
1.2 Methods for Crystal Growth.....	ix
ABSTRACT	X
2 INTRODUCTION	1
2.1 Supramolecular Chemistry	1
2.1.1 Non-covalent interactions	2
2.1.2 Design strategies	5
2.1.3 d-Block Chemistry	5
2.1.4 Coordination number two	7
2.2 Mass spectrometry in Inorganic Chemistry.....	15
2.3 Anion binding	23
2.3.1 Electrostatic interactions in anion binding	24
2.3.2 Hydrogen bonding in anion binding.....	25
2.3.3 Lewis acidic hosts	30
2.3.4 Combined interactions for anion recognition	31
2.4 Direct C-H Transformation via Iron Catalysis	33
2.4.1 C-H bond activation	34
2.4.2 Mechanistic studies of C-H transformations via iron catalysis	40
3 IN-SITU STOICHIOMETRIC CONTROL OF COORDINATION COMPLEXES	45
3.1 Mass spectrometry	52
3.1.1 In-situ Mass Spectrometry	55
3.2 Conclusions.....	62
3.3 Experimental.....	65
3.3.1 1,3,5-Cyclohexanetrionetrioxime (chtt, 1).....	65
3.3.2 cis,cis- and cis,trans-1,3,5-Triaminocyclohexane (cis-tach, 2 and trans-tach, 3)	66

3.3.3	Separation of cis- and trans-tach by Complexation with Nickel (II) Nitrate.....	67
3.3.4	Synthesis of $[\text{Cu}(\text{ttop})\text{Cl}]\text{Cl}(\text{CH}_3\text{OH})_2$, 5	70
3.3.5	Synthesis of $[\text{Cu}_2(\text{ttop})\text{Cl}_4](\text{CH}_3\text{OH})$, 6.....	71
3.3.6	Synthesis of $[\text{Cu}(\text{H}(\text{trans-1-amino-cis-3,5-N}',\text{N}''-2\text{-imidopyridine}))(\text{H}_2\text{O})\text{Cl}]\text{Cl}_2$, 7	72
3.3.7	Synthesis of $\{[\text{Cu}_2(\text{cis-3-amino-cis,trans-N}',\text{N}''-2\text{-imidopyridine})_2]\}_2(\text{NO}_3)_4$, 8	73
3.3.8	Synthesis of $\{[\text{Cu}_2(\text{ttop})\text{Cl}_3]\text{Cl}\}_2$, 9.....	74
3.3.9	Synthesis of $[\text{Zn}(\text{ttop})\text{Cl}]\text{Cl}(\text{H}_2\text{O})_2$, 10.....	75
3.3.10	Synthesis of $[\text{Zn}(\text{ttop})\text{I}]\text{I}(\text{CH}_3\text{OH})$, 11	76
3.3.11	Synthesis of $[\text{Co}_2(\text{ttop})(\text{NO}_3)_3(\text{H}_2\text{O})_2](\text{NO}_3)(\text{CH}_3\text{CN})_2$, 12.....	77
3.3.12	Synthesis of $[\text{Cu}_2(\text{ttop})(\text{NO}_3)_4(\text{H}_2\text{O})](\text{CH}_3\text{OH})$, 13	78
3.3.13	Electrospray and cryospray mass spectrometry (ESI-MS and CSI-MS).....	78
3.3.14	In-situ mass spectrometry	79
4	DIRECT C-H TRANSFORMATION VIA IRON CATALYSIS.....	80
4.1	Temperature controlled cryospray mass spectrometry.....	83
4.1.1	Isotopic labelling mass spectrometry experiments.....	85
4.1.2	Dihydroxylation reactions.....	92
4.2	Conclusions.....	105
4.3	Experimental.....	111
4.3.1	Synthesis of $[\text{FeII}(\text{CF}_3\text{SO}_3)_2(\text{PyMe}_2\text{tacn})]$, 14.....	111
4.3.2	Synthesis of 1-(<i>p</i> -toluensulfonyl)-1,4,7-triazacyclononane, tacnmt	111
4.3.3	Synthesis of 1,4-dimethyl-7-(2-pyridylmethyl)-1,4,7-triazacyclononane, PyMe ₂ tacn.....	113
4.3.4	Observation of the Fe(V)-oxo species using cryospray mass spectrometry (CSI- MS)	114
5	VALIDATING ANION BINDING USING ELECTROSPRAY MASS SPECTROMETRY	144
5.1	Conclusions.....	156
5.2	Experimental.....	158
5.2.1	Synthesis of cis,cis-1,3,5-tris-acetylamino-cyclohexane, 40.....	158
5.2.2	Job plot analysis in ESI-MS.....	158
5.2.3	Job plot analysis in ¹ H NMR.....	159
6	MASS SPECTROMETRIC STUDIES OF INORGANIC COMPLEXES	160

6.1	Mass spectrometric studies of chiral cyanide-bridged {Ni ₆ Fe ₄ } cages.....	160
6.2	Mass spectrometric studies of the self-assembly of heterometallic clusters	164
6.3	Other CSI-MS measurements of heterometallic structures	174
6.4	Conclusions.....	182
6.4.1	Mass spectrometric studies of inorganic complexes	182
6.4.2	Mass spectrometric studies of chiral cyanide-bridged {Ni ₆ Fe ₄ } cages.....	182
6.4.3	Mass Spectrometric Studies of the Self-Assembly of Heterometallic Clusters.	183
6.4.4	Other CSI-MS measurements of heterometallic structures	186
6.5	Experimental.....	188
6.5.1	Mass spectrometric studies of inorganic complexes	188
6.5.2	Mass spectrometric studies of chiral cyanide-bridged {Ni ₆ Fe ₄ } cages.....	188
6.5.3	Mass spectrometric studies of the Self-Assembly of Heterometallic Clusters..	189
6.5.4	Synthesis of heterometallic helix, 45, and grid, 46, clusters	189
7	CRYSTALLOGRAPHY	192
7.1	[Cu(ttop)Cl]Cl(CH ₃ OH) ₂ , 5	193
7.2	[Cu ₂ (ttop)Cl ₄](CH ₃ OH), 6	194
7.3	[Cu(H(<i>trans</i> -1-amino- <i>cis</i> -3,5- <i>N',N''</i> -2-imidopyridine)))(H ₂ O)Cl]Cl ₂ , 7.....	195
7.4	{[Cu ₂ (<i>cis</i> -3-amino- <i>cis,trans</i> - <i>N',N''</i> -2-imidopyridine) ₂]} ₂ (NO ₃) ₄ , 8	196
7.5	{[Cu ₂ (ttop)Cl ₃]Cl} ₂ , 9	197
7.6	[Zn(ttop)Cl]Cl(H ₂ O) ₂ , 10.....	198
7.7	[Zn(ttop)I]I(CH ₃ OH), 11	199
7.8	[Co ₂ (ttop)(NO ₃) ₃ (H ₂ O) ₂](NO ₃)(CH ₃ CN) ₂ , 12	200
7.9	[Cu ₂ (ttop)(NO ₃) ₄ (NO ₃) ₄ (H ₂ O)](CH ₃ OH), 13	201

PUBLICATIONS

The following articles and communications were published, or are in preparation as a result of the work undertaken over the course of this Ph.D. programme.

“Monitoring the Formation of Coordination Complexes Using Electrospray Mass Spectrometry” Mathieson J. S., Cooper J. T., Pickering A. L., Keller M., Long D.-L., Newton G. N., Cronin L., *Chem. Asian J.* **2009**, *4*, 681.

“Ferromagnetically coupled chiral cyanide-bridged $\{Ni_6Fe_4\}_0$ cages” Shiga T., Newton G.N., Mathieson J.S., Tetsuka T., Nihei M., Cronin L., Oshio H., *Dalton Trans*, **2010**, *39*, 4730.

“Assembly of Modular Asymmetric Organic-Inorganic Polyoxometalate Hybrids into Anisotropic Nanostructures” Rosnes M. H., Musumeci C., Pradeep C. P., Mathieson J. S., Long D.-L., Song Y.-F., Pignataro B., Cogdell R, Cronin L. *J. Am. Chem. Soc.*, **2010**, *132*, 15490.

“Mapping the Sequential Self-Assembly of Heterometallic Clusters: From a Helix to a Grid” Newton G. N., Onuki T., Shiga T., Noguchi M., Matsumoto T., Mathieson J. S., Nihei M., Nakano M., Cronin L., Oshio H. *Angew. Chem. Int. Ed.* **2011**, *123*, 4946.

“Observation of Fe(V)=O using Temperature Variable Mass Spectrometry and its Enzyme-like C-H and C=C Oxidation Reactions” Prat I Casellasa I., Mathieson J. S., Güell M., Ribasa X., M. Luis J. M., Cronin L., Costas M., **2011**, *under review at Nature Chemistry*.

“Validating Anion Binding Using Electrospray Mass Spectrometry” Mathieson J. S., Cronin L., **2011**, *in preparation*.

ABBREVIATIONS

In addition to standard notation, the following abbreviations were used in this thesis:

DNA	deoxyribonucleic acid
Tachpyr	1,3,5-tris[(2-pyridylmethyl)amino]cyclohexane
TOFMS	time-of-flight mass spectrometer
POM	polyoxometalate
chtt	1,3,5-Cyclohexanetrionetrioime
<i>Cis</i> -tach	<i>cis,cis</i> -1,3,5-Triaminocyclohexane
<i>Trans</i> -tach	<i>cis,trans</i> -1,3,5-Triaminocyclohexane
Ttop	<i>cis,trans</i> -1,3,5-tris(pyridine-2-carboxaldimino)cyclohexane
m.p.	melting point
MS	mass spectrometry
TACN	triazacyclononane
PyMe ₂ tacn	1-(2-pyridylmethyl)-4,7-dimethyl-1,4,7-triazacyclononane
Tacnmt	1-(<i>p</i> -toluenesulfonyl)-1,4,7-triazocyclononane
Me ₂ tacnmt	1,4-dimethyl-7-(<i>p</i> -toluenesulfonyl)-1,4,7-triazocyclononane
4Me-PyMe ₂ tacn	1,4-dimethyl-7-(4-methyl-2-pyridylmethyl)-1,4,7-triazacyclononane
TPA	tris(2-pyridylmethyl)amine
PDP	2-((<i>S</i>)-1-pyridin-2-ylmethyl)pyrrolidin-2-yl)methyl)pyridine
NBS	<i>N</i> -bromosuccinamide
TBHP	<i>tert</i> -butyl hydroperoxide
tBuOK	potassium- <i>tert</i> -butoxide
TBABr	tetrabutylammonium bromide
ESI-MS	electrospray ionisation mass spectrometry
CSI-MS	cryospray ionisation mass spectrometry
MALDI	matrix assisted laser desorption ionisation
FAB	fast atom bombardment
APCI	atmospheric pressure chemical ionisation
MeOH	methanol
DMSO	dimethyl sulphoxide
CD ₃ OH	d ³ deuterated methanol

CH ₂ Cl ₂	dichloromethane
NOESY	Nuclear Overhauser effect spectroscopy

Throughout this thesis crystal structures are coloured by atom using the following colour scheme except otherwise stated:

Carbon	Grey
Nitrogen	Dark Blue
Copper	Pink
Chloride	Lime Green
Oxygen	Red
Nickel	Aqua
Iron(III)	Dark yellow
Iron(II)	Orange
Cobalt	Royal blue
Manganese	Purple

Mass spectra are coloured where the black lines are the observed spectra and the red bars are the calculated spectra. The bar graphs are representations of the simulated spectra that were achieved by taking the calculated data from the mass spectrometry analysis software and inputting it into an excel worksheet. A bar graph was then formed and placed in a diagram with the observed spectrum to show the fit of the two envelopes.

Except where stated hydrogen atoms, counterions and non-coordinates solvent molecules are excluded for clarity.

INSTRUMENTATION

Kugelrohr distillation:	Büchi Glass Oven B-580; the cited temperatures are those read from the internal thermometer.
Melting Point:	Electrothermal IA 9000 digital melting point apparatus. The given temperatures are uncorrected.
pH measurements:	Hanna Instruments HI 9025C microcomputer pH meter with a BCH combination pH electrode (309-1065) and HI 7669/2W temperature probe.
Microanalysis:	EA-1110 CHNS, CE-440 Elemental Analyser.
Mass spectrometry:	Bruker microTOFQ Spectrometer used for ESI-MS, and with Cryospray attachment for CSI-MS.
FT-IR spectroscopy:	Shimadzu FTIR-8300 and Jasco FTIR-410 spectrometers, manipulation with Shimadzu HyperIR and JASCO software.
UV-Vis spectroscopy:	Shimadzu UV-3101PC UV-VIS-NIR Scanning Spectrophotometer. Manipulation using Shimadzu software.
NMR spectroscopy:	Bruker DPX-400 and Avance-400 (400 MHz ^1H , 100 MHz ^{13}C , 2D experiments). Manipulation with XwinNMR and Mestre-C2.3a.
Single-crystal X-ray:	Nonius Kappa-CCD (Mo- K_{α}) and Bruker Apex II (Mo- K_{α} , Cu- K_{α}) diffractometers.

The following instrumentation was used to obtain the analytical and spectroscopic data reported herein:

All NMR spectra were recorded at room temperature unless otherwise stated. Chemical shifts are reported using the δ -scale, referenced to the residual solvent protons in the deuterated solvent for ^1H - and ^{13}C -NMR. The coupling constants (J) are reported in Hz as absolute values. Characterisation of spin multiplicities: s = singlet, d = doublet, t = triplet, q = quartet, quint = quintet, m = multiplet, b = broad, p = pseudo.

FT-IR spectra of solid materials were measured in KBr pellets unless otherwise stated while all liquid / oil samples were measured as thin film on a diamond anvil. Notation used in the interpretation of FT-IR spectra are as follows: sh = shoulder, w = weak, m = medium, s = strong, vs = very strong. Some peaks identified as OH stretches may have some contribution from residual water in the KBr used in the KBr disc.

1.1 Materials

Gases and liquid ammonia were supplied by *B. O. C. Ltd.* and were used without any further purification. Reactions in water were carried out using deionised water prepared using an ELGASTAT B118/B deioniser. Other solvents were supplied by *Fisher Chemicals* and were used without further purification. Deuterated solvents were obtained from *Aldrich Chemical Company Ltd.* while all other reagents were supplied by *Aldrich Chemical Company Ltd.*, *Fisher Chemicals* or *VWR International* and were used without further purification unless otherwise stated.

1.2 Methods for Crystal Growth

Crystal growth of metal complexes was achieved using two methods; slow evaporation and solvent diffusion. In the first instance, the nascent solution was concentrated nearly to the point of precipitation and placed in a small sample vial fitted with a perforated lid. In the second method, solvent diffusion, the nascent solution was placed into a small vial which is then placed in a larger sealed vial containing the diffusing solvent. A successful diffusion solvent must be sufficiently volatile to diffuse into the small vial as well as being miscible with the nascent solution while causing precipitation of the complex. The small vial may, in some cases, be fitted with a perforated lid or cotton wool plug to reduce the rate of diffusion and allow slower crystal growth. In both cases, the crystallisations were allowed to stand undisturbed in a crystallisation room with vibration free surfaces which is maintained at a constant temperature of 18 °C.

ABSTRACT

Electrospray (ESI-MS) and cryospray mass spectrometry (CSI-MS) techniques were developed to analyse and investigate the self-assembly, reactivity and structure of supramolecular architectures.

Using ESI-MS, the complexation reactions of the ligand *cis,trans*-1,3,5-tris(pyridine-2-carboxaldimino)cyclohexane (ttop) with divalent first row transition metal salts to form complexes with nuclearities 1,2 and 4 were followed. *In-situ* mass spectrometry was also utilised to show the stepwise formation of the ligand-metal complexes.

Mass spectrometry has been used to identify the reactive species in the catalytic oxidation of conventionally hard to activate C-H and C=C moieties. The identity of the reactive species under catalytic conditions has been postulated as Fe(V)=O but direct observation of this species has not been possible before. Using cryospray mass spectrometry, the Fe(V)=O reactive intermediate within the synthetic $[\text{Fe}^{\text{V}}(\text{O})(\text{OH})(\text{PyMe}_2\text{tacn})]^+$ (PyMe₂tacn = 1-(2'-pyridylmethyl)-4,7-dimethyl-1,4,7-triazacyclononane) complex at -40 °C and its reaction with an olefin was observed. Oxygen atom transfer from H₂O₂ / H₂O was followed through Fe(V)=O to the products with isotopic labelling, and the reactivity was probed as a function of temperature.

Mass spectrometry has been used as both a qualitative and quantitative tool to deduce the stoichiometry of an anion receptor and the corresponding anion. Job plots of mass spectrometry data have been compared to the conventional ¹H NMR job plot data to give corresponding results therefore providing evidence of the use of mass spectrometry as a quantitative and qualitative analytical tool.

Mass spectrometry has been used to follow the formation of heterometallic complexes and provide evidence of their building block in solution. The formation of the complexes has been followed using time-resolved mass spectrometry experiments and the building blocks analysed.

2 INTRODUCTION

2.1 Supramolecular Chemistry

Supramolecular chemistry – “chemistry beyond the molecule”. Jean-Marie Lehn coined this phrase in 1967 in his study of inclusion compounds and cryptands. During a Nobel Lecture in 1987 he went on to describe supramolecular chemistry as “organized entities of higher complexity that result from the association of two or more chemical species held together by intermolecular forces”.¹ The idea behind supramolecular chemistry came from nature, with some of the most important biological phenomena having no bond making or breaking involved instead being held together by weak, non-covalent interactions.

Supramolecular complexes have to be complementary to one another, the ‘lock and key’ principle. In 1894, Emil Fischer proposed the now famous ‘lock and key’ analogy, that enzymes interact with their substrates like a key does with its lock.² This breakthrough would lead to an ever expanding field of chemistry that would produce structures not feasible with other fields of chemistry. The most famous and important example of this complementarity is the base pairing in the DNA double helix. The complementary hydrogen bonds between base pairs complex together to form the antiparallel strands of the double helix (see Figure 1).³

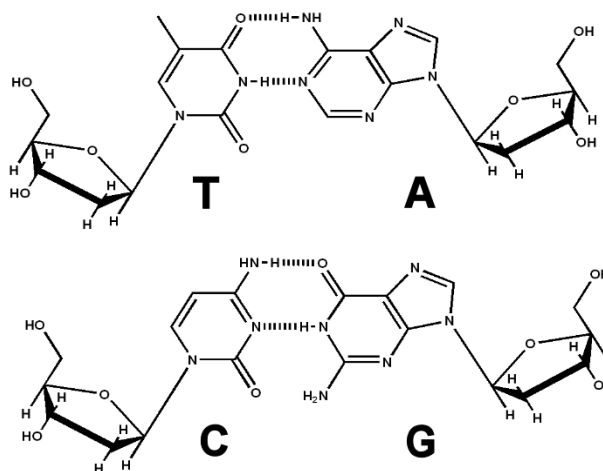


Figure 1. Hydrogen bonded complementary Adenine(A)-Thymine(T) and Guanine(G)-Cytosine(C) base pairing in DNA.

The hydrogen bond donors and acceptors on the nucleic acid bases are arranged in such a way that only adenine and thymine can hydrogen bond to one another in the same way as for guanine and cytosine.³

The design, synthesis, coordination and assembly process of a supramolecular system can be related to non-covalent interactions with a number of non-covalent interactions being utilised. They include electrostatic interactions (ion-ion, ion-dipole and dipole-dipole), hydrogen bonding, π - π interactions, dispersion and induction forces and hydrophobic or solvophobic effects.⁴⁻⁶ The bond energy of a non-covalent interaction (from 2 kJ mol⁻¹ for a dispersion force to 250 kJ mol⁻¹ for a ion-ion interaction) is generally much weaker than a covalent bond (from around 350 kJ mol⁻¹ to 942 kJ mol⁻¹ for a triple bond N₂). Therefore, supramolecular architectures are thermodynamically less stable and kinetically more labile than covalently bonded compounds and therefore a knowledge of the dynamic behaviour, i.e. the interactions between the subunits of such complexes, is critical for the control of such assemblies.^{7,8}

2.1.1 Non-covalent interactions

Electrostatic interactions (such as dipole-dipole or ion-dipole interactions) are attributed to coulombic attractions between opposite charges (see Figure 2). Ion-ion interactions have bond energies up to 350 kJ mol⁻¹⁹ and are non-directional whilst ion-dipole interactions (with bond energies from 40-600 kJ mol⁻¹)⁹ must be aligned to allow optimal binding. The strength of such interactions has been utilised by chemists to achieve strong, stable binding e.g. cation and anion binding.¹⁰

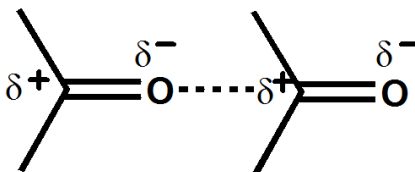


Figure 2. A dipole-dipole electrostatic interaction.

A hydrogen bond is an attractive force between a hydrogen atom bonded to a very electronegative atom (O, N or F) and an unshared electron pair on another electronegative atom. Hydrogen bonds arise because the O-H, N-H and F-H bonds are highly polar, with a partial positive charge on the hydrogen and a partial negative charge on the electronegative atom. Along with its small size, the hydrogen atom has no core electrons to shield its nucleus and so can be approached closely by other molecules resulting in a strong dipole-dipole attraction (see Figure 3). The bonds can occur intermolecularly i.e. between two different molecules, or intramolecularly i.e. between two functional groups in the same molecule. An example of such interactions can be seen in the DNA double helix (see Figure 1). The directional nature of hydrogen bonding means that the design of molecules capable of hydrogen bonding has to be precise, making the design of such molecules interesting.¹¹

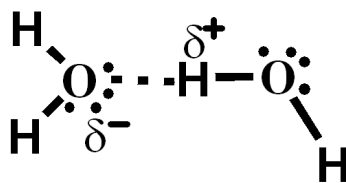


Figure 3. A hydrogen bond between a hydrogen atom and an electronegative oxygen.

Dispersion interactions (or induced dipole-dipole interactions) are attractive forces that occur when instantaneous dipoles in electron clouds interact with each other. These Van der Waals forces (also called London forces after Fritz London who first postulated the idea of such interactions) are non-directional and so receptors that take advantage of this type of interaction are hard to design and synthesise.¹²

π - π stacking interactions occur in systems containing delocalised aromatic substituents. Such interactions can either be ‘face-to-face’ or ‘edge-to-face’ (see Figure 4). The ‘edge-to-face’ arrangement can be described as weak hydrogen bonds between the electrodeficient hydrogen of one molecule and the negatively charged π -electron system of the other molecule.¹³ ‘Face-to-face’ motifs are held together by a number of contributing factors, these being dipole-dipole interactions, electrostatic interactions, London dispersion forces and system dependent factors such as solvophobic effects and polarisation of the π -

electron system due to substituents on the aromatic ring. They can be found in a number of systems ranging from biological to crystal engineering to coordination chemistry.^{3,14,15}

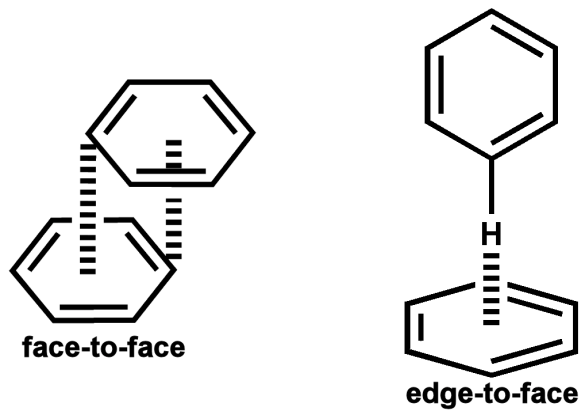


Figure 4. π - π stacking interactions.

The hydrophobic effect allows the formation of apolar binding partners in aqueous solution. Water molecules from an apolar hydrophobic pocket will be released by the binding of a guest and become disordered, leading to a favourable increase in entropy (see Figure 5). There is also an enthalpic force for apolar guest coordination as the hydrogen bonds between water molecules are larger and therefore more favourable than the interactions between the water molecules and the apolar solutes, due to the water molecules being able to maximise their hydrogen bonding interactions once released into the bulk solvent.¹⁶

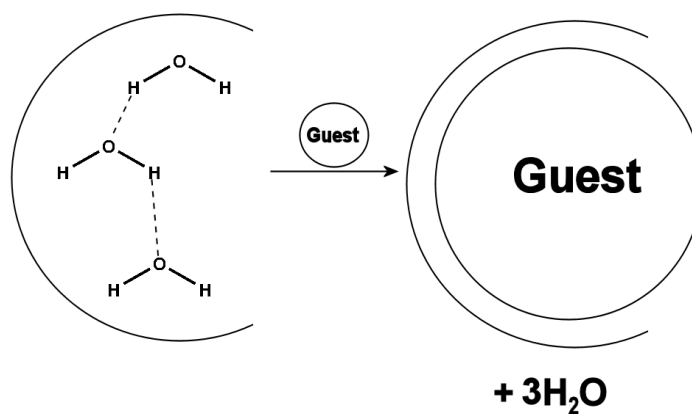


Figure 5. Hydrophobic effect where an increase in disorder, ΔS , causes a guest to enter the hydrophobic pocket releasing disordered water.

Classic coordination chemistry can also come into play when describing supramolecular interactions. Although it is not technically a non-covalent interaction, the coordination of metals by donation of two electrons from a ligand to form a dative bond has been used to construct complex topologies such as cantananes and molecular grids.¹⁷

2.1.2 Design strategies

The design of the ligand is vitally important in supramolecular chemistry. If the design is not complementary to the architecture then the system will not form. Ligand design can be used to implement such a strategy where the pre-determined aim can be obtained simply.

Coordination chemistry ligands can be described as a molecular species that possesses at least one lone pair of electrons in an accessible electronic orbital allowing them to form a coordination bond with a metal centre.^{18,19} The geometry of the ligand is important i.e. are the binding sites positioned correctly to allow optimal binding with the degree of structural rigidity also being important in the design of supramolecular coordination complexes. If two or more binding sites are brought close to one another it is likely that there will be multiple coordination to one metal ion but if the binding sites are held further apart then a bridging mode is likely to be favoured.^{20,21} The overall product will then gain its topology from the geometry of the metal ion and its ligand. Therefore, it is important when designing a ligand to have some degree of flexibility along with multiple discreet binding sites to achieve a stable supramolecular complex. Too much structural rigidity prevents the ligand from being able to move in such a way as to take full advantage of its multiple binding sites and so reduces the potential binding modes of the ligand.²²

2.1.3 d-Block Chemistry

d-block metals have a total of 5 valence orbitals, some of these being used to form bonds with ligands with the others being non-bonding. The general rule for the geometry

of many coordination complexes is that the ligands are set as far apart as possible from each other.

d-block metal ions readily form complexes with complexation often being accompanied by a change in colour (see Figure 6) and can have a variety of coordination modes. The colour is generated from the partially filled *d*-orbitals where energy from white light passing through a solution of the complex is used to promote an electron from the lower set of t_{2g} orbitals up to a partially filled or unfilled orbital in the e_g orbital level.

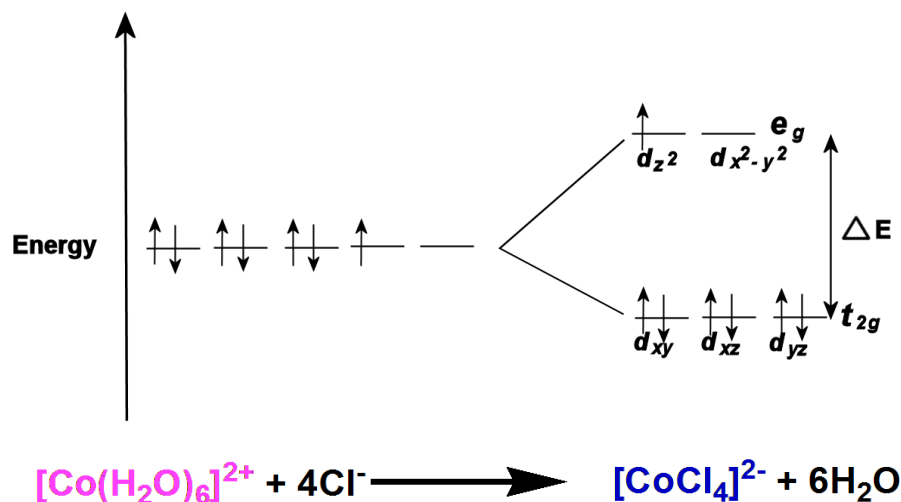


Figure 6. Octahedral *d*-orbital energy level diagram showing the unfilled and partially filled d_{x^2} and $d_{x^2-y^2}$ orbitals for Co^{2+} ions and an equation showing change in colour when complexation occurs.

The size of the energy gap varies with the nature of the transition metal ions, the oxidation state and the nature of the ligands where different ligands have different effects on the energies of the *d*-orbitals of the central ion. Some ligands will have a strong electrical field which causes a large energy gap while ligands with much weaker fields will give a smaller energy gap (see Figure 7). It is the size of this energy gap that determines what wavelength of light is going to be absorbed and hence what colour will be observed in solution. In the case of $[\text{Co}(\text{H}_2\text{O})_6]^{2+}$ the solution would be a pink colour due to the relatively large splitting effect the water ligands have on the *d*-orbitals with the energy gap absorbing in the ultraviolet region of the visible light spectrum. When the water ligands are replaced with chloride ligands in a tetrahedral geometry the energy splitting effect of the ligands is

smaller than that seen with water and so the energy is absorbed more towards the infra-red region of the visible light spectrum and so giving a blue coloured solution.

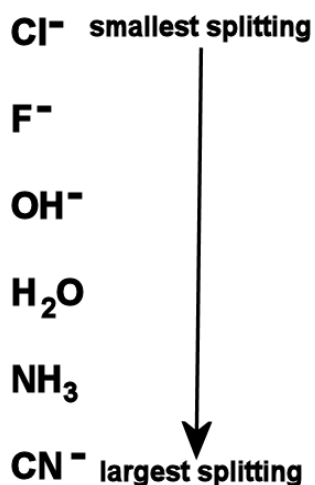


Figure 7. Common ligands used in the complexation with d-block metals and the energy splitting effects they have on t_{2g} and e_g orbitals.

2.1.4 Coordination number two

d -block metal compounds of coordination number two are generally uncommon and are restricted to d^{10} ions such as Cu(I), Ag(I), Au(I) and Hg(II). Examples of such are $[\text{CuCl}_2]^-$, $[\text{Ag}(\text{NH}_3)_2]^+$ and $[\text{Au}(\text{CN})_2]^-$, the metal centre of each being in a linear environment.

2.1.4.1 Coordination number three

d -block metal compounds of coordination number three are also uncommon and are usually found in an approximately trigonal geometry with d^{10} ions. In many cases, the metal is prevented from bonding to more than three ligands by the steric shielding of the ligands. Examples of such compounds are $[\text{Cu}(\text{Me}_3\text{PS})_3]^+$ and $[\text{Pt}(\text{PPh}_3)_3]$.²³

2.1.4.2 Coordination number four

This type of coordination compound is very common with the tetrahedral geometry being most often observed. They can be found in a number of oxidation states from d^0 to d^{10} . Simple tetrahedral species include: d^0 : $[\text{VO}_4]^{3-}$, $[\text{CrO}_4]^{2-}$; d^1 : $[\text{MnO}_4]^{2-}$, $[\text{RuO}_4]^-$; d^2 : $[\text{FeO}_4]^{2-}$, $[\text{RuO}_4]^{2-}$; d^5 : $[\text{FeCl}_4]^-$, $[\text{MnCl}_4]^{2-}$; d^6 : $[\text{FeCl}_4]^{2-}$, $[\text{FeI}_4]^{2-}$; d^7 : $[\text{CoCl}_4]^{2-}$; d^8 : $[\text{NiCl}_4]^{2-}$, $[\text{NiBr}_4]^{2-}$; d^9 : $[\text{CuCl}_4]^{2-}$; d^{10} : $[\text{ZnCl}_4]^{2-}$, $[\text{HgBr}_4]^{2-}$.

Square planar complexes are rarer than tetrahedral complexes and are usually associated with d^8 configurations where Jahn-Teller distortions force a square planar geometry e.g. $[\text{PdCl}_4]^{2-}$ and $[\text{PtCl}_4]^{2-}$.

2.1.4.3 Coordination number five

Compounds with a coordination number of five usually have trigonal bipyramidal and square pyramidal geometries. Most structures lie within the two geometries, with the energy differences between the two being small. Trigonal bipyramidal structures are often d^{10} species such as $[\text{CdCl}_5]^{3-}$, $[\text{HgCl}_5]^{3-}$ and $[\text{NiCN}_5]^{3-}$ with the square pyramidal complexes such as $[\text{NbCl}_4\text{O}]^-$ (d^0), $[\text{WCl}_4\text{O}]^-$ (d^1), $[\text{ReCl}_4\text{O}]^-$ (d^2).

2.1.4.4 Coordination number six

Octahedral complexes are common and have a coordination number of six. They can be found with electronic configurations of d^0 to d^{10} e.g. $[\text{TiF}_6]^{2-}$ (d^0), $[\text{Ti}(\text{H}_2\text{O})_6]^{3+}$ (d^1), $[\text{V}(\text{H}_2\text{O})_6]^{3+}$ (d^2), $[\text{Cr}(\text{H}_2\text{O})_6]^{3+}$ (d^3), $[\text{Mn}(\text{H}_2\text{O})_6]^{3+}$ (d^4), $[\text{Fe}(\text{H}_2\text{O})_6]^{3+}$ (d^5), $[\text{Fe}(\text{H}_2\text{O})_6]^{2+}$ (d^6), $[\text{Co}(\text{H}_2\text{O})_6]^{2+}$ (d^7), $[\text{Ni}(\text{H}_2\text{O})_6]^{2+}$ (d^8), $[\text{Cu}(\text{NO}_2)_6]^{2+}$ (d^9) and $[\text{Zn}(\text{H}_2\text{O})_6]^{2+}$ (d^{10}), with each of these complexes being high-spin. An example of a low-spin complex is $[\text{Mn}(\text{CN})_6]^{3-}$ (d^4). The d^4 and d^9 metal complexes tend to be distorted by Jahn-Teller forces.²⁴

Complexes of coordination number seven, eight, nine and above are observed for ions of the early second and third row *d*-block metals but are less common. Ligand-ligand interactions are more important with the higher coordination numbers and so it tends to be smaller ligands which allow these coordination numbers.

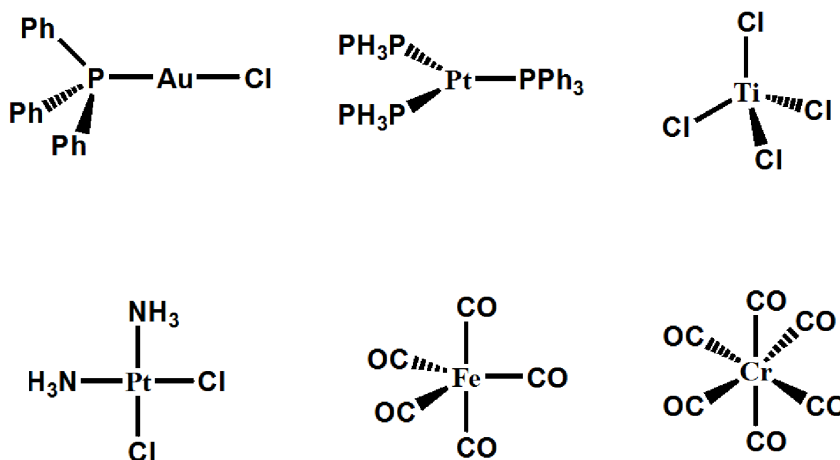


Figure 8. Examples of coordination complexes ranging from linear (two ligands) to octahedral (six ligands).

2.1.4.5 Lanthanides and actinides

The lanthanides and actinides are collectively known as the inner transition metals. The large size of these metals means that high coordination numbers are common. The splitting of the degenerate *f* orbitals in crystal fields is small ($\Delta_{\text{oct}} \sim 1 \text{ kJ mol}^{-1}$) with preference between different coordination numbers and geometries being controlled by steric effects. Most inorganic compounds and coordination complexes containing lanthanides are found in the +3 oxidation state, but a wider variation of oxidation number is observed for the actinide metals. Examples of inner transition metal complexes are $[\text{Ln}(\text{OH})_6]^{3-}$ and CeF_4 for the lanthanides and UCl_5 for the actinides (with this complex usually being found as a dimer).

2.1.4.6 The Chemistry of 1,3,5-triaminocyclohexane

The triamine cyclohexane ligand 1,3,5-triaminocyclohexane can be used in ligand design due to the directing nature of its two isomers, *cis,cis*-1,3,5-triaminocyclohexane (*cis*-tach, 2) and *cis,trans*-1,3,5-triaminocyclohexane (*trans*-tach, 3) (see Figure 9). *Cis*-tach is made up of a cyclohexane backbone with three triequatorial amino groups or the ring-flipped triaxial conformation (in the chair conformation). The coordinating properties of *cis*-tach have been thoroughly investigated where the ring-flipped structure forms a face-capping, tridentate ligand which can coordinate to a number of first row transition metals such as chromium(III) and cobalt(III) where *cis*-tach is used as a capping ligand to generate metal-cyanide cage clusters.²⁵

Cis-tach can also be coordinated with silver(I) ions to form polymeric silver(I) coordination tubes. In this case one *cis*-tach molecule coordinates to a silver(I) ion through each of its nitrogens, which hydrogen bond to each other through a triflate counterion to form one-dimensional tubes.²⁶

Cis-tach can also be used in the synthesis of Zn-based artificial nucleases. For example, Zagotto *et al* have published zinc(II)-(*cis*-tach) intercalators which have been shown to be DNA cleaving agents.²⁷ The means by which this ligand carries out intercalation of the DNA is through the use of a *cis*-tach platform with alkyl chains linked to an anthraquinone group which is able to intercalate to the DNA. Zinc(II) was the active metal of choice due to it being a strong Lewis acid and the fast rate which it can exchange its ligands, while *cis*-tach was used as one site can be derivatised for intercalation while coordination of a first row transition metal is still allowed. It was also shown that the coordination of the Zn(II) to the *cis*-tach leads to a 15-fold increase in activity when compared to the complex minus the Zn(II) centre.

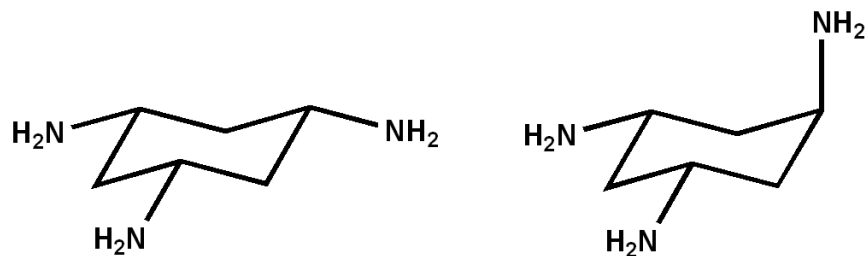


Figure 9. isomers *cis,cis*-1,3,5-triaminocyclohexane and *cis,trans*-1,3,5-triaminocyclohexane.

Cis,trans-1,3,5-triaminocyclohexane (*trans*-tach) can be found in two conformational forms: *bisaxial*-*monoequatorial* and *bisequatorial*-*monoaxial* (see Figure 10). It has two distinctive sites suitable for both metal ion coordination and protonation, allowing for the formation of polynuclear and extended hydrogen bonded architectures.

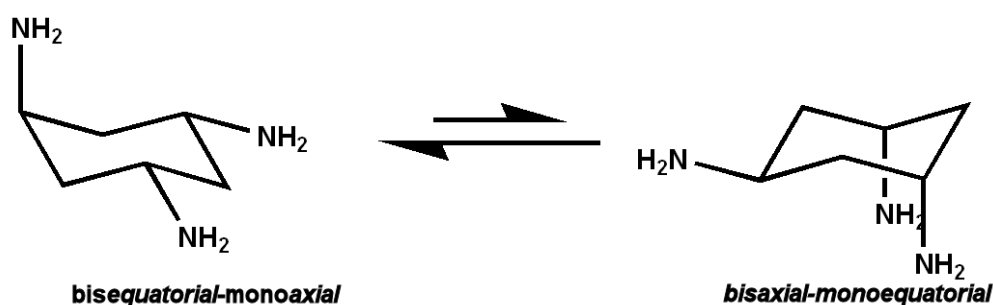


Figure 10. The two conformers of *trans*-tach with the equilibrium more towards the *bisequatorial*-*monoaxial* conformation when un-coordinated.

Recently a paper has been published by Cronin *et al* where the *bisaxial*-*monoequatorial* isomer has been seen to complex copper(II) salts (CuF_2 and CuSO_4) and form self-assembled nanoscale networks through coordination and hydrogen bonding interactions.²⁸ The resulting complex with CuF_2 and HF produced a tetranuclear cubane-type structure where four protonated *trans*-tach ligands, each with one metal centre and one oxo ligand, come together when the four capped *trans*-tach ligands and the four oxo ligands are placed alternatively on the vertices of the cube. When CuSO_4 was used along with H_2SO_4 a diligand complex was formed where the two axial groups of two *trans*-tach ligands are coordinated to the copper(II) centre in a tetragonal pyramidal coordination sphere. Even

though the building blocks are relatively simple and similar, the extended networks of the two molecules are very different. The cubanes that are formed with CuF_2 come together to surround a disordered methanol in a truncated octahedral cage structure. These structures in turn assemble into a three dimensional supramolecular MOF architecture. Three diligand molecules formed from *trans*-tach and CuSO_4 arrange in a trigonal fashion around disordered methanol which then further arrange into paired trigonal prismatic units. These paired units then coordinate together via their edges to give a three dimensional nanotube architecture (see Figure 11).

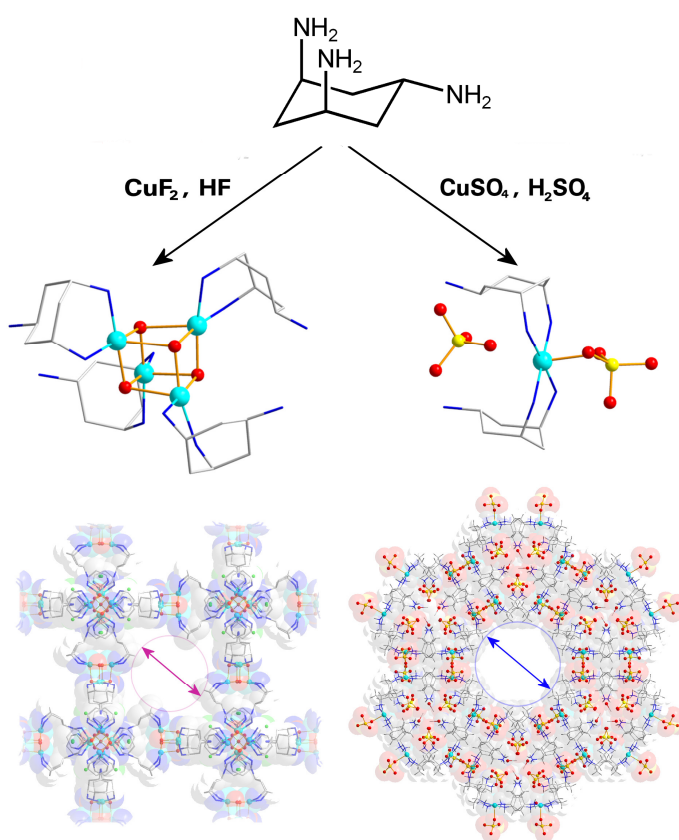


Figure 11. Schematic showing the difference in architecture formed when *trans*-tach is reacted with CuF_2 and CuSO_4 .²⁸

Trans-tach can also be used to template high-nuclearity $\{\text{Ni}_{12}\}$ and $\{\text{Co}_{12}\}$ architectures.²⁹ Here, *trans*-tach was used in conjunction with a bridging acetate and templating carbonate ligands to form $\{\text{M}_{12}\}$ coordination clusters. The $\{\text{Co}_{12}\}$ cluster was prepared by the addition of cobalt(II) acetate to a solution of *trans*-tach (with addition of

perchloric (or acetic) acid to obtain a pH of 8.5, giving a purple solution from which crystals of $[\text{Co}^{\text{II}}_{12}(\text{trans-tachH})_6(\text{OH})_{12}(\text{OAc})_9(\text{CO}_3)](\text{ClO}_4)_7 \cdot 12\text{MeOH}$ were isolated. The same was carried out with nickel(II) acetate but leaving the pH unchanged to yield green crystals of $[\text{Ni}^{\text{II}}_{12}(\text{trans-tachH})_6(\text{OMe})_{12}(\text{OAc})_9(\text{CO}_3)](\text{OAc})_7 \cdot 10\text{MeOH} \cdot 6\text{H}_2\text{O}$. The only difference between the core of the two structures is the number of μ_3 -hydroxo and μ_3 -methoxy groups found in the cubane units, but the crystal packing of the two structures differed. With the $\{\text{Ni}_{12}\}$ architectures the hydroxy ligands in the outer face cubane vertices also hydrogen bond to solvent molecules leading to a hexagonal crystal system, while for $\{\text{Co}_{12}\}$ no hydrogen bonding to solvent takes place therefore leading to an orthorhombic system (see Figure 12).

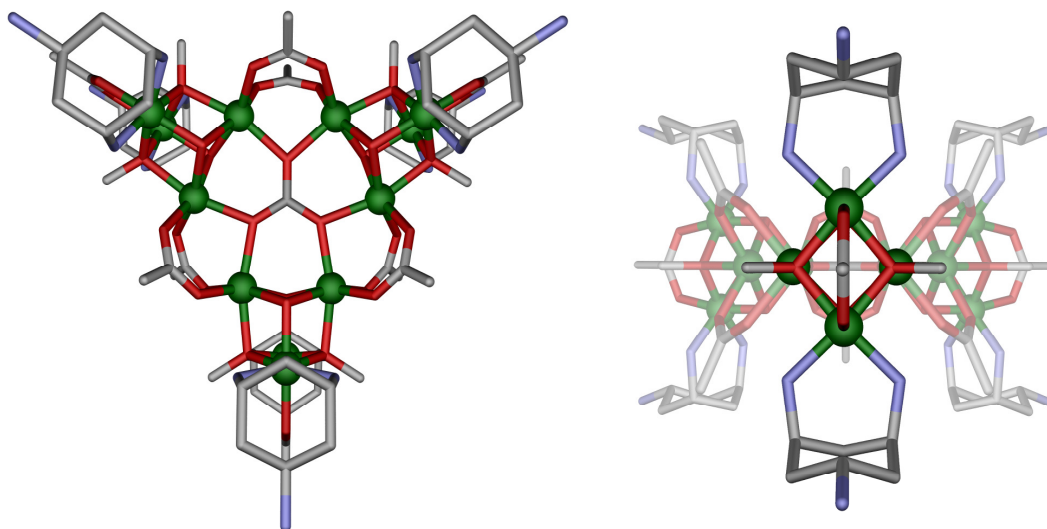


Figure 12. Structure of the $\{\text{Ni}_{12}\}$ complex along the C_3 axis (left) and the C_2 axis (right).²⁹

2.1.4.7 The chemistry of *cis,trans*-1,3,5-tris(pyridine-2-carboxaldimino) cyclohexane (ttop)

The ligand *trans*-ttop consists of a cyclohexane backbone with three pyridine groups attached through an imine bond. In the lowest energy isomer three binding sites are open for independent coordination whilst in the ring-flipped conformation both a

tetradentate and a bidentate chelating site are formed. This ligand will be discussed later in this thesis (see section 3).

Over the years much research has looked at the synthesis and properties of *cis,cis*-1,3,5-tris(pyridine-2-carboxaldimino)cyclohexane (*cis*-ttop) (see Figure 13). It has been observed that it will coordinate exclusively in the tris-axial conformation via the hexadentate chelating pocket, where one metal centre is coordinated by three imine and three pyridyl nitrogens. A preferred octahedral geometry is the most widely observed with metal centres such as copper(II),³⁰ zinc,^{30,31} iron(II),³² cobalt(II),^{30,32} nickel(II),³⁰ manganese(II),³⁰ indium(II),³¹ gallium(III),³³ mercury(III) and cadmium(II).³¹ being used.

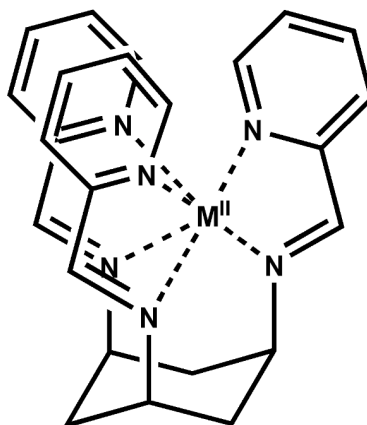


Figure 13. Complex of *cis*-ttop.

A derivative of *cis*-ttop, 1,3,5-tris[(2-pyridylmethyl)amino]cyclohexane (tachpyr) (see Figure 14), has been shown to readily complex divalent 3d transition metals and has been studied as a chemotherapeutic agent.^{30,31,34,35} This molecule has been seen to be strongly cytotoxic to a variety of tumour cells as well as binding to zinc(II) and Fe(II) in cells. As metal complexes are known to promote oxidative damage by catalysing production of OH, O₂ and other radicals, the tachpyr molecule was researched to show if the molecule could kill cancer cells by either deprivation of essential biometals required for cell growth and/or oxidative damage. A number of different first row transition metal ions were coordinated to the tachpyr ligand, the metals being manganese, iron, nickel, copper and zinc, to form the complex [M^{II}(tachpyr)]²⁺. The results showed that tachpyr and its derivatives are effective chelators and have cytotoxic properties.³⁶

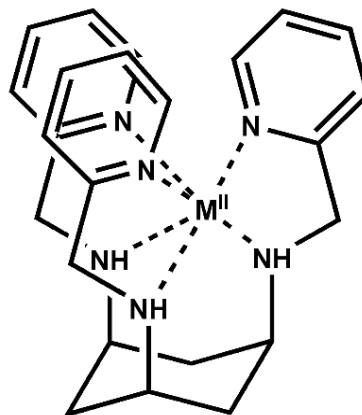


Figure 14. Complex of tachpyr.

2.2 Mass spectrometry in Inorganic Chemistry

Due to the labile nature of supramolecular complexes the techniques used to analyse such complexes need to reflect the weak character of the bonds formed. Mass spectrometry (electrospray and cryospray ionisation) is one such technique that can be used to analyse supramolecular complexes.

Mass spectrometry is considered to be unique when compared to typical analytical techniques such as UV/vis or FTIR spectroscopy.³⁷ For any given analyte, the MS response of the species in solution can be accurately calculated from its mass and charge using the relative isotope distribution of the elements involved. Mass spectrometry also has an advantage in that the theoretical response can be calculated very accurately from relative ion abundances and have a discrete function of mass-to-charge (m/z) values. This means that the non-zero ion abundances can only be observed at the m/z values that correspond to the isotopic abundances of the species analysed. Mass spectrometry will also allow the resolution of major isotope clusters giving not only information on the mass and composition of the species but also the charge.

Early mass spectrometers produced a large amount of data that the computers of the time could not process. To overcome this problem the acquired raw MS data was reduced

into a stick spectrum, or centroid data in a process known as centroiding (a centroid being the centre of gravity of a detected peak).³⁸ The problem with this type of data processing meant that a lot of information such as noise characteristics, interfering ions and isotope fine features was lost. Nowadays centroiding is not so important due to the data storage and processing abilities available today, but is still used on many mass spectrometers and will still be discussed in this chapter as a background to mass spectrometry (see Figure 15).

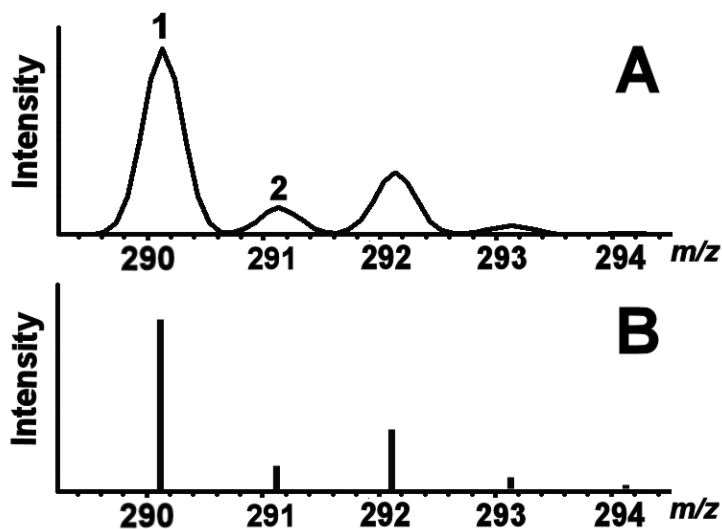


Figure 15. A. Raw data MS profile of $[\text{C}_6\text{H}_{12}\text{N}_3(\text{C}_2\text{H}_3\text{O})_3\text{Cl}]^+$; B. MS profile of $[\text{C}_6\text{H}_{12}\text{N}_3(\text{C}_2\text{H}_3\text{O})_3\text{Cl}]^+$ after centroiding.

For a small organic species, $[(\text{C}_6\text{H}_{12}\text{N}_3)(\text{C}_2\text{H}_3\text{O})_3\text{Cl}]^+$, the isotope distribution is relatively simple compared to those compounds containing metals. The first peak in the envelope, 1 (see Figure 15), is called the monoisotopic peak because it comes from the combination of the lightest isotopes of all the elements present in the species. The next peak, 2 (see Figure 15), can be obtained from more than one combination of the isotopes, e.g. one ^{13}C and the lightest isotopes for all the other elements and one ^{37}Cl and all the other lightest isotopes for the rest of the elements, with all the different isotope combinations forming an isotopic envelope that is distinct for that species. A number of different species can be assigned to the same m/z values and so raw data without centroiding has to be used to ascertain which species has the best fit. The high mass positioning accuracy from high resolution mass spectrometers can be obtained from the

monoisotope peak but the other peaks present in the envelope are needed to determine the correct formula.

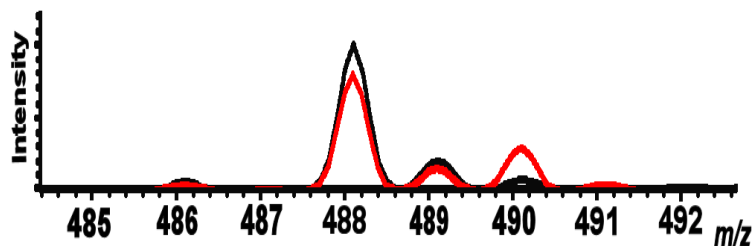


Figure 16. MS simulated raw data for $[\text{C}_{14}\text{H}_{24}\text{N}_4\text{Fe}(\text{CF}_3\text{SO}_3)(\text{OH})(\text{H}_2\text{O})]^+$ (black) and $[\text{C}_{14}\text{H}_{24}\text{N}_4\text{Fe}(\text{CF}_3\text{SO}_3)(\text{Cl})]^+$ (red).

From Figure 16 it can be seen that high resolution mass spectrometers can produce enough raw data to differentiate between the different species i.e. the shape of each envelope is slightly different. Isotope clusters with more elements present, and therefore more complex, will have more isotope fine features overlapping and so the need for analysis of the raw data and not the centroid data is needed.

The information obtained from a mass spectrometer is a continuous response curve similar to the spectrum shown in Figure 15 (top), which is a mathematical convolution between the discrete theoretical isotope distribution and a continuous function called the peak shape function. The spectrum can then be explained as a numerical representation of the spatial and velocity dispersion of the ions in the source. On a typical Time-of-flight mass spectrometer (TOFMS) the peak shape function, which can be described as a sharp rise followed by a slower decline, can be explained by the arrival time distribution of a population of isotopically pure ions, which have different arrival times due to their different molecular weights. This means that different species will collide with the various lenses at different times due to their different energies and velocities within the flight tube.³⁷

One of the most important aspects of mass spectrometry is the type of ionisation used, with the type used being dependent upon how stable the material is. The two main

types of ionisation techniques are Hard ionisation and Soft ionisation. Hard ionisation techniques are modes of ionisation that will produce significant enough energy to fragment the compound whilst the soft ionisation technique will only ionise the species and so can be used for labile species such as supramolecular and coordination compounds.^{39,40} Fast Atom Bombardment (FAB), Matrix Assisted Laser Desorption Ionisation (MALDI) and Electrospray Ionisation (ESI-MS) are all types of soft ionisation whilst Atmospheric Pressure Chemical Ionisation is a hard technique. FAB and MALDI techniques are both effective and quick when analysing singly charged, small organic compounds but both have drawbacks. FAB can only be used for species that come within the m/z range of 200-2000 but is fast and accurate, while with MALDI species at higher m/z ranges can be resolved well but species of a higher charge than 1 cannot be resolved. Another technique that can be used is called Cryospray Ionisation Mass Spectrometry (CSI-MS) which allows the formation of highly unstable species using cryogenic conditions.^{28,41} The majority of the mass spectral analysis in this research will be carried out in Electrospray Ionisation Mass Spectrometry (ESI-MS) (see Figure 17) or Cryospray Ionisation Mass Spectrometry (CSI-MS) as both techniques allow the resolution of labile, highly charged species at varying temperatures.

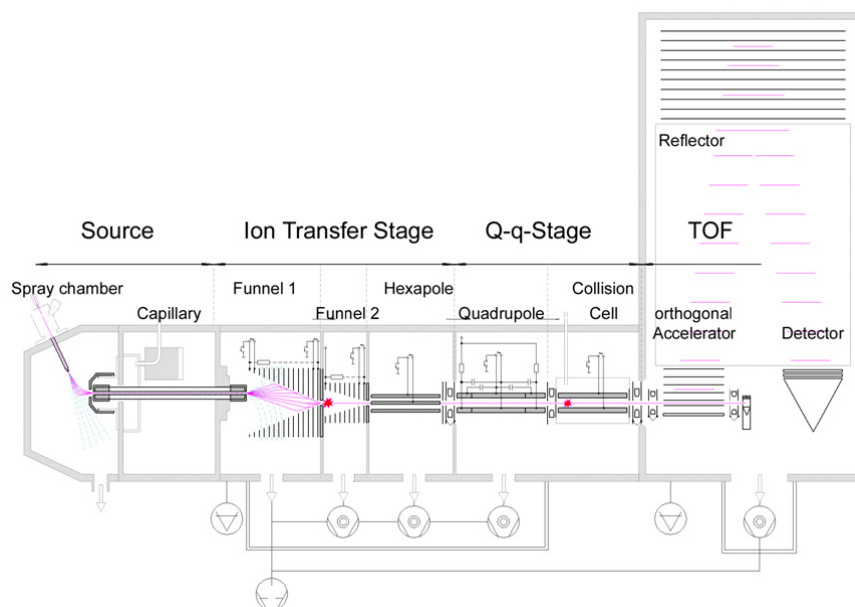


Figure 17. Representation of a microOTOF-Q mass spectrometer with an electrospray ionisation source.⁴²

Ion sources exist under two types: liquid-phase and solid-state. For liquid-phase mass spectrometry the compound to be analysed is in solution. This solution is then introduced into the spray chamber through a nebuliser where the solution comes into contact with a nebuliser gas, usually nitrogen. The solution is then dispersed into small charged droplets which are introduced into the mass spectrometer through a glass capillary. Electrospray ionisation (ESI), Atmospheric Pressure Chemical Ionisation (APCI) and Atmospheric Pressure Photoionisation (APP) are all types of liquid-phase ion sources. In solid-state ion sources, such as that used for MALDI, the analyte is transferred onto matrix where it will co-crystallise. The matrix is then irradiated with photons that desorb ions near the surface which then in turn ionise the analyte by protonation and deprotonation. FAB is also a type of solid-state ionisation (see Figure 18).

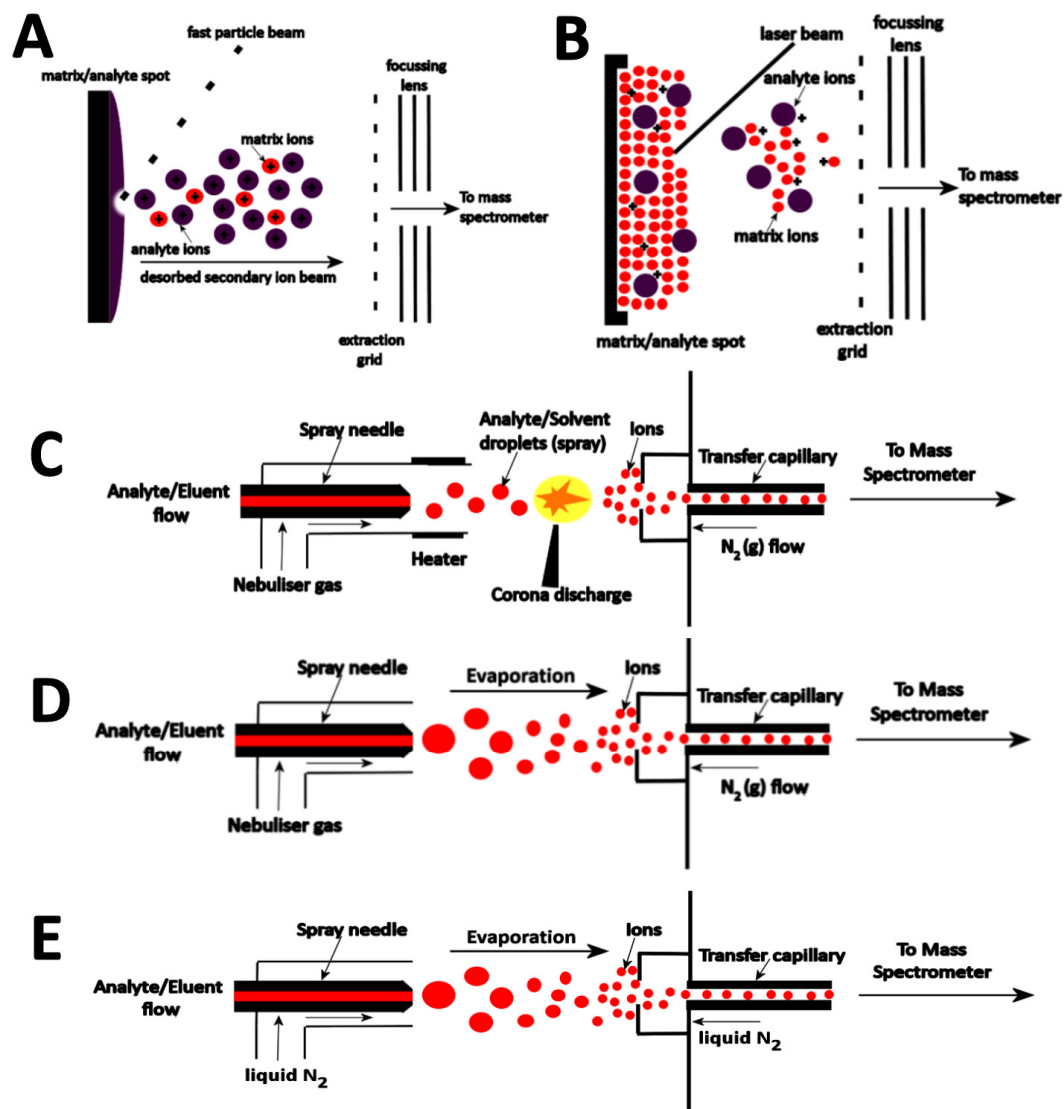


Figure 18. Schematic representation five different types of mass spectrometry ionisation - A) fast atom bombardment ionisation (FAB), B) Matrix Assisted Laser Desorption Ionisation(MALDI), C)Atmospheric Pressure Chemical Ionisation (APCI), D) Electrospray Ionisation Mass Spectrometry (ESI-MS) and E) Cryospray Ionisation Mass Spectrometry (CSI-MS).⁴³

Cryospray mass spectrometry (CSI-MS) was first introduced by Yamaguchi *et al* in 2000 where labile metal-organic coordination clusters were observed in the mass spectrometer.⁴⁴ Labile complexes such as adamantanoid type Pt(II) complexes were compared in both electrospray and cryospray ionisation modes to show that the softer CSI-MS does not fragment unstable species like electrospray allowing the analysis of labile,

reactive species (see Figure 19). The higher temperature of the electrospray ionisation (from room temperature to temperatures beyond 180 °C) can also cause decomposition of unstable species and so cryospray ionisation (which works at temperatures down to approx. -60 °C depending on the solvent used) can be used to work at lower temperatures, therefore removing decomposition from the factors that do not allow mass spectral analysis.

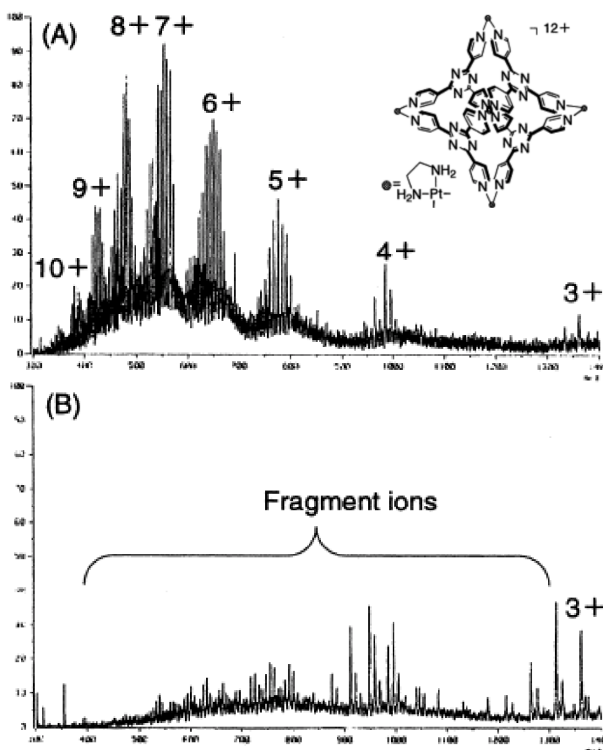


Figure 19. Spectral comparison between A) CSI-MS and B) ESI-MS.⁴⁴

Cronin *et al* used ESI and CSI-MS to investigate the self-assembly of labile, cluster based supramolecular systems in solution.⁴¹ In one example, mass spectrometry is used to understand the self-assembly process by which $(\text{TBA}_{2n}[\text{Ag}_2\text{Mo}_8\text{O}_{26}]_n)$ is produced. The rearrangement of the Lindqvist anions ($\text{M}_6\text{O}_{19}^{n-}$) into the $\{\text{Ag}(\text{Mo}_8)\text{Ag}\}$ synthons and the subsequent formation of the TBA salt was observed by following the real-time formation of the building blocks. The species identified within the results were (i) $[\text{Mo}_m\text{O}_{3m}]^-$ where $m = 2, 3$ or 5 ; (ii) $[\text{HMo}_m\text{O}_{3m+1}]^-$ where $m = 2$ to 6 ; (iii) $[\text{H}_7\text{Mo}_m\text{O}_{3m+2}]^-$ where $m = 2$ to 6 ; (iv) $[\text{H}_7\text{Mo}_m\text{O}_{3m+3}]^-$ where $m = 2$ to 5 ; (v) $[\text{H}_9\text{Mo}_m\text{O}_{3m+4}]^-$ where $m = 2$ to 6 ; (vi) $[\text{AgMo}_m\text{O}_{3m+1}]^-$ where $m = 2$ to 4 (see Figure 20).

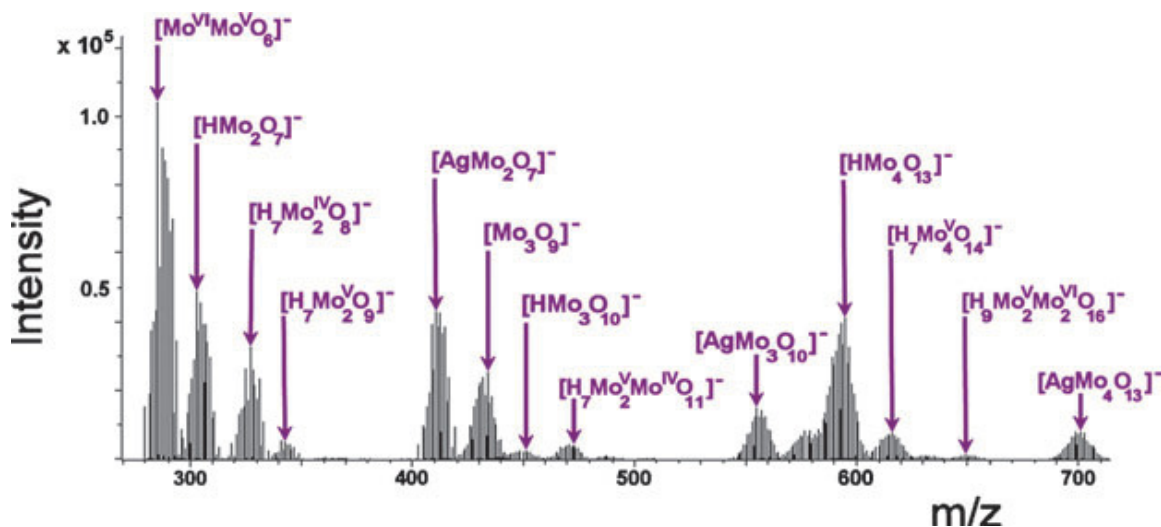


Figure 20. CSI-MS data collected for the reaction solution. The six mono-anionic series identified within these results are highlighted. The steps towards the assembly of the $\{\text{Ag}(\text{Mo}_8)\text{Ag}\}$ synthon units can be observed by examination of anion series (vi) which highlights the role of the Ag^+ in the re-arrangement process of these clusters. Of particular note from this series are the peaks at 410.7 m/z and 700.5 m/z which are attributed to the species $[\text{AgMo}_2\text{O}_7]^-$ and $[\text{AgMo}_4\text{O}_{13}]^-$, respectively.⁴¹

The results published by Cronin *et al* detected a $[\text{AgMo}_2\text{O}_7]^-$ fragment at 410 m/z which they state supports the theory that the Lindqvist anion rearranges into $[\text{AgMo}_2\text{O}_7]^-$. The species $[\text{AgMo}_4\text{O}_{13}]^-$ at 700.5 m/z was said to be half of the $\{\text{Ag}(\text{Mo}_8)\text{Ag}\}$ unit and so is probably the next step in the formation of the silver-linked octamolybdate species. The group had also previously postulated that organic cations will have a structure-directing effect on the formation of the POM.⁴⁵ The work carried out using CSI-MS detected species $[(\text{AgMo}_8\text{O}_{26})\text{TBA}_2]^-$ (peak at 1776.6 m/z), $[(\text{Ag}_2\text{Mo}_8\text{O}_{26})(\text{Mo}_4\text{O}_{13})\text{TBA}_3]^-$ (peak at 2718.3 m/z) and $[(\text{Ag}_2\text{Mo}_8\text{O}_{26})(\text{Mo}_8\text{O}_{26})\text{TBA}_5]^-$ (peak at 3796.5 m/z) showing an increase in organic cation contribution. This observation can be said to be the beginning of the self-assembly process where the monomeric units assemble into the larger fragments.

In the work that will be reported in this thesis both electrospray and cryospray ionisation will be used to look at reaction mechanisms, binding stoichiometries and the self-assembly of labile architectures.

2.3 Anion binding

An anion receptor (or binder) is a molecule that contains an electron deficient moiety that is able to accept the electron pair donor of an electronegative anion and hence form a host-guest complex. Anions can be found in many biological and chemical systems, from catalysts to pollutants in the environment.

Anion binders can be used in medicine, catalysis and molecular recognition with research into the supramolecular chemistry of anion binding yielding methods to achieve the sensing of anionic guests in organic media and the development of highly selective anion transporters with the potential to become future therapeutics.⁴⁶⁻⁴⁸

Compared to cation binding, anion binding is a relatively new research area with the design of anion receptors coming with its own challenges. To strongly bind an anion a number of anionic properties have to be taken into account. Compared to their positive counterparts, anions are larger with a smaller charge to radius ratio therefore their electrostatic interactions can be less effective. They also do not have uniform shapes and so challenge the designer to create a complementary binding site. Therefore, the design of an anion binder has to take into consideration a number of factors. Receptors to bind spherical anions such as chloride and bromide can be simple, whilst those with a more complex shape like $[\text{Fe}(\text{CN})_6]^{4-}$ require a more elaborate host. Also many anions (e.g. carboxylates) are pH dependent, at low pH they become protonated and lose their negative charge. Solvation can also play a part in binding selectivity. A hydrophobic binding site will allow the less hydrated anions to bind, whilst a site that can be easily accessed by polar solvents the more hydrated anions will bind. The degree of aqueous solvation of an anion is shown in the Hofmeister series (see Figure 21).

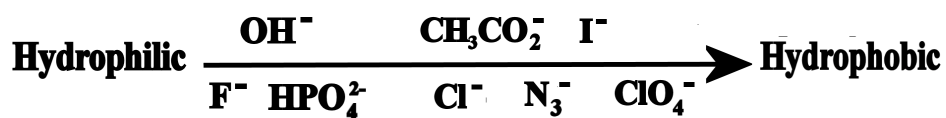


Figure 21. The Hofmeister series showing increasing hydrophobicity of anions.

2.3.1 Electrostatic interactions in anion binding

The most simple way to bind an ion is with electrostatic ion-ion interactions. The negatively charged anion will be attracted to the positively charged receptor. To stabilise such a structure more than one positively charged moiety can be built into the molecule, but such an array can cause problems due to repulsion. The constraint of such a molecule comes from rigid or cyclic structures that also serve as a binding cavity (see Figure 22).

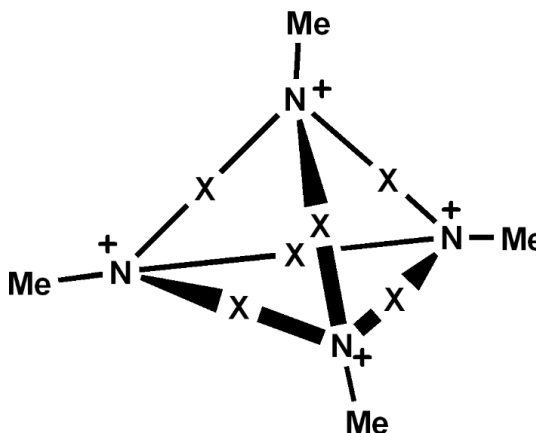


Figure 22. Receptor with an electron deficient cavity suitable for anion binding (where $x = (\text{CH}_2)_6$ or $(\text{CH}_2)_8$).

Schmidtchen *et al* published a structure that, due to its corners containing quaternary nitrogens, can form 1:1 complexes with electron rich anions.⁴⁹ The size of the cavity formed could also be controlled by the number of carbons contained in the X group i.e. a larger cavity can bind larger anion like iodide while the smaller cavity can bind anions such as chloride. The only problem with this type of molecule was that to remain stable a counterion was needed which usually competed with the anion for the binding site. This problem was addressed by synthesising zwitterionic hosts (see Figure 23) which had no net charge, therefore proving that this type of molecule could bind anions by electrostatic interactions alone.

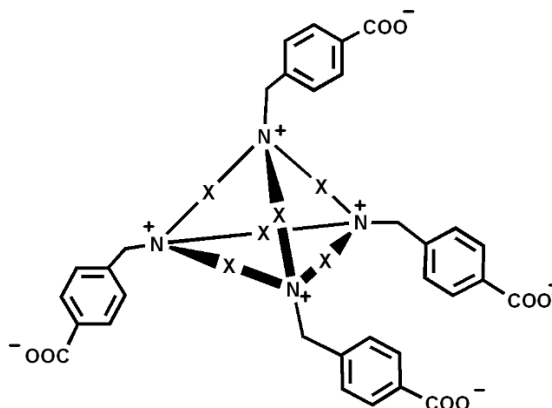


Figure 23. A zwitterionic host allowing anionic guest binding by electrostatic interactions alone.

2.3.2 Hydrogen bonding in anion binding

Electrostatic interactions are not the only way of binding anionic guests. Hydrogen bonding can be used in anion binding, as an anion can be considered as an electron pair donor with the receptor being the electron pair acceptor. As with dipoles, it is important that the hydrogen bonds are correctly orientated, with the hydrogen atoms arranged in a convergent manner.¹⁰ The most common type of hydrogen bond acceptor in anion binding chemistry is an electropositive atom such as hydrogen which is covalently bound to electronegative atom (such as nitrogen or oxygen). Due to the electronegative nature of the anions the hydrogen will try to take electrons from the anion and so form a hydrogen bond (see Figure 24).

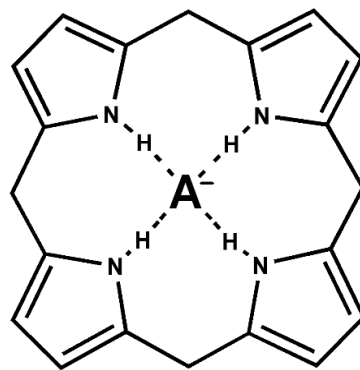


Figure 24. A calix[4]pyrrole group showing hydrogen bonding with an anion located in the central cavity.

Secondary amide groups have been widely used in anion receptor systems due to their ability to hydrogen bond (see Figure 25). The first receptor of this type was bicyclic katapinand complex that could bind chloride and was synthesised by Park and Simmons in 1968.⁵⁰

Hydrogen bonding anion receptors can be classed into coordination numbers like *d*-block metals. This number can be described as the number of moieties contained in the molecule capable of binding.

2.3.2.1 Coordination number two

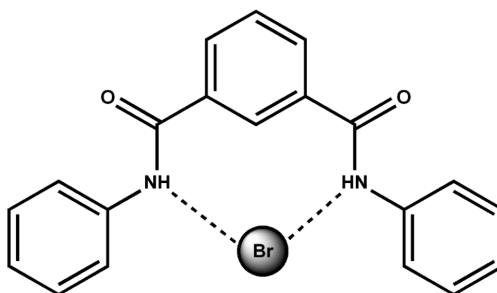


Figure 25. A simple amide containing anion receptor.⁵¹

Figure 25 shows a v-shaped receptor with a coordination number of two.⁵¹ This corresponds to the receptor having two moieties capable of coordinating to an anion (in this case bromide).

2.3.2.2 Coordination number three

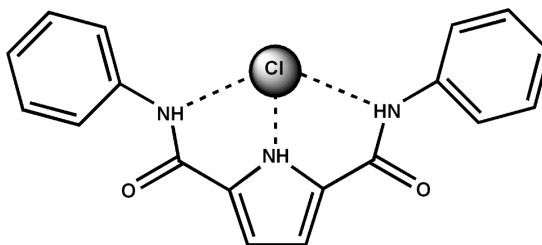


Figure 26. Simple amide containing receptor with coordination number three.⁵²

A receptor with a coordination number of three is often observed as a pincer type shape with three moieties available for binding. Zieliński *et al* synthesised a diamidopyrrole receptor (see Figure 26) to which chloride can bind with two hydrogen bonds to the amides and one hydrogen bond to the pyrrole NH. Due to the rigid ligand framework a pincer like structure is formed.⁵²

2.3.2.3 Coordination number four

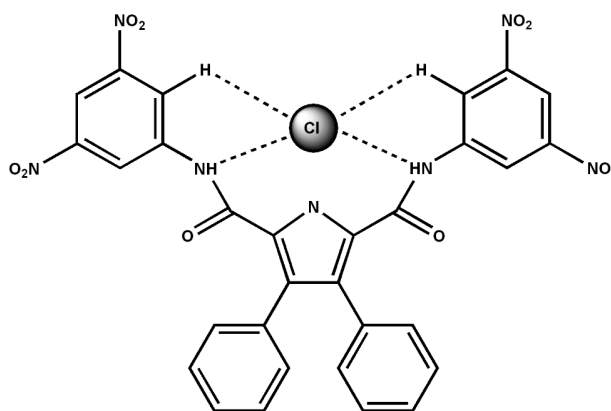


Figure 27. Acyclic pyrrole based ligand with coordination number four.⁵³

The most common type of anion receptor is one that has a coordination number of four with a distorted tetrahedral geometry. An acyclic pyrrole based receptor (see Figure 27) shows a four-coordinate geometry, bonding to two hydrogen atoms from the amides as expected but also coordinating to the hydrogens on the dinitrophenyl rings.⁵³ This occurs because the electron withdrawing NO₂ groups cause the 5-position hydrogen to become electron deficient and therefore able to fill its vacant orbitals with electrons from the electronegative anion.

2.3.2.4 Coordination number five

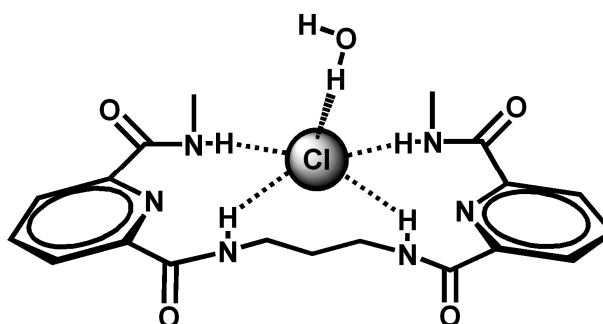


Figure 28. Tetraamide receptor showing five coordinate binding.⁵⁴

Five-coordinate receptors usually bind anions in square pyramidal or trigonal bipyramidal geometries. The most common type of five-coordinate receptors are simple tetraamide hosts. Figure 28 shows an acyclic host where two planar 2,6-pyridinedicarbamoyl groups are tilted with respect to each other.⁵⁴ The chloride ion acts as a template and forms four hydrogen bonds to the amide hydrogens with an additional water molecule binding to the chloride giving a distorted square pyramidal binding geometry.

2.3.2.5 Coordination number six

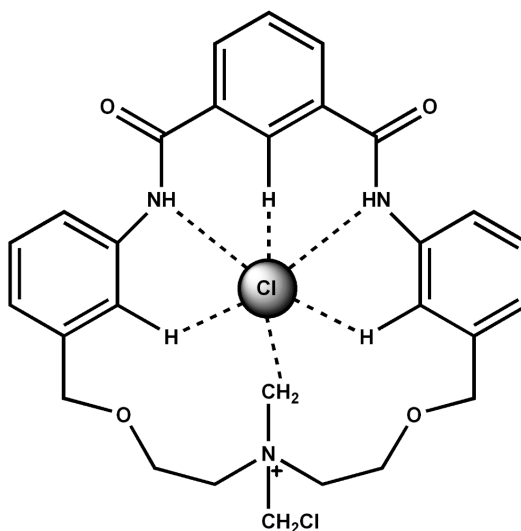


Figure 29. Macrocyclic amine receptor showing a coordination number of six.⁵⁵

Six-coordinate hydrogen bonding complexes are relatively common. Smith *et al* synthesised a macrocyclic amine receptor that can bind halides through six coordination sites (see Figure 29).⁵⁵ The halide is hydrogen bonded to the two amide NH groups, three aromatic CH groups and a methyl CH. The complex came about by the free macrocycle being reacted with CH_2Cl_2 which undergoes nucleophilic attack by the lone pair of the amine, with a chloride being released for hydrogen bonding in the cavity.

Anion hydrogen bond receptors can also have coordination numbers of seven, eight and nine but such examples are very rare. Most surprisingly the smallest anion, fluoride, can bind in a nine-coordinate state when bound to a cryptand like structure (see Figure 30).⁵⁶

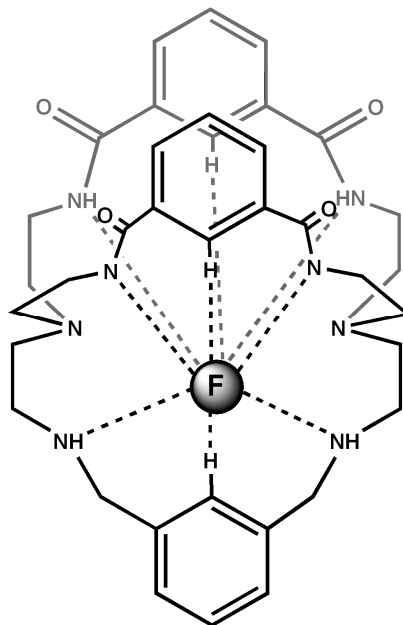


Figure 30. Cryptand receptor allowing nine-coordination of fluoride.⁵⁶

2.3.3 Lewis acidic hosts

An emerging area of anion receptor chemistry is that of Lewis acidic hosts. Lewis acids being capable of accepting electrons due to their incomplete electron shells and so from this a range of receptors have been designed and synthesised. One such example of this is the organoboron compound reported by Shriver and Biallis in 1967 (see Figure 31).⁵⁷ This receptor can be described as being analogous to ethylene diamine, but instead of donating two electrons to an electron deficient metal centre, the receptor can receive two electrons from the electronegative anion (to complete the boron valence shell).

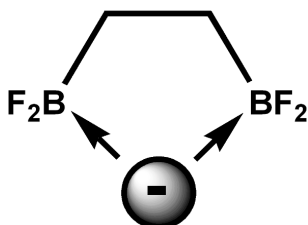


Figure 31. First organoboron receptor synthesised by Shriver and Biallis.⁵⁷

Boromycin, a naturally occurring antibiotic, has also been seen to be structurally reliant on Lewis acidic hosts for its formation.⁵⁸ The boron-oxygen donor interactions act as a template, holding the structure together and forming a tetrahedral anionic boron centre.

Organomercury receptors have also attracted interest due to their hybridised sp mercury atom and therefore two unfilled π orbitals. In addition to the ability to gain electrons from an anion this receptor type has a linear geometry, allowing the synthesis of square like receptors. Hawthorne *et al* have synthesised a mercuracarborand type receptor (see Figure 32) that contains four carborane clusters linked together with carbon-mercury-carbon bonds, with the formation being templated by the presence of a chloride anion.⁵⁹

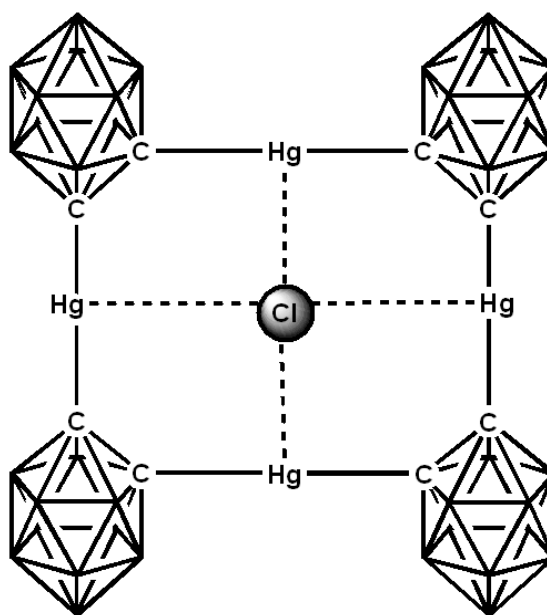


Figure 32. A mercuracarborand receptor synthesised by Hawthorne *et al*.⁵⁹

2.3.4 Combined interactions for anion recognition

Stability and selectivity of a receptor can be enhanced by the use of multiple coordinative interactions, such as hydrogen bonding and electrostatic interactions. Amide functionalised metallo-compounds use both hydrogen bonds and electrostatic interactions to bind anions. Beer *et al* have synthesised a receptor that contains both a metal centre (the

positive charge for electrostatic interactions) and a secondary amide group (for hydrogen bonding) (see Figure 33).⁶⁰

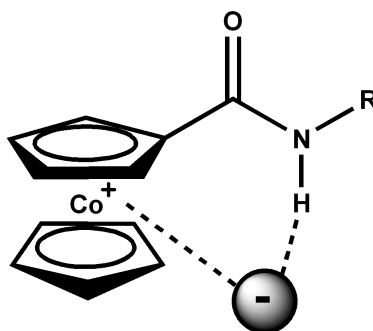


Figure 33. An amide functionalised cobaltocenium receptor that allows both electrostatic interactions and hydrogen bonding.⁶⁰

Such metallo-receptors are easily tunable and so the anions that can be bound are easily varied. An example of a receptor that utilises both hydrogen bonds and Lewis acid chemistry was reported by Reinhoudt *et al* where a Lewis acidic uranyl salene group is combined with secondary amines capable of hydrogen bonding (see Figure 34).⁶¹

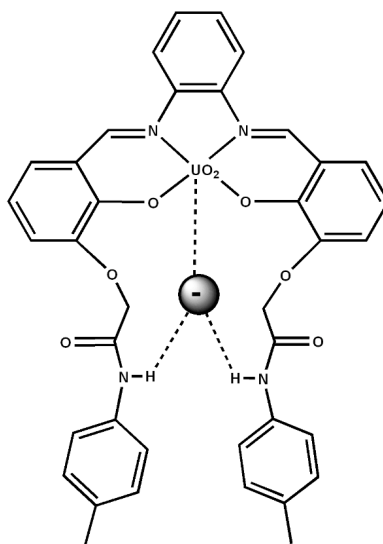


Figure 34. An amide functionalised uranyl salene receptor that combines an uranyl group with two amide functionalities to allow Lewis acidic and hydrogen bonding binding of an anion.⁶¹

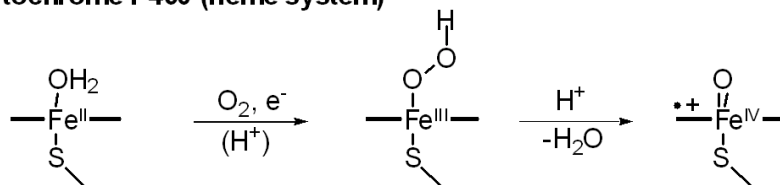
More complex anion receptors are being developed as the factors that control the strength and selectivity of anion binding are becoming better defined. Chemists are now turning their attention to the design of functional devices based on the anion recognition process, for example molecular sensors and supramolecular catalysts.

2.4 Direct C-H Transformation via Iron Catalysis

The direct transformation of C-H bonds by iron catalysis is a synthetically important field of chemistry. Nature has utilised iron in a number of biologically important reactions due to its ability to perform chemically challenging oxidative processes with high precision and reaction rates.

Oxygen-activating enzymes with non-heme iron active sites are important in many biological reactions. Enzymes such as Cytochrome P450 and Rieske dioxygenases use an oxidising ferryl species to catalyse highly selective C-H and C=C oxidation reactions (see Figure 35).^{62,63} Another example are Lipooxygenases, which oxidise unsaturated fatty acids into precursors of leukotrienes and lipoxins and can be used as potential anti-inflammatory drugs.⁶⁴

Cytochrome P450 (heme system)



Rieske dioxygenases (non-heme system)

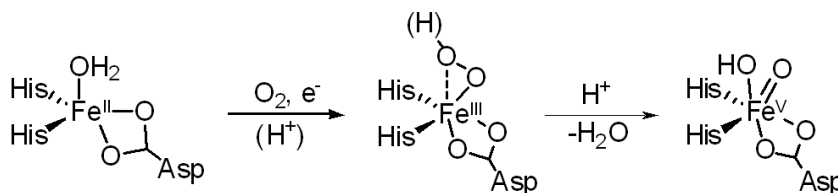


Figure 35. Mechanistic proposal for the formation of oxo-iron(V) species in Cytochrome P450 and Rieske dioxygenases.^{62,63}

Non-heme iron enzymes have been shown to promote novel oxidative chemistry.^{65,66} The Rieske dioxygenases, which catalyse the *cis*-dihydroxylation of arenes in nature utilise a mononuclear iron centre which is ligated to a 2-His-1-carboxylate facial triad, this motif being a reoccurring structure amongst oxygen activating mononuclear non-heme iron enzymes.^{67,68} Two *cis*-coordination sites on the octahedral iron centre can be used for the side-on binding of O₂ (see Figure 36).⁶⁹ This O₂ adduct was proposed to be an iron(III)-peroxo intermediate⁷⁰ that either attacks the substrate directly or undergoes O-O bond heterolysis to give a HO-Fe(V)=O species that then goes on to give the *cis*-dihydroxylated product.⁷¹

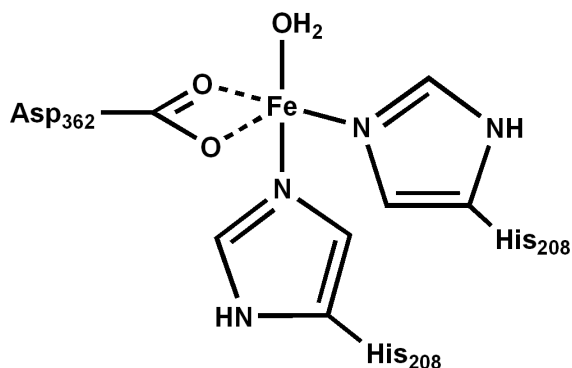


Figure 36. Active site of a non-heme iron enzyme showing the two *cis*-coordination sites available for side-on binding of O₂.⁶⁹

2.4.1 C-H bond activation

C-H bond oxidation is one of the most common processes that occurs in nature. Single electron transfer (SET) is thought to be one way in which C-H oxidation occurs.⁷²⁻⁷⁴ Laboratory synthesis of iron-catalysed C-H oxidations can be traced back a century ago to Gif and Fenton chemistry.^{75,76} Gif chemistry was first reported in 1983 by Barton *et al* where adamantane was oxidised to its respective alcohol and ketones using iron catalysis in what was thought to be a non-radical process.⁷⁷ This type of chemistry can be explained by the formation of a Fe(V)=O species, formed by the reaction of Fe(II) with a superoxide. Fenton chemistry is the oxidation of ferrous iron(II) by hydrogen peroxide to iron(III) with the production of a hydroxyl radical and anion. The iron(III) is then reduced back to iron(II) with hydrogen peroxide to form a peroxide radical and a proton (see Figure 37).

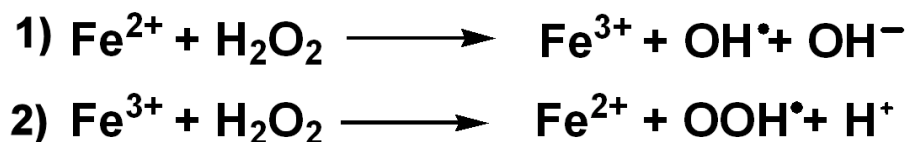


Figure 37. The Fenton reaction.⁷⁵

Olefin *cis* dihydroxylation typically involves the use of OsO₄⁷⁸ but recently the *cis*-dihydroxylation of olefins has been carried out using synthetic iron^{79,80} as well as manganese^{81,82} catalysts with H₂O₂ as the oxidant. This type of chemistry was a major breakthrough in non-heme oxidation as H₂O₂ was generally seen to react with iron generating hydroxyl radicals that then gave rise to non-specific oxidation products. The most effective iron complexes have been found to be tetradentate N₄ ligands that have two *cis*-orientated coordination sites available for O₂ coordination and that allow O-O bond cleavage.⁷⁹

In 1997 Que *et al* reported the first example of a non-heme iron catalyst capable of stereospecific alkane hydroxylation when reacted with H₂O₂ that did not conform to the pattern of reactivity postulated before.⁸³ [Fe(TPA)(CH₃CN)₂](ClO₄)₂ (TPA = tris(2-pyridylmethyl)amine) reacted with H₂O₂ to give an alcohol as the major product while the ratio of alcohol to ketone produced in the Haber-Weiss reaction was 50:50 (where the Haber-Weiss reaction generates hydroxyl radicals from hydrogen peroxide and a superoxide). The reaction was also insensitive to O₂ and stereospecific, both of which were problems associated with Haber Weiss chemistry.

More recently iron-catalysed C-H oxidations have focused upon sulphide oxidations, epoxidation and olefin dihydroxylations.⁸⁴⁻⁸⁸ Que *et al* reported a tetradentate N₄ iron complex that showed high catalytic reactivity for the oxidation of alkanes such as cyclohexane, adamantane and 2,3-dimethylbutane. This molecule, [Fe^{II}(PyMe₂TACN)(CF₃SO₃)₂] (PyMe₂TACN = 1-(2'-pyridylmethyl)-4,7-dimethyl-1,4,7-triazacyclononane), contained a distorted octahedral iron(II) centre bound to a tetradentate PyMe₂TACN ligand and two *cis* triflate anions (see Figure 38). H₂¹⁸O labelling experiments indicated that the incorporation of the labelled water was higher in some oxidated alkanes than others. This result was also proved to be substrate concentration

independent and it was found that the key reaction intermediate in this reaction mechanism was an HO-Fe(V)=O species.⁸³ A unique structural feature of the non-heme complex was the *cis* configuration of the two hydroxy groups in the catalytic system, compared to the *trans* configuration of the heme complex.

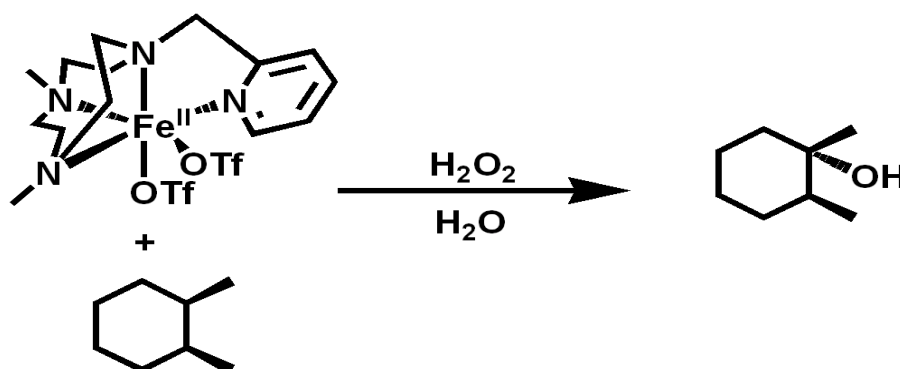


Figure 38. A mechanistic representation of $[\text{Fe}^{\text{II}}(\text{PyMe}_2\text{TACN})(\text{CF}_3\text{SO}_3)_2]$ and its hydroxylation of an alkane in the presence of water and hydrogen peroxide.⁸⁹

It was also found that both alkanes and alkenes can be oxidised by $[\text{Fe}^{\text{II}}(\text{PyMe}_2\text{TACN})(\text{CF}_3\text{SO}_3)_2]$ (see Figure 38 and Figure 39).

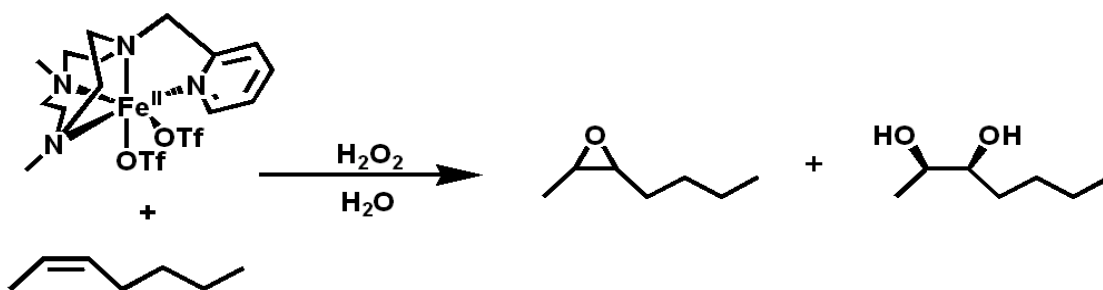


Figure 39. Mechanistic diagram for the selective hydroxylation of an alkene.⁹⁰

These bioinspired catalysts have provided key insights into the reaction mechanism by which the oxidation of alkanes takes place. The mechanism follows that of the heme paradigm where the iron(II) species reacts with the oxidant hydrogen peroxide to form an iron(III)-OOH species. The addition of water allows for O-O water-assisted heterolysis to form the unstable Fe(V)=O intermediate. This unstable intermediate will then react with

the sp^3 alkane/alkene C-H/C=C bond to give the desired C-O bond and iron(III)-OH (see Figure 40). Labelling studies also showed intriguing differences between the non-heme N_4Fe systems used before and $[Fe^{II}(\text{PyMe}_2\text{TACN})(\text{CF}_3\text{SO}_3)_2]$. The oxidation of cyclohexane with $[Fe^{II}(\text{PyMe}_2\text{TACN})(\text{CF}_3\text{SO}_3)_2]$, 10 equivalents of $\text{H}_2^{18}\text{O}_2$ and 1000 equivalents of H_2^{16}O gave a yield of 47% ^{18}O labelled cyclohexanol. When H_2^{18}O was used along with unlabelled hydrogen peroxide the same high yield was found. This high level of oxygen incorporation from water was the highest found of any non-heme catalyst to that date. The oxidation of cyclohexane was also carried out at differing H_2^{18}O concentrations and showed that the amount of ^{18}O -labelled cyclohexanol produced increased linearly when the amount of H_2^{18}O was increased at low concentrations but plateaued at 42% when at higher concentrations suggesting a water binding pre-equilibrium (the same being for the catalyst $\text{Fe}(\text{TPA})$). These results supported the mechanism in which a $\text{Fe}(\text{V})=\text{O}$ intermediate is formed via water assisted heterolysis of the O-O bond to form a $\text{H}_2\text{O}-\text{Fe}(\text{III})-\text{OOH}$ intermediate. The results also showed that the oxygen in the C-O bond formed can come from both the hydrogen peroxide or water in equal proportion.⁸⁹

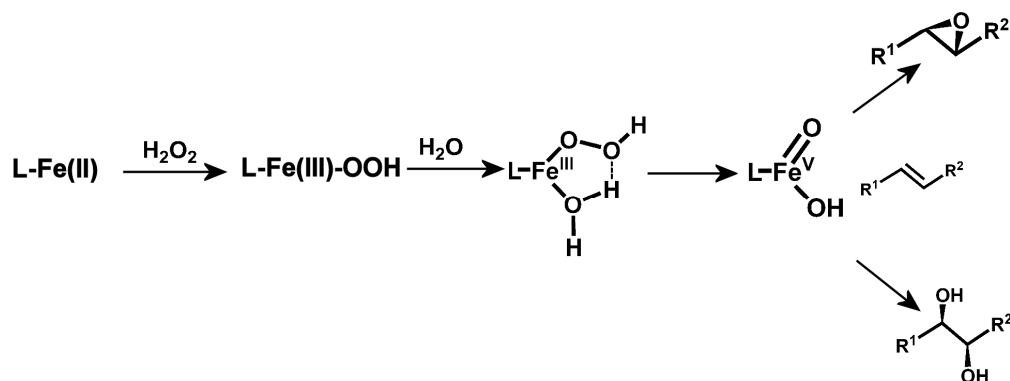


Figure 40. Olefin hydroxylation catalytic cycle (where L = a multidentate nitrogen containing ligand).⁹⁰

Costas *et al* have synthesised a TACN ligand family, each of which retains the triazacyclononane (TACN) backbone shown before (see Figure 41).⁹¹ This family of iron complexes has exhibited an unprecedented efficacy in the stereospecific oxidation of alkanes and the dihydroxylation or epoxidation of alkenes. These results have shown that by modifying the structure the selectivity of the complex can be tuned.

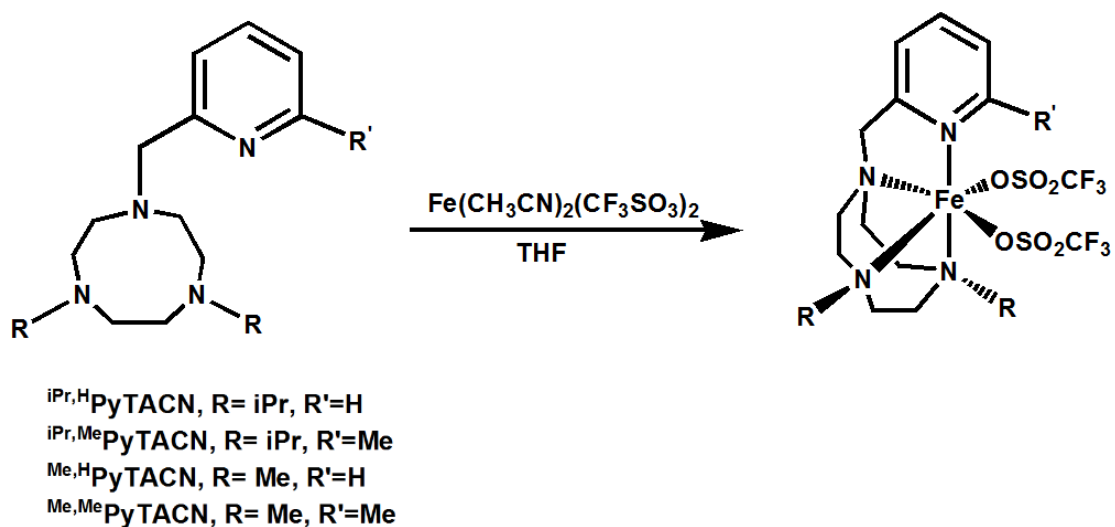


Figure 41. Iron-TACN family synthesised by Costas *et al.*⁹¹

In 2007, White *et al* reported highly selective iron catalysed aliphatic C-H oxidations by an iron PDP complex (PDP = 2-((S)-2-[(S)-1-pyridin-2-ylmethyl]pyrrolidin-2-yl]pyrrolidin-1-yl)methyl)pyridine] (see Figure 42).⁹² The rigid PDP backbone gave an increase in activity compared to previous non-heme catalysts such as Fe(TPA) and was inexpensive compared to the precious late transition metals used before. The difference of this type of chemistry compared to that reported before by Que⁸³ and Costas⁸⁹ was that it was the electronic features and not the steric effect of the C-H bonds that played a role in the oxidation. It was also reported that electron-withdrawing groups on the α or β carbon decreased the activity while carbonyl, esters, acetates and halogen functional groups increased the activity. It was also found that remote tertiary C-H bonds have greater reactivity due to decreased electron density from other C-H bonds.

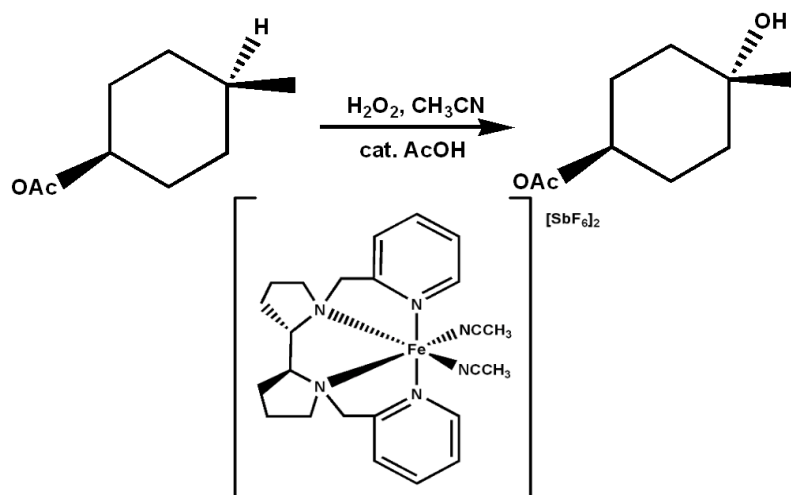


Figure 42. Iron catalysed aliphatic C-H oxidation; iron(PDP) complex.⁹²

Based on the selectivity mentioned above this field of non-heme catalysed chemistry was applied to the sp^3 C-H oxidation of the natural product (+)-artemisinin, where oxidation takes place at the most electron-rich and least sterically hindered site. This process gave a higher yield, a higher volume throughput and a much shorter reaction time than previously seen (see Figure 43).

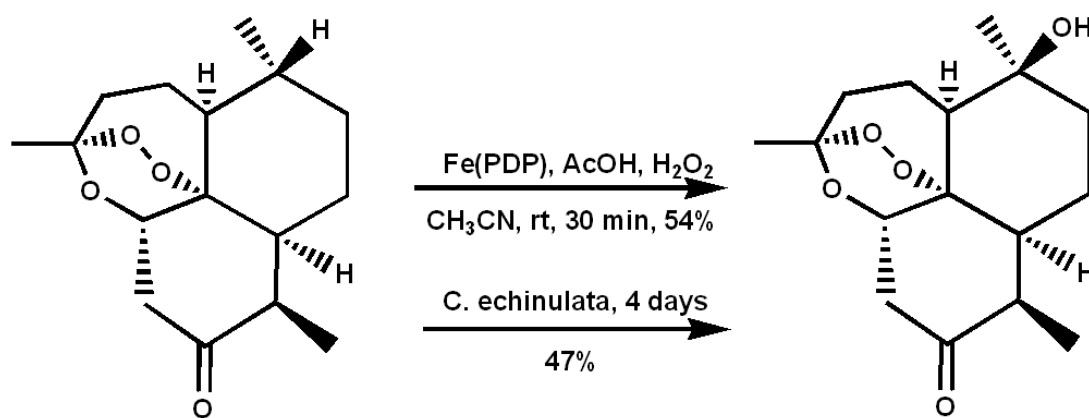


Figure 43. C-H oxidation of (+)-artemisinin using Fe(PDP) and *C. Echinulata*.⁹²

White *et al* also developed the selective bond oxidation of secondary C-H bonds using iron-catalysed reactions. Due to the lower electron density but higher steric accessibility of

secondary C-H bonds moderate selectivity was reported. It was also seen that secondary C-H bonds are common within ring systems and therefore the selective oxidation of secondary C-H bonds for methylene functionalisation was carried out. From previous work it was concluded that electronic, stereoelectronic and functional group factors could all take part in the oxidation process. This theory was proved correct as an increased level of chemo- and diastereoselective oxidation occurred (see Figure 44).

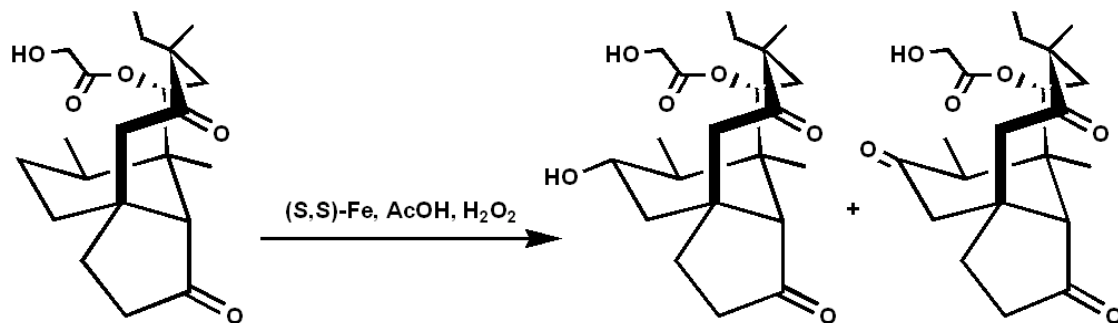


Figure 44. Combined electronic, stereoelectronic and functional group factors leading to the diastereoselective methylene oxidation.⁹²

Iron catalysis can also be used in other types of chemistry such as C-N bond formation and cross-coupling reactions.

2.4.2 Mechanistic studies of C-H transformations via iron catalysis

The selective oxidation of organic molecules is important in both nature and industry.^{93,94} Such catalytic reactions may be carried out by metalloenzymes using molecular oxygen (O_2) with this type of oxidation exhibiting substrate specificity, regioselectivity and/or stereoselectivity, and can operate under mild conditions through inherently 'green' processes. For these reasons chemists have studied O_2 -activating metalloenzyme structure-function relationships in order to find the mechanism by which these enzymes operate.

The understanding of how metalloenzymes function has advanced due to high resolution X-ray crystal structures of resting states and reactive intermediates,

spectroscopic characterisation and from detailed mechanistic studies of kinetics, synthetic modeling and theoretical investigations. Findings from these studies have fuelled a debate about the mechanism by which these enzymes operate, with the main issue being if the O-O bond cleavage occurs before, during or after attack on the organic substrate.⁹⁵

Iron is one of the most commonly found metals in biological oxidations due to its abundance in nature, inherent electronic properties and accessible redox potentials. The most extensively studied oxygen-activating enzymes are the cytochromes P450.⁹⁶ These enzymes carry out the hydroxylation of aliphatic C-H bonds and the epoxidation of C=C bonds with high regioselectivity and stereoselectivity. The active site consists of an iron porphyrin cofactor attached to the protein backbone through coordination of a cysteine at one of the axial positions on the metal, leaving the other axial positions available for O₂ binding and activation. The activation of the O₂ at the metal centre generally entails a two electron reduction from an iron(II) state to an iron(III) peroxy state and subsequent O-O cleavage. In the initial step, O₂ coordinates to the reduced iron centre where it is progressively reduced to the superoxy and peroxy forms, where it then undergoes O-O cleavage to generate the iron(IV) oxo oxidant that carries out the two-electron oxidation of the substrate. For haem enzymes, the two oxidising equivalents are not stored at the iron centre but are delocalised across the porphyrin unit with the delocalisation allowing access to a potent oxidant that can hydroxylate a variety of substrates (see Figure 45).

The proposed mechanism for non-haem iron enzymes in general is very similar to that for haem enzymes, with evidence for iron(III) peroxy and high valent iron oxo intermediates obtained. Rieske dioxygenases (enzymes that can catalyse the *cis*-dihydroxylation of arene double bonds to initiate the biodegradation of aromatics in soil) activate O₂ at a mononuclear iron(II) centre that is bound to a 2-His-1-carboxylate facial triad motif.⁶³ The only available redox centre that can store two electrons is at the iron atom in such enzymes and so an iron(V) oxo intermediate has been postulated for this reaction (see Figure 45), with an iron(III) peroxy precursor being characterised by X-ray crystallography. Several examples of iron(IV) oxo intermediates have been observed and characterised⁹⁷ but up until now no evidence for the iron(V) oxo intermediate has been found.

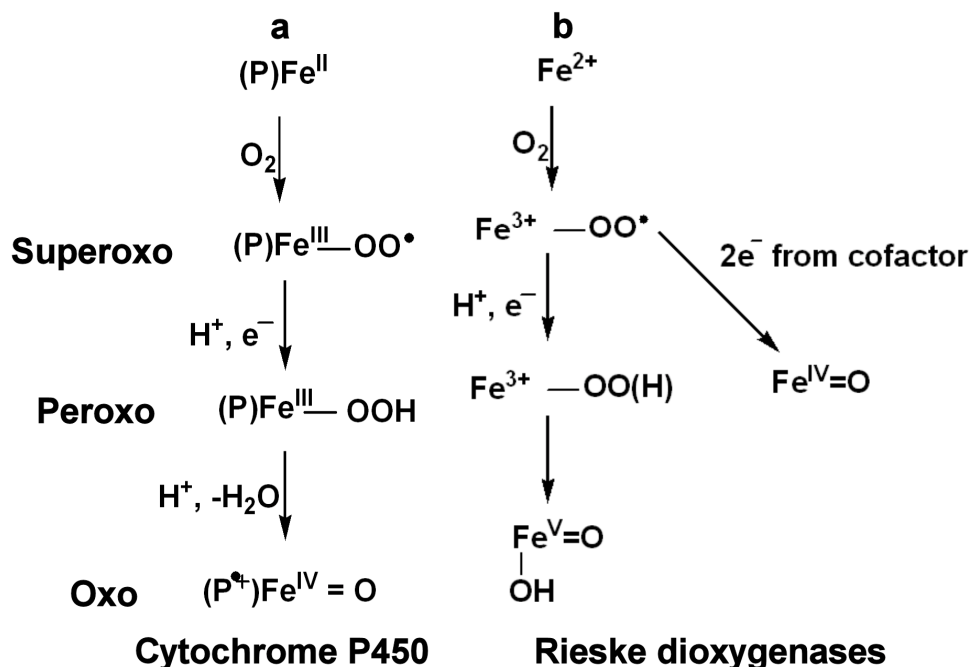


Figure 45. Proposed mechanism for O₂ activation by a) Cytochrome P450 and b) Rieske dioxygenases.⁹⁵ Both involve the formation of an initial O₂ adduct (superoxo), conversion to a metal peroxide (peroxo) and the subsequent O-O bond cleavage to yield a high valent oxidant (oxo).

Recent studies have researched the use of H₂O₂ as an oxidant in iron catalysis. This type of catalytic reaction follows the peroxide pathway previously described and involves the reaction of iron(III) intermediates with H₂O₂.^{98,99} Much effort was invested in the development of metalloporphyrin catalysts that mimic the reactivity of cytochrome P450. One of the results was the synthesis of tetradentate nitrogen-donor ligands with topologies that allowed two *cis*-orientated coordination sites to be available for peroxide binding and activation, with this arrangement being analogous to that found for the Rieske dioxygenases (see Figure 46). These types of ligands had a wanted advantage in that the catalytic oxidation took place in the presence of dilute H₂O₂, therefore minimizing side reactions such as the production of highly reactive radicals.¹⁰⁰

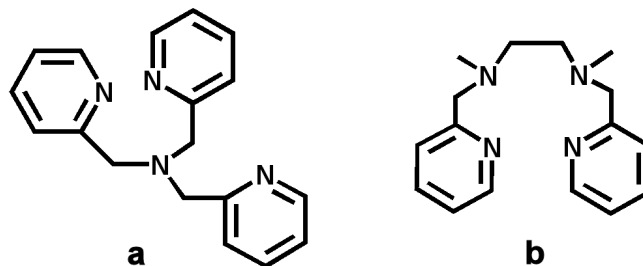


Figure 46. Two of the first ligands used in iron-catalysed oxidations.¹⁰¹

The catalytic mechanism for the oxidation of olefins using prototypical iron catalysts was deduced from a combination of low temperature spectroscopic studies and room temperature ^{18}O -labelling experiments.¹⁰² At $-40\text{ }^{\circ}\text{C}$ an iron(III)-OOH intermediate was trapped in acetonitrile and characterised by a variety of spectroscopic methods such as UV. It was proposed that this iron(III)-OOH intermediate underwent O-O bond cleavage to form the highly reactive Fe(V)(O)(OH) oxidant. Labelling experiments were also used to give further evidence for the oxidant being the Fe(V)(O)(OH) species, where H_2^{18}O was incorporated into the products with the retention of the stereochemistry. The ^{18}O -labelling results provided evidence that the *cis*-diol product incorporated one oxygen from H_2O_2 and the other from H_2O and also provided evidence for the existence of a proximal proton donor (the metal-bound water in this example) that plays a critical role in promoting the heterolytic cleavage of the O-O bond (see Figure 47).

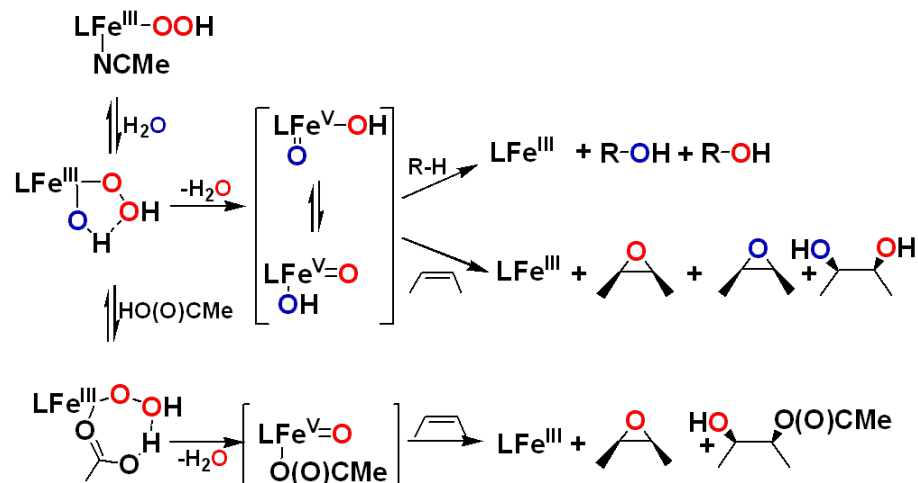


Figure 47. Proposed iron-catalysed oxidation mechanism of alkenes and alkanes by invoking an iron(V)=O oxidant. Oxygen derived from H_2O_2 are shown in red with oxygen atoms derived from H_2O shown in blue.⁹⁵

The ligands shown in Figure 46 are just a small part of the research that has gone into the understanding of biologically inspired oxidation catalysis. Many chemists are working on new and improved ligands that have a higher turnover and selectivity, also with the aim of fully understanding the mechanistic process that is taking place. As the mechanistic understanding of the oxidation of olefins by metalloenzymes increases, new types of biological mimics that can be used in technology will be uncovered.⁹⁵

3 IN-SITU STOICHIOMETRIC CONTROL OF COORDINATION COMPLEXES

Cis,trans-1,3,5-triaminocyclohexane (*trans*-tach) has been shown to be an excellent ligand in the synthesis of discrete complexes, molecular clusters and infinite architectures.¹⁰³ The control of such architectures is an area of great interest to chemists due to the vast potential for the design of functional compounds^{104,105} as well as expanding the understanding of the fundamental processes that underpin the formation of the complexes.^{106,107} Understanding the assembly of larger clusters remains a great challenge and arguably limits our ability to produce systems with new properties.¹⁰⁸ One route to address such problems is to design complexes and then follow their assembly using mass spectrometry.

Ideally, to engineer polynuclear coordination clusters, multiple discrete binding sites and a degree of structural rigidity are required. In this respect, the inclusion of a cyclohexane backbone in a ligand can satisfy both of these demands. In previous studies we have shown that the complexation of *trans*-tach with a variety of metals yielded a range of interesting complexes, from polynuclear clusters¹⁰⁹ and coordination networks¹¹⁰ to one dimensional chain complexes.²⁶

In this study, we chose to employ mass spectrometry and standard crystallography techniques to monitor the complexation process of the ligand *cis,trans*-1,3,5-tris(pyridine-2-carboxaldimino) cyclohexane (ttop) **4** to a variety of divalent metal salts and probe the assembly of the architecture using stoichiometric control.

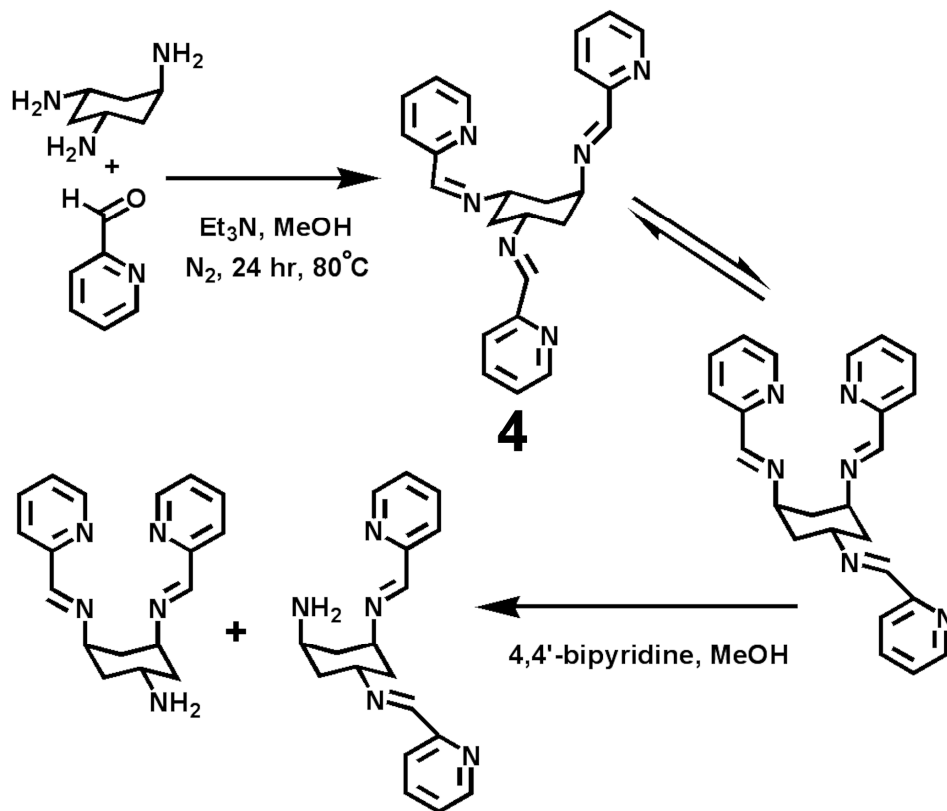


Figure 48. Reaction scheme describing the formation of *cis,trans*-1,3,5-tris(pyridine-2-carboxaldimino) cyclohexane (top) **4** from *trans*-tach and pyridine-2-carboxaldehyde in methanol.

Ligand **4** is highly labile and can flip between a bisaxial monoaxial and a bisaxial monoaxial conformation due to the ring-flip ability of the cyclohexane backbone. The energetically favoured ring-flipped ‘closed’ conformation contains two coordination sites, an axial tetradentate site constructed from the nitrogen atoms on both the pyridine groups and the associated imine groups, and an equatorial bidentate coordination site formed from the two nitrogen atoms from the *trans* arm. As expected, the axial tetradentate coordination site is the most favoured site for metal coordination and so will be filled first by the metal centre. The reaction of **4** with 4,4'-bipyridine facilitated the hydrolysis of an imine bond and the subsequent protonation of the amino group to give a further two ligands capable of metal coordination.

Control of the stoichiometry of the metal(II) salts (chloride and nitrate) to the ligand ttop **4**, where the ratio of metal salt to ligand was varied, produced five new structures. The ratio of ligand to metal salt was varied from 1:1 (ligand:metal salt) to give complex **5** where only one coordination site was filled. The ratio was changed to 2:1 to give complex **6** where both the tetradentate and bidentate sites were filled. The reaction of complex **5** with 4,4'-bipyridine gave the monoligand complex **7** where the *trans*-arm had been cleaved. The reaction of copper(II) nitrate with ttop in a 1:1 stoichiometry produced complex **8**. The final structure was that of complex **9**, where a 2:1 ligand:metal salt ratio gave a two ligand-four metal centre complex.

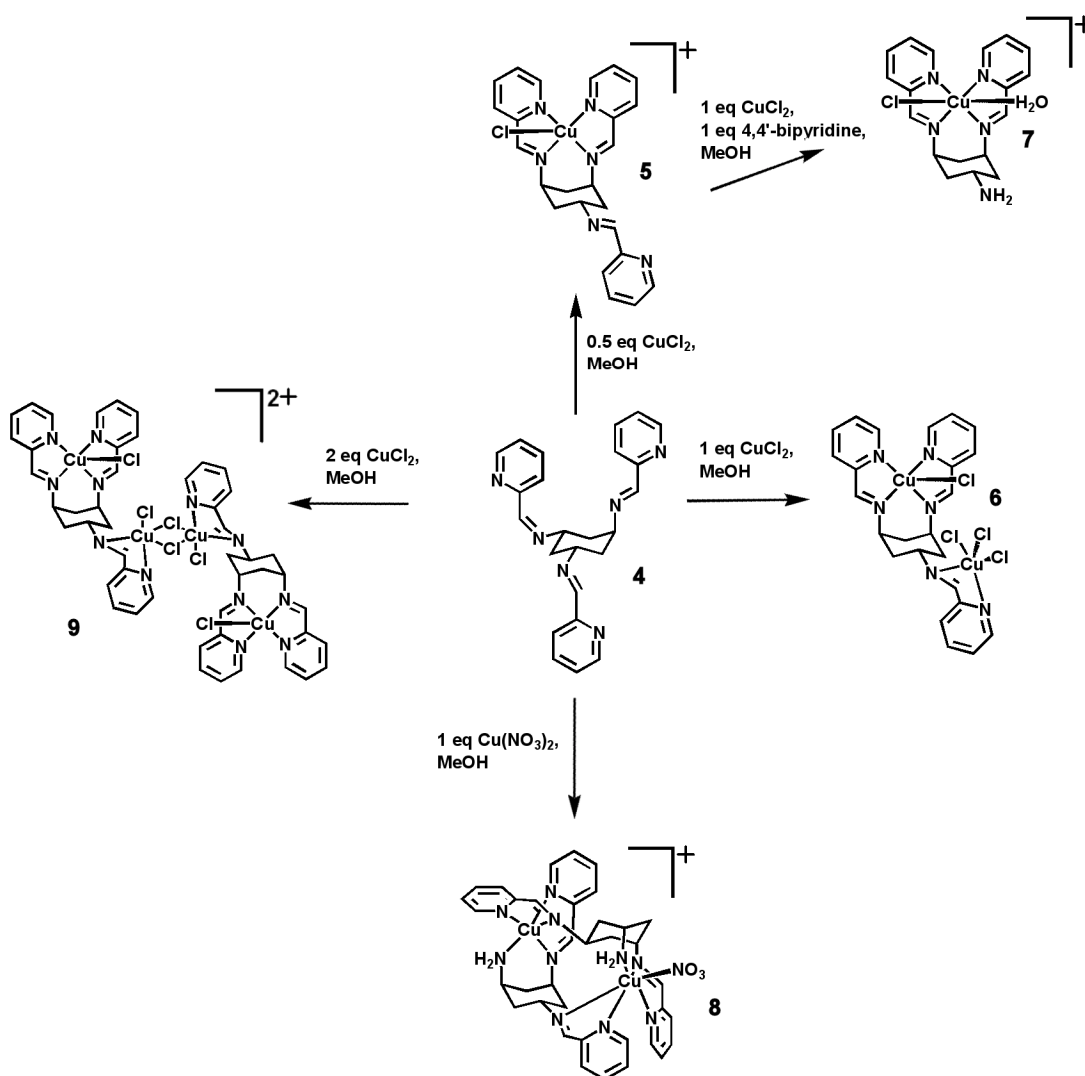


Figure 49. Summary of complexes **5-9** obtained from ttop **4** under different stoichiometries and reaction conditions.

[Cu(ttop)Cl]Cl(CH₃OH)₂ **5** was synthesised from copper(II) chloride and ttop where a 1:2 stoichiometry of Cu^{II}Cl₂:ttop was used (see Figure 50). Using ether diffusion into methanol, single crystals were formed after two weeks to give the mono complexed ligand. The conformation of the complex is that of the energetically favoured ring-flipped ‘closed’ conformer where the imine double bonds are substituted in the sterically favoured *E*-conformation. The copper(II) ion is coordinated within the tetradentate binding site in a distorted square-pyramidal geometry by basal coordination to each of the four nitrogen atoms of the *cis*-imido pyridyl moieties. The Cu1-N bond lengths for the imine groups are 1.997(2) and 2.019(2) Å, with the bond lengths for the pyridyl Cu1-N being 2.099(2) and 2.035(2) Å, which lie within expected ranges¹¹¹⁻¹¹³ and an apical coordination of one chloride ion with a bond length of 2.4198(7) Å. The chloride ligand is oriented above the cyclohexane ring with the copper(II) ion also oriented towards the center of the molecule at an angle of 166.5(8)°, placing it over the cyclohexane backbone. The bidentate binding site is not involved in the coordination of a metal centre. The nitrogen atoms of the imine and pyridyl groups are oriented *anti* with respect to each other to minimise electronic repulsion between the lone pair on each nitrogen. The trans-imido pyridine arm is twisted with respect to the cyclohexane ring at an angle of 60.0(1)°.

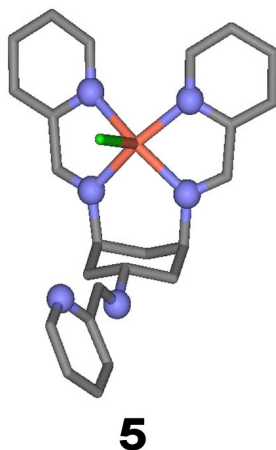


Figure 50. Partial single crystal structure of [Cu(ttop)Cl]Cl(CH₃OH)₂, **5**, showing the copper(II) chloride coordinated to the tetradentate site.

When the stoichiometry was changed to 1:1 Cu^{II}Cl₂:ttop the complex [Cu₂(ttop)Cl₄]CH₃OH, **6**, (see Figure 51) was crystallised from an ether diffusion into a methanol solution over two weeks. From **6** it can be seen that both binding sites have been

filled by copper(II) centres. One copper(II) ion is coordinated in the tetradentate binding site in a distorted square-pyramidal geometry by a basal coordination to each of the four nitrogen donors, with a chloride ligand occupying the apical binding site oriented away from the cyclohexane ring. The Cu1-N bond lengths for the imine groups of the *cis* arms are 1.998(2) and 1.980(2) Å, and 2.081(2) and 2.026(2) Å for the pyridyl nitrogen to copper(II) bond lengths. The apical coordination of one chloride ligand (Cu1-Cl bond length of 2.429(8) Å) completes the square pyramidal coordination sphere. The bidentate site of the *trans* arm binds a second copper(II) ion, which is coordinated, in square-pyramidal geometry, by the imido and pyridyl nitrogen atoms, with bond lengths of Cu2-N imido of 2.026(2) Å and Cu2-N pyridyl of 2.074(2) Å. The final three coordination sites are occupied by chloride anions, with binding distances of 2.282(8), 2.273(8), and 2.562(8) Å. The trans-imido pyridyl arm is oriented perpendicular to the two axial pyridine rings, as with the mononuclear complex **5**, and is twisted with respect to the cyclohexane ring at an angle of 66.1(2)°.

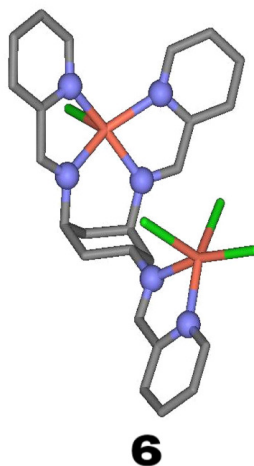


Figure 51. Partial single crystal structure of $[\text{Cu}_2(\text{ttop})\text{Cl}_4]\text{CH}_3\text{OH}$, **6, showing copper(II) chloride coordinated to both the tetradentate and bidentate site.**

Complex **5** was reacted with 4,4'-bipyridine resulting in the formation of the monoligand complex $[\text{Cu}(\text{ttop})\text{Cl}(\text{H}_2\text{O})]\text{Cl}_2$ **7** (see Figure 52). Using ether diffusion into a methanol solution of **7**, single crystals were formed after two weeks to give the mono complexed ligand. The trans arm is hydrolysed and protonated preventing coordination and has increased the donor ability of the amino group to form hydrogen bonded interactions

with the chloride counterions. The tetradentate pocket, formed by the *cis* arms of the ring-flipped cyclohexane backbone, coordinates to one copper(II) ion with the octahedral geometry being completed by one chloride ion and one water molecule. The Cu-N bond lengths for the imine groups are 1.9991(3) Å and 2.022(3) Å, and 2.066(3) Å and 2.030(3) Å for the pyridyl nitrogens. The Cu-Cl bond length is 2.6590(11) Å with the Cu-OH₂ bond length being 2.407(3) Å.

The Cu-Cl and Cu-OH₂ bond lengths for the octahedral coordination sphere of complex **7** were found to be longer than expected at 2.6590(11) Å and 2.407(3) Å respectively. This is due to Jahn-Teller distortions that occur in octahedral complexes of d⁹ ions due to the d_{x²-y²} orbital being half filled and so the electron density being concentrated along the z axis therefore causing the elongation of the Cu-Cl and Cu-OH₂ bonds.

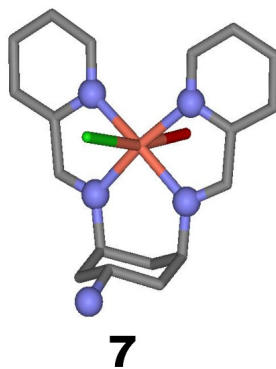


Figure 52. Partial single crystal structure of [Cu(H(*trans*-1-amino-*cis*-3,5-*N',N''*-2-imidopyridine))(H₂O)Cl] Cl₂, **7**, showing the *trans*-hydrolysed ttop where only the tetradentate site is available for coordination by copper(II) chloride and one water molecule to give an octahedral binding geometry.

When the stoichiometry and counterions were changed to 1:1 Cu^{II}(NO₃)₂:ttop, a dinuclear, diligand complex [Cu₂(ttop)₂(NO₃)](NO₃)₃, **8**, (see Figure 53) was formed. The copper(II) is coordinated at the hydrolysed *cis* amine and the *cis* imido pyridyl arm of the first ligand, and the *trans* imido pyridyl arm from the second ligand. The octahedral coordination sphere is completed by an axial nitrate group. The Cu1-N bond distances are 1.999(5) Å and 2.279(5) Å for the imine groups, 2.023(5) Å and 2.045(5) Å for the pyridyl nitrogens, and 2.035(5) Å for the amine group. Cu2 has a distorted octahedral coordination

geometry with the Cu2-N bond distances for the imine groups being 2.333(5) Å, 2.010(5) Å, 2.054(5) Å, and 2.034(5) Å for the pyridyl nitrogens, 2.014(5) Å for the amine group, and 2.827(5) Å for the nitrate ion. Cu2 also exhibits long range axial coordination to the neighboring nitrate of the nearest ligand, forming a coordination polymer. The Cu2-O(NO₂) bond length is 2.635(5) Å, this bond length lying within the range previously reported for highly distorted octahedra.¹¹⁴

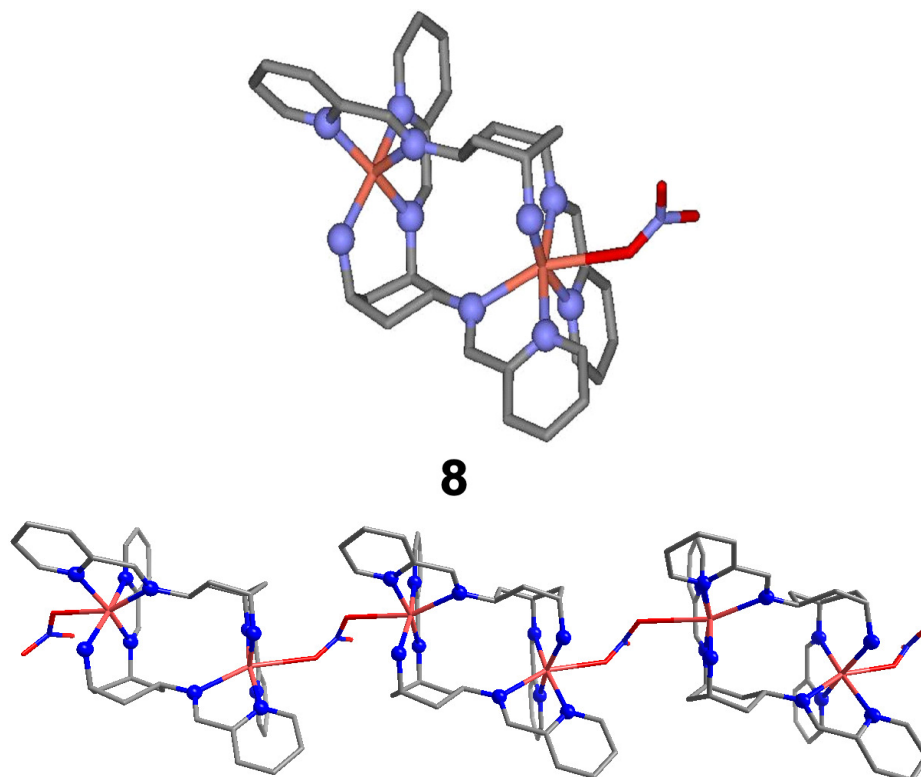


Figure 53. Partial single crystal structure of $\{[\text{Cu}_2(\text{cis-3-amino-cis,trans-}N',N''\text{-2-imidopyridine})_2]\}_2(\text{NO}_3)_4$, **8**, showing two hydrolysed ligands complexed with two metals and the coordination polymer formed by long range axial coordination of Cu2 to a neighbouring nitrate. The two axial pyridine groups are twisted relative to each other and the equatorial *trans* pyridine arm has been cleaved off to allow the nitrogen from the *trans*-arm to coordinate to the adjacent copper(II) centre.

A change in stoichiometry to 2:1 Cu^{II}Cl₂:ttop gave a two ligand-four metal centre complex $\{[\text{Cu}_2(\text{ttop})\text{Cl}_3]\text{Cl}\}_2$, **9**, (see Figure 54). Both coordination sites on each ligand are complexed to copper(II) ions in a square-pyramidal geometry. As with the mononuclear and dinuclear complexes, **5** and **6** respectively, the tetradentate binding site coordinates Cu1 by its four nitrogen atoms available upon ring-flip of the cyclohexane ring

(with Cu1-N imine groups bond lengths of 1.996(2) and 2.004(6) Å, and Cu1-N pyridyl bond lengths of 2.036(6) and 2.069(5) Å). The coordination sphere of Cu1 is completed by one chloride ligand, which like **6**, is pointing away from the cyclohexane ring (with a Cu1-Cl bond length of 2.427(2) Å). The bidentate binding site coordinates a second copper(II) with its two nitrogen atoms (Cu2-N imine bond length of 2.046(6) Å and Cu2-N pyridyl bond length of 2.045(6) Å), along with one terminal chloride ligand (Cu2-Cl bond lengths of 2.256(2)) and two bridging chloride ligands (Cu2-Cl bond lengths of 2.284(18) and 2.651(2) Å). The Cu2-Cu2* distance of 3.497 Å lies within the reported range of μ_2 -chloride bridged copper(II) dimers.¹¹⁵⁻¹¹⁷

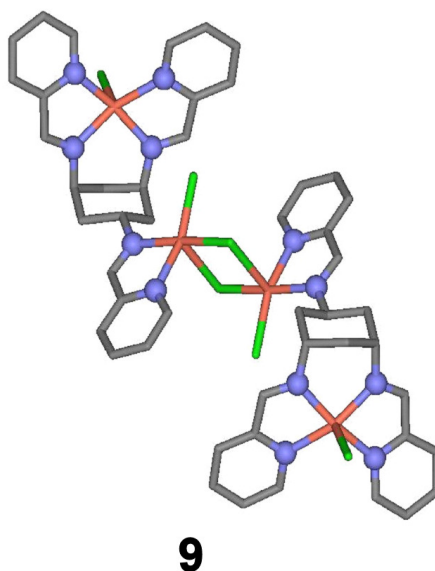
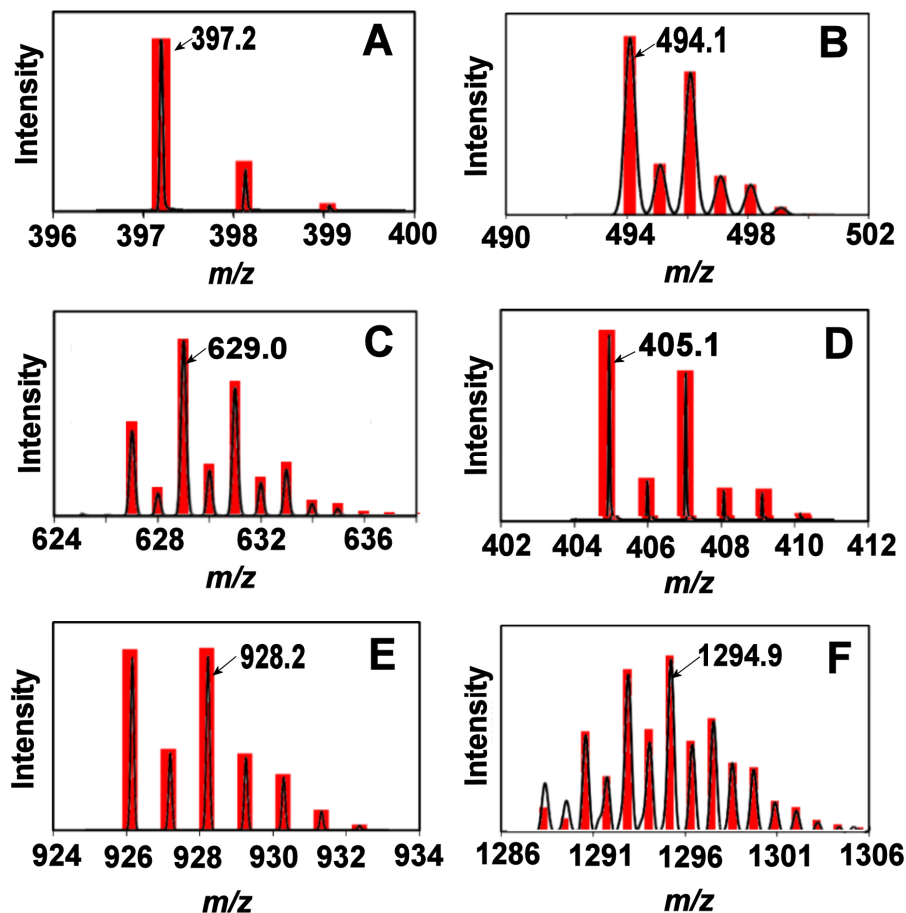


Figure 54. Partial single crystal structure of $\{[Cu_2(ttop)Cl_3]\}_2$, **9, showing the two ligand, four metal centre complex. The two ligands are held together by two bridging chlorides coordinating to the bidentate copper(II) centres.**

3.1 Mass spectrometry

Mass spectrometry can be used as a tool in the qualitative analysis of crystal structures where a single crystal is dissolved in a polar solvent. Using ESI-MS, solution studies can be carried out to confirm the empirical formula of the crystal. In this research, ESI-MS studies were used to observe the stepwise construction of **5–9** (see Figure 49).

From the electrospray measurements, it can be seen that the labile ttop ligand can complex with the copper(II) chloride first to form the mononuclear complex $[\text{Cu}(\text{ttop})\text{Cl}]^+$ **5**, while a change in the stoichiometry gives higher nuclearity complexes **6-9**. The ability to observe the formation of the complexes from low to higher nuclearity probably arises from the most favorable site (the tetradentate binding site) being filled first, and therefore allowing control over the nuclearity of the complex. ESI-MS measurements of ttop **4** in methanol (10^{-5} M) gave the ESI-MS spectrum A ($[\text{ttopH}]^+$, $m/z = 397.2$); half an equivalent of copper(II) chloride to one equivalent of **4** produced spectrum B ($[\text{Cu}(\text{ttop})\text{Cl}]^+$, $m/z = 494.1$); one equivalent of copper(II) chloride reacted with one equivalent of ttop produced spectrum C ($[\text{Cu}_2(\text{ttop})\text{Cl}_3]^+$, $m/z = 629.0$); one equivalent of 4,4'-bipyridine reacted with one equivalent of complex **5** and gave spectrum D ($[\text{Cu}(\text{H}(\text{trans-1-amino-cis-3,5-}N',N''\text{-2-imidopyridine})\text{Cl})]^+$, $m/z = 405.1$); one equivalent of copper(II) nitrate reacted with one equivalent of ttop producing complex **8** and gave spectrum E ($[\text{Cu}_2(\text{cis-3-amino-cis,trans-}N',N''\text{-2-imidopyridine})_2(\text{NO}_3)_3]^+$, $m/z = 928.2$); two equivalents of copper(II) chloride with one equivalent of ttop produced spectrum F (ESI-MS of $[\text{Cu}_4(\text{ttop})_2\text{Cl}_7]^+$, $m/z = 1294.9$). From the spectra produced, it can be seen that the stoichiometry of the reactant used in the reaction is the predominant factor in the formation of the complex (see Figure 55).



Label	m/z	Formula
A	397.2	$[\text{C}_{24}\text{H}_{24}\text{N}_6]^+$
B	494.1	$[\text{Cu}(\text{C}_{24}\text{H}_{24}\text{N}_6)\text{Cl}]^+$
C	629.0	$[\text{Cu}_2(\text{C}_{24}\text{H}_{24}\text{N}_6)\text{Cl}_3]^+$
D	405.1	$[\text{Cu}(\text{C}_{18}\text{H}_{21}\text{N}_5)\text{Cl}]^+$
E	928.2	$[\text{Cu}_2(\text{C}_{18}\text{H}_{21}\text{N}_5)(\text{NO}_3)_3]^+$
F	1294.9	$[\text{Cu}_4(\text{C}_{24}\text{H}_{24}\text{N}_6)\text{Cl}_7]^+$

Figure 55. A. ESI-MS measurement of $[\text{ttopH}]^+$, 4; B. ESI-MS measurement of $[\text{Cu}(\text{ttop})\text{Cl}]^+$, 5; C. ESI-MS measurement of $[\text{Cu}_2(\text{ttop})\text{Cl}_3]^+$, 6; D. ESI-MS measurement of $[\text{Cu}(\text{H}(\text{trans-1-amino-cis-3,5-}N',N''\text{-2-imidopyridine})\text{Cl})]^+$, 7; E. ESI-MS measurement of $[\text{Cu}_2(\text{cis-3-amino-cis,trans-}N',N''\text{-2-imidopyridine})_2(\text{NO}_3)_3]^+$, 8; F. ESI-MS measurement of $[\text{Cu}_4(\text{ttop})_2\text{Cl}_7]^+$, 9.

3.1.1 In-situ Mass Spectrometry

The combination of pre-diluted reactants *in-situ* was investigated using ESI-MS to allow the kinetically favored product to be observed and analysed. To create such experimental conditions, a tee-piece was used to enable the input and subsequent mixing of the reactants (see Figure 56).

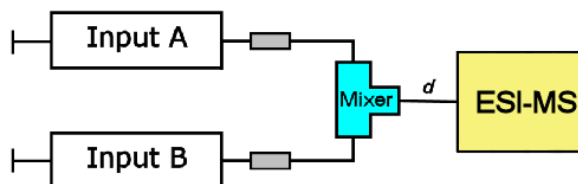


Figure 56. Schematic of tee-piece (mixer) combining two inputs to ESI-MS. The distance d is variable, but for these experiments was set at 5cm. The mixer had no dead volume and the tubing had a diameter of 0.9 mm. Inputs were set to a rate of approximately $100 \mu\text{L h}^{-1}$, and thus a combined input of approximately $200 \mu\text{L h}^{-1}$ was obtained.

Initially, input A contained ttop **4** in methanol (10^{-5} M) and input B was a blank control containing only methanol. This reaction mixture resulted in a spectrum with a predominant peak at $397 m/z$, this being analysed as ttop. Replacing the blank with 0.5 equivalents, 1 equivalent, and 2 equivalents of copper(II) chloride produced spectra b) to d), respectively (see Figure 57): 0.5 equivalents of copper(II) chloride gave the species $[\text{Cu}(\text{ttop})(\text{H}_2\text{O})_4(\text{OH})]^+$; the predominant species with 1 equivalent of copper(II) chloride being $[\text{Cu}(\text{ttop})\text{Cl}]^+$ and 2 equivalents of copper(II) chloride produced a spectrum showing the species $[\text{Cu}_2(\text{ttop})\text{Cl}_3]^+$ (see Figure 57). The use of a tee-piece allows a combination of dilute reactants to be observed directly after mixing. By using the most simple of building blocks, clusters were formed almost instantaneously, providing further evidence of the coordination self-assembly processes occurring in ttop Cu^{II} systems. It is interesting to note that the stoichiometry used to produce the crystal product is different to that used to produce the same complex when using *in-situ* mass spectrometry.

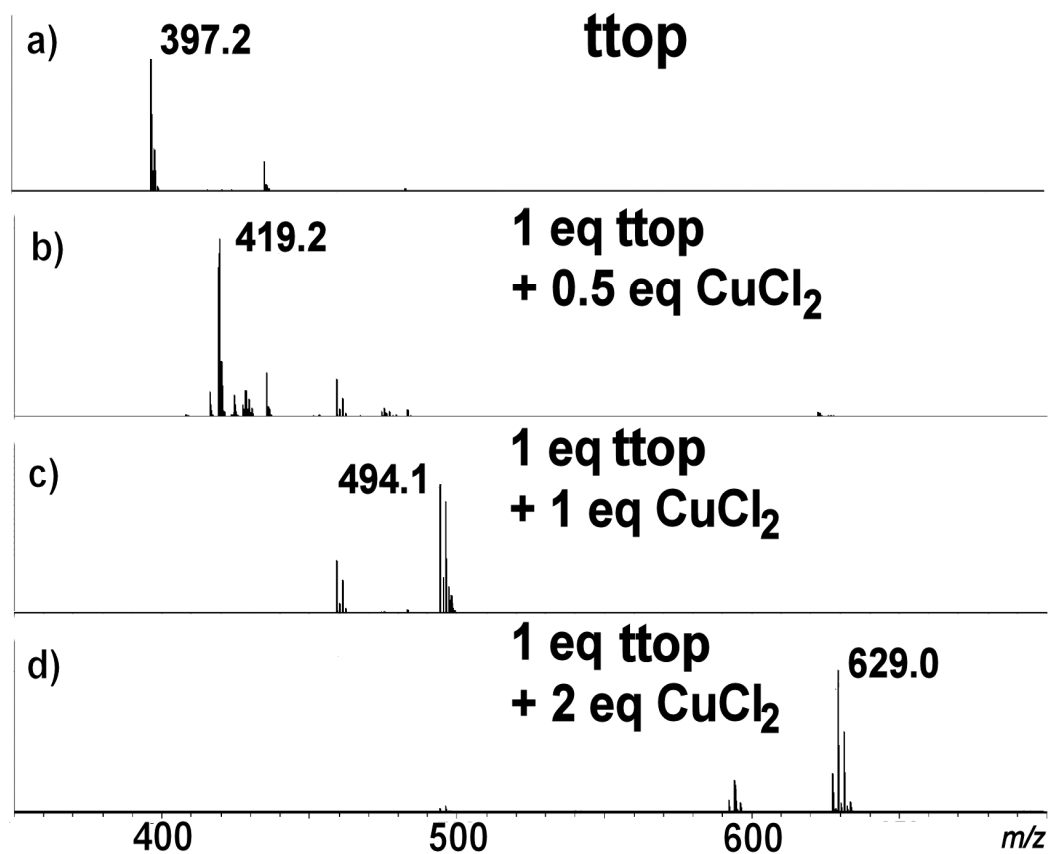


Figure 57. ESI-MS measurement of a) Input A: ttop in methanol (10^{-5} M), Input B: methanol, predominant species $[\text{ttopH}]^+$, $m/z = 397$; b) Input A: ttop in methanol (10^{-5} M), Input B: 0.5 equivalents copper(II) chloride, predominant species $[\text{Cu}(\text{hydrolysedttop})(\text{H}_2\text{O})_4(\text{OH})]^+$, $m/z = 419$; c) Input A: ttop in methanol (10^{-5} M), Input B: 1 equivalent copper(II) chloride, predominant species $[\text{Cu}(\text{ttop})\text{Cl}]^+$, $m/z = 494$; d) Input A: ttop in methanol (10^{-5} M), Input B: 2 equivalents copper(II) chloride, predominant species $[\text{Cu}_2(\text{ttop})\text{Cl}_3]^+$, $m/z = 629$.

Other first row transition metals were also complexed to the ttop ligand. Metal salts such as zinc iodide, zinc chloride and cobalt nitrate were reacted with ttop to give a number of different structures. $[\text{Zn}(\text{ttop})\text{Cl}]\text{Cl}(\text{H}_2\text{O})_2$ **10** was synthesised from zinc(II) chloride and ttop where a stoichiometry of 1:1 $\text{Zn}^{\text{II}}\text{Cl}_2$:ttop was used. The conformation of the complex is that of the energetically favoured ring-flipped ‘closed’ conformer where the imine double bonds are substituted in the sterically favoured *E*-conformation. The zinc(II) ion is coordinated within the tetradentate binding site in a distorted square-pyramidal

geometry by basal coordination to each of the four nitrogen atoms of the *cis*-imido pyridyl moieties. The Zn1-N bond lengths for the imine groups are 2.126(1) and 2.136(2) Å, with the bond lengths for the pyridyl Zn1-N being 2.131(1) and 2.158(2) Å with an apical coordination of one chloride ion with a bond length of 2.269(1) Å that is orientated towards the cyclohexane ring. The bidentate binding site is not involved in the coordination of a metal centre. The nitrogen atoms of the imine group and pyridyl group are oriented *anti* with respect to each other to minimise electronic repulsion between the lone pair on each nitrogen. The trans-imido pyridyl arm is twisted with respect to the cyclohexane ring at an angle of 79.8(1)° (see Figure 58).

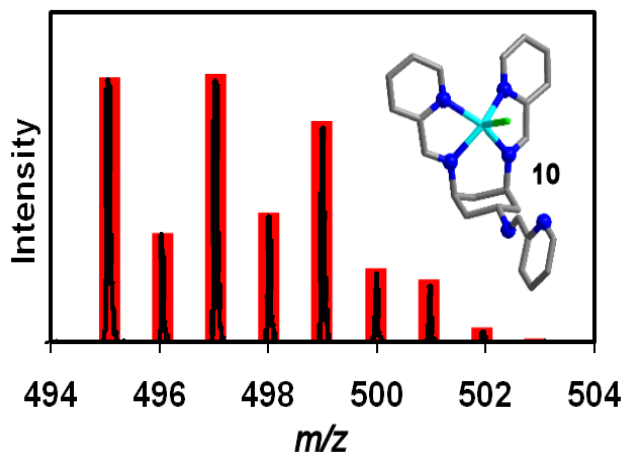


Figure 58. ESI-MS spectrum and partial single crystal structure of [Zn(ttop)Cl]⁺, 10.

[Zn(ttop)I]I(CH₃OH), **11**, was synthesised from zinc(II) iodide and ttop where a stoichiometry of 1:1 Zn^{II}:ttop was used. The conformation of the complex is that of the energetically favoured ring-flipped ‘closed’ conformer where the imine double bonds are substituted in the sterically favoured *E*-conformation. The zinc(II) ion is coordinated within the tetradentate binding site in a distorted square-pyramidal geometry by basal coordination to each of the four nitrogen atoms of the *cis*-imido pyridyl moieties. The Zn1-N bond lengths for the imine groups are 2.126(1) and 2.136(2) Å, with the bond lengths for the pyridyl Zn1-N being 2.131(1) and 2.158(2) Å with an apical coordination of one chloride ion with a bond length of 2.269(1) Å that is orientated towards the cyclohexane ring. The bidentate binding site is not involved in the coordination of a metal centre. The nitrogen atoms of the imine group and pyridyl group are oriented *anti* with respect to each

other to minimise electronic repulsion between the lone pair on each nitrogen. The trans-imido pyridine arm is twisted with respect to the cyclohexane ring at an angle of $75.1(1)^\circ$ (see Figure 59).

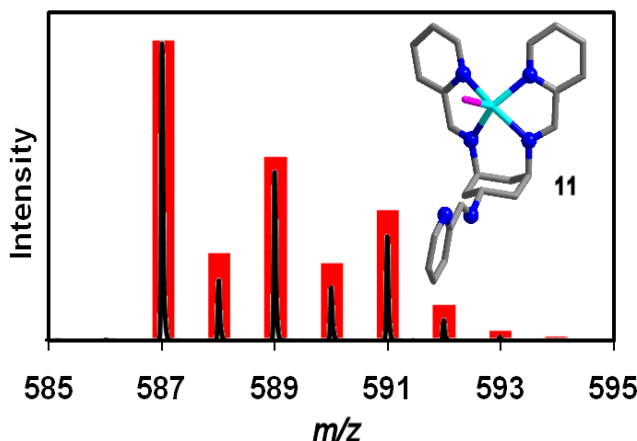


Figure 59. ESI-MS spectrum and partial single crystal structure of $[\text{Zn}(\text{ttop})\text{I}]^+$, **11**.

$[\text{Co}_2(\text{ttop})(\text{NO}_3)_3(\text{H}_2\text{O})_2](\text{NO}_3)(\text{CH}_3\text{CN})_2$, **12**, was synthesised from cobalt(II) nitrate and ttop where a stoichiometry of 1:1 $\text{Co}^{\text{II}}(\text{NO}_3)_2:\text{ttop}$ was used. Both coordination sites on each ligand are complexed to cobalt(II) ions in a distorted octahedral geometry. As with the mononuclear and dinuclear complexes **5** and **6**, respectively, the tetradentate binding site coordinates Co1 by its four nitrogen atoms available upon ring-flip of the cyclohexane ring (Co1-N imine groups bond lengths of 2.114(1) and 2.087(1) Å, Co1-N pyridyl bond lengths of 2.168(1) and 2.135(1) Å). The coordination sphere of Co1 is completed by one nitrate and one water ligand (Co1-NO_3 bond lengths of 2.088(1) Å, Co1-OH_2 bond lengths of 2.103(1) Å). The bidentate binding site coordinates a second cobalt(II) with its two nitrogen atoms (Co2-N imine bond lengths of 2.122(1) Å, Co2-N pyridyl bond lengths of 2.124(1) Å), along with one terminal water ligand ($\text{Co2-OH}_2 = 2.105(1)$ Å) and two nitrate ligands (Co2-NO_3 bond lengths of 2.056(1) and 2.229(1) Å). The trans-imido pyridine arm is twisted with respect to the cyclohexane ring at an angle of $73.7(1)^\circ$ (see Figure 60).

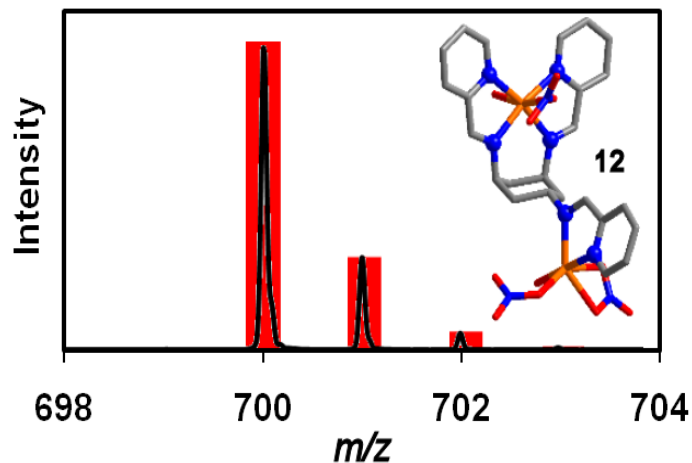


Figure 60. ESI-MS spectrum and partial crystal structure of $[\text{Co}_2(\text{ttop})(\text{NO}_3)_3]^+$, **12**.

$[\text{Cu}_2(\text{ttop})(\text{NO}_3)_4(\text{H}_2\text{O})](\text{CH}_3\text{OH})$, **13**, was synthesised from copper(II) nitrate and ttop where a stoichiometry of 1:1 $\text{Cu}^{\text{II}}(\text{NO}_3)_2$:ttop was used. Both coordination sites on each ligand are complexed to copper(II) ions in a distorted octahedral geometry. The tetradentate binding site coordinates Cu1 by its four nitrogen atoms available upon ring-flip of the cyclohexane ring (Cu1-N imine groups bond lengths of 2.009(1) and 2.017(1) Å, Cu1-N pyridyl bond lengths of 2.042(1) and 2.036(1) Å). The coordination sphere of Cu1 is completed by two nitrate (Cu1- NO_3 bond lengths of 2.310(1) Å, 2.702(1) Å). The bidentate binding site coordinates a second cobalt(II) with its two nitrogen atoms (Cu2-N imine bond lengths of 2.004(1) Å, Cu2-N pyridyl bond lengths of 1.993(1) Å), along with one terminal water ligand (Cu2- OH_2 bond lengths of 1.968(1) Å) and two nitrate ligands (Cu2- NO_3 bond lengths of 1.994(1) and 2.256(1) Å). The *trans*-imido pyridine arm is twisted with respect to the cyclohexane ring at an angle of 52.6(2)°.

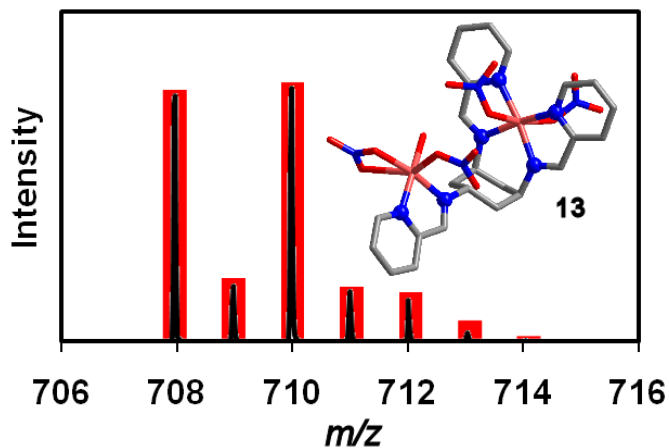


Figure 61. ESI-MS spectrum and partial crystal structure of $[\text{Cu}_2(\text{ttop})(\text{NO}_3)_3]^+$ 13.

A number of other complexes can also be formed with ttop, from complexes containing other first row divalent transition metal salts like nickel chloride to mixed metal complexes. Figure 62 shows the ESI-MS measurement of a mixed metal ttop complex where it is postulated that one of the two binding sites of the ligand has been filled with a copper(II) centre and the other site has been filled by a zinc(II) centre. The observed spectrum also showed the presence of the singly occupied species $[\text{Cu}(\text{ttop})(\text{NO}_3)]^+$ and $[\text{Zn}(\text{ttop})(\text{NO}_3)]^+$ with $[\text{Zn}_2(\text{ttop})(\text{NO}_3)_3]^+$ also being present.

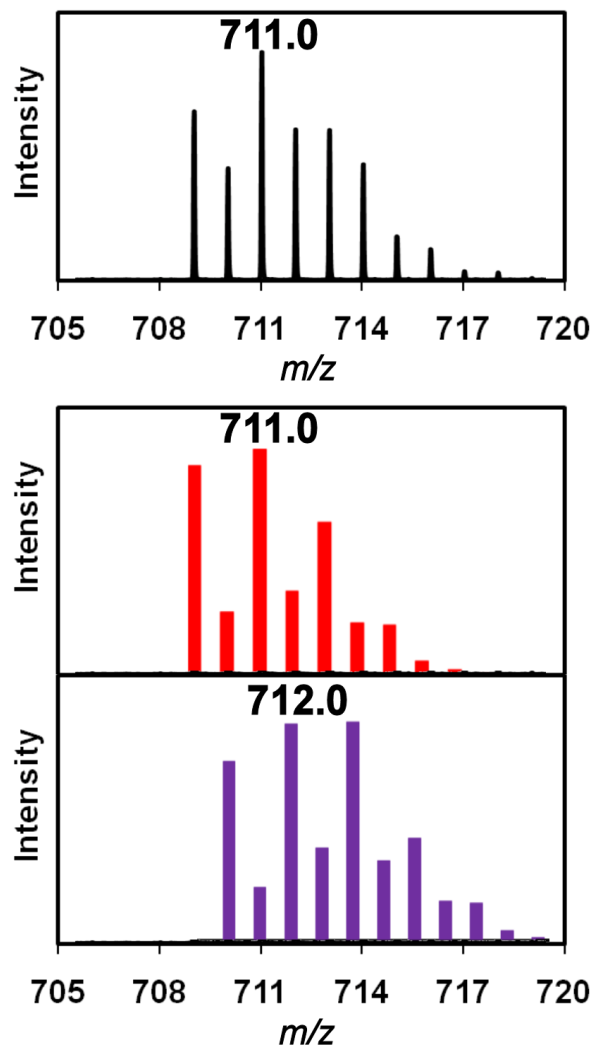


Figure 62. ESI-MS of a mixed metal ttop complex where the envelope at 711.0 m/z contains two species; $[\text{CuZn}(\text{ttop})(\text{NO}_3)_3]^+$ (711.0 m/z) (middle) and $[\text{Zn}_2(\text{ttop}(\text{NO}_3)_3)]^+$ (bottom).

In-situ mass spectrometry is an emerging method in monitoring the assembly of systems, such as the formation of polyoxometalates, using a variety of control parameters (stoichiometry, REDOX reagent, concentration, range, and rigidity of ligands). This technique removes the period of time that allows the thermodynamic product to be favoured and may have potential benefits for the analysis of unstable materials, which may be synthesised under closed flow conditions without the presence of oxygen. Mass spectrometry can also be used to probe reaction mechanisms and provide the existence of new complexes that have never before been observed.

3.2 Conclusions

Electrospray mass spectrometry was used to follow the formation of a range of coordination complexes synthesised from the labile ligand ttop, **4**, and divalent metal salts, with control of the stoichiometry and reaction conditions allowing the formation of complexes with different metal to ligand ratios (see Figure 63).

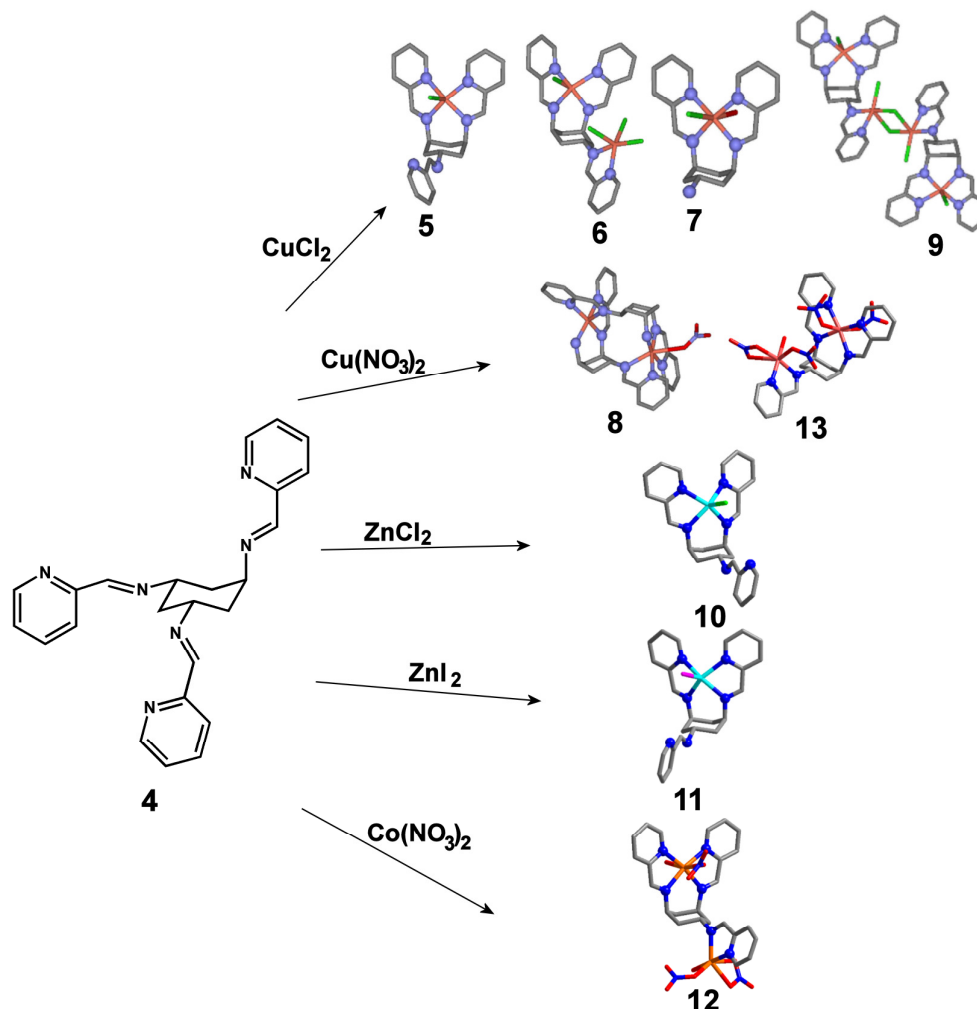


Figure 63. Summary of the complexes **5-13** formed when divalent salts are reacted with ttop **4**.

The reaction of copper(II) chloride with ttop, **4**, gave four structures. Complex **5** was synthesised from a 1:2 CuCl_2 :ttop stoichiometry where only the tetradentate coordination site was filled to give the complex $[\text{Cu}(\text{ttop})\text{Cl}]\text{Cl}(\text{CH}_3\text{OH})_2$. When the stoichiometry was changed to 1:1 CuCl_2 :ttop both the tetradentate and bidentate coordination sites were filled

by a copper(II) centre to give $[\text{Cu}_2(\text{ttop})\text{Cl}_4]\text{CH}_3\text{OH}$ **6**. Complex **7** was formed from the reaction of complex **2** with 4,4'-bipyridine to give the *trans*-hydrolysed mono-ligand complex $[\text{Cu}(\text{H}(\text{trans-1-amino-cis-3,5-}N',N''\text{-2-imidopyridine}))(\text{H}_2\text{O})\text{Cl}]\text{Cl}_2$. Here the *trans*-arm of the ligand was hydrolysed and protonated allowing for hydrogen-bonding interactions with counterions, the tetradentate binding site coordinating to a copper(II) centre also. A stoichiometry of 2:1 $\text{CuCl}_2:\text{ttop}$ gave complex $\{[\text{Cu}_2(\text{ttop})\text{Cl}_3]\}_2$, **9**, where two ligands were coordinated by a chloride bridge at the bidentate coordination site.

When the counterion was changed from chloride to nitrate two further complexes were formed. A stoichiometry of 1:1 $\text{Co}(\text{NO}_3)_2:\text{ttop}$ gave a dinuclear, diligand $\{[\text{Cu}_2(\text{cis-3-amino-cis,trans-}N',N''\text{-2-imidopyridine})_2]\}_2(\text{NO}_3)_4$, **8**, where one of the *cis*-arms of each ligand had been cleaved. The second complex that was synthesised was $[\text{Cu}_2(\text{ttop})(\text{NO}_3)_4(\text{H}_2\text{O})](\text{CH}_3\text{OH})$ **13** which was formed from a 1:1 $\text{Cu}(\text{NO}_3)_2:\text{ttop}$ stoichiometry to give a complex where both the tetradentate and bidentate sites were filled.

The reaction of ttop with zinc chloride in a 1:1 $\text{ZnCl}_2:\text{ttop}$ gave $[\text{Zn}(\text{ttop})\text{Cl}]\text{Cl}(\text{H}_2\text{O})_2$, **10**, where only the tetradentate site is filled. Complexes with both sites filled have been seen using ESI-MS but as yet no crystal structure has been obtained.

Zinc iodide was also coordinated to ttop, **4**, to give the complex $[\text{Zn}(\text{ttop})\text{I}]\text{I}(\text{CH}_3\text{OH})$, **11**, where, as with zinc chloride a 1:1 $\text{ZnI}_2:\text{ttop}$ stoichiometry gave a complex containing only one metal centre coordinated to the tetradentate site. ESI-MS also gave results indicative towards the formation of a two-metal one-ligand (M_2L) structure but no crystal structure has been obtained.

The final complex $[\text{Co}_2(\text{ttop})(\text{NO}_3)_3(\text{H}_2\text{O})_2](\text{NO}_3)(\text{CH}_3\text{CN})_2$ **12** was synthesised from a 1:1 $\text{Co}(\text{NO}_3)_2:\text{ttop}$ stoichiometry. Here a M_2L was formed with both the tetradentate and bidentate sites being filled. The ML complex can also be seen using ESI-MS but as yet no crystal structure has been acquired.

In-situ mass spectrometry was also used to follow the formation of complexes in solution allowing the kinetically favoured product to be observed and analysed. A tee-

piece was used to enable the input and subsequent mixing of the reactants to give the observed spectra shown in Figure 64. It can be seen that a solution containing a 1:2 CuCl₂:ttop stoichiometry gave the complex [Cu(*trans*-1-amino-*cis*-3,5-*N,N'*-2-imidopyridine)(H₂O)₄(OH)]⁺ (419.2 *m/z*); a 1:1 CuCl₂:ttop stoichiometry gave the complex [Cu(ttop)Cl]⁺ (494.1 *m/z*) and a 1:2 CuCl₂:ttop stoichiometry gave the complex [Cu₂(ttop)Cl₃]⁺ (629.0 *m/z*).

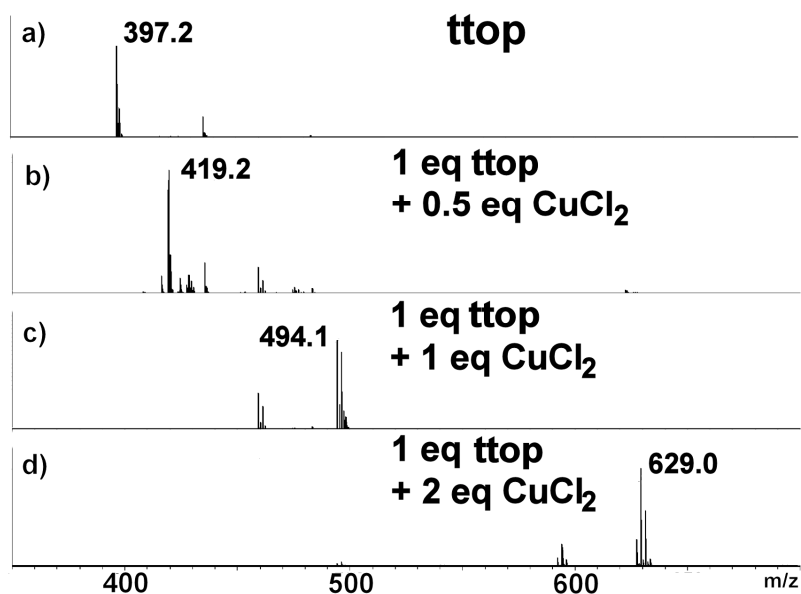


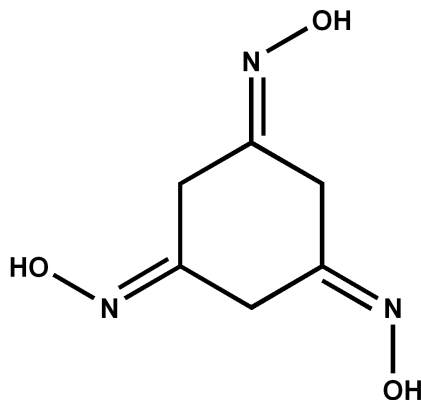
Figure 64. Summary of the *in-situ* ESI-MS measurements showing the formation of the kinetically favoured species.

The use of the tee-piece allowed the combination of dilute reactants to be observed directly after mixing. By using simple building blocks clusters were formed instantaneously, providing further evidence of the coordination self-assembly process occurring in ttop systems.

Future work on the coordination of divalent metal salts to ttop will be to complete the series of complexes that can be formed e.g. obtaining a crystal structure of a M₂L complex for zinc iodide and zinc chloride. The synthesis of other mixed metal complexes will be researched further to show which interesting properties that the system may exhibit.

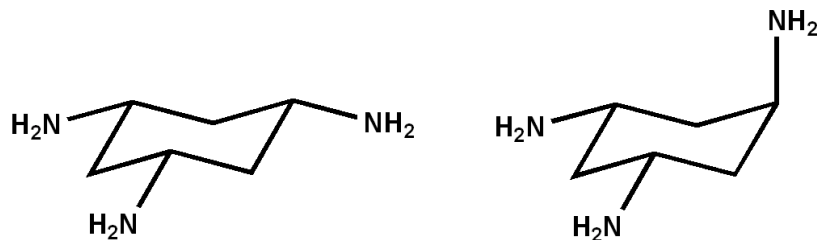
3.3 Experimental

3.3.1 1,3,5-Cyclohexanetrionetrioxime (chtt, 1)



Anhydrous 1,3,5-trihydroxybenzene (18.58 g, 0.15 mol) and anhydrous potassium carbonate (58.37 g, 0.42 mol) were dissolved in water (450 ml) and heated to 50 °C to aid complete dissolution during which, the solution changed from light violet to brown. The flask was covered in aluminium foil so as to exclude light from the reaction and hydroxylamine hydrochloride (54.34 g, 0.78 mol) was added slowly over a period of about five minutes. The resulting solution was stirred for a further 4 hours whereupon a grey precipitate was produced. This was recovered by filtration on a sintered (D3) funnel under vacuum and then washed with water (400 ml) and then acetone (300 ml) until the filtrate was colourless. The solid was dried overnight to give 1 as a yellow-grey powder (*ca.* 17 g, 0.10 mol, 66%). The product was found to be air and light sensitive and so was stored in a foil covered vial under nitrogen for a maximum of two days before use in further synthesis. M.p. 135-137 °C. FT-IR (Golden Gate) ν / cm^{-1} 3500-2500(s) (O-H, C-H), 1670(s) (C=N), 1470(s) (-CH₂-), 1425(s), 1375(s), 1120(s), 960(s), 940(s), 850(s), 820(s), 700(s), 620(s), 520(s).

3.3.2 cis,cis- and cis,trans-1,3,5-Triaminocyclohexane (cis-tach, 2 and trans-tach, 3)

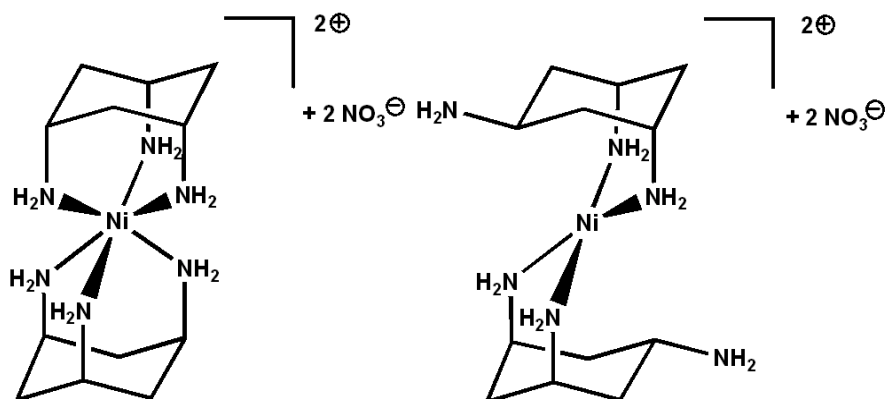


In a three-necked, 5 l flask equipped with a cold finger (cooled with dry ice-acetone), overhead stirrer and ammonia inlet, chtt (1, 12.0 g, 0.07 mol) was dissolved in liquid ammonia (1000 ml). Absolute ethanol (90 ml) was added to the ammonia solution followed by thinly sliced sodium (29.3 g, 1.28 mol), during which the vessel immersed in a dry ice-acetone bath (-78 °C). Dissolution of the sodium in the liquid ammonia gave a colour change from light yellow to a deep blue. The reaction was initiated by lowering the cooling bath and the resulting exothermic reaction was continuously monitored and controlled by re-applying the bath and continuously stirring (caution!). Reaction was complete in 15 to 20 minutes and the deep blue ammonia solution became colourless revealing a large amount of white precipitate. Water (25 ml) was added cautiously to the ammonia solution after 10 minutes and the mixture was stirred for a further 5 minutes to ensure that any remaining sodium had been quenched. The mixture was filtered through a büchner funnel using suction filtration. The filtrate was reduced by evaporation at 50 °C with continuous air flow to give a brown oil. This residue was made strongly alkaline with sodium hydroxide (7 g) and extracted with diethyl ether (800 ml) for 3 hours.

In parallel, the solid from the filtration was washed thoroughly with diethyl ether (800 ml) in the presence of sodium hydroxide (5 g) and then filtered. The filtrate from subsequent suction filtration was stirred with sodium hydroxide (7 g) for 3 hours.

Both mixtures were then filtered again and the colourless filtrates combined. Reduction of the diethyl ether solution *in vacuo* afforded a crude brown oil containing both tach-isomers (2 and 3, 7 - 9 g crude), which was taken up in methanol (20 ml).

3.3.3 Separation of *cis*- and *trans*-tach by Complexation with Nickel (II) Nitrate.



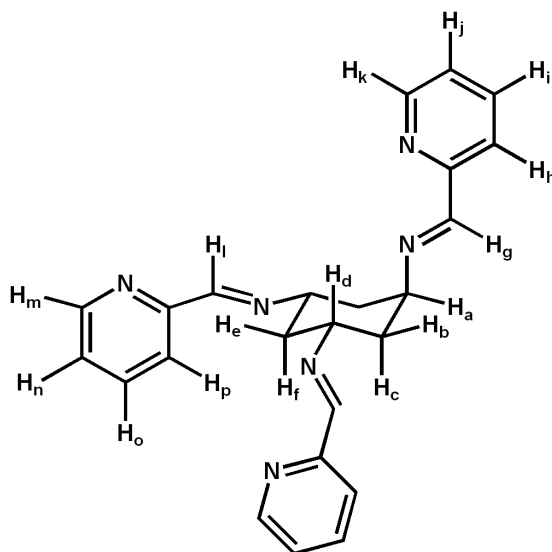
A standard solution of nickel (II) nitrate (9 g in 250 ml methanol) was added dropwise to the methanolic solution of 2 and 3 over a period of 1.5 hours. During the addition, a pink precipitate formed and was continuously filtered off, washed with ethanol and diethyl ether and dried in air to give the Ni-*bis*(*cis*-tach)nitrate complex (2a, 3.195 g, 7.24 mmol, 20 %). This was treated with concentrated hydrochloric acid (100 ml) to decompose the metal complex. After dissolving and stirring for half an hour, ethanol (250 ml) was added and *cis*-tach 3HCl precipitated as a white solid. The solid was filtered off, washed with ethanol (100 ml) and diethyl ether (100 ml) and dried in air to give 2 3HCl . $\text{C}_6\text{H}_{18}\text{Cl}_3\text{N}_3$ (238.58 g mol $^{-1}$): actual (expected): % C 29.97 (30.20), H 7.70 (7.60), N 17.19 (17.61); ^1H NMR (D_2O): δ /ppm 0.80 (ddd, 3H, J 12.1, 12.2, 12.2 Hz, H_a), 1.86 (ddd, 3H, J 11.4 Hz, 11.4, <2 H_b), 2.66 (ddd, 3H, J 12.1, 6.06, 6.05 Hz, H_c); ^{13}C NMR (D_2O): δ /ppm 41.40 (CH_2), 45.82 (C); MS (CI): m/z 130 (M^++1), m.p. 70 $^\circ\text{C}$ (10^{-2} mbar, subl); FT-IR (Golden Gate) ν / cm^{-1} 3277 (m) (N-H stretch), 3190 (m) (N-H stretch), 2920 (s) (C-H stretch), 2853 (s) (C-H stretch), 1597 (s), 1460 (s) (C-H bend), 1373 (m), 1146 (s), 974 (w), 856 (w), 671 (m).

The *tris*-hydrochloride salt 2 3HCl was suspended in methanol and a methanolic solution containing four equivalents of sodium hydroxide was added. The solution was stirred until full dissolution and filtered. The methanol was removed *in vacuo* resulting in a slightly pink solid, which was sublimed to yield 2. ^1H NMR (D_2O): δ /ppm 1.65 (ddd, 1H, J 11.5, 11.5, 11.6 Hz, H_c), 1.90 (ddd, 2H, J 12.3, 12.3, 3.8 Hz, H_b), 2.30 (ddd, 2H, J 13.8,

13.8 Hz, <2 NH₂), 2.45 (H_a, ddd, 1H, *J* 11.9, 11.9, <2 Hz, H_c), 3.65 (ddd, 2H, *J* 12.3, 12.3, 3.0 Hz, H_d), 4.00 (ddd, 1H, *J* 12.4, 12.4, 3.3 Hz, H_a); ¹³C NMR (D₂O): δ /ppm 35.12 (CH₂), 48.02 (CH); M.p. 180 °C (1 mbar, subl); FT-IR (Golden Gate) ν /cm⁻¹ 2870 (s) (C-H stretch), 2781 (s) (C-H stretch), 2550 (m) (C-H stretch), 1605 (m) (N-H bend), 1520 (m), 1408 (m) (C-H bend), 1331 (w), 1204 (w), 1006 (w), 994 (w), 910 (w), 883 (w), 660 (w).

After 2a had precipitated from the solution of mixed isomers, a small addition of the nickel(II)nitrate solution was used to initiate precipitation of the Ni-*bis(trans-tach)*nitrate (3a), which was cooled overnight and all precipitation of 3a removed by filtration. Reduction of the mother liquor yielded the remaining uncomplexed *trans-tach* (3). Purification was achieved by Kugelrohr distillation (131 °C, 1 mbar) gave 3 as a clear oil (2.34 g, 18.11 mmol, 25 %). C₆H₁₅N₃·0.6CH₃OH (148.42 g mol⁻¹): actual (expected): % C: 52.88 (53.41), H: 11.86 (11.82), N: 28.26 (28.31); ¹H NMR (D₂O): δ /ppm 0.84 (q, 1H, *J* 11.8 Hz), 1.17 (td, 2H, *J* 11.8, 3.2 Hz), 1.69 (dd, 2H, *J* 11.8, 3.7 Hz), 1.91 (dtt, 1H, *J* 11.8, 3.7, 2.2 Hz), 2.91 (tt, 2H, *J* 11.8, 3.7 Hz), 3.24 (*p*quint, 1H, *J* 3.2-3.5 Hz); ¹³C NMR (D₂O): δ /ppm 42.84 (CH₂), 45.97 (CH₂), 46.86 (CH), 48.26 (CH); MS (CI) *m/z* 130 (M⁺+1); B.p. 131 °C (1 mbar); FT-IR (Golden Gate) ν /cm⁻¹ 3344 (m) (N-H stretch), 3279 (m) (N-H stretch), 3190 (m) (N-H stretch), 2924 (s) (C-H stretch), 2851 (s) (N-H stretch), 1589 (s), 1458 (m) (C-H bend), 1377 (m), 1339 (w), 1269 (w), 1030 (w), 953 (w).

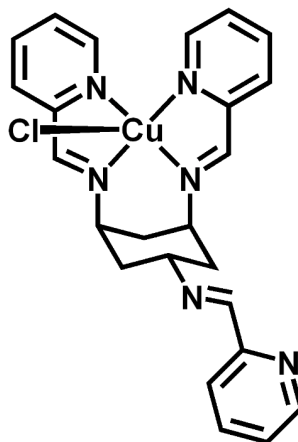
3.3.3.1 *Cis,trans* -1,3,5-tris-(pyridine-2-carboxaldimino)-cyclohexane (*trans-ttop*, 4)



To a methanolic solution (100 ml) of *cis,trans*-1,3,5-triaminocyclohexane (1 g, 7.85 mmol) and triethylamine (2.38 g, 23.55 mmol) pyridine-2-carboxaldehyde (2.38 g, 23.18 mmol) was added and refluxed for 24 hrs under nitrogen. The solvent was removed under reduced pressure, the resulting brown product was taken up in dichloromethane (150 ml) and washed with water (3 x 50 ml). The organic layer was dried over magnesium sulphate and the dichloromethane was removed in vacuo. Yield: 2.24 g (5.64 mmol, 72 %). M.p. 75 °C. $^1\text{H-NMR}$ (400 MHz, CDCl_3) δ /ppm 8.56 (d, 1H, J 4.9 Hz, H_k), 8.55 (d, 2H, J 5.0 Hz, H_m), 8.40 (s, 2H, H_l), 8.38 (s, 1H, H_g), 8.02 (d, 1H, J 8.0 Hz, H_n), 7.90 (d, 2H, J 8.0 Hz, H_p), 7.68 (d, 1H, J 8.0, 7.5 Hz, H_i), 7.62 (ddd, 2H, J 1.2, 7.4, 4.8 Hz, H_o), 7.23 (ddd, 1H, J 1.1, 7.4, 4.9 Hz, H_j), 7.12 (ddd, 2H, 1.1, 7.4, 5.1 Hz, H_n), 4.11 (dddd, 2H, J 3.7, 4.1, 11.3, 11.3 Hz, H_d), 3.97 (bs, 1H, H_a), 2.07 (m, 3H, H_b , H_e), 1.95 (bd, 1H, J 12.5 Hz, H_f), 1.80 (bd, 2H, J 12.5 Hz, H_c). $^{13}\text{C-NMR}$ (75 MHz, CDCl_3) δ /ppm 159.16 (CH_2), 158.83 (CH), 153.38 (C), 153.33 (C), 147.95 (CH), 147.84 (CH), 135.00 (CH), 123.20 (CH), 123.10 (CH), 119.99 (CH), 119.75 (CH) 63.48 (CH), 61.68 (CH), 39.90 (CH_2), 38.68 (CH_2). IR (Golden Gate) ν /cm $^{-1}$ 3059 (b) (N-H stretch), 2928 (m) (C-H stretch), 2858 (m) (C-H stretch), 1643 (s) (C=N), 1585 (s) (C-H bend), 1566 (s), 1466 (s) (aromatic C=C), 1435 (s), 1373 (m), 1319 (w), 1288 (w), 1227 (w), 1134 (m), 1080 (m), 1042 (m), 1018 (w), 991 (s), 972 (s), 860 (s), 772 (s), 741 (s), 664 (m), 650 (m), 617 (s), 662 (m), 517 (s). MS: m/z 419

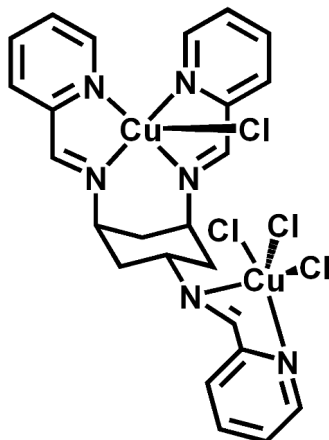
([M⁺Na]⁺). Elemental analysis for C₂₄H₂₄N₆, found (expected) %: C 72.53 (72.70), H 6.31 (6.10), N 20.90 (21.20).

3.3.4 Synthesis of [Cu(ttop)Cl]Cl(CH₃OH)₂, 5



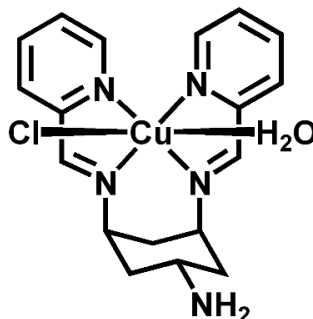
A methanolic solution (20 ml) of ttop **4** (100 mg, 0.25 mmol) was added to a solution of copper (II) chloride (30 mg, 0.23 mmol) in methanol (5 ml). The solution changed from a pale yellow colour to dark green. The solution was stirred for 30 mins and reduced in volume to ca. 5 ml. Crystallisation by diffusion of ether resulted in dark green crystals. Yield: 20 mg (0.034 mmol, 13%). IR (KBr) ν /cm⁻¹ 3433 (s) (N-H stretch), 2928 (w) (C-H stretch), 2356 (w) (C-H stretch), 1644 (m) (C=N), 1602 (m) (C-H bend), 1385 (s) (aromatic C=C), 1309 (m), 1242 (s), 1135 (m), 978 (w), 867 (w). Elemental analysis for C₂₄H₂₄Cl₂CuN₆O, found (expected) %: C 53.18 (52.84), H 4.63 (4.43), N 15.54 (15.41).

3.3.5 Synthesis of $[\text{Cu}_2(\text{ttop})\text{Cl}_4](\text{CH}_3\text{OH})_6$, **6**



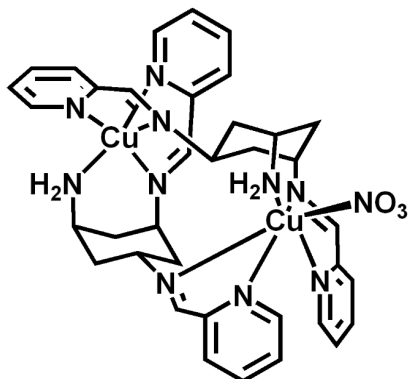
A methanolic solution (20 ml) of ttop **4** (100 mg, 0.25 mmol) was added to a solution of copper (II) chloride (34 mg, 0.25 mmol) in methanol (5 ml). The solution changed from a pale yellow colour to dark green. The solution was stirred for 30 mins and reduced in volume to ca. 5 ml. Crystallisation by diffusion of ether resulted in dark green crystals. Yield: 133.9 mg (0.192 mmol, 76%). IR (KBr) ν / cm^{-1} 3430 (s) (N-H stretch), 2926 (w) (C-H stretch), 2065 (w) (C-H stretch), 1638 (s) (C=N), 1598 (s) (C-H bend), 1478 (m) (aromatic C=C), 1446 (m), 1384 (m) 1305 (m), 1271 (w), 1226 (m), 1158 (w), 1132 (m), 1048 (w), 1019 (w), 992 (w), 926 (w), 874 (w), 775 (m). Elemental analysis for $\text{Cu}_2\text{C}_{25}\text{H}_{28}\text{N}_6\text{Cl}_5\text{O}$, found (expected) %: C 40.78 (41.15), H 3.98 (3.87), N 11.19 (11.52).

3.3.6 Synthesis of $[\text{Cu}(\text{H}(\text{trans-1-amino-cis-3,5-N',N''-2-imidopyridine}))(\text{H}_2\text{O})\text{Cl}]\text{Cl}_2$, 7



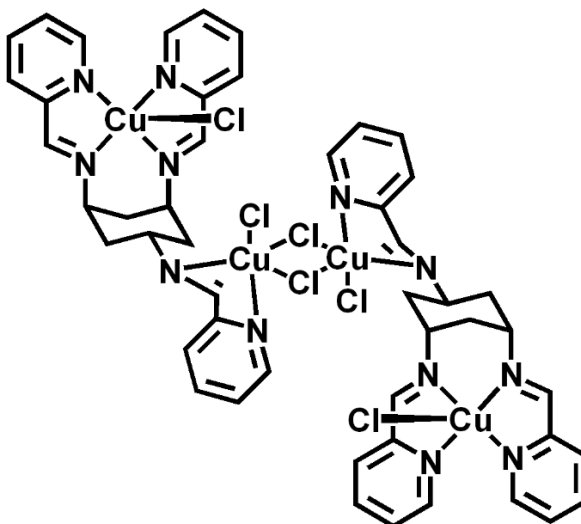
A methanolic solution (20 ml) of **4** (55 mg, 0.041 mmol) was added to a solution of 4,4'-bipyridine (6 mg, 0.041 mmol) in methanol (5 ml). A green-brown precipitation formed immediately. Methanol was added until the volume was 75 ml and solution refluxed for 30 minutes. After evaporation of methanol to a volume of ca. 5 ml, filtration through cotton wool afforded a clear brown solution. Crystallisation by diffusion with ether resulted in brown/green crystals. Yield: 5.1 mg (0.0095 mmol, 23 %). IR (KBr) v/cm^{-1} 3424 (s) (N-H stretch), 2857 (w) (C-H stretch), 2057 (w) (C-H stretch), 1639 (s) (C=N), 1598 (s) (C-H bend), 1479 (w) (aromatic C=C), 1444 (w), 1383 (m), 1303 (w), 1269 (w), 1227 (w), 1157 (m), 1132 (w), 1101 (w), 1047 (w), 1019 (w), 882 (m), 776 (m). Elemental analysis for $\text{CuC}_{19}\text{H}_{27}\text{N}_5\text{O}_4\text{Cl}_3$, found (expected) %: C 40.61 (40.79), H 4.46 (4.86) N 12.33 (12.52).

3.3.7 Synthesis of $\{[\text{Cu}_2(\text{cis-3-amino-cis,trans-N',N''-2-imidopyridine})_2]\}_2(\text{NO}_3)_4$, **8**



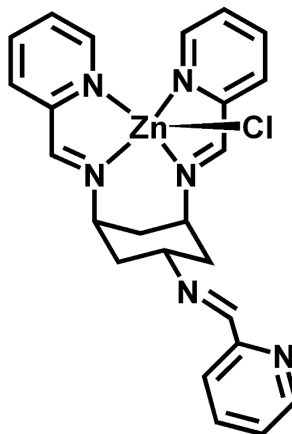
A methanolic solution (20 ml) of ttop **4** (80 mg, 0.20 mmol) was added to a solution of copper(II) nitrate (48.32 mg, 0.20 mmol) in methanol. The colour changed from colourless to dark green. The solution was stirred for one hour and reduced in volume to ca. 5 ml. Crystallisation by diffusion of ether resulted in green crystals. Yield: 169.4 mg (0.156 mmol, 78 %). IR (KBr) ν/cm^{-1} 3444 (s) (N-H stretch), 3203(w) (N-H stretch), 3104 (w), 2906 (w) (C-H stretch), 2426 (w) (C-H stretch), 1763 (w), 1639 (m) (C=N), 1600 (m), 1482 (w) (aromatic C=C), 1383 (s), 1225 (w), 1159 (w), 1133 (w), 1108 (w), 1075 (w), 1042 (w), 1023 (w), 959 (w), 910 (w), 887 (w), 826 (w), 781 (s). Elemental analysis for $\text{Cu}_2\text{C}_{39}\text{H}_{52}\text{O}_{15}\text{N}_{14}$, found (expected) %: C 43.55 (43.21), H 4.39 (4.84), N 18.38 (18.09).

3.3.8 Synthesis of $\{[\text{Cu}_2(\text{ttop})\text{Cl}_3]\text{Cl}\}_2$, **9**



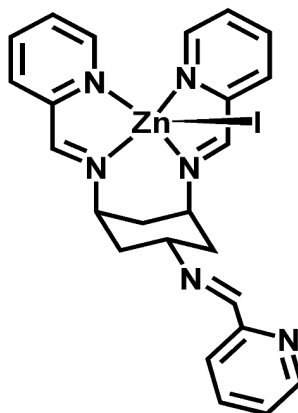
A methanolic solution (20ml) of ttop **4** (100 mg, 0.25 mmol) was added to a solution of copper (II) chloride (68 mg, 0.50 mmol) in methanol (5 ml). The solution changed from a pale yellow colour to a dark green. The solution was stirred for 30 mins and reduced in volume to ca. 5 ml. Crystallisation by diffusion of ether resulted in dark green crystals. Yield: 278.1 mg (0.209 mmol, 83 %). IR (Golden Gate) ν/cm^{-1} 3435(m) (N-H stretch), 3037(m) (N-H stretch), 2951(m) (C-H stretch), 2925(m) (C-H stretch), 1643(s) (C=N), 1597(s), 1567(m), 1479(m) (aromatic C=C), 1444(s), 1398(w), 1381(w), 1323(w), 1302(s), 1269(w), 1227(s), 1159(w), 1132(s), 1105(m), 1049(m), 1014(m), 980(s), 935(w), 881(m), 768(s), 742(m), 696(w), 642(s). Elemental analysis for $\text{Cu}_2\text{C}_{26}\text{H}_{32}\text{N}_6\text{Cl}_6$, found (expected) %: C 40.78 (40.64), H 3.98 (4.19), N 11.19 (10.94).

3.3.9 Synthesis of $[\text{Zn}(\text{ttop})\text{Cl}]\text{Cl}(\text{H}_2\text{O})_2$, 10

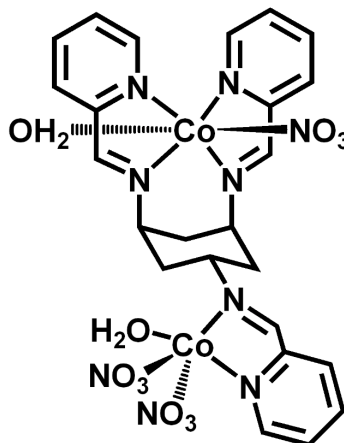


A methanolic solution (20ml) of ttop **4** (80 mg, 0.20 mmol) was added to a solution of zinc (II) chloride (27 mg, 0.20 mmol) in methanol (5 ml). The solution changed from a pale yellow colour to a dark yellow. The solution was stirred for 30 mins and reduced in volume to ca. 5 ml. Crystallisation by diffusion of ether resulted in yellow crystals. Yield: 73.4 mg (0.146 mmol, 73 %). IR (Golden Gate) ν / cm^{-1} 3402 (m) (N-H stretch), 3055 (m) (N-H stretch), 2931 (m) (C-H stretch), 2862 (m) (C-H stretch), 2037(m), 2051(m), 2025(m), 2037(w), 1643(s) (C=N), 1589(s), 1566(s), 1465(m) (aromatic C=C), 1435(s), 1381(s), 1311(w), 1226(m), 1134(m), 1072(m), 1049(m), 1018(m), 987(m), 864(m), 771(s), 740(s), 709(s), 671(s), 640(s). Elemental analysis for $\text{ZnC}_{24}\text{H}_{24}\text{N}_6\text{Cl}$, found (expected) %: C 58.72 (58.16), H 4.26 (4.88), N 17.12 (16.97).

3.3.10 Synthesis of [Zn(ttop)I]I(CH₃OH), 11

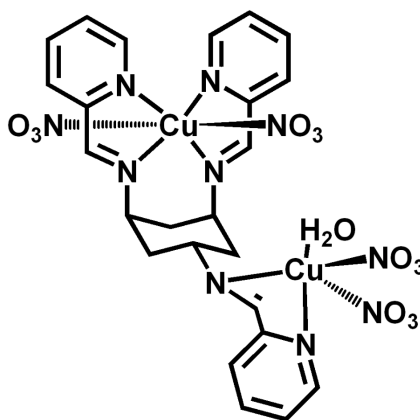


A methanolic solution (20ml) of ttop **4** (80 mg, 0.20 mmol) was added to a solution of zinc (II) iodide (64 mg, 0.20 mmol) in methanol (5 ml). The solution changed from a pale yellow colour to a dark yellow. The solution was stirred for 30 mins and reduced in volume to ca. 5 ml. Crystallisation by diffusion of ether resulted in yellow crystals. Yield: 71.2 mg (0.121 mmol, 60 %). IR (Golden Gate) ν /cm⁻¹ 3425(m) , 3286(m) (N-H stretch), 3055(w), 2931(m) (C-H stretch), 2854(m) (C-H stretch), 2337(w), 1643(s) (C=N), 1589(s), 1558(s), 1465(w) (aromatic C=C), 1435(m), 1388(s), 1303(s), 1226(w), 1134(m), 1049(w), 1018(m), 987(m), 864(m), 771(s), 709(s), 671(s), 640(s). Elemental analysis for ZnC₂₄H₂₄N₆I, found (expected) %: C 49.54 (49.06), H 4.28 (4.12), N 14.13 (14.31).

3.3.11 Synthesis of $[\text{Co}_2(\text{ttop})(\text{NO}_3)_3(\text{H}_2\text{O})_2](\text{NO}_3)(\text{CH}_3\text{CN})_2$, 12

An acetonitrile solution (20ml) of ttop **4** (100 mg, 0.25 mmol) was added to a solution of cobalt (II) iodide (67 mg, 0.25 mmol) in acetonitrile (5 ml) under nitrogen. The solution changed from colourless to red. The solution was stirred for 2 hrs and reduced in volume to ca. 5 ml. Crystallisation by diffusion of ether resulted in red/brown crystals. Yield: 102.5 mg (0.146 mmol, 58 %). IR (Golden Gate) ν / cm^{-1} 3520(s) (N-H stretch), 3448(s) (N-H stretch), 2951(m) (C-H stretch), 2341(w), 1770(w), 1620(s) (C=N), 1431(s) (aromatic C=C), 1274(s), 1047(s), 1016(m), 883(w), 864(w), 808(s), 758(m), 725(m). Elemental analysis for $\text{Co}_2\text{C}_{27}\text{H}_{42}\text{N}_{10}\text{O}_{18}$, found (expected) %: C 35.35 (34.93), H 4.02 (4.17), N 17.7 (17.25).

3.3.12 Synthesis of $[\text{Cu}_2(\text{ttop})(\text{NO}_3)_4(\text{H}_2\text{O})](\text{CH}_3\text{OH})$, 13



A methanolic solution (20ml) of ttop **4** (80 mg, 0.20 mmol) was added to a solution of copper (II) nitrate (49 mg, 0.20 mmol) in methanol (5 ml). The solution changed from colourless to a dark green. The solution was stirred for 1 hr and reduced in volume to ca. 5 ml. Crystallisation by diffusion of ether resulted in green crystals. Yield: 51.2 mg (0.07 mmol, 35 %). IR (Golden Gate) ν/cm^{-1} 3088 (m) (N-H stretch), 2322(w) (C-H stretch), 1643(m) (C=N), 1602(s), 1573(w), 1467(s) (aromatic C=C), 1402(s), 1450(s), 1226(s), 1157(m), 1109(m), 1095(w), 1010(s), 922(w), 910(w), 881(w), 806(s), 773(s), 752(m), 694(m), 678(m), 646(m), 632(m). Elemental analysis for $\text{Cu}_2\text{C}_{26}\text{H}_{34}\text{N}_9\text{O}_{12}$, found (expected) %: C 39.15 (39.49), H 4.18 (4.33), N 15.80 (15.95).

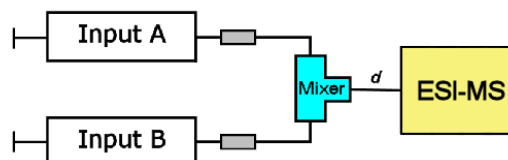
3.3.13 Electrospray and cryospray mass spectrometry (ESI-MS and CSI-MS)

All MS data were collected using a Q-trap, time-of-flight MS (MicroTOF-Q MS) instrument supplied by Bruker Daltonics Ltd. A cryospray source, also supplied by Bruker Ltd., was used to collect data under the conditions specified below. The detector was a time-of-flight, microchannel plate detector, and all data were processed using the Bruker Daltonics Data Analysis 4.0 software, while simulated isotope patterns were investigated using Bruker Isotope Pattern software and Molecular Weight Calculator 6.45. The following parameters were consistent for all CSI-MS scans given below. The calibration solution used was Agilent ES tuning mix solution, Recorder No. G2421A, enabling

calibration between $-100\ m/z$ and $3000\ m/z$. This solution was diluted 60:1 with acetonitrile. Samples were introduced into the MS *via* direct injection at $180\ \mu\text{L}/\text{h}$ having been diluted to $10^{-5}\ \text{M}$ in methanol. The drying nitrogen gas temperature was at $180\ ^\circ\text{C}$. The ion polarity for all MS scans recorded was positive, with the voltage of the capillary tip set at $4500\ \text{V}$, end plate offset at $-500\ \text{V}$, funnel 1RF at $300\ \text{Vpp}$, and funnel 2 RF at $400\ \text{Vpp}$.

All theoretical peak assignments were determined *via* comparison of the experimentally determined isotopic patterns for each peak, with simulated isotopic patterns. For relatively small complexes such as the ttop complexes, the isotopic pattern is quite distinct and comparison between experimental and simulated patterns is more meaningful (see Figure 2), than in the case of larger fragments where the isotopic pattern takes on a Gaussian shape and it cannot be said with certainty that the suggested peak is unequivocally correct.

3.3.14 In-situ mass spectrometry



A tee-piece was used to enable the input and subsequent mixing of the reactants. The distance d is variable, but for these experiments was set at 5cm . The mixer had no dead volume and the tubing had a diameter of $0.9\ \text{mm}$. Each solution was injected into the mass spectrometer at approximately $100\ \mu\text{L}\ \text{h}^{-1}$, and thus a combined input of approximately $200\ \mu\text{L}\ \text{h}^{-1}$ was obtained. Initially input A was 4 in methanol ($10^{-5}\ \text{M}$) and input B was a blank control only containing methanol which were reacted together in the mixer. The blank was then replaced with 0.5 equivalents, 1 equivalent and 2 equivalents of copper(II) chloride to give four different spectra each showing a different stoichiometric species being formed.

4 DIRECT C-H TRANSFORMATION VIA IRON CATALYSIS

As previously mentioned (see section 1.4) iron-oxo chemistry plays a vital role in many biological processes such as the catalytic oxidation of C-H and C=C moieties.^{62,65,118} It has been postulated by many that the catalytic cycle of such a process involves an unstable, reactive iron(V) species but it has never before been directly observed.^{92,95,119} Due to the unstable d^3 configuration of the iron(V) species, where the three t_{2g} orbitals are only half filled, the reactive species will attempt to gain electrons to become the preferred iron(II) or iron(III) species and so will decompose quickly. To slow down this decomposition, cryospray mass spectrometry was used to lower the temperature of the solution spray and so slow the reaction in order to observe the postulated reactive intermediate.

The research in this chapter focusses primarily on the reaction between an iron(II) complex and H_2O_2 . Ever since this type of chemistry was discovered by Fenton almost a decade ago¹²⁰ a debate has been raised about the reactive oxidant that is formed by O-O bond cleavage, whether it was homolytically cleaved to produce the OH radical, or heterolytically to produce an Fe(V)=O intermediate. DFT computational analysis proposed a mechanistic cycle where the Fe(V)=O species was the reactive intermediate (see Figure 65)^{89,90} but no direct spectroscopic evidence has been obtained.

With the use of cryospray mass spectrometry, the iron(V)-oxo species was directly observed within the complex $[Fe^V(O)(OH)(PyMe_2tacn)]^+$ (PyMe₂tacn = 1-(2'-pyridylmethyl)-4,7-dimethyl-1,4,7-triazacyclononane) and the subsequent dihydroxylation reaction with an olefin. Oxygen atom transfer was also followed using isotopic labelling with temperature variable mass spectrometry being used to investigate the reactive intermediates.

The ligand **14** was synthesised by Costas *et al.*⁹¹ It was postulated that this ligand undergoes a dihydroxylation reaction with an olefin through the catalytic cycle shown in Figure 65. Ligand **14** is reacted with an oxidant (such as H_2O_2) in acetonitrile to form an

iron(III)-OH species. Next the addition of water allows water assisted heterolytical O-O cleavage to occur to give a reactive iron(V)=O intermediate, it is this intermediate that is thought to be the important species that allows the *cis*-dihydroxylation reaction to take place. The olefin then coordinates to the iron complex to give the *cis*-dihydroxylated product. The iron(III)-OH is then regenerated by the addition of water.

The heterolytical water assisted O-O cleavage of the bound OOH moiety was followed using ^{18}O -labelled reagents. Complex **15** was first reacted with H_2^{18}O and $\text{H}_2^{16}\text{O}_2$ to give a species that contained one ^{18}O -labelled oxygen and one ^{16}O -labelled oxygen, the same being seen when H_2^{16}O and H_2^{18}O were used. Both H_2^{18}O and $\text{H}_2^{18}\text{O}_2$ were also used in the reaction to give a species that contained two labelled oxygen atoms therefore providing evidence for the heterolytical O-O cleavage of the bound OOH moiety (see Figure 65).

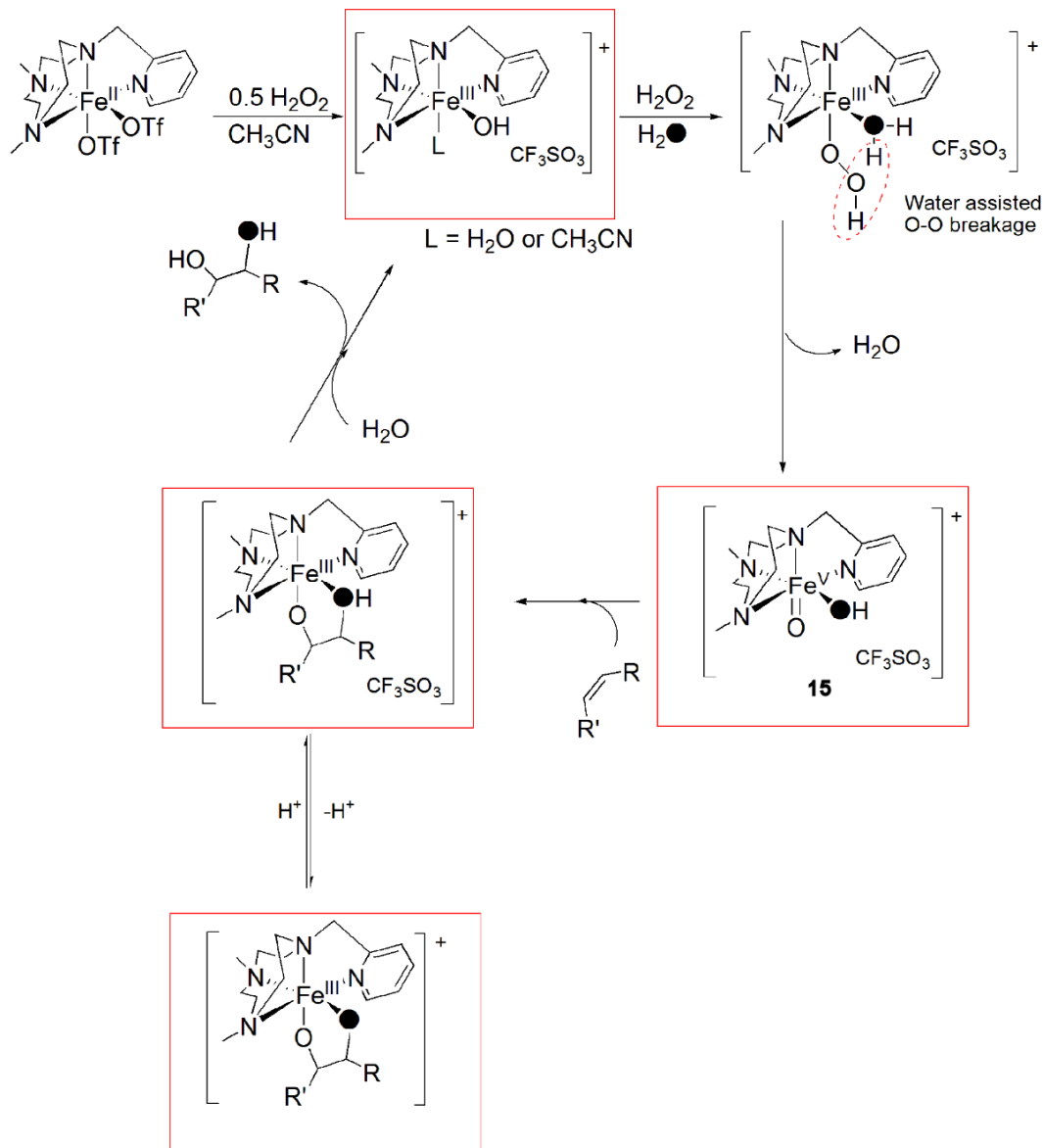


Figure 65. Representation of the mechanistic scheme for the formation of the Fe(V)=O compound $[\text{Fe}^{\text{V}}(\text{O})(\text{OH})(\text{PyMe}_2\text{tacn})](\text{CF}_3\text{SO}_3)_2$ **15** and the dihydroxylation reaction with cyclooctene. The boxed structures represent the species found in the mass spectrometry experiments (shaded O = labelled oxygen).

4.1 Temperature controlled cryospray mass spectrometry

Temperature controlled cryospray mass spectrometry allows the study of highly reactive intermediate species at very low reagent concentrations without the need of large product accumulation required for most spectroscopic techniques. The use of temperature controlled CSI-MS to follow the emergence of a reactive species at low temperatures minimises the biomolecular decomposition commonly associated with highly-reactive species and allows much colder conditions than previously allowed with ESI-MS.

The formation of the iron(V) species was explored using temperature controlled cryospray mass spectrometry (CSI-MS) where both the sample and the spray had been cooled to 4 °C and -40 °C respectively. The spectrum was recorded for 20 minutes with the temperature being increased by 20 °C every 5 minutes. It was postulated that the reactive intermediate would be seen at the lower temperature of -40 °C and as the temperature was increased the intermediate would destabilise and decompose. CSI-MS analysis of the reaction of **14** with H₂O₂ (100 eq) between -40 °C and 20 °C showed the formation of a species at 486.1 *m/z* which could have been attributed to either {[Fe^{III}(OOH)(PyMe₂tacn)](CF₃SO₃)}⁺ or {[Fe^V(O)(OH)(PyMe₂tacn)](CF₃SO₃)}⁺. As this peak decreased in intensity as the temperature increased it was concluded that this peak was that of the {[Fe^V(O)(OH)(PyMe₂tacn)](CF₃SO₃)}⁺ species as the iron(III) species is very stable and so would not have been decomposed with increased temperature. It was concluded that other species were also present in the reaction as it can be seen that the envelope at 486.1 *m/z* never completely disappears (see Figure 66 and Figure 67).

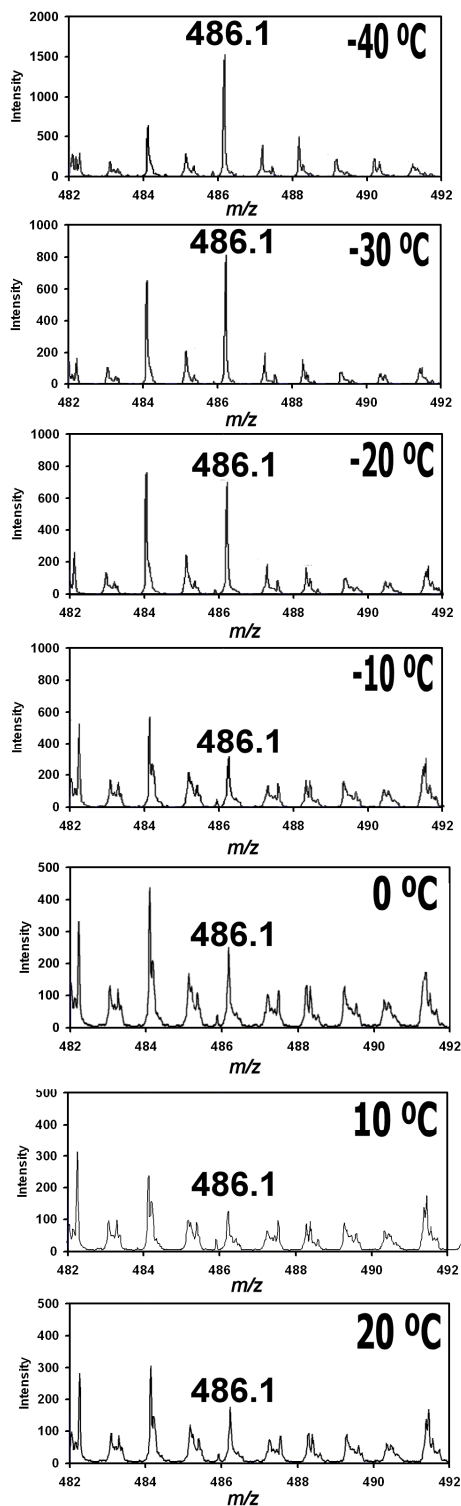


Figure 66. Observed chromatographs showing the 486 m/z ($\{[\text{Fe}^{\text{V}}(\text{O})(\text{OH})(\text{PyMe}_2\text{tacn})](\text{CF}_3\text{SO}_3)^+\}$, 15) species disappear with increasing temperature from $-40\text{ }^\circ\text{C}$ to $20\text{ }^\circ\text{C}$ showing the intensity decrease from ca. 1500 in the top panel at -40 to ca. 200 in the bottom panel at $20\text{ }^\circ\text{C}$.

In-depth analysis of the envelope presented data corresponding to there being three species present in the envelope at 486 m/z , the three species being $\{[\text{Fe}^{\text{V}}(\text{O})(\text{OH})(\text{PyMe}_2\text{tacn})](\text{CF}_3\text{SO}_3)\}^+$, **15**, $\{[\text{Fe}^{\text{III}}(\text{OOH})(\text{PyMe}_2\text{tacn})](\text{CF}_3\text{SO}_3)\}^+$ and $\{[\text{Fe}^{\text{III}}(\text{Cl})(\text{CF}_3\text{SO}_3)(\text{PyMe}_2\text{tacn})]\}^+$. From the decrease in intensity compared to that of the peak at 470.1 m/z (assigned to the stable $\{[\text{Fe}^{\text{III}}(\text{OH})(\text{PyMe}_2\text{tacn})](\text{CF}_3\text{SO}_3)\}^+$ species), it can be concluded that the iron(V) species was present and has decomposed with increased temperature.

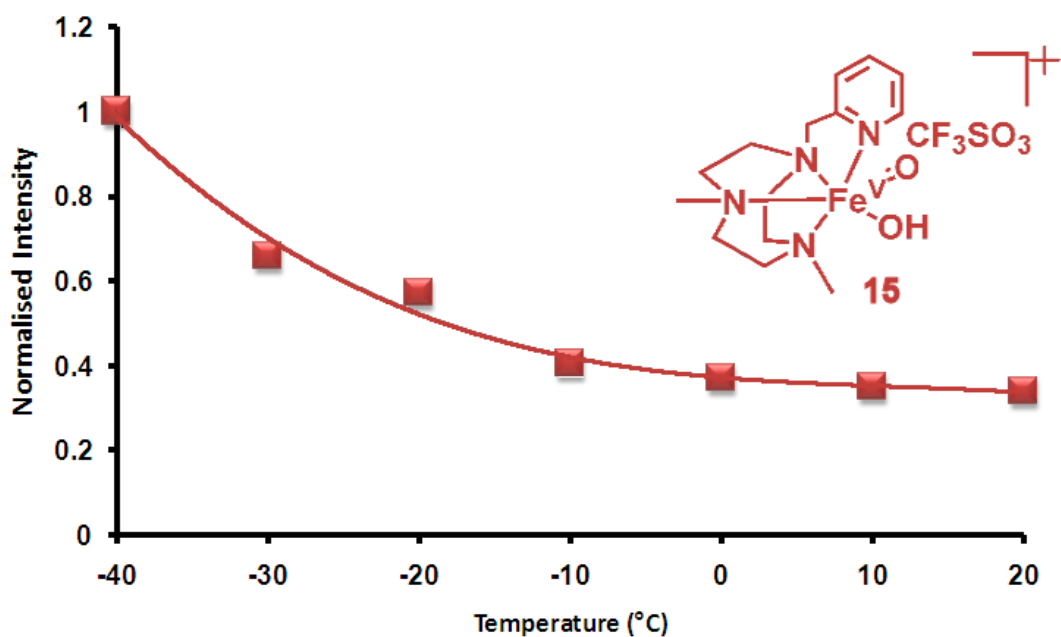


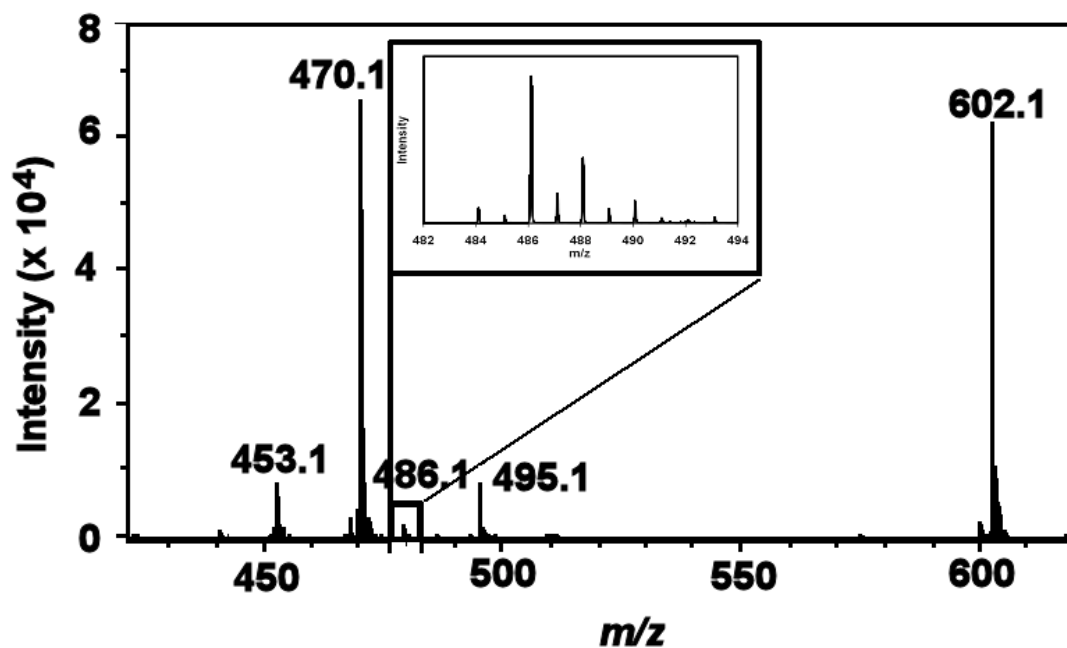
Figure 67. Graph showing the decomposition of $\{[\text{Fe}^{\text{V}}(\text{O})(\text{OH})(\text{PyMe}_2\text{tacn})](\text{CF}_3\text{SO}_3)\}^+$ **15** (486 m/z) when the temperature is increased from -40 °C to 20 °C.

4.1.1 Isotopic labelling mass spectrometry experiments

In order to distinguish between the two possible formulations for the peak at 486.1 m/z , isotopic labelling experiments were conducted. The experiments carried out were 1) the reaction of **14** with H_2O_2 (10 equiv) in the presence of H_2^{18}O (1000 equiv), 2) the complementary experiment involving the reaction of **14** with $\text{H}_2^{18}\text{O}_2$ (16 equiv.) in the presence of H_2O (1000 equiv) and 3) the reaction of **14** with $\text{H}_2^{18}\text{O}_2$ (10 equiv.) in the presence of H_2^{18}O (1000 equiv) (due to the experimental limitations of the isotopically

labelled reagent $\text{H}_2^{18}\text{O}_2$ being 2% in H_2^{16}O over 300 equiv of H_2^{16}O are also present in solution in this experiment).

When $[\text{Fe}(\text{PyMe}_2\text{tacn})(\text{CF}_3\text{SO}_3)_2]$ **14** was reacted with unlabelled H_2O_2 and H_2O the spectrum in Figure 68 was observed using CSI-MS (-40°C).



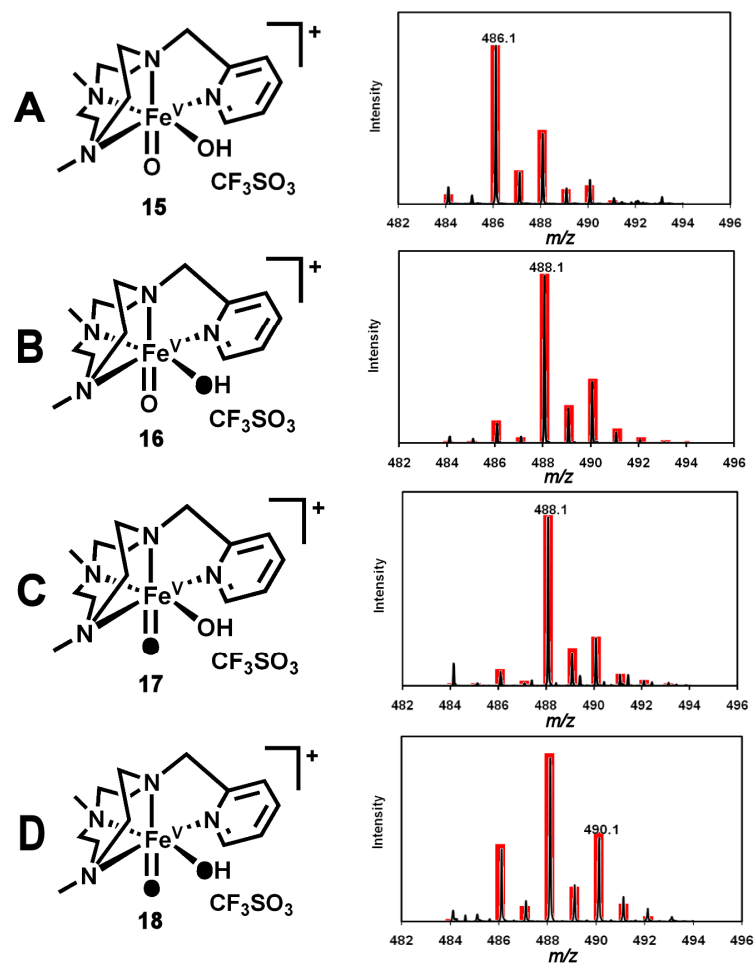
<i>m/z</i>	Formula
453.1	$\{[\text{Fe}^{\text{II}}(\text{CF}_3\text{SO}_3)(\text{PyMe}_2\text{tacn})]\}^+$
470.1	$\{[\text{Fe}^{\text{III}}(\text{OH})(\text{CF}_3\text{SO}_3)(\text{PyMe}_2\text{tacn})]\}^+$
486.1	$\{[\text{Fe}^{\text{V}}(\text{O})(\text{OH})(\text{PyMe}_2\text{tacn})](\text{CF}_3\text{SO}_3)\}^+$
495.1	$\{[\text{Fe}^{\text{III}}(\text{H})(\text{CF}_3\text{SO}_3)(\text{PyMe}_2\text{tacn})](\text{CH}_3\text{CN})\}^+$
602.1	$\{[\text{Fe}^{\text{III}}(\text{CF}_3\text{SO}_3)_2(\text{PyMe}_2\text{tacn})]\}^+$

Figure 68. Full CSI-MS spectrum of the reaction mixture (**14** + H_2O (1000 equiv) + H_2O_2 (100 equiv) in acetonitrile at -40°C).

From the chromatograph it can be seen that a number of different species are present when **14** is reacted with H_2O_2 and H_2O . The most abundant species are that of the most stable iron(III) species $\{[\text{Fe}^{\text{III}}(\text{OH})(\text{CF}_3\text{SO}_3)(\text{PyMe}_2\text{tacn})]\}^+$ (470.1 *m/z*) and $\{[\text{Fe}^{\text{III}}(\text{CF}_3\text{SO}_3)_2(\text{PyMe}_2\text{tacn})]\}^+$ (602.1 *m/z*). Other species present are that of the starting material $\{[\text{Fe}^{\text{II}}(\text{CF}_3\text{SO}_3)(\text{PyMe}_2\text{tacn})]\}^+$ (453.1 *m/z*) and

$\{[\text{Fe}^{\text{III}}(\text{H})(\text{CF}_3\text{SO}_3)(\text{PyMe}_2\text{tacn})](\text{CH}_3\text{CN})\}^+$ (495.1 m/z). The most important peak is that of the peak of low intensity at 486.1 m/z which can be assigned to either the species $\{[\text{Fe}^{\text{V}}(\text{O})(\text{OH})(\text{PyMe}_2\text{tacn})](\text{CF}_3\text{SO}_3)\}^+$ **15** or $\{[\text{Fe}^{\text{III}}(\text{OOH})(\text{PyMe}_2\text{tacn})](\text{CF}_3\text{SO}_3)\}^+$.

When $\text{H}_2^{16}\text{O}_2$ was reacted with $[\text{Fe}^{\text{II}}(\text{PyMe}_2\text{tacn})(\text{CF}_3\text{SO}_3)_2]$ **14** in the presence of H_2^{18}O , a spectrum was observed showing the peak at 486.1 m/z had shifted by two m/z units to 488.1 m/z . The complementary reaction with $\text{H}_2^{18}\text{O}_2$ and H_2^{16}O showed the same shift in the observed spectrum and the reaction of $[\text{Fe}^{\text{II}}(\text{PyMe}_2\text{tacn})(\text{CF}_3\text{SO}_3)_2]$ **14** with $\text{H}_2^{18}\text{O}_2$ and H_2^{18}O showed a shift of 4 m/z units from 486.1 m/z to 490.1 m/z . Since the iron(III) peroxide species $\{[\text{Fe}^{\text{III}}(\text{OOH})(\text{PyMe}_2\text{tacn})](\text{CF}_3\text{SO}_3)\}^+$ does not exchange oxygen atoms with H_2O ¹²¹ then it can be concluded that this species is not the major species present here. The isotopic labelling experiments provide strong indication that the species at 486.1 m/z is that of $\{[\text{Fe}^{\text{V}}(\text{O})(\text{OH})(\text{PyMe}_2\text{tacn})](\text{CF}_3\text{SO}_3)\}^+$ **15** where one oxygen is derived from H_2O_2 and the other from H_2O via water assisted heterolytic O-O cleavage (see Figure 69).¹²² These experiments confirmed the postulation by Costas *et al* that the catalytic oxidation of C=C and C-H moieties goes through an unstable iron(V) species.^{79,101}



Label	m/z	Formula
A	486.1	$\{[\text{Fe}^{\text{V}}(\text{O})(\text{OH})(\text{PyMe}_2\text{tacn})](\text{CF}_3\text{SO}_3)\}^+$
B	488.1	$\{[\text{Fe}^{\text{V}}(\text{O})(^{18}\text{OH})(\text{PyMe}_2\text{tacn})](\text{CF}_3\text{SO}_3)\}^+$
C	488.1	$\{[\text{Fe}^{\text{V}}(^{18}\text{O})(\text{OH})(\text{PyMe}_2\text{tacn})](\text{CF}_3\text{SO}_3)\}^+$
D	488.1	$\{[\text{Fe}^{\text{V}}(^{18}\text{O})(^{18}\text{OH})(\text{PyMe}_2\text{tacn})](\text{CF}_3\text{SO}_3)\}^+$

Figure 69. CSI-MS spectra in acetonitrile solution at $-40\text{ }^\circ\text{C}$. Red correspond to the simulated data, black correspond to the experimental data. A) 15 generated with $\text{H}_2^{16}\text{O}_2$ (10 equiv.) in the presence of H_2^{16}O (1000 equiv). B) 16 generated with $\text{H}_2^{16}\text{O}_2$ (10 equiv.) in the presence of H_2^{18}O (1000 equiv). C) 17 generated with $\text{H}_2^{18}\text{O}_2$ (16 equiv.) in the presence of H_2^{16}O (1000 equiv). D) 18 generated with $\text{H}_2^{18}\text{O}_2$ (10 equiv.) in the presence of H_2^{18}O (1000 equiv).

Detailed analysis of the spectra provided evidence that multiple species were present in one isotope envelope observed as the observed and calculated isotope envelopes did not match. It was found that a combination of three species $\{[\text{Fe}^{\text{V}}(\text{O})(\text{OH})(\text{PyMe}_2\text{tacn})](\text{CF}_3\text{SO}_3)\}^+$ **15**, $\{[\text{Fe}^{\text{III}}(\text{OH})(\text{OH}_2)(\text{PyMe}_2\text{tacn})](\text{CF}_3\text{SO}_3)\}^+$ and $\{[\text{Fe}^{\text{III}}(\text{Cl})(\text{CF}_3\text{SO}_3)(\text{PyMe}_2\text{tacn})]\}^+$ were present (see Figure 70).

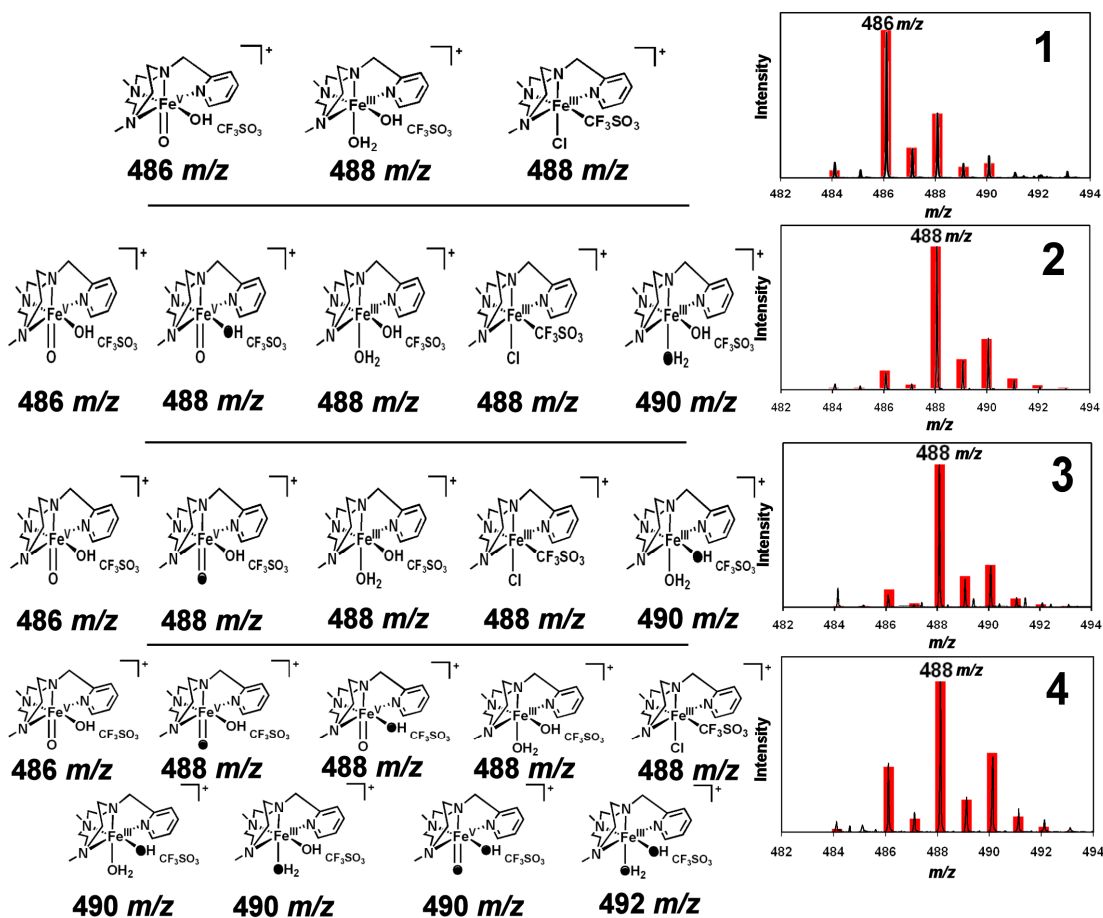


Figure 70. Statistical representation of the species present in each isotopic envelope.

Mass spectrometric isotopic envelopes do not always contain one species and so the isotopic envelopes of all the species at this given range overlay to form a new envelope with its own distinct pattern. With the experiment shown in this research, this was the case as the difference in heights between the peaks in the isotopic pattern were not as expected. From this it was found that at the m/z range where the $\text{Fe}(\text{V})=\text{O}$ species $\{[\text{Fe}^{\text{V}}(\text{O})(\text{OH})(\text{PyMe}_2\text{tacn})](\text{CF}_3\text{SO}_3)\}^+$ (486 m/z , 63 % of total amount of species present

in envelope, calculated using an isotope distribution pattern software) isotope pattern was present, as well as the species $\{[\text{Fe}^{\text{III}}(\text{OH})(\text{OH}_2)(\text{PyMe}_2\text{tacn})](\text{CF}_3\text{SO}_3)\}^+$ (488 m/z , 10 %) with an impurity of $\{[\text{Fe}^{\text{III}}(\text{Cl})(\text{CF}_3\text{SO}_3)(\text{PyMe}_2\text{tacn})]\}^+$ (488 m/z , 27 %). This meant that the peak at 486 m/z was the most intense as the peak at 486 m/z was of the higher percentage (63 % overall).

When H_2^{18}O was added, the isotope envelope shifted by 2 m/z units as expected but, as before, did not contain only one species. The envelope constructed from four different species: the unlabelled $\{[\text{Fe}^{\text{V}}(\text{O})(\text{OH})(\text{PyMe}_2\text{tacn})](\text{CF}_3\text{SO}_3)\}^+$ (486 m/z , 5 %), the singly labelled $\{[\text{Fe}^{\text{V}}(\text{O})(^{18}\text{OH})(\text{PyMe}_2\text{tacn})](\text{CF}_3\text{SO}_3)\}^+$ (488 m/z , 48 %), the unlabelled $\{[\text{Fe}^{\text{III}}(\text{OH})(\text{OH}_2)(\text{PyMe}_2\text{tacn})](\text{CF}_3\text{SO}_3)\}^+$ (488 m/z , 8 %), $\{[\text{Fe}^{\text{III}}(\text{Cl})(\text{CF}_3\text{SO}_3)(\text{PyMe}_2\text{tacn})]\}^+$ (488 m/z , 24 %) and the singly labelled $\{[\text{Fe}^{\text{III}}(\text{OH})(^{18}\text{OH}_2)(\text{PyMe}_2\text{tacn})](\text{CF}_3\text{SO}_3)\}^+$ (490 m/z , 15 %). Statistics depict that since three out of five species (overall 80 %) have a m/z of 488 whilst one of five (5 %) has a m/z of 486 and the other one species (15%) has a m/z of 490 then the peak of highest intensity will be at 488 m/z . Please note that the percentage values given here are only estimated representations to show which peak should be of the highest intensity and not the exact amounts that are present in the actual envelope; the percentage of the peaks with the same m/z can be any percentage up to the total for all 488 m/z peaks.

When $\text{H}_2^{18}\text{O}_2$ was added the isotopic envelope also shifted by 2 m/z as with H_2^{18}O and also contains four species as before. The species present were the unlabelled $\{[\text{Fe}^{\text{V}}(\text{O})(\text{OH})(\text{PyMe}_2\text{tacn})](\text{CF}_3\text{SO}_3)\}^+$ (486 m/z , 5 %), the singly labelled $\{[\text{Fe}^{\text{V}}(^{18}\text{O})(\text{OH})(\text{PyMe}_2\text{tacn})](\text{CF}_3\text{SO}_3)\}^+$ (488 m/z , 50 %), the unlabelled $\{[\text{Fe}^{\text{III}}(\text{OH})(\text{OH}_2)(\text{PyMe}_2\text{tacn})](\text{CF}_3\text{SO}_3)\}^+$ (488 m/z , 8 %), $\{[\text{Fe}^{\text{III}}(\text{Cl})(\text{CF}_3\text{SO}_3)(\text{PyMe}_2\text{tacn})]\}^+$ (488 m/z , 27 %) and the singly labelled $\{[\text{Fe}^{\text{III}}(^{18}\text{OH})(\text{OH}_2)(\text{PyMe}_2\text{tacn})](\text{CF}_3\text{SO}_3)\}^+$ (490 m/z , 10 %). As with H_2^{18}O , the peak at 488 m/z will have the highest intensity due to three of five species (85 %) having a m/z of 488 whilst one of five (5 %) has a m/z of 486 and the other one species (10 %) a m/z of 490.

When both H_2^{18}O and $\text{H}_2^{18}\text{O}_2$ are added the peak should shift by 4 m/z units with the peak of highest intensity being at 490 m/z . This was not that case here though due to

the higher percentage of peaks present in the envelope having a m/z of 488. The peaks present are the unlabelled $\{[\text{Fe}^{\text{V}}(\text{O})(\text{OH})(\text{PyMe}_2\text{tacn})](\text{CF}_3\text{SO}_3)\}^+$ (486 m/z , 20 %), the singly labelled $\{[\text{Fe}^{\text{V}}(^{18}\text{O})(\text{OH})(\text{PyMe}_2\text{tacn})](\text{CF}_3\text{SO}_3)\}^+$ (488 m/z , 17 %), the singly labelled $\{[\text{Fe}^{\text{V}}(\text{O})(^{18}\text{OH})(\text{PyMe}_2\text{tacn})](\text{CF}_3\text{SO}_3)\}^+$ (488 m/z , 17 %), the unlabelled $\{[\text{Fe}^{\text{III}}(\text{OH})(\text{OH}_2)(\text{PyMe}_2\text{tacn})](\text{CF}_3\text{SO}_3)\}^+$ (488 m/z , 17 %), $\{[\text{Fe}^{\text{III}}(\text{Cl})(\text{CF}_3\text{SO}_3)(\text{PyMe}_2\text{tacn})]\}^+$ (488 m/z , 5 %), the singly labelled $\{[\text{Fe}^{\text{III}}(\text{OH})(^{18}\text{OH}_2)(\text{PyMe}_2\text{tacn})](\text{CF}_3\text{SO}_3)\}^+$ (490 m/z , 1 %), the singly labelled $\{[\text{Fe}^{\text{III}}(^{18}\text{OH})(\text{OH}_2)(\text{PyMe}_2\text{tacn})](\text{CF}_3\text{SO}_3)\}^+$ (490 m/z , 1 %), the doubly labelled $\{[\text{Fe}^{\text{V}}(^{18}\text{O})(^{18}\text{OH})(\text{PyMe}_2\text{tacn})](\text{CF}_3\text{SO}_3)\}^+$ (490 m/z , 21 %), and the doubly labelled $\{[\text{Fe}^{\text{III}}(^{18}\text{OH})(^{18}\text{OH}_2)(\text{PyMe}_2\text{tacn})](\text{CF}_3\text{SO}_3)\}^+$ (492 m/z , 1 %). The peak of highest intensity was that of 488 m/z (and not that of 490 m/z) due to four out of nine species (56 % overall) having a m/z of 488 whilst one out of nine (20 %) had a m/z of 486, three out of nine (23 %) has a m/z of 490 and one out of nine (1 %) had a m/z of 492. Therefore the peak of highest intensity came at 488 m/z and not 490 m/z as calculated.

Label	Species present in envelope	Percentage (%)
1 (486 <i>m/z</i>)	$\{[\text{Fe}^{\text{V}}(\text{O})(\text{OH})(\text{PyMe}_2\text{tacn})](\text{CF}_3\text{SO}_3)\}^+$	63
	$\{[\text{Fe}^{\text{III}}(\text{OH})(\text{OH}_2)(\text{PyMe}_2\text{tacn})](\text{CF}_3\text{SO}_3)\}^+$	10
	$\{[\text{Fe}^{\text{III}}(\text{Cl})(\text{CF}_3\text{SO}_3)(\text{PyMe}_2\text{tacn})]\}^+$	27
2 (488 <i>m/z</i>)	$\{[\text{Fe}^{\text{V}}(\text{O})(\text{OH})(\text{PyMe}_2\text{tacn})](\text{CF}_3\text{SO}_3)\}^+$	5
	$\{[\text{Fe}^{\text{V}}(\text{O})(^{18}\text{OH})(\text{PyMe}_2\text{tacn})](\text{CF}_3\text{SO}_3)\}^+$	48
	$\{[\text{Fe}^{\text{III}}(\text{OH})(\text{OH}_2)(\text{PyMe}_2\text{tacn})](\text{CF}_3\text{SO}_3)\}^+$	8
	$\{[\text{Fe}^{\text{III}}(\text{Cl})(\text{CF}_3\text{SO}_3)(\text{PyMe}_2\text{tacn})]\}^+$	24
	$\{[\text{Fe}^{\text{III}}(\text{OH})(^{18}\text{OH}_2)(\text{PyMe}_2\text{tacn})](\text{CF}_3\text{SO}_3)\}^+$	15
3 (488 <i>m/z</i>)	$\{[\text{Fe}^{\text{V}}(\text{O})(\text{OH})(\text{PyMe}_2\text{tacn})](\text{CF}_3\text{SO}_3)\}^+$	5
	$\{[\text{Fe}^{\text{V}}(^{18}\text{O})(\text{OH})(\text{PyMe}_2\text{tacn})](\text{CF}_3\text{SO}_3)\}^+$	50
	$\{[\text{Fe}^{\text{III}}(\text{OH})(\text{OH}_2)(\text{PyMe}_2\text{tacn})](\text{CF}_3\text{SO}_3)\}^+$	8
	$\{[\text{Fe}^{\text{III}}(\text{Cl})(\text{CF}_3\text{SO}_3)(\text{PyMe}_2\text{tacn})]\}^+$	27
	$\{[\text{Fe}^{\text{III}}(^{18}\text{OH})(\text{OH}_2)(\text{PyMe}_2\text{tacn})](\text{CF}_3\text{SO}_3)\}^+$	10
4 (488 <i>m/z</i>)	$\{[\text{Fe}^{\text{V}}(\text{O})(\text{OH})(\text{PyMe}_2\text{tacn})](\text{CF}_3\text{SO}_3)\}^+$	20
	$\{[\text{Fe}^{\text{V}}(^{18}\text{O})(\text{OH})(\text{PyMe}_2\text{tacn})](\text{CF}_3\text{SO}_3)\}^+$	17
	$\{[\text{Fe}^{\text{V}}(\text{O})(^{18}\text{OH})(\text{PyMe}_2\text{tacn})](\text{CF}_3\text{SO}_3)\}^+$	17
	$\{[\text{Fe}^{\text{III}}(\text{OH})(\text{OH}_2)(\text{PyMe}_2\text{tacn})](\text{CF}_3\text{SO}_3)\}^+$	17
	$\{[\text{Fe}^{\text{III}}(\text{Cl})(\text{CF}_3\text{SO}_3)(\text{PyMe}_2\text{tacn})]\}^+$	5
	$\{[\text{Fe}^{\text{III}}(\text{OH})(^{18}\text{OH}_2)(\text{PyMe}_2\text{tacn})](\text{CF}_3\text{SO}_3)\}^+$	1
	$\{[\text{Fe}^{\text{III}}(^{18}\text{OH})(\text{OH}_2)(\text{PyMe}_2\text{tacn})](\text{CF}_3\text{SO}_3)\}^+$	1
	$\{[\text{Fe}^{\text{V}}(^{18}\text{O})(^{18}\text{OH})(\text{PyMe}_2\text{tacn})](\text{CF}_3\text{SO}_3)\}^+$	21
	$\{[\text{Fe}^{\text{III}}(^{18}\text{OH})(^{18}\text{OH}_2)(\text{PyMe}_2\text{tacn})](\text{CF}_3\text{SO}_3)\}^+$	1

Table 1. Tabulated analysis of the species present in the isotope envelopes shown in Figure 70

4.1.2 Dihydroxylation reactions

Further proof of the unstable $\{[\text{Fe}^{\text{V}}(\text{O})(\text{OH})(\text{PyMe}_2\text{tacn})](\text{CF}_3\text{SO}_3)\}^+$ being present came from *cis*-dihydroxylation reactions with the olefins cyclooctene, 1-octene and cyclohexene along with isotopic labelling experiments as before (see Figure 71).

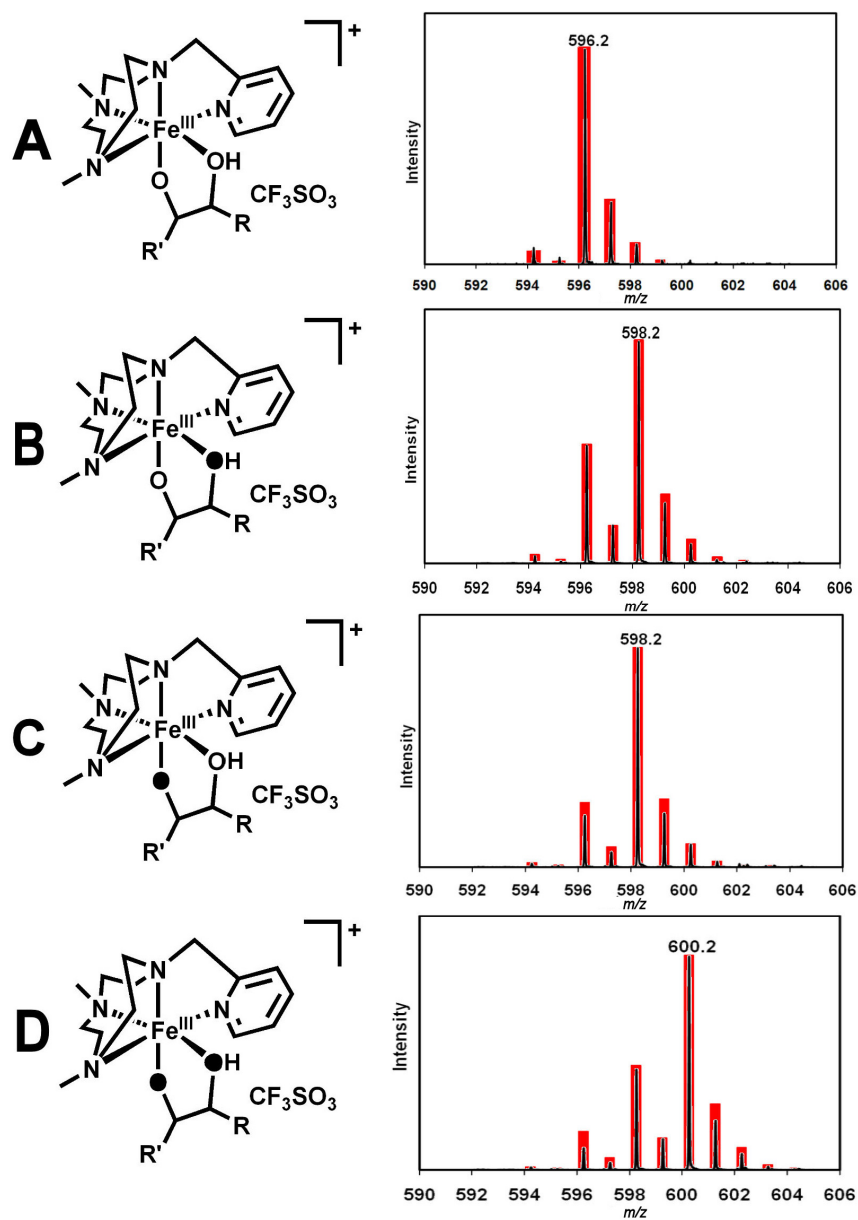


Figure 71. CSI-MS spectra in acetonitrile solution at $-40\text{ }^\circ\text{C}$. A) formed by reaction of cyclooctene (100 equiv.) with 15 (generated with $\text{H}_2^{16}\text{O}_2$ (3 equiv.) in the presence of H_2^{16}O (1000 equiv)). B) formed by reaction of cyclooctene (100 equiv.) with 15 (generated with $\text{H}_2^{16}\text{O}_2$ (3 equiv.) in the presence of H_2^{18}O (1000 equiv)). C) formed by reacting cyclooctene (100 equiv.) with 15 (generated with $\text{H}_2^{18}\text{O}_2$ (3 equiv.) in the presence of H_2^{16}O (1000 equiv)). D) formed by reacting cyclooctene (100 equiv.) with 15 (generated with $\text{H}_2^{18}\text{O}_2$ (3 equiv.) in the presence of H_2^{18}O (1000 equiv)).

First, the complex $[\text{Fe}^{\text{II}}(\text{PyMe}_2\text{tacn})(\text{CF}_3\text{SO}_3)_2]$, **14**, was reacted with H_2O_2 and H_2O in acetonitrile as before to generate the $\{[\text{Fe}^{\text{V}}(\text{O})(\text{OH})(\text{PyMe}_2\text{tacn})](\text{CF}_3\text{SO}_3)\}^+$ species. Cyclooctene (1000 equivalents) was then added to the solution and injected into the mass spectrometer at $-40\text{ }^\circ\text{C}$ (CSI-MS). Analysis of the observed spectrum showed that the $\{[\text{Fe}^{\text{V}}(\text{O})(\text{OH})(\text{PyMe}_2\text{tacn})](\text{CF}_3\text{SO}_3)\}^+$ peak at $486.1\text{ }m/z$ had disappeared and peaks at $596.2\text{ }m/z$ and $446.2\text{ }m/z$ had appeared. These peaks could be assigned to $\{[\text{Fe}^{\text{III}}(\text{C}_8\text{H}_{14}(\text{O})(\text{OH}))(\text{PyMe}_2\text{tacn})](\text{CF}_3\text{SO}_3)\}^+$, **19**, and $[\text{Fe}^{\text{III}}(\text{C}_8\text{H}_{14}\text{O}_2)(\text{PyMe}_2\text{tacn})]^+$, **19-H+CF₃SO₃**. Labelling experiments with $\text{H}_2^{16}\text{O}_2$ and H_2^{18}O gave a spectrum where the peak had shifted by two m/z units to give the species $\{[\text{Fe}^{\text{III}}(\text{C}_8\text{H}_{14}(\text{O})(^{18}\text{OH}))(\text{PyMe}_2\text{tacn})](\text{CF}_3\text{SO}_3)\}^+$, **20**, ($598.2\text{ }m/z$) and $[\text{Fe}^{\text{III}}(\text{C}_8\text{H}_{14}^{18}\text{OO})(\text{PyMe}_2\text{tacn})]^+$, **20-H+CF₃SO₃**, ($448.2\text{ }m/z$), as was seen before with the iron(V) isotope labelling experiments (see Figure 71 B). Labelling experiments with $\text{H}_2^{18}\text{O}_2$ and H_2^{16}O also gave a spectrum that had shifted by two m/z units to $\{[\text{Fe}^{\text{III}}(\text{C}_8\text{H}_{14}(^{18}\text{O})(\text{OH}))(\text{PyMe}_2\text{tacn})](\text{CF}_3\text{SO}_3)\}^+$, **21**, ($598.2\text{ }m/z$) and $[\text{Fe}^{\text{III}}(\text{C}_8\text{H}_{14}\text{O}^{18}\text{O})(\text{PyMe}_2\text{tacn})]^+$, **21-H+CF₃SO₃**, ($448.2\text{ }m/z$). When both $\text{H}_2^{18}\text{O}_2$ and H_2^{18}O were added to the reaction the observed spectrum showed a shift in four m/z units from $596.2\text{ }m/z$ and $446.2\text{ }m/z$ to $600.2\text{ }m/z$ $\{[\text{Fe}^{\text{III}}(\text{C}_8\text{H}_{14}(^{18}\text{O})(^{18}\text{OH}))(\text{PyMe}_2\text{tacn})](\text{CF}_3\text{SO}_3)\}^+$, **22**, and $450.2\text{ }m/z$ $[\text{Fe}^{\text{III}}(\text{C}_8\text{H}_{14}\text{O}^{18}\text{O})(\text{PyMe}_2\text{tacn})]^+$, **22-H+CF₃SO₃**, (see Figure 71 D).

Analysis of the isotope envelopes observed gave evidence that more than one species was present in each. When analysing the unlabelled hydroxyglycolate species it was found that $\{[\text{Fe}^{\text{III}}(\text{C}_8\text{H}_{14}(\text{O})(\text{OH}))(\text{PyMe}_2\text{tacn})](\text{CF}_3\text{SO}_3)\}^+$, **19**, was the only species present in the envelope observed at $596.2\text{ }m/z$ but when H_2^{18}O was used two species were found to be present in the envelope. From Figure 72 it can be seen that the observed and calculated spectra do not match as the peak at $596.2\text{ }m/z$ was of a higher than expected intensity. It was found that the envelope contained a mixture of $\{[\text{Fe}^{\text{III}}(\text{C}_8\text{H}_{14}(\text{O})(\text{OH}))(\text{PyMe}_2\text{tacn})](\text{CF}_3\text{SO}_3)\}^+$, **19**, ($596.2\text{ }m/z$) (23%) and $\{[\text{Fe}^{\text{III}}(\text{C}_8\text{H}_{14}(\text{O})(^{18}\text{OH}))(\text{PyMe}_2\text{tacn})](\text{CF}_3\text{SO}_3)\}^+$, **20**, ($598.2\text{ }m/z$) (77%) (see Figure 73). (It has to be noted that all percentages given for the mass spectra are an approximate value).

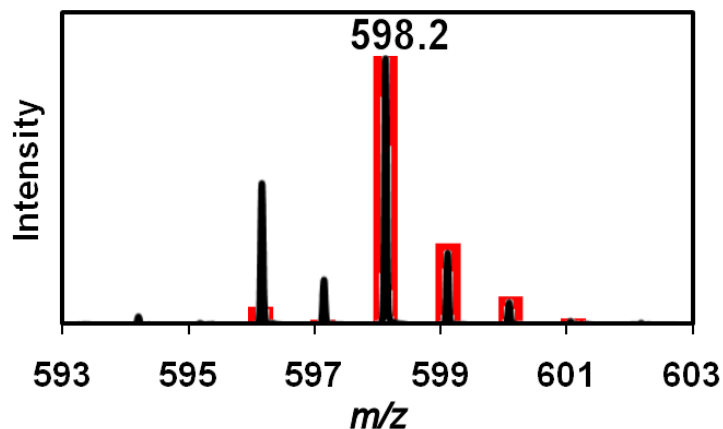
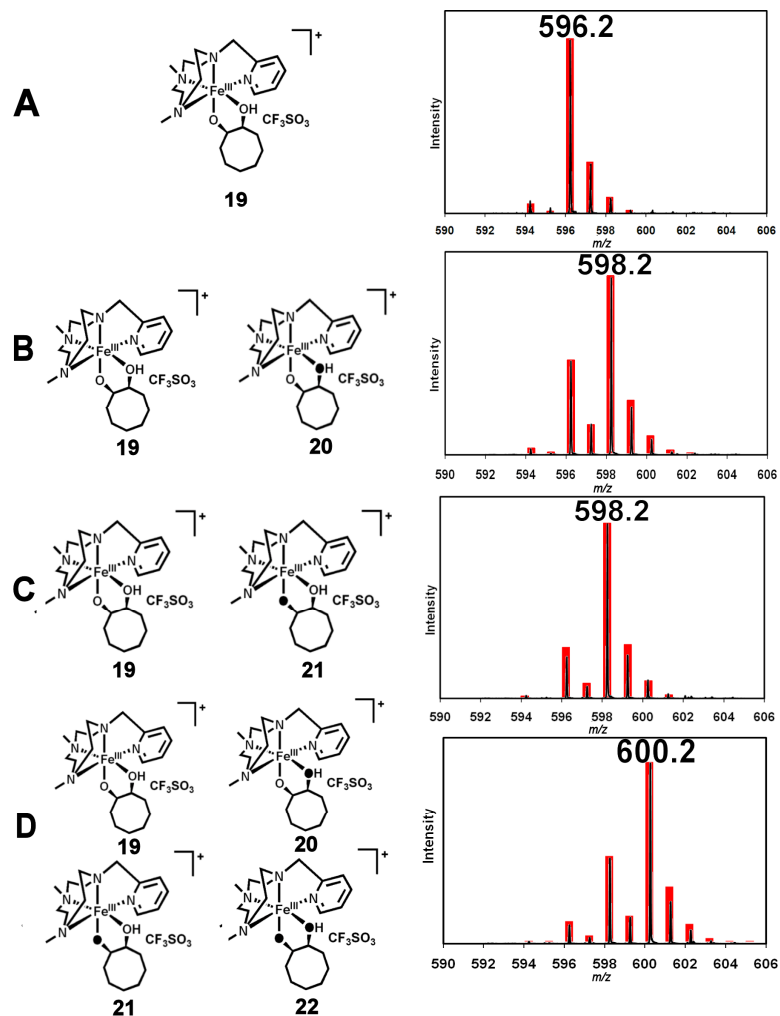


Figure 72. ESI-MS of $\{[\text{Fe}^{\text{III}}(\text{C}_8\text{H}_{14}(\text{O})(^{18}\text{OH}))(\text{PyMe}_2\text{tacn})](\text{CF}_3\text{SO}_3)\}^+$, **20**, showing that another species must be present in the spectrum (black = observed spectrum, red = calculated spectrum).

As with H_2^{18}O , the reaction of cyclooctene with **14** and $\text{H}_2^{18}\text{O}_2$ gave a spectrum that contained the two species $\{[\text{Fe}^{\text{III}}(\text{C}_8\text{H}_{14}(\text{O})(\text{OH}))(\text{PyMe}_2\text{tacn})](\text{CF}_3\text{SO}_3)\}^+$, **19**, (596.2 m/z) (20%) and $\text{Fe}^{\text{III}}(\text{C}_8\text{H}_{14}(^{18}\text{O})(\text{OH}))(\text{PyMe}_2\text{tacn})](\text{CF}_3\text{SO}_3)\}^+$, **21**, (598.2 m/z) (80%) (see Figure 73). The unlabelled species was present due to the isotopic labelling reagent containing unlabelled water. When both H_2^{18}O and $\text{H}_2^{18}\text{O}_2$ were used four species were present in the envelope, those being $\{[\text{Fe}^{\text{III}}(\text{C}_8\text{H}_{14}(\text{O})(\text{OH}))(\text{PyMe}_2\text{tacn})](\text{CF}_3\text{SO}_3)\}^+$, **19**, (596.2 m/z) (6%), $\text{Fe}^{\text{III}}(\text{C}_8\text{H}_{14}(^{18}\text{O})(\text{OH}))(\text{PyMe}_2\text{tacn})](\text{CF}_3\text{SO}_3)\}^+$, **20**, (598.2 m/z) (13%), $\text{Fe}^{\text{III}}(\text{C}_8\text{H}_{14}(\text{O})(^{18}\text{OH}))(\text{PyMe}_2\text{tacn})](\text{CF}_3\text{SO}_3)\}^+$, **21**, (598.2 m/z) (15%) and $\text{Fe}^{\text{III}}(\text{C}_8\text{H}_{14}(^{18}\text{O})(^{18}\text{OH}))(\text{PyMe}_2\text{tacn})](\text{CF}_3\text{SO}_3)\}^+$, **22**, (600.2 m/z) (66%) (see Figure 73).



Label	Species present	Percentage (%)
A	$\{[\text{Fe}^{\text{III}}(\text{C}_8\text{H}_{14}(\text{O})(\text{OH}))(\text{PyMe}_2\text{tacn})](\text{CF}_3\text{SO}_3)\}^+$	100
B	$\{[\text{Fe}^{\text{III}}(\text{C}_8\text{H}_{14}(\text{O})(\text{OH}))(\text{PyMe}_2\text{tacn})](\text{CF}_3\text{SO}_3)\}^+$	23
	$\{[\text{Fe}^{\text{III}}(\text{C}_8\text{H}_{14}(\text{O})(^{18}\text{OH}))(\text{PyMe}_2\text{tacn})](\text{CF}_3\text{SO}_3)\}^+$	77
C	$\{[\text{Fe}^{\text{III}}(\text{C}_8\text{H}_{14}(\text{O})(\text{OH}))(\text{PyMe}_2\text{tacn})](\text{CF}_3\text{SO}_3)\}^+$	20
	$\{[\text{Fe}^{\text{III}}(\text{C}_8\text{H}_{14}(\text{O})(^{18}\text{O})(\text{OH}))(\text{PyMe}_2\text{tacn})](\text{CF}_3\text{SO}_3)\}^+$	80
D	$\{[\text{Fe}^{\text{III}}(\text{C}_8\text{H}_{14}(\text{O})(\text{OH}))(\text{PyMe}_2\text{tacn})](\text{CF}_3\text{SO}_3)\}^+$	6
	$\{[\text{Fe}^{\text{III}}(\text{C}_8\text{H}_{14}(\text{O})(^{18}\text{OH}))(\text{PyMe}_2\text{tacn})](\text{CF}_3\text{SO}_3)\}^+$	13
	$\{[\text{Fe}^{\text{III}}(\text{C}_8\text{H}_{14}(\text{O})(^{18}\text{O})(\text{OH}))(\text{PyMe}_2\text{tacn})](\text{CF}_3\text{SO}_3)\}^+$	15
	$\{[\text{Fe}^{\text{III}}(\text{C}_8\text{H}_{14}(\text{O})(^{18}\text{O})(^{18}\text{OH}))(\text{PyMe}_2\text{tacn})](\text{CF}_3\text{SO}_3)\}^+$	66

Figure 73. Representation of the species **19- 22**, formed in the dihydroxylation of cyclooctene, present in each isotopic envelope and its tabulated data.

1-octene was also used in a dihydroxylation reaction with $[\text{Fe}^{\text{II}}(\text{CF}_3\text{SO}_3)_2(\text{PyMe}_2\text{tacn})]$, **14**. As with cyclooctene both unlabelled and labelled reagents were used to follow the incorporation of the oxygen atoms in the dihydroxylation product. When unlabelled H_2O and H_2O_2 were reacted with $[\text{Fe}^{\text{II}}(\text{CF}_3\text{SO}_3)_2(\text{PyMe}_2\text{tacn})]$, **14**, the species $\{[\text{Fe}^{\text{III}}(\text{C}_8\text{H}_{16}(\text{O})(\text{OH}))(\text{PyMe}_2\text{tacn})](\text{CF}_3\text{SO}_3)\}^+$, **23**, was observed in 100% yield. When H_2^{18}O was reacted a peak shifted by two m/z units from 598.2 m/z to 600.2 m/z with the same being observed when $\text{H}_2^{18}\text{O}_2$ was used. When both H_2^{18}O and $\text{H}_2^{18}\text{O}_2$ were used a shift of four m/z units was observed (see Figure 74) clearly indicating the oxygen atoms coming from H_2O and H_2O_2 . Like before, multiple species were present in the isotopic envelopes observed. With unlabelled reagents, the peak at 598.2 m/z was assigned to $\{[\text{Fe}^{\text{III}}(\text{C}_8\text{H}_{16}(\text{O})(\text{OH}))(\text{PyMe}_2\text{tacn})](\text{CF}_3\text{SO}_3)\}^+$, **23**, in 100% yield. With H_2^{18}O the two species present in the one isotope envelope were $\{[\text{Fe}^{\text{III}}(\text{C}_8\text{H}_{16}(\text{O})(\text{OH}))(\text{PyMe}_2\text{tacn})](\text{CF}_3\text{SO}_3)\}^+$, **23**, and $\{[\text{Fe}^{\text{III}}(\text{C}_8\text{H}_{16}(\text{O})(^{18}\text{OH}))(\text{PyMe}_2\text{tacn})](\text{CF}_3\text{SO}_3)\}^+$, **24**, in 72% and 28% respectively. When $\text{H}_2^{18}\text{O}_2$ was used the two species present in the envelope were $\{[\text{Fe}^{\text{III}}(\text{C}_8\text{H}_{16}(\text{O})(\text{OH}))(\text{PyMe}_2\text{tacn})](\text{CF}_3\text{SO}_3)\}^+$, **23**, (75%) and $\{[\text{Fe}^{\text{III}}(\text{C}_8\text{H}_{16}(^{18}\text{O})(\text{OH}))(\text{PyMe}_2\text{tacn})](\text{CF}_3\text{SO}_3)\}^+$, **25**, (25%). With H_2^{18}O and $\text{H}_2^{18}\text{O}_2$ added four species were present in the isotope envelope, the four species being $\{[\text{Fe}^{\text{III}}(\text{C}_8\text{H}_{16}(\text{O})(\text{OH}))(\text{PyMe}_2\text{tacn})](\text{CF}_3\text{SO}_3)\}^+$, **23**, (18%) $\{[\text{Fe}^{\text{III}}(\text{C}_8\text{H}_{16}(\text{O})(^{18}\text{OH}))(\text{PyMe}_2\text{tacn})](\text{CF}_3\text{SO}_3)\}^+$, **24**, (15%) $\{[\text{Fe}^{\text{III}}(\text{C}_8\text{H}_{16}(^{18}\text{O})(\text{OH}))(\text{PyMe}_2\text{tacn})](\text{CF}_3\text{SO}_3)\}^+$, **25**, (15%) and $\{[\text{Fe}^{\text{III}}(\text{C}_8\text{H}_{16}(^{18}\text{O})(\text{OH}))(\text{PyMe}_2\text{tacn})](\text{CF}_3\text{SO}_3)\}^+$, **26**, (52%) (see Figure 74).

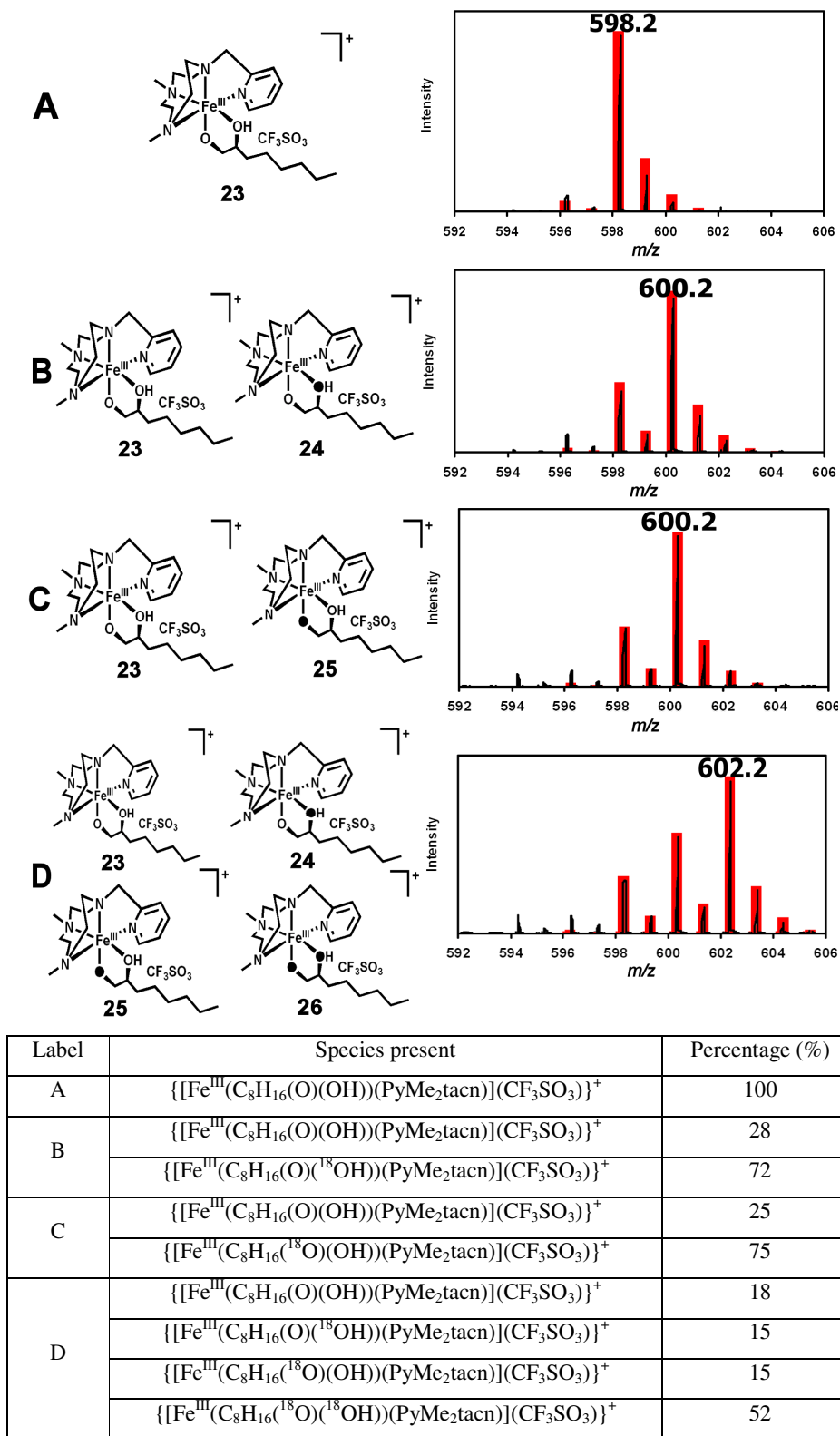
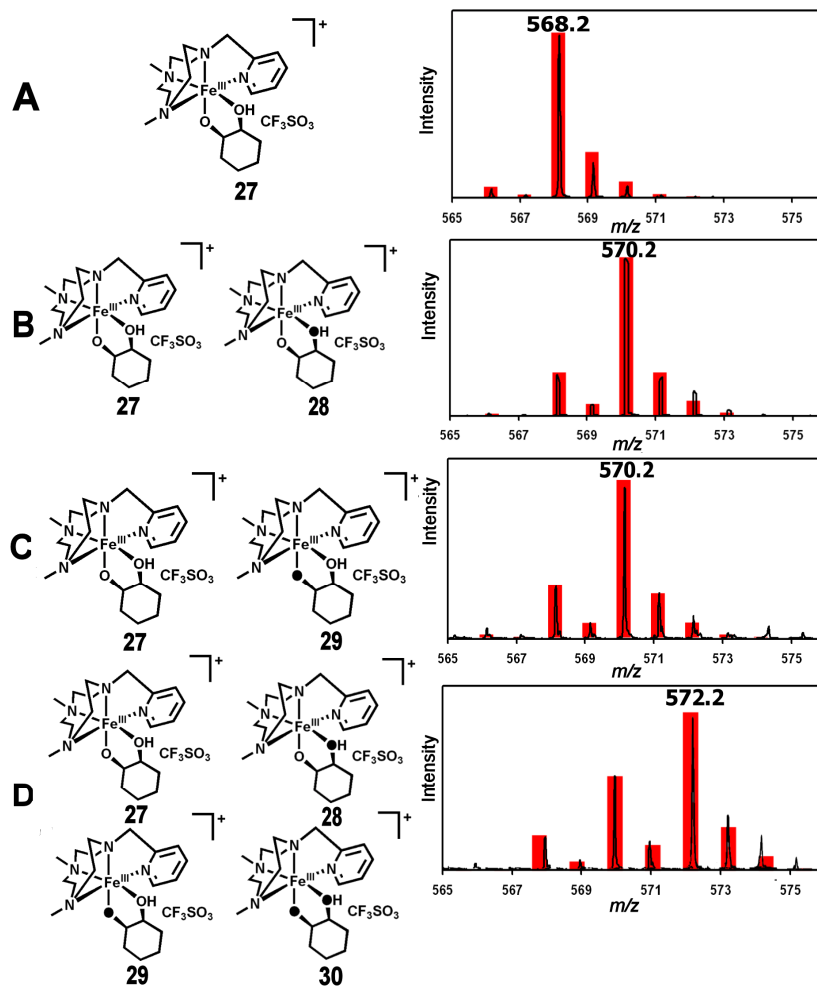


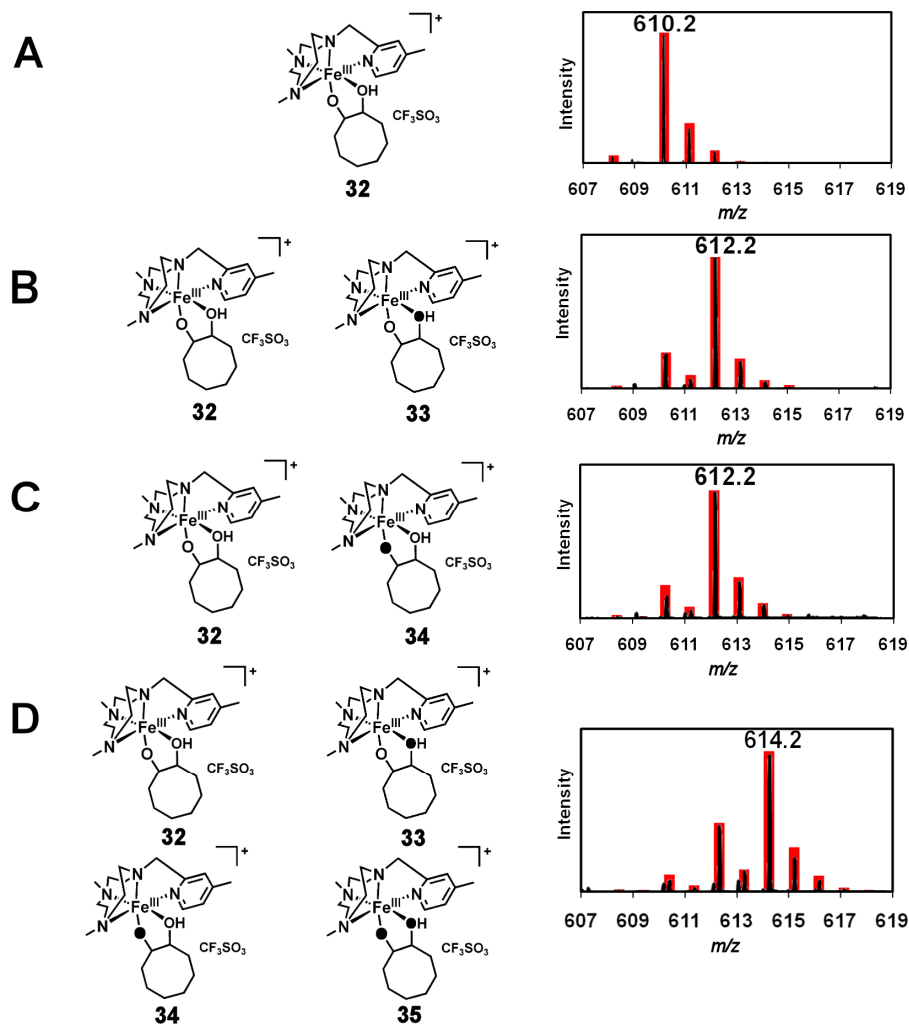
Figure 74. Representation of the species 23- 26, formed in the dihydroxylation of 1-octene, present in each isotopic envelope and its tabulated data.

Finally, the dihydroxylation of cyclohexene was carried out using $[\text{Fe}^{\text{II}}(\text{CF}_3\text{SO}_3)_2(\text{PyMe}_2\text{tacn})]$, **14**. As with both cyclooctene and 1-octene isotope labels were also used to follow the inclusion of oxygens from H_2O and H_2O_2 . The reaction of $[\text{Fe}^{\text{II}}(\text{CF}_3\text{SO}_3)_2(\text{PyMe}_2\text{tacn})]$, **14**, with H_2^{16}O and $\text{H}_2^{16}\text{O}_2$ gave a spectrum at $568.2\ m/z$ that was analysed as $\{[\text{Fe}^{\text{III}}(\text{C}_6\text{H}_{10}\text{O}_2)(\text{PyMe}_2\text{tacn})](\text{CF}_3\text{SO}_3)\}^+$, **27**, (100%) but when H_2^{18}O was used the peak shifted by two m/z units to $570.2\ m/z$ where the envelope contained the two species $\{[\text{Fe}^{\text{III}}(\text{C}_6\text{H}_{10}(\text{O})(\text{OH}))(\text{PyMe}_2\text{tacn})](\text{CF}_3\text{SO}_3)\}^+$, **27**, (18%) and $\{[\text{Fe}^{\text{III}}(\text{C}_6\text{H}_{10}(\text{O})(^{18}\text{OH}))(\text{PyMe}_2\text{tacn})](\text{CF}_3\text{SO}_3)\}^+$, **28**, (82 %). A shift of two m/z from $568.2\ m/z$ to $570.2\ m/z$ was also seen with $\text{H}_2^{18}\text{O}_2$ with the isotope envelope containing the species $\{[\text{Fe}^{\text{III}}(\text{C}_6\text{H}_{10}(\text{O})(\text{OH}))(\text{PyMe}_2\text{tacn})](\text{CF}_3\text{SO}_3)\}^+$, **27**, and $\{[\text{Fe}^{\text{III}}(\text{C}_6\text{H}_{10}(\text{O})(^{18}\text{OH}))(\text{PyMe}_2\text{tacn})](\text{CF}_3\text{SO}_3)\}^+$, **29**, in 22% and 78% yields respectively. When both H_2^{18}O and $\text{H}_2^{18}\text{O}_2$ were used there was a shift of four m/z units from $568.2\ m/z$ to $572.2\ m/z$. Full analysis of the peak demonstrated the presence of four different species in the isotope envelope at $572.2\ m/z$, the four peaks being $\{[\text{Fe}^{\text{III}}(\text{C}_6\text{H}_{10}(\text{O})(\text{OH}))(\text{PyMe}_2\text{tacn})](\text{CF}_3\text{SO}_3)\}^+$, **27**, (12%) and $\{[\text{Fe}^{\text{III}}(\text{C}_6\text{H}_{10}(\text{O})(^{18}\text{OH}))(\text{PyMe}_2\text{tacn})](\text{CF}_3\text{SO}_3)\}^+$, **28**, (18 %). $\{[\text{Fe}^{\text{III}}(\text{C}_6\text{H}_{10}(^{18}\text{O})(\text{OH}))(\text{PyMe}_2\text{tacn})](\text{CF}_3\text{SO}_3)\}^+$, **29**, (15%) and $\{[\text{Fe}^{\text{III}}(\text{C}_6\text{H}_{10}(^{18}\text{O})(^{18}\text{OH}))(\text{PyMe}_2\text{tacn})](\text{CF}_3\text{SO}_3)\}^+$, **30**, (55 %) (see Figure 75).



Label	Species present	Percentage (%)
A	$\{[\text{Fe}^{\text{III}}(\text{C}_6\text{H}_{10}(\text{O})(\text{OH}))(\text{PyMe}_2\text{tacn})](\text{CF}_3\text{SO}_3)\}^+$	100
B	$\{[\text{Fe}^{\text{III}}(\text{C}_6\text{H}_{10}(\text{O})(\text{OH}))(\text{PyMe}_2\text{tacn})](\text{CF}_3\text{SO}_3)\}^+$	18
	$\{[\text{Fe}^{\text{III}}(\text{C}_6\text{H}_{10}(\text{O})(^{18}\text{OH}))(\text{PyMe}_2\text{tacn})](\text{CF}_3\text{SO}_3)\}^+$	82
C	$\{[\text{Fe}^{\text{III}}(\text{C}_6\text{H}_{10}(\text{O})(\text{OH}))(\text{PyMe}_2\text{tacn})](\text{CF}_3\text{SO}_3)\}^+$	22
	$\{[\text{Fe}^{\text{III}}(\text{C}_6\text{H}_{10}(^{18}\text{O})(\text{OH}))(\text{PyMe}_2\text{tacn})](\text{CF}_3\text{SO}_3)\}^+$	78
D	$\{[\text{Fe}^{\text{III}}(\text{C}_6\text{H}_{10}(\text{O})(\text{OH}))(\text{PyMe}_2\text{tacn})](\text{CF}_3\text{SO}_3)\}^+$	12
	$\{[\text{Fe}^{\text{III}}(\text{C}_6\text{H}_{10}(\text{O})(^{18}\text{OH}))(\text{PyMe}_2\text{tacn})](\text{CF}_3\text{SO}_3)\}^+$	18
	$\{[\text{Fe}^{\text{III}}(\text{C}_6\text{H}_{10}(^{18}\text{O})(\text{OH}))(\text{PyMe}_2\text{tacn})](\text{CF}_3\text{SO}_3)\}^+$	15
	$\{[\text{Fe}^{\text{III}}(\text{C}_6\text{H}_{10}(^{18}\text{O})(^{18}\text{OH}))(\text{PyMe}_2\text{tacn})](\text{CF}_3\text{SO}_3)\}^+$	55

Figure 75. Representation of the species 27- 30, formed in the dihydroxylation of cyclohexene, present in each isotopic envelope and its tabulated data.

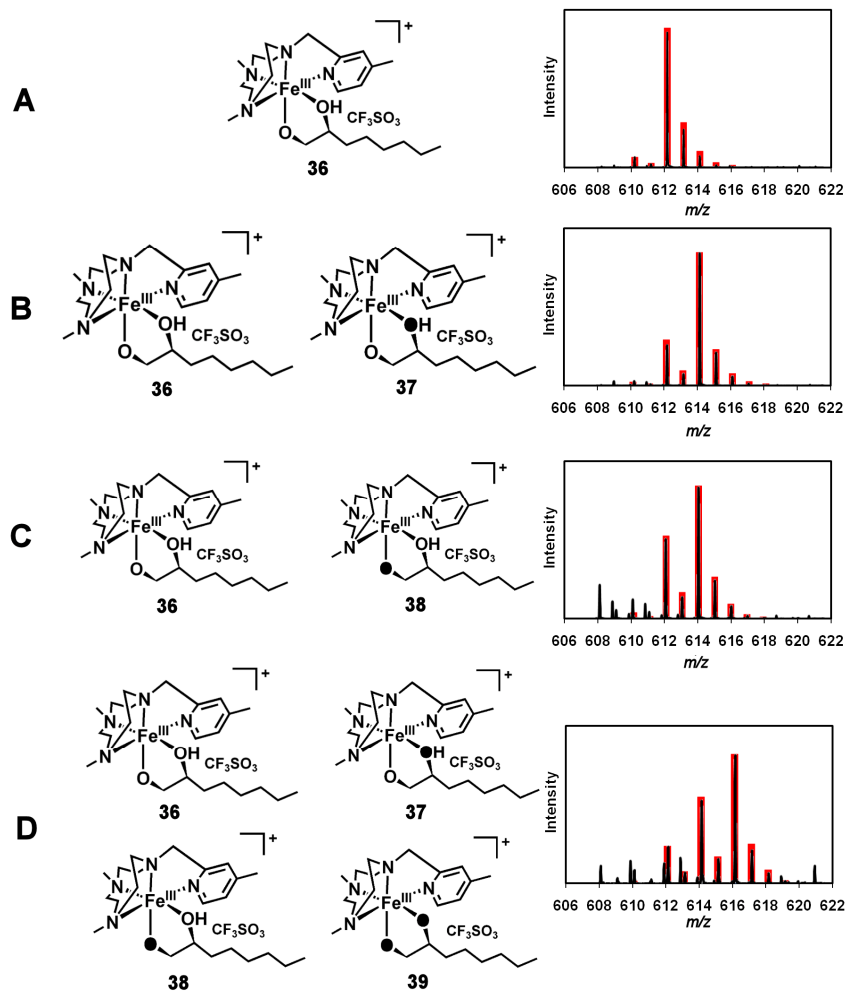


Label	Species present	Percentage (%)
A	$\{[\text{Fe}^{\text{III}}(\text{C}_8\text{H}_{14}(\text{O})(\text{OH}))(\text{4Me-PyMe}_2\text{tacn})](\text{CF}_3\text{SO}_3)\}^+$	100
B	$\{[\text{Fe}^{\text{III}}(\text{C}_8\text{H}_{14}(\text{O})(\text{OH}))(\text{4Me-PyMe}_2\text{tacn})](\text{CF}_3\text{SO}_3)\}^+$	16
	$\{[\text{Fe}^{\text{III}}(\text{C}_8\text{H}_{14}(\text{O})(^{18}\text{OH}))(\text{4Me-PyMe}_2\text{tacn})](\text{CF}_3\text{SO}_3)\}^+$	84
C	$\{[\text{Fe}^{\text{III}}(\text{C}_8\text{H}_{14}(\text{O})(\text{OH}))(\text{4Me-PyMe}_2\text{tacn})](\text{CF}_3\text{SO}_3)\}^+$	21
	$\{[\text{Fe}^{\text{III}}(\text{C}_8\text{H}_{14}(^{18}\text{O})(\text{OH}))(\text{4Me-PyMe}_2\text{tacn})](\text{CF}_3\text{SO}_3)\}^+$	79
D	$\{[\text{Fe}^{\text{III}}(\text{C}_8\text{H}_{14}(\text{O})(\text{OH}))(\text{4Me-PyMe}_2\text{tacn})](\text{CF}_3\text{SO}_3)\}^+$	7
	$\{[\text{Fe}^{\text{III}}(\text{C}_8\text{H}_{14}(\text{O})(^{18}\text{OH}))(\text{4Me-PyMe}_2\text{tacn})](\text{CF}_3\text{SO}_3)\}^+$	12
	$\{[\text{Fe}^{\text{III}}(\text{C}_8\text{H}_{14}(^{18}\text{O})(\text{OH}))(\text{4Me-PyMe}_2\text{tacn})](\text{CF}_3\text{SO}_3)\}^+$	16
	$\{[\text{Fe}^{\text{III}}(\text{C}_8\text{H}_{14}(^{18}\text{O})(^{18}\text{OH}))(\text{4Me-PyMe}_2\text{tacn})](\text{CF}_3\text{SO}_3)\}^+$	65

Figure 76. Representation of the species 32- 35, formed in the dihydroxylation of cyclooctene, present in each isotopic envelope and its tabulated data.

The above experiments were also carried out with $[\text{Fe}(\text{4Me-PyMe}_2\text{tacn})(\text{CF}_3\text{SO}_3)_2]$ **31** producing the same trend. Figure 76 shows the spectrum produced when $[\text{Fe}^{\text{II}}(\text{CF}_3\text{SO}_3)_2(\text{4Me-PyMe}_2\text{tacn})]$ **31** was used in the catalytic dihydroxylation of cyclooctene.

As with $[\text{Fe}^{\text{II}}(\text{CF}_3\text{SO}_3)_2(\text{PyMe}_2\text{tacn})]$ **14** isotope labelling was used to follow the incorporation of the oxygen atoms from water and hydrogen peroxide. As before the incorporation of the labelled oxygen atoms can be shown by a shift in the m/z of the peak assigned to $\{[\text{Fe}^{\text{III}}(\text{C}_6\text{H}_{10}(\text{O})(\text{OH}))(\text{4Me-PyMe}_2\text{tacn})](\text{CF}_3\text{SO}_3)\}^+$ **32** (610.2 m/z) by two m/z units to 612.2 m/z ($\{[\text{Fe}^{\text{III}}(\text{C}_6\text{H}_{10}(\text{O})(^{18}\text{OH}))(\text{4Me-PyMe}_2\text{tacn})](\text{CF}_3\text{SO}_3)\}^+$ **33** and $\{[\text{Fe}^{\text{III}}(\text{C}_6\text{H}_{10}(^{18}\text{O})(\text{OH}))(\text{4Me-PyMe}_2\text{tacn})](\text{CF}_3\text{SO}_3)\}^+$ **34**) when H_2^{18}O and $\text{H}_2^{18}\text{O}_2$ were used independently and a shift of four m/z units to 614.2 m/z ($\{[\text{Fe}^{\text{III}}(\text{C}_6\text{H}_{10}(^{18}\text{O})(^{18}\text{OH}))(\text{4Me-PyMe}_2\text{tacn})](\text{CF}_3\text{SO}_3)\}^+$ **35**) when both H_2^{18}O and $\text{H}_2^{18}\text{O}_2$ were reacted together with $[\text{Fe}^{\text{II}}(\text{CF}_3\text{SO}_3)_2(\text{4Me-PyMe}_2\text{tacn})]$ (see Figure 76). The dihydroxylation of 1-octene by $[\text{Fe}^{\text{II}}(\text{CF}_3\text{SO}_3)_2(\text{4Me-PyMe}_2\text{tacn})]$, H_2^{18}O and $\text{H}_2^{18}\text{O}_2$ was also carried out to give spectrum comparable to the results given above with the free *cis*-dihydroxylated product not being observed in the mass spectrometer due to the uncharged nature of the species.



Label	Species present	Percentage (%)
A	$\{[\text{Fe}^{\text{III}}(\text{C}_8\text{H}_{16}(\text{O})(\text{OH}))(\text{4Me-PyMe}_2\text{tacn})](\text{CF}_3\text{SO}_3)\}^+$	100
B	$\{[\text{Fe}^{\text{III}}(\text{C}_8\text{H}_{16}(\text{O})(\text{OH}))(\text{4Me-PyMe}_2\text{tacn})](\text{CF}_3\text{SO}_3)\}^+$	22
	$\{[\text{Fe}^{\text{III}}(\text{C}_8\text{H}_{16}(\text{O})(^{18}\text{OH}))(\text{4Me-PyMe}_2\text{tacn})](\text{CF}_3\text{SO}_3)\}^+$	78
C	$\{[\text{Fe}^{\text{III}}(\text{C}_8\text{H}_{16}(\text{O})(\text{OH}))(\text{4Me-PyMe}_2\text{tacn})](\text{CF}_3\text{SO}_3)\}^+$	37
	$\{[\text{Fe}^{\text{III}}(\text{C}_8\text{H}_{16}(^{18}\text{O})(\text{OH}))(\text{4Me-PyMe}_2\text{tacn})](\text{CF}_3\text{SO}_3)\}^+$	63
D	$\{[\text{Fe}^{\text{III}}(\text{C}_8\text{H}_{16}(\text{O})(\text{OH}))(\text{4Me-PyMe}_2\text{tacn})](\text{CF}_3\text{SO}_3)\}^+$	14
	$\{[\text{Fe}^{\text{III}}(\text{C}_8\text{H}_{16}(\text{O})(^{18}\text{OH}))(\text{4Me-PyMe}_2\text{tacn})](\text{CF}_3\text{SO}_3)\}^+$	17
	$\{[\text{Fe}^{\text{III}}(\text{C}_8\text{H}_{16}(^{18}\text{O})(\text{OH}))(\text{4Me-PyMe}_2\text{tacn})](\text{CF}_3\text{SO}_3)\}^+$	16
	$\{[\text{Fe}^{\text{III}}(\text{C}_8\text{H}_{16}(^{18}\text{O})(^{18}\text{OH}))(\text{4Me-PyMe}_2\text{tacn})](\text{CF}_3\text{SO}_3)\}^+$	53

Figure 77. Representation of the species 36- 39, formed in the dihydroxylation of 1-octene, present in each isotopic envelope and its tabulated data

The observations in this work have led us to conclude that **15** is the reaction intermediate in the catalytic oxidation of C-H moieties mediated by iron complexes. Taking into consideration that computational DFT methods predict a very small (< 7 Kcal/mol) energy barrier for the *cis*-dihydroxylation of an olefin by related Fe^V(O)(OH) species, it is very likely that **15** is the executor of the *cis*-dihydroxylation event.

CSI-MS analysis of the reaction between the non-heme iron catalyst **14** with H₂O₂ at -40 °C has allowed the first observation of evidence for the reactive intermediate {[Fe^V(O)(OH)(PyMe₂tacn)](CF₃SO₃)}⁺ **15**. With the use of isotope labelling experiments, **15** was shown to contain one oxygen atom originating from H₂O₂ with the second oxygen originating from H₂O. This evidence confirms previous research that postulated the existence of a water-assisted path for the generation of the iron(V) intermediate. Isotope labelling of *cis*-dihydroxylation reactions also provided evidence of the existence of the {[Fe^V(O)(OH)(PyMe₂tacn)](CF₃SO₃)}⁺ **15** species because if the species was in fact the species {[Fe^{III}(OOH)(PyMe₂tacn)](CF₃SO₃)}⁺ that has the same *m/z* value as **15** then the *cis*-dihydroxylation reaction would not take place.

The formation of the Fe(V)(O)(OH) species in catalytic C-H hydroxylation and C=C *cis*-dihydroxylation reactions has previously been predicted by computational and product analysis experiments.^{79,89,90,101,123,124} The research presented above provides the first experimental evidence for the formation of the Fe(V)(O)(OH) intermediate and so provides a new framework in the understanding of non-heme ligands and how they perform alkane hydroxylation and olefin *cis*-dihydroxylation in synthetic and enzymatic systems.

4.2 Conclusions

Temperature variable CSI-MS experiments were carried out to observe the reactive Fe(V)=O intermediate in the catalytic oxidation of C-H and C=C moieties. The ligand [Fe(CF₃SO₃)₂(PyMe₂tacn)], **14**, synthesised by Costas *et al* was reacted with hydrogen peroxide and water to form the highly unstable {[Fe^V(O)(OH)(PyMe₂tacn)](CF₃SO₃)}⁺, **15**, species.⁹¹ As this species has the same *m/z* value as {[Fe^{III}(OOH)(PyMe₂tacn)](CF₃SO₃)}⁺ experiments were undertaken to prove the existence of the Fe(V)=O species. To do this ¹⁸O-labelled experiments were carried out where ¹⁸O-labelled hydrogen peroxide and water were used. This gave spectra where the observed peak (at 486.1 *m/z*) was shifted by two *m/z* units to 488.1 *m/z* ([Fe^V(¹⁸O)(OH)(PyMe₂tacn)](CF₃SO₃)}⁺ **16**) when H₂¹⁸O and H₂O₂ were used, the same being observed when H₂O and H₂¹⁸O₂ were added (peak observed was {[Fe^V(O)(¹⁸OH)(PyMe₂tacn)](CF₃SO₃)}⁺, **17**). When both H₂¹⁸O and H₂¹⁸O₂ were used the peak shifted by the expected four *m/z* units to 490 *m/z*, this species being analysed as {[Fe^V(¹⁸O)(¹⁸OH)(PyMe₂tacn)](CF₃SO₃)}⁺, **15** (see Figure 78).

Time resolved CSI-MS was carried out to observe the decomposition of the species {[Fe^V(O)(OH)(PyMe₂tacn)](CF₃SO₃)}⁺ **15** as the temperature was increased. This reaction was carried out using a cryospray attachment where nebuliser gas (nitrogen in the case of ESI-MS) was replaced with liquid nitrogen and the temperature decreased to -40 °C where the Fe(V)=O species was observed. The temperature was then slowly increased from -40 °C to 20 °C over twenty minutes to show the decreased intensity of the {[Fe^V(O)(OH)(PyMe₂tacn)](CF₃SO₃)}⁺ **15** peak at 486.1 *m/z*. This observation provided further evidence that the species was that of the highly unstable {[Fe^V(O)(OH)(PyMe₂tacn)](CF₃SO₃)}⁺ **15** intermediate.

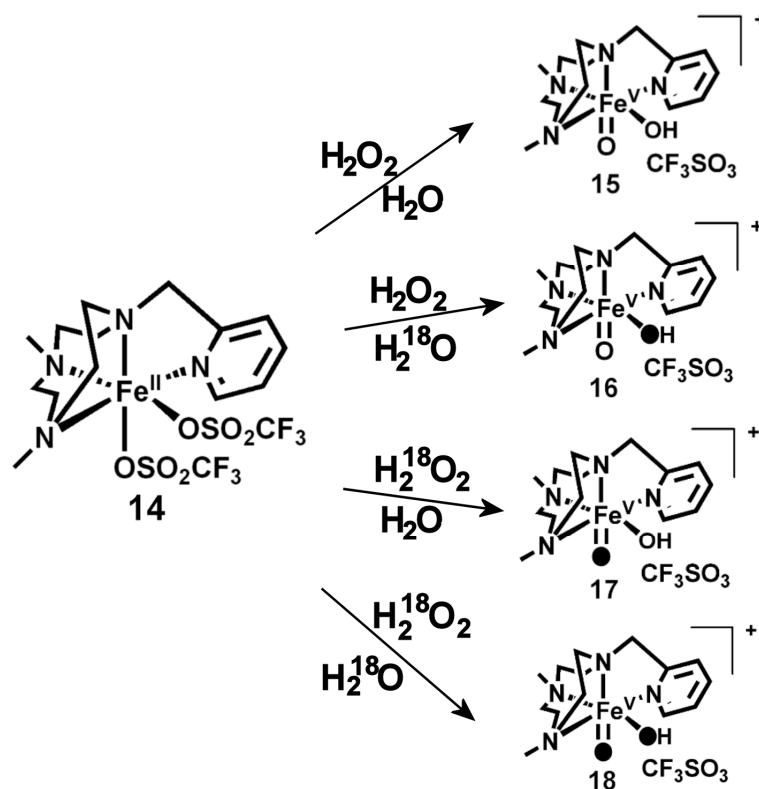


Figure 78. Summary of the Fe(V)=O species that could be observed using CSI-MS.

To further confirm the presence of the $\{[\text{Fe}^{\text{V}}(\text{O})(\text{OH})(\text{PyMe}_2\text{tacn})](\text{CF}_3\text{SO}_3)\}^+$, **15**, species CSI-MS *cis*-dihydroxylation reactions were carried out with **14** and three olefins, cyclooctene, 1-octene and cyclohexene. A species correlating to $\{[\text{Fe}^{\text{III}}(\text{C}_8\text{H}_{14}(\text{O})(\text{OH}))(\text{PyMe}_2\text{tacn})](\text{CF}_3\text{SO}_3)\}^+$, **19**, was observed in the reaction with cyclooctene at 596.2 *m/z*, with the peak shifting by two *m/z* units to 598.2 *m/z*, this peak being analysed as $\{[\text{Fe}^{\text{III}}(\text{C}_8\text{H}_{14}(\text{O})(\text{OH}))(\text{PyMe}_2\text{tacn})](\text{CF}_3\text{SO}_3)\}^+$, **20**, and $\{[\text{Fe}^{\text{III}}(\text{C}_8\text{H}_{14}(\text{O})(\text{OH}))(\text{PyMe}_2\text{tacn})](\text{CF}_3\text{SO}_3)\}^+$, **21**, when ¹⁸O-labelled water and hydrogen peroxide were added respectively. When both H₂¹⁸O₂ and H₂¹⁸O were added the peak shifted by four *m/z* units to 600.2 *m/z* ($\{[\text{Fe}^{\text{III}}(\text{C}_8\text{H}_{14}(\text{O})(\text{OH}))(\text{PyMe}_2\text{tacn})](\text{CF}_3\text{SO}_3)\}^+$, **22**) as before (see Figure 79).

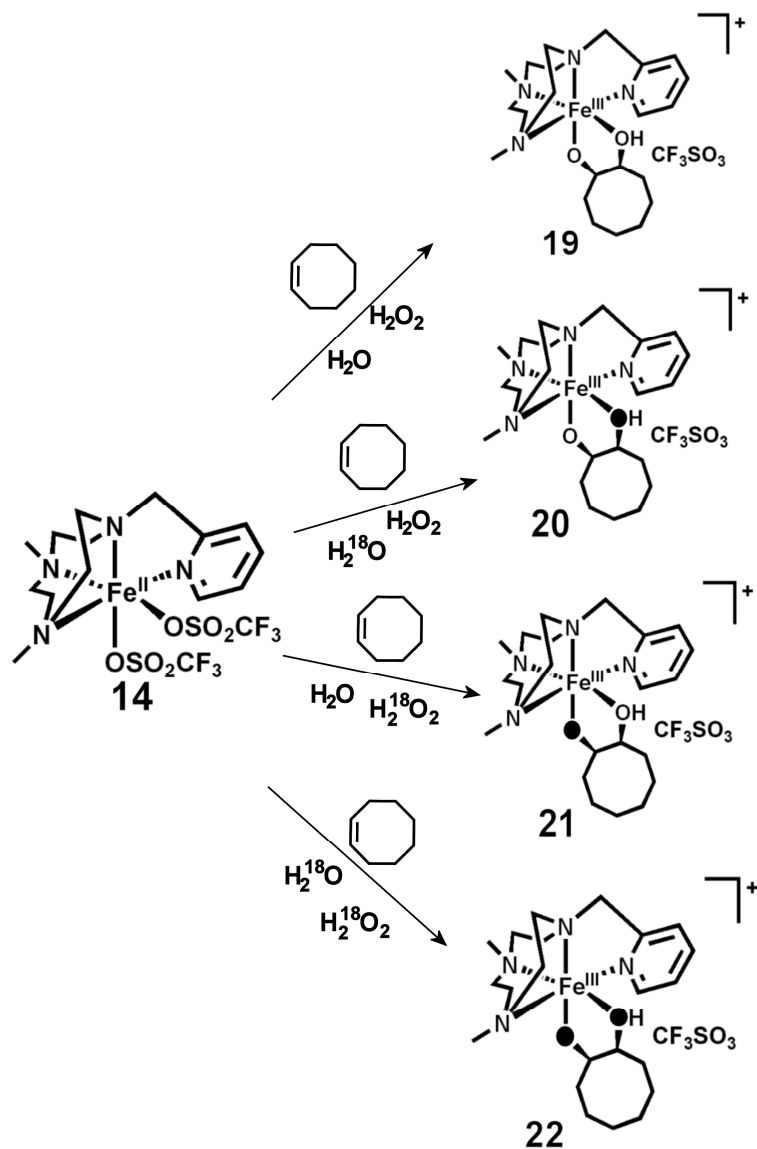


Figure 79. Summary of the reaction of **14** with cyclooctene, hydrogen peroxide and water and their ^{18}O -labelled counterparts.

Reactions with **14** and 1-octene, H_2O and H_2O_2 gave a spectrum that contained the species $\{[\text{Fe}^{\text{III}}(\text{C}_8\text{H}_{16}(\text{O})(\text{OH})(\text{PyMe}_2\text{tacn})](\text{CF}_3\text{SO}_3)]^+\}$, **23**, at 598.2 m/z . When **14** was reacted with 1-octene, H_2^{18}O and H_2O_2 the peak shifted by two m/z units to 600.2 m/z ($\{[\text{Fe}^{\text{III}}(\text{C}_8\text{H}_{16}(^{18}\text{O})(\text{OH})(\text{PyMe}_2\text{tacn})](\text{CF}_3\text{SO}_3)]^+\}$, **24**), the same when **14**, 1-octene, H_2O and $\text{H}_2^{18}\text{O}_2$ were reacted together (the species observed was $\{[\text{Fe}^{\text{III}}(\text{C}_8\text{H}_{16}(\text{O})(^{18}\text{OH})(\text{PyMe}_2\text{tacn})](\text{CF}_3\text{SO}_3)]^+\}$, **25**). The reaction of **14** with 1-octene,

H_2^{18}O and $\text{H}_2^{18}\text{O}_2$ gave a spectrum that had shifted by four m/z units to 602.2 m/z ($\{[\text{Fe}^{\text{III}}(\text{C}_8\text{H}_{16}({}^{18}\text{O})({}^{18}\text{OH})(\text{PyMe}_2\text{tacn})](\text{CF}_3\text{SO}_3)]^+\}$, **26**) (see Figure 80).

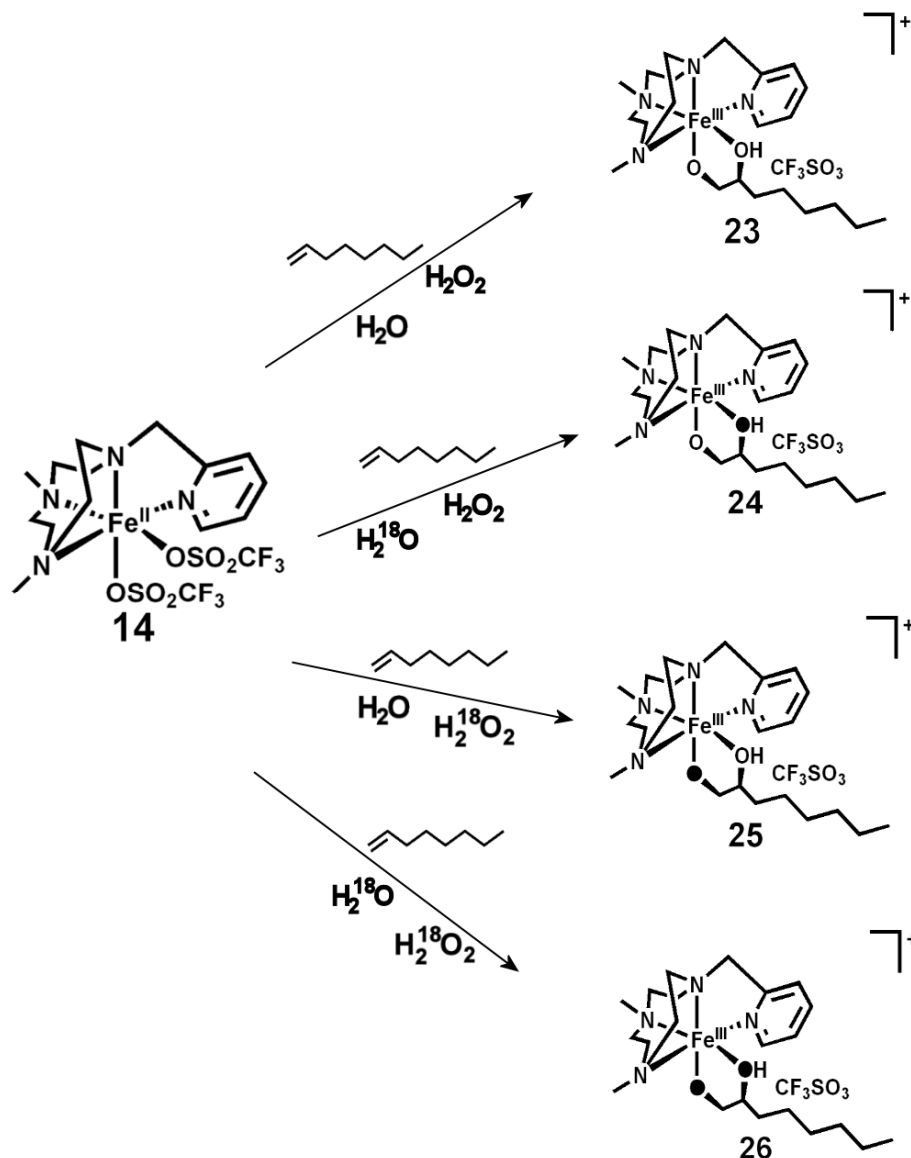


Figure 80. Summary of the reaction of **14** with 1-octene, hydrogen peroxide and water and their ^{18}O -labelled counterparts.

The final olefin to be used in the *cis*-dihydroxylation reaction was cyclohexene. As with cyclooctene and 1-octene both unlabelled and ^{18}O -labelled reactants were used. When **14** was reacted with cyclohexene, H_2O and H_2O_2 a peak was observed at 568.2 m/z , this corresponding to the species $\{[\text{Fe}^{\text{III}}(\text{C}_8\text{H}_{10}(\text{OH})(\text{PyMe}_2\text{tacn})](\text{CF}_3\text{SO}_3)]^+\}$, **27**. When H_2^{18}O was reacted the peak shifted by two m/z units to 570.2 m/z units

($\{[\text{Fe}^{\text{III}}(\text{C}_8\text{H}_{10}({}^{18}\text{O})(\text{OH})(\text{PyMe}_2\text{tacn})](\text{CF}_3\text{SO}_3)\}^+$, **28**), the same when $\text{H}_2{}^{18}\text{O}_2$ was used (the species observed with $\text{H}_2{}^{18}\text{O}_2$ analysed as $\{[\text{Fe}^{\text{III}}(\text{C}_8\text{H}_{10}(\text{O})({}^{18}\text{OH})(\text{PyMe}_2\text{tacn})](\text{CF}_3\text{SO}_3)\}^+$, **29**). The reaction of **14** with cyclohexene, $\text{H}_2{}^{18}\text{O}$ and $\text{H}_2{}^{18}\text{O}_2$ gave a spectrum where the peak had shifted by four m/z units to 572.2 m/z ($\{[\text{Fe}^{\text{III}}(\text{C}_8\text{H}_{10}({}^{18}\text{O})({}^{18}\text{OH})(\text{PyMe}_2\text{tacn})](\text{CF}_3\text{SO}_3)\}^+$, **30**).

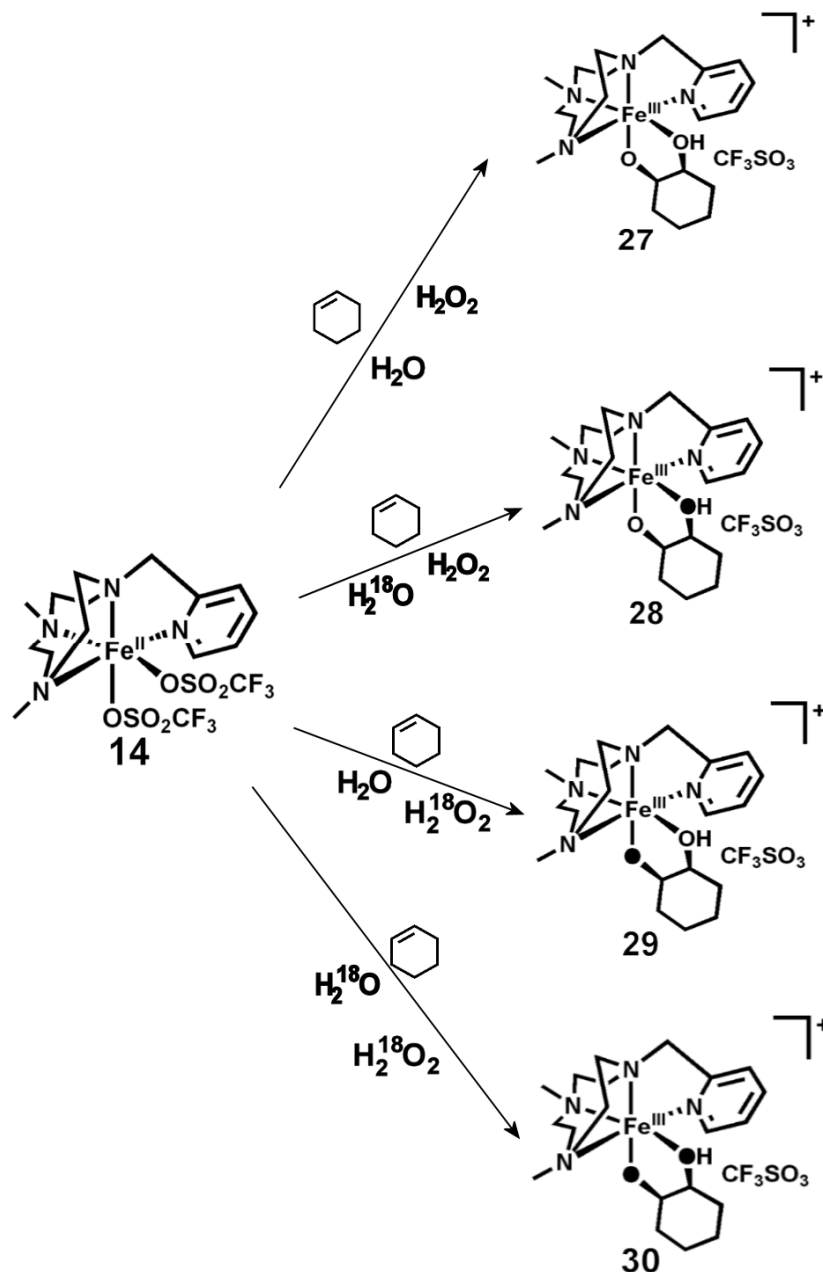
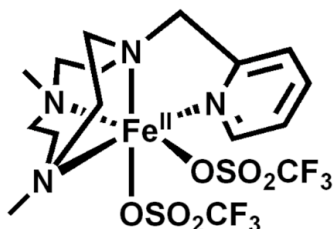


Figure 81. Summary of the reaction of **14** with cyclooctene, hydrogen peroxide and water and their ${}^{18}\text{O}$ -labelled counterparts.

The research carried out here provides evidence of the unstable intermediate Fe(V)=O species that has been postulated as the reactive species in the catalytic oxidation of C-H and C=C bonds.⁸⁹ Temperature variable mass spectrometry has been used to show the decomposition of the unstable reactive intermediate therefore disregarding the possibility that the observed peak is that of a species with the same m/z value. The use of ¹⁸O-labelled reagents also provides evidence that the catalytic reaction takes place by heterolytic water assisted cleavage where one oxygen of the [Fe^V(O)(OH)(PyMe₂tacn)]⁺ species comes from water and one from hydrogen peroxide.

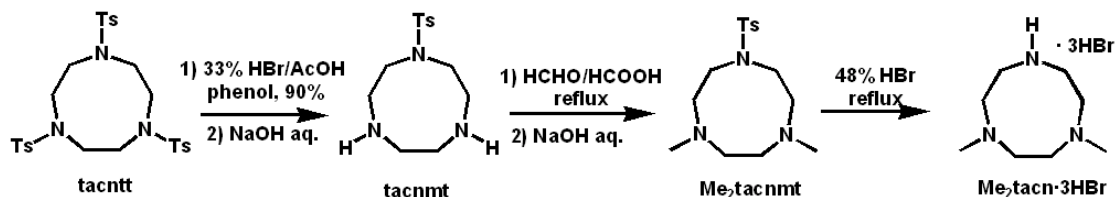
4.3 Experimental

4.3.1 Synthesis of $[\text{FeII}(\text{CF}_3\text{SO}_3)_2(\text{PyMe}_2\text{tacn})]$, 14



The ligand $[\text{Fe}(\text{CF}_3\text{SO}_3)_2(\text{PyMe}_2\text{tacn})]$ 14 ((PyMe₂tacn), = 1-(2-pyridylmethyl)-4,7-dimethyl-1,4,7-triazacyclononane). was synthesised by Costas et al.⁹¹

4.3.2 Synthesis of 1-(*p*-toluensulfonyl)-1,4,7-triazacyclononane, tacnmt



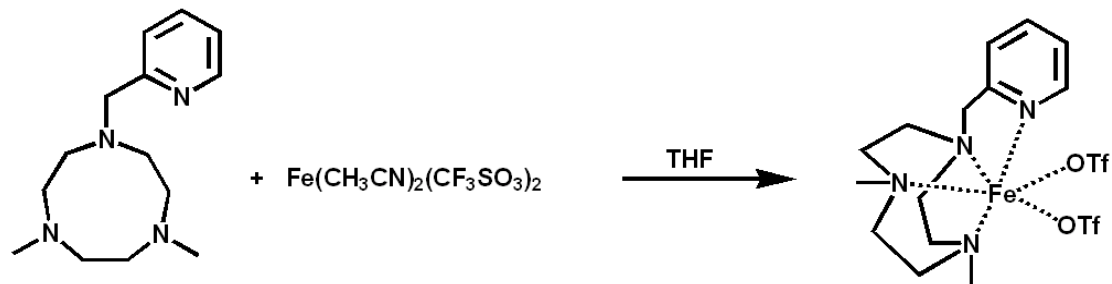
1-(*p*-toluensulfonyl)-1,4,7-triazacyclononane, tacnmt. tacntt (24.6 g, 41.6 mmol) and phenol (35.2 g, 374 mmol) were mixed in a 500 ml flask. A solution of HBr in acetic acid (33%, 380 ml) was added with extreme care as an important evolution of HBr_(g) takes place. The mixture was gently heated with stirring to 90°C which caused the complete dissolution of all the starting reactivities giving rise to the formation of a dark solution. A colorless precipitate of 1-(*p*-toluensulfonyl)-1,4,7-triazacyclononane·2HBr appeared within 2-4 h. After heating for 36 h, the mixture was cooled to room temperature and filtered. The solid was washed with diethyl ether (125 ml) and then dissolved in aqueous NaOH 1M (320 ml). The resultant pink aqueous mixture was then extracted with CH₂Cl₂ (3 x 190 ml) and the organic extracts dried with anhydrous MgSO₄, filtered and evaporated under reduced pressure. Drying the resultant oil under vacuum afforded 9.88 g of the pure

product (34.9 mmol, 84 %). Anal. Calcd for C₁₃H₂₁O₂N₃S (MW = 283.39 g/mol): C, 55.10; H, 7.47; N, 14.83; S, 11.31 %. Found: C, 54.49; H, 7.41; N, 14.71; S, 11.38 %. FT-IR (ATR) ν , cm⁻¹: 3302 (N-H), 2914, 2855 (C-H)_{sp3}, 1328, 1152 (R-SO₂-N). ¹H-NMR (CDCl₃, 200 MHz, 300K) δ , ppm: 7.70 (d, J 8.2 Hz, 2H, ArH), 7.34 (d, J 8.2 Hz, 2H, ArH), 3.23 - 3.18 (m, 4H, TsN-CH₂-CH₂-NH), 3.12 - 3.09 (m, 4H, TsN-CH₂-CH₂-NH), 2.90 (s, 4H, HN-CH₂-CH₂-NH), 2.44 (s, 3H, Ar-CH₃), 1.85 (s, 2H, NH). ¹³C-NMR (CDCl₃, 50 MHz, 300K) δ , ppm: 143.16 (arC-CH₃), 135.60 (arC-SO₂), 129.59, 127.16 (arC-H), 53.91 (TsN-CH₂-C), 49.63, 49.46 (CH₂-NH-CH₂), 21.41 (Ar-CH₃). ESI-MS (m/z): 283.7 [M+H]⁺.

1,4-dimethyl-7-(*p*-toluenesulfonyl)-1,4,7-triazacyclononane, Me₂tacnmt. tacnmt (8.5 g, 30 mmol) was dissolved in 37 % formaldehyde (25 ml) and 98 % formic acid (25 ml) and the resulting orange solution was refluxed for 24 h. After cooling to room temperature, 10 ml HCl cc were added and the mixture was left stirring for 10 min. The solvent was removed under vacuum and a small amount of water (10 ml) was added to the resulting residue. The solution was brought to pH > 14 by addition of NaOH 4 M. This caused the slow formation of a white precipitate corresponding to the desired product. After stirring for 20 h at room temperature, filtration of the mixture gave a white precipitate which was dissolved in 50 ml CH₂Cl₂ (50 ml) giving a pale yellow solution which was treated with 4M NaOH (50 ml). The aqueous layer was further extracted with CH₂Cl₂ (2 x 50 ml). The combined organic layers were dried over anhydrous MgSO₄ and the solvent was removed under reduced pressure to yield 8.3 g of a crystalline white solid (27 mmol, 90 %). ¹H-NMR (CDCl₃, 200 MHz, 300K) δ , ppm: 7.67 (d, J = 8.2 Hz, 2H, ArH), 7.30 (d, J = 8.2 Hz, 2H, ArH), 3.27 - 3.23 (m, 4H, N-CH₂-CH₂), 2.92 - 2.88 (m, 4H, N-CH₂-CH₂), 2.69 (s, 4H, N-CH₂-CH₂), 2.42 (s, 3H, Ar-CH₃), 2.39 (s, 6H, N-CH₃).

1,4-dimethyl-1,4,7-triazacyclononane trihydrobromide, Me₂tacn·3HBr. Me₂tacnmt (8.6 g, 27 mmol) was dissolved in 48 % HBr (86 ml) and refluxed for 48 h. After cooling at room temperature, the solvent of the black crude mixture was removed under reduced pressure. Addition of acetone (100 ml) and stirring for 3 hours afforded a fine pale precipitate which was filtered off and washed with acetone. The resulting pale grey solid was dissolved with boiling water (75 ml) and filtered. The solvent from the yellow filtrates was removed under reduced pressure and the resulting residue was treated with absolute ethanol (100 ml). A fine pale yellow precipitate appeared which was filtered off and dried under vacuum to yield 5.3 g of the desired product (13 mmol, 49%). ¹H-NMR (D₂O, 200

4.3.3.1 Synthesis of $[\text{Fe}^{\text{II}}(\text{PyMe}_2\text{tacn})(\text{CF}_3\text{SO}_3)_2]$, **14**



A solution of $\text{Fe}(\text{CH}_3\text{CN})_2(\text{CF}_3\text{SO}_3)_2$ (90 mg, 0.21 mmol) in anhydrous THF (2 ml) is added dropwise to a vigorously stirred solution of PyMe₂tacn (55 mg, 0.21 mmol) in THF (1.5 ml). After a few seconds the solution becomes cloudy and a pale yellow precipitate appears. After stirring for 1 hour the solution is filtered off and the resultant yellow solid dried under vacuum. This solid is dissolved in CH_2Cl_2 and filtered through Celite. Slow diethyl ether diffusion over the resultant solution affords, in a few days, 109 mg of yellow crystals (0.18 mmol, 86 %). Anal. Calcd for $\text{C}_{16}\text{H}_{24}\text{F}_6\text{FeN}_4\text{O}_6\text{S}_2 \cdot 1/4\text{CH}_3\text{CN}$: C, 32.35; H, 4.07; N, 9.76; S, 10.47 %. Found: C, 32.49; H, 4.04; N, 9.66; S, 10.30 %. FT-IR (ATR) ν , cm^{-1} : 2862 (C-H)_{sp3}, 1285 (py), 1224, 1158, 1026, 634 (CF_3SO_3). ¹H-NMR (CD_3CN , 200 MHz, 300K) δ , ppm: 13.69, 10.32, 8.40, 6.25, 4.33, 1.97. ¹H-NMR (CD_2Cl_2 , 200 MHz, 300K) δ , ppm: 118.53, 92.45, 49.92, 36.52, 32.30, 17.73. ESI-MS (m/z): 192.8 $[\text{M}+2\text{CH}_3\text{CN}-2\text{OTf}]^{2+}$, 453.1 $[\text{M}-\text{OTf}]^+$, 494.1 $[\text{M}+\text{CH}_3\text{CN}-\text{OTf}]^+$.

4.3.4 Observation of the Fe(V)-oxo species using cryospray mass spectrometry (CSI-MS)

All MS data for the analysis of the $[\text{Fe}(\text{CF}_3\text{SO}_3)_2(\text{PyMe}_2\text{tacn})]$ **14** catalytic cycle was collected using a Q-trap, time-of-flight MS (MicrOTOF-Q MS) instrument supplied by Bruker Daltonics Ltd. This instrument was equipped either with a cryospray source, both of which was supplied by Bruker Daltonics Ltd. and the detector was a time-of-flight, microchannel plate detector.

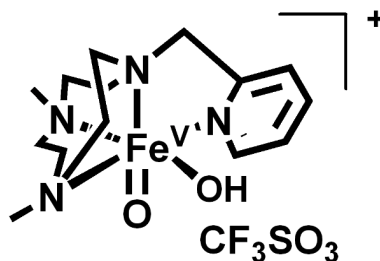
4.3.4.1 Time resolved mass spectrometry analysis of $\{[\text{Fe}^{\text{V}}(\text{O})(\text{OH})(\text{PyMe}_2\text{tacn})](\text{CF}_3\text{SO}_3)\}^+$, **15, generated with $\text{H}_2^{16}\text{O}_2/\text{H}_2^{16}\text{O}$, when temperature increases.**

$[\text{Fe}(\text{PyMe}_2\text{tacn})(\text{CF}_3\text{SO}_3)_2]$, **14**, (0.5 mg, 8×10^{-4} mmol) was dissolved in MeCN (~7 ml) and the solution cooled to 4 °C. A solution of H_2O_2 (10 mM in 10 ml MeCN) was made up and also cooled to 4 °C. The solution of **14** (300 μl) was added to a vial that was cooled in a dry ice/MeCN bath and H_2O (15 μl , 0.83 mmol) added. To this stirring solution H_2O_2 (300 μl , 3×10^{-3} mmol) was added and the solution injected directly into the mass spectrometer (CSI-MS -40°C). The spectrum was collected immediately for 20 minutes. MS (CSI-MS) m/z 486.1 $[\text{M}]^+$.

4.3.4.2 Time resolved mass spectrometry analysis of $\{[\text{Fe}^{\text{V}}(\text{O})(^{18}\text{OH})(\text{PyMe}_2\text{tacn})](\text{CF}_3\text{SO}_3)\}^+$, **16, generated with $\text{H}_2^{16}\text{O}_2/\text{H}_2^{18}\text{O}$, when temperature increases.**

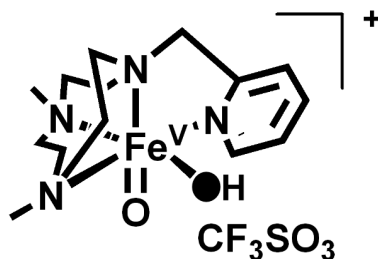
$[\text{Fe}(\text{PyMe}_2\text{tacn})(\text{CF}_3\text{SO}_3)_2]$, **14**, (0.5 mg, 8×10^{-4} mmol) was dissolved in MeCN (~7 ml) and the solution cooled to 4 °C. A solution of H_2O_2 (10 mM in 10 ml MeCN) was made up and also cooled to 4 °C. The solution of **14** (300 μl) was added to a vial that was cooled in a dry ice/MeCN bath and H_2^{18}O (15 μl , 0.83 mmol) added. To this stirring solution H_2O_2 (300 μl , 3×10^{-3} mmol) was added and the solution injected directly into the mass spectrometer (CSI-MS -40°C). The spectrum was collected immediately for 20 minutes. MS (CSI-MS) m/z 488.1 $[\text{M}+2]^+$.

4.3.4.3 Sample preparations of $[\text{Fe}^{\text{II}}(\text{PyMe}_2\text{tacn})(\text{CF}_3\text{SO}_3)_2]$, **14, catalytic cycle experiments and observation of $\{[\text{Fe}^{\text{V}}(\text{O})(\text{OH})(\text{PyMe}_2\text{tacn})](\text{CF}_3\text{SO}_3)\}^+$, **15****



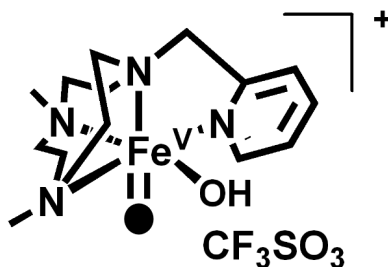
$[\text{Fe}^{\text{II}}(\text{PyMe}_2\text{tacn})(\text{CF}_3\text{SO}_3)_2]$, **14**, (0.5 mg, 8×10^{-4} mmol) was dissolved in MeCN (~ 7 ml) and the solution cooled to 4 °C. A solution of H_2O_2 (10 mM in 10 ml MeCN) was made up and also cooled to 4 °C. The solution of **14** (300 μl) was added to a vial that was cooled in a dry ice/MeCN bath and H_2O (15 μl , 0.83 mmol) added. To this stirring solution H_2O_2 (300 μl , 3×10^{-3} mmol) was added and the solution injected directly into the mass spectrometer (CSI-MS -40°C). The spectrum was collected immediately for 2 minutes. MS (CSI-MS) m/z 486.1 $[\text{M}+\text{CF}_3\text{SO}_3]^+$.

4.3.4.4 Sample preparations of $[\text{Fe}^{\text{II}}(\text{PyMe}_2\text{tacn})(\text{CF}_3\text{SO}_3)_2]$, **14, catalytic cycle experiments with H_2^{18}O and $\text{H}_2^{16}\text{O}_2$ and observation of $\{[\text{Fe}^{\text{V}}(\text{O})(^{18}\text{OH})(\text{PyMe}_2\text{tacn})](\text{CF}_3\text{SO}_3)\}^+$, **16****



$[\text{Fe}(\text{PyMe}_2\text{tacn})(\text{CF}_3\text{SO}_3)_2]$, **14**, (0.5 mg, 8×10^{-4} mmol) was dissolved in MeCN (~7 ml) and the solution cooled to 4 °C. A solution of H_2O_2 (10 mM in 10 ml MeCN) was made up and also cooled to 4 °C. The solution of **14** (300 μl) was added to a vial that was cooled in a dry ice/MeCN bath and H_2^{18}O (15 μl , 0.83 mmol) added. To this stirring solution H_2O_2 (300 μl , 3×10^{-3} mmol) was added and the solution injected directly into the mass spectrometer (CSI-MS -40°C). The spectrum was collected immediately for 2 minutes. MS (CSI-MS) m/z 488.1 $[\text{M}+2+\text{CF}_3\text{SO}_3]^+$.

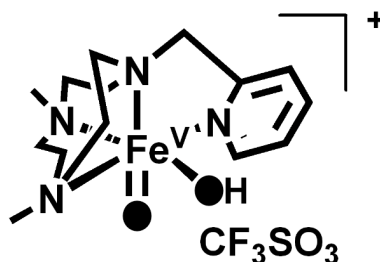
4.3.4.5 Sample preparations of $[\text{Fe}^{\text{II}}(\text{PyMe}_2\text{tacn})(\text{CF}_3\text{SO}_3)_2]$, **14, catalytic cycle experiments with H_2^{16}O and $\text{H}_2^{18}\text{O}_2$ and observation of $\{[\text{Fe}^{\text{V}}(^{18}\text{O})(\text{OH})(\text{PyMe}_2\text{tacn})](\text{CF}_3\text{SO}_3)\}^+$, **17****



$[\text{Fe}(\text{PyMe}_2\text{tacn})(\text{CF}_3\text{SO}_3)_2]$, **14**, (0.5 mg, 8×10^{-4} mmol) was dissolved in MeCN (~7 ml) and the solution cooled to 4 °C. A solution of $\text{H}_2^{18}\text{O}_2$ (10 mM in 10 ml MeCN) was made up and also cooled to 4 °C. The solution of **14** (300 μl) was added to a vial that was

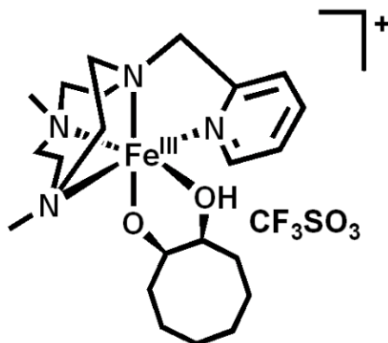
cooled in a dry ice/MeCN bath and H_2^{16}O (15 μl , 0.83 mmol) added. To this stirring solution H_2O_2 (300 μl , 3×10^{-3} mmol) was added and the solution injected directly into the mass spectrometer (CSI-MS -40°C). The spectrum was collected immediately for 2 minutes. MS (CSI-MS) m/z 488.1 $[\text{M}+2+\text{CF}_3\text{SO}_3]^+$.

4.3.4.6 Sample preparations of $[\text{Fe}^{\text{II}}(\text{PyMe}_2\text{tacn})(\text{CF}_3\text{SO}_3)_2]$, **14, catalytic cycle experiments with H_2^{18}O and $\text{H}_2^{18}\text{O}_2$ and observation of $\{[\text{Fe}^{\text{V}}(^{18}\text{O})(^{18}\text{OH})(\text{PyMe}_2\text{tacn})](\text{CF}_3\text{SO}_3)\}^+$, **18****



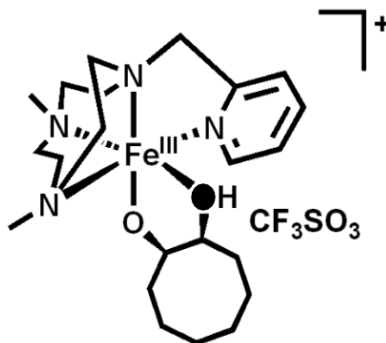
$[\text{Fe}(\text{PyMe}_2\text{tacn})(\text{CF}_3\text{SO}_3)_2]$, **14**, (0.5 mg, 8×10^{-4} mmol) was dissolved in MeCN (~7 ml) and the solution cooled to 4°C . A solution of $\text{H}_2^{18}\text{O}_2$ (10 mM in 10 ml MeCN) was made up and also cooled to 4°C . The solution of **14** (300 μl) was added to a vial that was cooled in a dry ice/MeCN bath and H_2^{18}O (15 μl , 0.83 mmol) added. To this stirring solution H_2O_2 (300 μl , 3×10^{-3} mmol) was added and the solution injected directly into the mass spectrometer (CSI-MS -40°C). The spectrum was collected immediately for 2 minutes. MS (CSI-MS) m/z 490.1 $[\text{M}+4+\text{CF}_3\text{SO}_3]^+$.

4.3.4.7 Sample preparations of the dihydroxylation of cyclooctene with [Fe(PyMe₂tacn)(CF₃SO₃)₂], **14, H₂¹⁶O and H₂¹⁶O₂ and observation of {[Fe^{III}(C₈H₁₄(O)(OH))(PyMe₂tacn)](CF₃SO₃)}⁺, **19**.**



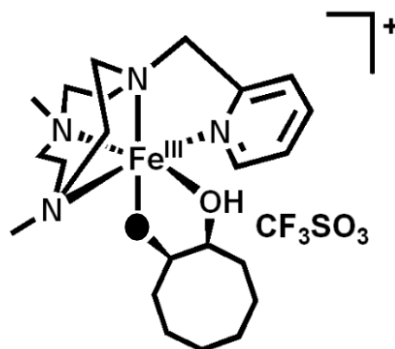
[Fe(PyMe₂tacn)(CF₃SO₃)₂] **14** (0.5 mg, 8 × 10⁻⁴ mmol) was dissolved in MeCN (~7 ml) and the solution cooled to 4 °C. A solution of H₂O₂ (10 mM on 10 ml MeCN) was made up and also cooled to 4 °C. The solution of **14** (300 μl) was added to a vial that was cooled in a dry ice/MeCN bath and H₂O (15 μl, 0.83 mmol) added. To this stirring solution H₂O₂ (300 μl, 3 × 10⁻³ mmol) and cyclooctene (10 μl, 0.08 mmol) were added and the solution injected directly into the mass spectrometer (ESI-MS). The spectrum was collected for 2 mins. MS (ESI-MS) *m/z* 446.2 [M]⁺, 596.2 [M+H+CF₃SO₃]⁺.

4.3.4.8 Sample preparations of the dihydroxylation of cyclooctene with [Fe(PyMe₂tacn)(CF₃SO₃)₂] **14, H₂¹⁸O and H₂¹⁶O₂ and observation of {[Fe^{III}(C₈H₁₄(O)(¹⁸OH))(PyMe₂tacn)](CF₃SO₃)⁺, **20**.**



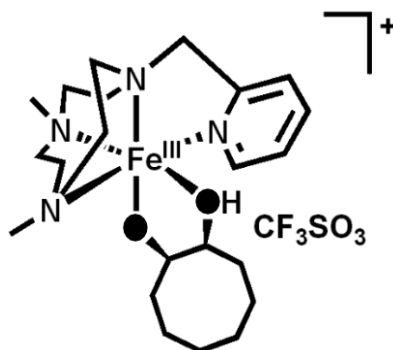
[Fe(PyMe₂tacn)(CF₃SO₃)₂] **14** (0.5 mg, 8 × 10⁻⁴ mmol) was dissolved in MeCN (~7 ml) and the solution cooled to 4 °C. A solution of H₂O₂ (10 mM on 10 ml MeCN) was made up and also cooled to 4 °C. The solution of **14** (300 μl) was added to a vial that was cooled in a dry ice/MeCN bath and H₂¹⁸O (15 μl, 0.83 mmol) added. To this stirring solution H₂O₂ (300 μl, 3 × 10⁻³ mmol) and cyclooctene (10 μl, 0.08 mmol) were added and the solution injected directly into the mass spectrometer (ESI-MS). The spectrum was collected for 2 mins. MS (ESI-MS) *m/z* 448.2 [M+2]⁺, 598.2 [M+2+H+CF₃SO₃]⁺.

4.3.4.9 Sample preparations of the dihydroxylation of cyclooctene with [Fe(PyMe₂tacn)(CF₃SO₃)₂] **14, H₂¹⁶O and H₂¹⁸O₂ and observation of {[Fe^{III}(C₈H₁₄(¹⁸O)(OH))(PyMe₂tacn)](CF₃SO₃)⁺, **21**.**



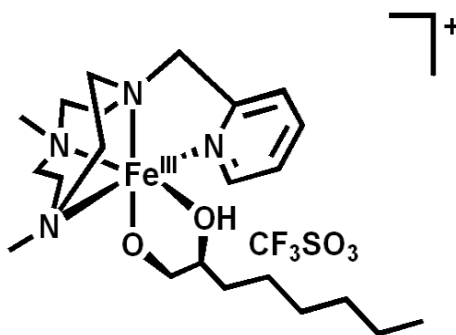
[Fe(PyMe₂tacn)(CF₃SO₃)₂] **14** (0.5 mg, 8 × 10⁻⁴ mmol) was dissolved in MeCN (~ 7 ml) and the solution cooled to 4 °C. A solution of H₂¹⁸O₂ (10 mM on 10 ml MeCN) was made up and also cooled to 4 °C. The solution of **14** (300 μl) was added to a vial that was cooled in a dry ice/MeCN bath and H₂O (15 μl, 0.83 mmol) added. To this stirring solution H₂¹⁸O₂ (300 μl, 3 × 10⁻³ mmol) and cyclooctene (10 μl, 0.08 mmol) were added and the solution injected directly into the mass spectrometer (ESI-MS). The spectrum was collected for 2 mins. MS (ESI-MS) *m/z* 448.2 [M+2]⁺, 598.2 [M+2+H+CF₃SO₃]⁺.

4.3.4.9.1 Sample preparations of the dihydroxylation of cyclooctene with [Fe(PyMe₂tacn)(CF₃SO₃)₂] **14, H₂¹⁸O and H₂¹⁸O₂ and observation of {[Fe^{III}(C₈H₁₄(¹⁸O)(¹⁸OH))(PyMe₂tacn)](CF₃SO₃)⁺, **22**.**



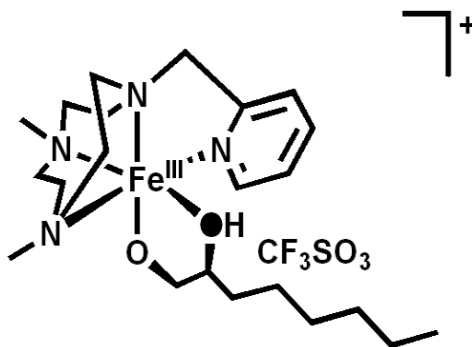
[Fe(PyMe₂tacn)(CF₃SO₃)₂] **14** (0.5 mg, 8×10^{-4} mmol) was dissolved in MeCN (~ 7 ml) and the solution cooled to 4 °C. A solution of H₂¹⁸O₂ (10 mM on 10 ml MeCN) was made up and also cooled to 4 °C. The solution of **14** (300 μ l) was added to a vial that was cooled in a dry ice/MeCN bath and H₂¹⁸O (15 μ l, 0.83 mmol) added. To this stirring solution H₂¹⁸O₂ (300 μ l, 3×10^{-3} mmol) and cyclooctene (10 μ l, 0.08 mmol) were added and the solution injected directly into the mass spectrometer (ESI-MS). The spectrum was collected for 2 mins. MS (ESI-MS) m/z 450.2 [M+4]⁺, 600.2 [M+4+H+CF₃SO₃]⁺.

4.3.4.9.2 Sample preparations of the dihydroxylation of 1-octene with [Fe(PyMe₂tacn)(CF₃SO₃)₂] **14, H₂¹⁶O and H₂¹⁶O₂ and observation of {[Fe^{III}(C₈H₁₆(O)(OH))(PyMe₂tacn)](CF₃SO₃)⁺, **23**.**



[Fe(PyMe₂tacn)(CF₃SO₃)₂] **14** (0.5 mg, 8 × 10⁻⁴ mmol) was dissolved in MeCN (~ 7 ml) and the solution cooled to 4 °C. A solution of H₂O₂ (10 mM on 10 ml MeCN) was made up and also cooled to 4 °C. The solution of **14** (300 μl) was added to a vial that was cooled in a dry ice/MeCN bath and H₂O (15 μl, 0.83 mmol) added. To this stirring solution H₂O₂ (300 μl, 3 × 10⁻³ mmol) and 1-octene (10 μl, 0.06 mmol) were added and the solution injected directly into the mass spectrometer (ESI-MS). The spectrum was collected for 2 mins. MS (ESI-MS) *m/z* 448.2 [M]⁺, 598.2 [M+H+CF₃SO₃]⁺.

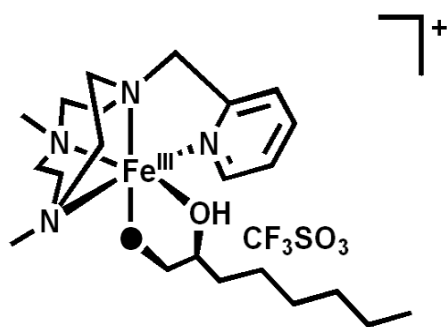
4.3.4.9.3 Sample preparations of the dihydroxylation of 1-octene with [Fe(PyMe₂tacn)(CF₃SO₃)₂] **14, H₂¹⁸O and H₂¹⁶O₂ and observation of {[Fe^{III}(C₈H₁₆(O)(¹⁸OH))(PyMe₂tacn)](CF₃SO₃)⁺, **24**.**



[Fe(PyMe₂tacn)(CF₃SO₃)₂] **14** (0.5 mg, 8 × 10⁻⁴ mmol) was dissolved in MeCN (~ 7 ml) and the solution cooled to 4 °C. A solution of H₂O₂ (10 mM on 10 ml MeCN) was

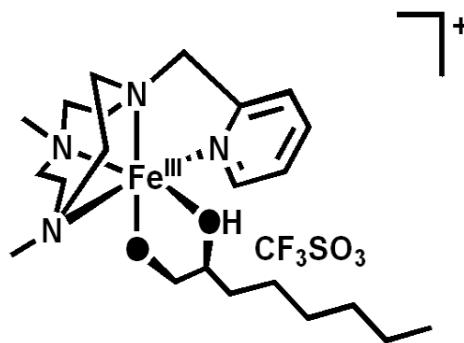
made up and also cooled to 4 °C. The solution of **14** (300 μ l) was added to a vial that was cooled in a dry ice/MeCN bath and H₂¹⁸O (15 μ l, 0.83 mmol) added. To this stirring solution H₂O₂ (300 μ l, 3 x 10⁻³ mmol) and 1-octene (10 μ l, 0.06 mmol) were added and the solution injected directly into the mass spectrometer (ESI-MS). The spectrum was collected for 2 mins. MS (ESI-MS) *m/z* 450.2 [M+2]⁺, 600.2 [M+2+H+CF₃SO₃]⁺.

4.3.4.9.4 Sample preparations of the dihydroxylation of 1-octene with [Fe(PyMe₂tacn)(CF₃SO₃)₂] **14, H₂¹⁶O and H₂¹⁸O₂ and observation of {[Fe^{III}(C₈H₁₆(¹⁸O)(OH))(PyMe₂tacn)](CF₃SO₃)⁺, **25**.**



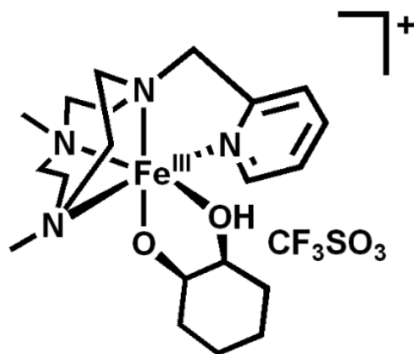
[Fe(PyMe₂tacn)(CF₃SO₃)₂] **14** (0.5 mg, 8 x 10⁻⁴ mmol) was dissolved in MeCN (~ 7 ml) and the solution cooled to 4 °C. A solution of H₂¹⁸O₂ (10 mM on 10 ml MeCN) was made up and also cooled to 4 °C. The solution of **14** (300 μ l) was added to a vial that was cooled in a dry ice/MeCN bath and H₂O (15 μ l, 0.83 mmol) added. To this stirring solution H₂¹⁸O₂ (300 μ l, 3 x 10⁻³ mmol) and 1-octene (10 μ l, 0.06 mmol) were added and the solution injected directly into the mass spectrometer (ESI-MS). The spectrum was collected for 2 mins. MS (ESI-MS) *m/z* 450.2 [M+2]⁺, 600.2 [M+2+H+CF₃SO₃]⁺.

4.3.4.9.5 Sample preparations of the dihydroxylation of 1-octene with [Fe(PyMe₂tacn)(CF₃SO₃)₂] **14, H₂¹⁸O and H₂¹⁸O₂ and observation of {[Fe^{III}(C₈H₁₆(¹⁸O)(¹⁸OH))(PyMe₂tacn)](CF₃SO₃)}⁺, **26**.**



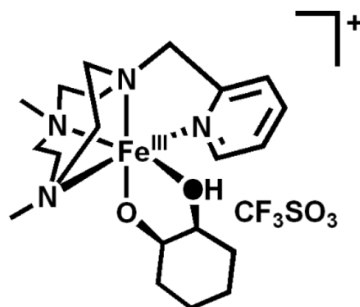
[Fe(PyMe₂tacn)(CF₃SO₃)₂] **14** (0.5 mg, 8 x 10⁻⁴ mmol) was dissolved in MeCN (~ 7 ml) and the solution cooled to 4 °C. A solution of H₂¹⁸O₂ (10 mM on 10 ml MeCN) was made up and also cooled to 4 °C. The solution of **14** (300 μl) was added to a vial that was cooled in a dry ice/MeCN bath and H₂¹⁸O (15 μl, 0.83 mmol) added. To this stirring solution H₂¹⁸O₂ (300 μl, 3 x 10⁻³ mmol) and 1-octene (10 μl, 0.06 mmol) were added and the solution injected directly into the mass spectrometer (ESI-MS). The spectrum was collected for 2 mins. MS (ESI-MS) *m/z* 452.2 [M+4]⁺, 602.2 [M+4+H+CF₃SO₃]⁺.

4.3.4.9.6 Sample preparations of the dihydroxylation of cyclohexene with [Fe(PyMe₂tacn)(CF₃SO₃)₂] **14, H₂¹⁶O and H₂¹⁶O₂ and observation of {[Fe^{III}(C₆H₁₀(O)(OH))(PyMe₂tacn)](CF₃SO₃)⁺,²⁷**



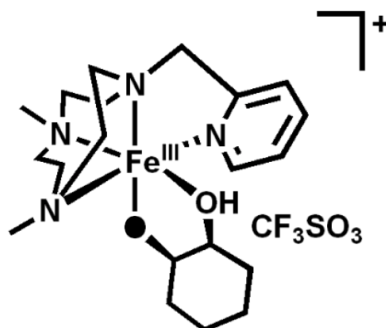
[Fe(PyMe₂tacn)(CF₃SO₃)₂] **14** (0.5 mg, 8 x 10⁻⁴ mmol) was dissolved in MeCN (~ 7 ml) and the solution cooled to 4 °C. A solution of H₂O₂ (10 mM on 10 ml MeCN) was made up and also cooled to 4 °C. The solution of **14** (300 μl) was added to a vial that was cooled in a dry ice/MeCN bath and H₂O (15 μl, 0.83 mmol) added. To this stirring solution H₂O₂ (300 μl, 3 x 10⁻³ mmol) and cyclohexene (10 μl, 0.10 mmol) were added and the solution injected directly into the mass spectrometer (ESI-MS). The spectrum was collected for 2 mins. MS (ESI-MS) *m/z* 418.2 [M]⁺, 568.2 [M+H+CF₃SO₃]⁺.

4.3.4.9.7 Sample preparations of the dihydroxylation of cyclohexene with [Fe(PyMe₂tacn)(CF₃SO₃)₂] **14, H₂¹⁸O and H₂¹⁶O₂ and observation of {[Fe^{III}(C₆H₁₀(O)(¹⁸OH))(PyMe₂tacn)](CF₃SO₃)⁺, **28**.**



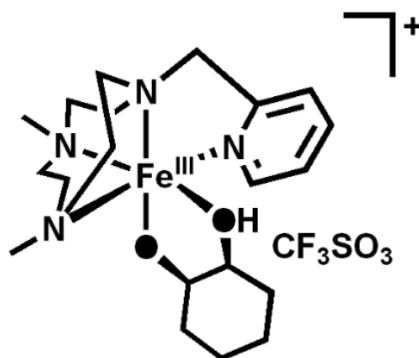
[Fe(PyMe₂tacn)(CF₃SO₃)₂] **14** (0.5 mg, 8 x 10⁻⁴ mmol) was dissolved in MeCN (~ 7 ml) and the solution cooled to 4 °C. A solution of H₂O₂ (10 mM on 10 ml MeCN) was made up and also cooled to 4 °C. The solution of **14** (300 μl) was added to a vial that was cooled in a dry ice/MeCN bath and H₂¹⁸O (15 μl, 0.83 mmol) added. To this stirring solution H₂O₂ (300 μl, 3 x 10⁻³ mmol) and cyclohexene (10 μl, 0.10 mmol) were added and the solution injected directly into the mass spectrometer (ESI-MS). The spectrum was collected for 2 mins. MS (ESI-MS) *m/z* 420.2 [M+2]⁺, 570.2 [M+2+H+CF₃SO₃]⁺.

4.3.4.9.8 Sample preparations of the dihydroxylation of cyclohexene with [Fe(PyMe₂tacn)(CF₃SO₃)₂] **14, H₂¹⁶O and H₂¹⁸O₂ and observation of {[Fe^{III}(C₆H₁₀(¹⁸O)(OH))(PyMe₂tacn)](CF₃SO₃)⁺, **29**.**



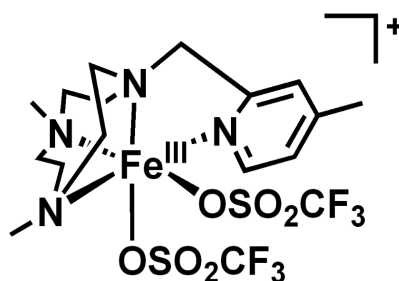
[Fe(PyMe₂tacn)(CF₃SO₃)₂] **14** (0.5 mg, 8 × 10⁻⁴ mmol) was dissolved in MeCN (~ 7 ml) and the solution cooled to 4 °C. A solution of H₂¹⁸O₂ (10 mM on 10 ml MeCN) was made up and also cooled to 4 °C. The solution of **14** (300 μl) was added to a vial that was cooled in a dry ice/MeCN bath and H₂O (15 μl, 0.83 mmol) added. To this stirring solution H₂¹⁸O₂ (300 μl, 3 × 10⁻³ mmol) and cyclohexene (10 μl, 0.10 mmol) were added and the solution injected directly into the mass spectrometer (ESI-MS). The spectrum was collected for 2 mins. MS (ESI-MS) *m/z* 420.2 [M+2]⁺, 570.2 [M+2+H+CF₃SO₃]⁺.

4.3.4.9.9 Sample preparations of the dihydroxylation of cyclohexene with [Fe(PyMe₂tacn)(CF₃SO₃)₂] **14, H₂¹⁸O and H₂¹⁸O₂ and observation of {[Fe^{III}(C₆H₁₀(¹⁸O)(¹⁸OH))(PyMe₂tacn)](CF₃SO₃)⁺, **30**.**



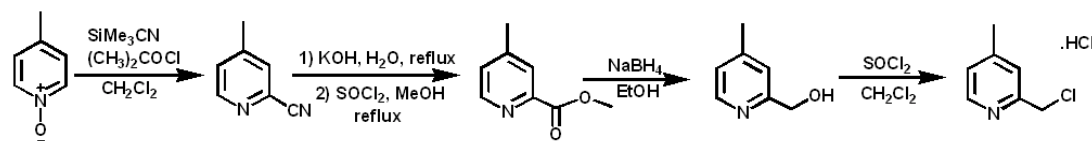
[Fe(PyMe₂tacn)(CF₃SO₃)₂] **14** (0.5 mg, 8 × 10⁻⁴ mmol) was dissolved in MeCN (~ 7 ml) and the solution cooled to 4 °C. A solution of H₂¹⁸O₂ (10 mM on 10 ml MeCN) was made up and also cooled to 4 °C. The solution of **14** (300 μl) was added to a vial that was cooled in a dry ice/MeCN bath and H₂¹⁸O (15 μl, 0.83 mmol) added. To this stirring solution H₂¹⁸O₂ (300 μl, 3 × 10⁻³ mmol) and cyclohexene (10 μl, 0.10 mmol) were added and the solution injected directly into the mass spectrometer (ESI-MS). The spectrum was collected for 2 mins. MS (ESI-MS) *m/z* 422.2 [M+4]⁺, 572.2 [M+4+H+CF₃SO₃]⁺.

4.3.4.10 Synthesis of $[\text{Fe}^{\text{II}}(\text{CF}_3\text{SO}_3)_2(4\text{Me-PyMe}_2\text{tacn})]$, 31



Ligand $[\text{Fe}^{\text{II}}(\text{CF}_3\text{SO}_3)_2(4\text{Me-PyMe}_2\text{tacn})]$ was synthesised by Costas *et al.*:

4.3.4.11 Synthesis of 2-chloromethyl-4-methylpyridine hydrochloride, 4Me-PyCH₂Cl



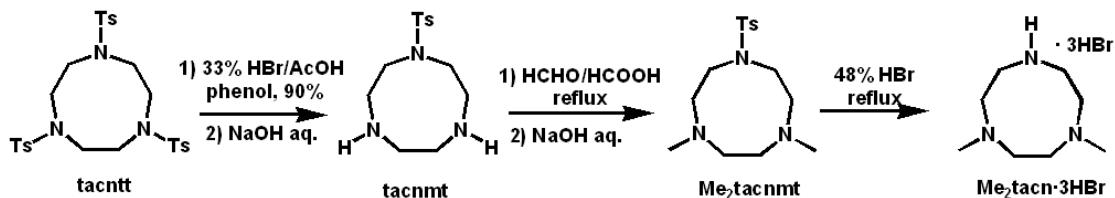
4-Methylpyridine-2-carbonitrile, 4Me-PyCN. 4-methylpyridine-*N*-oxide (7 g, 64 mmol) was placed in a round bottom flask, dissolved in dry dichloromethane (50 ml), and placed under a N₂ atmosphere. Trimethylsilyl cyanide (10.26 ml, 7.7 g, 77 mmol) was added dropwise. After 30 minutes, dimethyl carbamoyl chloride (7.1 ml, 8.22 g, 77 mmol) was added dropwise. The resulting mixture was stirred overnight. At this point, the reaction was quenched by addition of saturated aqueous NaHCO₃ (30 ml), and the organic fraction was extracted with dichloromethane (2 x 50 ml). The combined organic layers were washed with H₂O (50 ml), saturated aqueous NaHCO₃ (50 ml) and H₂SO₄ 1M (50 ml). The resulting organic fraction was dried over MgSO₄ and filtered and the solvent was removed under reduced pressure to yield the desired product as a white solid (6.7 g, 57 mmol, 89%). FT-IR (ATR) ν , cm⁻¹: 3505, 3049, 2233 (CN), 1598, 1506, 1408, 838. ¹H-NMR (CDCl₃, 200 MHz, 300K) δ , ppm: 8.58 (d, J = 5 Hz, 1H, py-H _{α}), 7.53 (m, 1H, py-H _{β}), 7.33 (m, 1H, py-H _{β}), 2.43 (s, CH₃, 3H).

4-Methyl-pyridine-2-carboxylic acid methyl ester, 4Me-PyCO₂Me. Potassium hydroxide (6.4 g, 114 mmol) was placed in a round bottom flask, and dissolved in water (60 ml). 4Me-PyCN (6.7 g, 57 mmol) was then suspended in this solution, and the mixture was refluxed during 1h, at which time a clear yellow-orange solution had formed. The solution was stirred at 40 °C for two days, and after cooling to room temperature, H₂SO₄ cc (6.1 ml) diluted in water (20 ml) was carefully added. The solution was then neutralized to pH 7 by careful addition of saturated aqueous NaHCO₃. The white solid that appeared was filtered off. The solvent from the filtrates was removed under reduced pressure and the resulting solid was extracted with AcOEt (2 x 50 ml) and absolute EtOH (2 x 50 ml). The filtrates were dried over MgSO₄ and filtered. The solvent was removed under vacuum to obtain 3.26 g of the carboxylic acid product as an oily solid that was used without further purification. The carboxylic acid was dissolved in dry methanol (50 ml), and SOCl₂ (4 ml) was added dropwise (caution, reaction is very exothermic). The resulting mixture was then refluxed during 16h. At this time, it was allowed to cool down to room temperature, and the solvent was removed under vacuum. The residue was treated with saturated aqueous NaHCO₃ (75 ml), and extracted with dichloromethane (3 x 50 ml). The organic phases were combined, dried over MgSO₄, filtered and the solvent was removed under reduced pressure to obtain the product as a pale yellow oil (2.05 g, 13.6 mmol, 24%). ¹H-NMR (CDCl₃, 200 MHz, 300K) δ, ppm: 8.59 (d, 1H, J = 4.8 Hz, py-H_α), 7.97 (s broad, 1H, py-H_β), 7.29 (d, J = 4.8 Hz, 1H, py-H_β), 4.01 (s, 3H, CO₂CH₃), 2.44 (s, 3H, pyCH₃).

4-methyl-2-picolylalcohol, 4Me-PyCH₂OH. 4Me-PyCO₂Me (2.05 g, 13.57 mmol) was placed in a round bottom flask and dissolved in dry methanol (50 ml). The mixture was placed under N₂, and NaBH₄ (3 g) was carefully added in small portions. The resulting mixture was stirred under N₂ at room temperature for 24h. After this time, a second portion of NaBH₄ (1 g) was slowly added in small portions and the mixture was stirred for further 12h at under N₂. 1 M HCl (10 ml) was added and the mixture was stirred for 30 min. The solvent was removed under reduced pressure and the resulting residue was treated with saturated aqueous NaHCO₃ (50 ml), and extracted with CH₂Cl₂ (3 x 50 ml). The combined organic layers were dried over MgSO₄, filtered and the solvent was removed under reduced pressure to obtain a pale yellow oil. (1.67 g, 13.56 mmol, 99%). ¹H-NMR (CDCl₃, 200 MHz, 300K) δ, ppm: 8.40 (d, J = 5.0 Hz, 1H, py-H_α), 7.04 (m, 2H, py-H_β), 4.72 (s, 2H, CH₂OH), 2.36 (s, 3H, CH₃).

2-Chloromethyl-4-methylpyridine hydrochloride, 4Me-PyCH₂Cl. 4Me-PyCH₂OH (1.67 g, 13.6 mmol) was placed in a round bottom flask and dissolved in dry CH₂Cl₂ (25 ml). SOCl₂ (4 ml) was added dropwise and the resulting mixture was stirred under N₂ overnight. After that time, methanol (10 ml) was added carefully and the resulting mixture was placed under a stream of N₂ until all solvent evaporated. The oily residue was then treated with diethyl ether (70 ml) which caused the formation of a solid. This compound was filtered and the desired product was obtained as a white-cream solid (1.98 g, 11.12 mmol, 82%). ¹H-NMR (D₂O, 200 MHz, 300K) δ, ppm: 8.63 (d, J = 5.8 Hz, 1H, py-H_α), 8.00 (s, 1H, py-H_β), 7.89 (d, J = 5.8 Hz, 1H, py-H_β), 5.00 (s, CH₂Cl, 2H), 2.71 (s, 3H, CH₃). ¹³C-NMR (D₂O, 50 MHz, 300K) δ, ppm: 162.34 (pyC_α-CH₂Cl), 149.29 (pyC_α-H), 140.68 (pyC_γ-CH₃), 127.69, 127.20 (pyC_β), 40.04 (py-CH₂Cl), 21.65 (py-CH₃).

4.3.4.12 Synthesis of 1-(*p*-toluenesulfonyl)-1,4,7-triazacyclononane, tacnmt

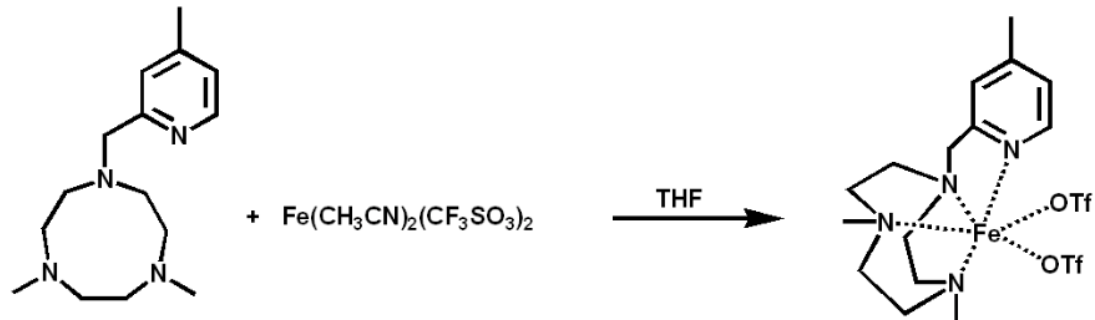


1-(*p*-toluenesulfonyl)-1,4,7-triazacyclononane, tacnmt. tacntt (24.6 g, 41.6 mmol) and phenol (35.2 g, 374 mmol) were mixed in a 500 ml flask. A solution of HBr in acetic acid (33%, 380 ml) was added with extreme care as an important evolution of HBr(g) takes place. The mixture was gently heated with stirring to 90°C which caused the complete dissolution of all the starting reagents giving rise to the formation of a dark solution. A colorless precipitate of 1-(*p*-toluenesulfonyl)-1,4,7-triazacyclononane·2HBr appeared within 2-4 h. After heating for 36 h, the mixture was cooled to room temperature and filtered. The solid was washed with diethyl ether (125 ml) and then dissolved in aqueous NaOH 1M (320 ml). The resultant pink aqueous mixture was then extracted with CH₂Cl₂ (3 x 190 ml) and the organic extracts dried with anhydrous MgSO₄, filtered and evaporated under reduced pressure. Drying the resultant oil under vacuum afforded 9.88 g of the pure product (34.9 mmol, 84 %). Anal. Calcd for C₁₃H₂₁O₂N₃S (MW = 283.39 g/mol): C, 55.10; H, 7.47; N, 14.83; S, 11.31 %. Found: C, 54.49; H, 7.41; N, 14.71; S, 11.38 %. FT-IR (ATR) ν, cm⁻¹: 3302 (N-H), 2914, 2855 (C-H)_{sp3}, 1328, 1152 (R-SO₂-N). ¹H-NMR (CDCl₃,

200 MHz, 300K) δ , ppm: 7.70 (d, $J = 8.2$ Hz, 2H, ArH), 7.34 (d, $J = 8.2$ Hz, 2H, ArH), 3.23 - 3.18 (m, 4H, TsN-CH₂-CH₂-NH), 3.12 - 3.09 (m, 4H, TsN-CH₂-CH₂-NH), 2.90 (s, 4H, HN-CH₂-CH₂-NH), 2.44 (s, 3H, Ar-CH₃), 1.85 (s, 2H, NH). ¹³C-NMR (CDCl₃, 50 MHz, 300K) δ , ppm: 143.16 (arC-CH₃), 135.60 (arC-SO₂), 129.59, 127.16 (arC-H), 53.91 (TsN-CH₂-C), 49.63, 49.46 (CH₂-NH-CH₂), 21.41 (Ar-CH₃). ESI-MS (m/z): 283.7 [M+H]⁺.

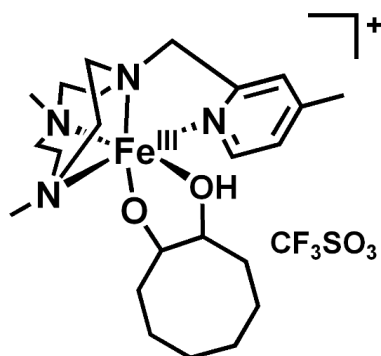
1,4-dimethyl-7-(*p*-toluenesulfonyl)-1,4,7-triazacyclononane, Me₂tacnmt. tacnmt (8.5 g, 30 mmol) was dissolved in 37 % formaldehyde (25 ml) and 98 % formic acid (25 ml) and the resulting orange solution was refluxed for 24 h. After cooling to room temperature, 10 ml HCl cc were added and the mixture was left stirring for 10 min. The solvent was removed under vacuum and a small amount of water (10 ml) was added to the resulting residue. The solution was brought to pH > 14 by addition of 4M NaOH. This caused the slow formation of a white precipitate corresponding to the desired product. After stirring for 20 h at room temperature, filtration of the mixture gave a white precipitate which was dissolved in CH₂Cl₂ (50 ml) giving a pale yellow solution which was treated with 4M NaOH (50 ml). The aqueous layer was further extracted with CH₂Cl₂ (2 x 50 ml). The combined organic layers were dried over anhydrous MgSO₄ and the solvent was removed under reduced pressure to yield 8.3 g of a crystalline white solid (27 mmol, 90 %). ¹H-NMR (CDCl₃, 200 MHz, 300K) δ , ppm: 7.67 (d, $J = 8.2$ Hz, 2H, ArH), 7.30 (d, $J = 8.2$ Hz, 2H, ArH), 3.27 - 3.23 (m, 4H, N-CH₂-CH₂), 2.92 - 2.88 (m, 4H, N-CH₂-CH₂), 2.69 (s, 4H, N-CH₂-CH₂), 2.42 (s, 3H, Ar-CH₃), 2.39 (s, 6H, N-CH₃).

1,4-dimethyl-1,4,7-triazacyclononane trihydrobromide, Me₂tacn-3HBr. Me₂tacnmt (8.6 g, 27 mmol) was dissolved in 48 % HBr (86 ml) and refluxed for 48 h. After cooling at room temperature, the solvent of the black crude mixture was removed under reduced pressure. Addition of acetone (100 ml) and stirring for 3 hours afforded a fine pale precipitate which was filtered off and washed with acetone. The resulting pale grey solid was dissolved with boiling water (75 ml) and filtered. The solvent from the yellow filtrates was removed under reduced pressure and the resulting residue was treated with absolute ethanol (100 ml). A fine pale yellow precipitate appeared which was filtered off and dried under vacuum to yield 5.3 g of the desired product (13 mmol, 49%). ¹H-NMR (D₂O, 200

4.3.4.14 Synthesis of [FePyTacn](CF₃SO₃)₂ 31

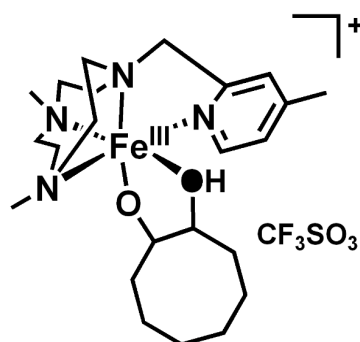
A solution of Fe(CH₃CN)₂(CF₃SO₃)₂ (90 mg, 0.21 mmol) in anhydrous THF (2 ml) is added dropwise to a vigorously stirred solution of 4Me-PyMe₂tacn (51 mg, 0.21 mmol) in THF (1.5 ml). After a few seconds the solution becomes cloudy and a pale yellow precipitate appears. After stirring for 1 hour the solution is filtered off and the resultant yellow solid dried under vacuum. This solid is dissolved in CH₂Cl₂ and filtered through Celite. Slow diethyl ether diffusion over the resultant solution affords, in a few days, 109 mg of yellow crystals (0.18 mmol, 86 %). Anal. Calcd for C₁₇H₂₆F₆FeN₄O₆S₂·1/4CH₃CN: C, 32.35; H, 4.07; N, 9.76; S, 10.47 %. Found: C, 32.49; H, 4.04; N, 9.66; S, 10.30 %. FT-IR (ATR) ν , cm⁻¹: 2862 (C-H)_{sp3}, 1285 (py), 1224, 1158, 1026, 634 (CF₃SO₃). ¹H-NMR (CD₃CN, 200 MHz, 300K) δ , ppm: 13.69, 10.32, 8.40, 6.25, 4.33, 1.97. ¹³C-NMR (CD₂Cl₂, 200 MHz, 300K) δ , ppm: 118.53, 92.45, 49.92, 36.52, 32.30, 17.73. ESI-MS (m/z):, 467.1 [M-OTf]⁺, 508.4 [M+CH₃CN-OTf]⁺.

4.3.4.15 Sample preparations of the dihydroxylation of cyclooctene with [Fe(4Me-PyMe₂tacn)(CF₃SO₃)₂] **14, H₂¹⁶O and H₂¹⁶O₂ and the observation of {[Fe^{III}(C₆H₁₀(O)(OH))(4Me-PyMe₂tacn)](CF₃SO₃)⁺, **32****



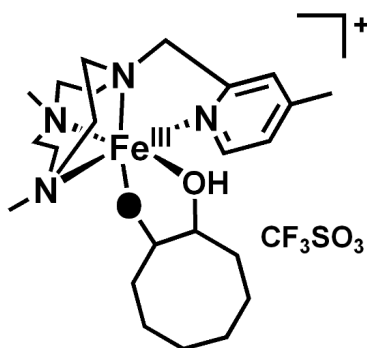
[Fe(4Me-PyMe₂tacn)(CF₃SO₃)₂] **31** (0.5 mg, 8 × 10⁻⁴ mmol) was dissolved in MeCN (~ 7 ml) and the solution cooled to 4 °C. A solution of H₂O₂ (10 mM on 10 ml MeCN) was made up and also cooled to 4 °C. The solution of **31** (300 μl) was added to a vial that was cooled in a dry ice/MeCN bath and H₂O (15 μl, 0.83 mmol) added. To this stirring solution H₂O₂ (300 μl, 3 × 10⁻³ mmol) and cyclooctene (10 μl, 0.08 mmol) were added and the solution injected directly into the mass spectrometer (ESI-MS). The spectrum was collected for 2 mins. MS (ESI-MS) *m/z* 460.2 [M]⁺, 610.2 [M+H+CF₃SO₃]⁺.

4.3.4.16 Sample preparations of the dihydroxylation of cyclooctene with [Fe(4Me-PyMe₂tacn)(CF₃SO₃)₂] **14, H₂¹⁸O and H₂¹⁶O₂ and the observation of {[Fe^{III}(C₆H₁₀(O)(¹⁸OH))(4Me-PyMe₂tacn)](CF₃SO₃)}⁺, **33****



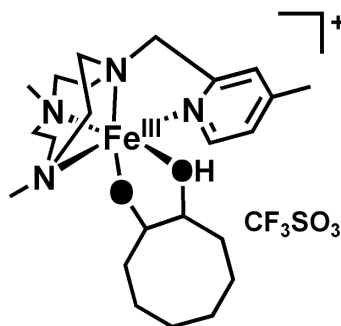
[Fe(4Me-PyMe₂tacn)(CF₃SO₃)₂] **31** (0.5 mg, 8 x 10⁻⁴ mmol) was dissolved in MeCN (~ 7 ml) and the solution cooled to 4 °C. A solution of H₂O₂ (10 mM on 10 ml MeCN) was made up and also cooled to 4 °C. The solution of **31** (300 μl) was added to a vial that was cooled in a dry ice/MeCN bath and H₂¹⁸O (15 μl, 0.83 mmol) added. To this stirring solution H₂O₂ (300 μl, 3 x 10⁻³ mmol) and cyclooctene (10 μl, 0.08 mmol) were added and the solution injected directly into the mass spectrometer (ESI-MS). The spectrum was collected for 2 mins. MS (ESI-MS) *m/z* 462.2 [M]⁺, 612.2 [M+H+CF₃SO₃]⁺.

4.3.4.17 Sample preparations of the dihydroxylation of cyclooctene with [Fe(4Me-PyMe₂tacn)(CF₃SO₃)₂] **14, H₂¹⁶O and H₂¹⁸O₂ and the observation of {[Fe^{III}(C₆H₁₀(¹⁸O)(OH))(4Me-PyMe₂tacn)](CF₃SO₃)⁺, **34****



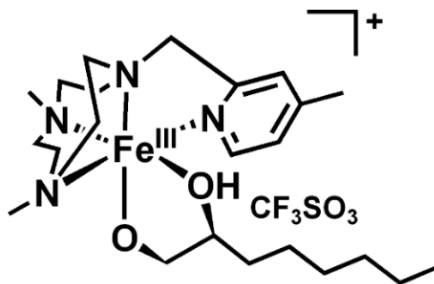
[Fe(4Me-PyMe₂tacn)(CF₃SO₃)₂] **31** (0.5 mg, 8 x 10⁻⁴ mmol) was dissolved in MeCN (~ 7 ml) and the solution cooled to 4 °C. A solution of H₂¹⁸O₂ (10 mM on 10 ml MeCN) was made up and also cooled to 4 °C. The solution of **31** (300 μl) was added to a vial that was cooled in a dry ice/MeCN bath and H₂O (15 μl, 0.83 mmol) added. To this stirring solution H₂¹⁸O₂ (300 μl, 3 x 10⁻³ mmol) and cyclooctene (10 μl, 0.08 mmol) were added and the solution injected directly into the mass spectrometer (ESI-MS). The spectrum was collected for 2 mins. MS (ESI-MS) *m/z* 462.2 [M]⁺, 612.2 [M+H+CF₃SO₃]⁺.

4.3.4.18 Sample preparations of the dihydroxylation of cyclooctene with [Fe(4Me-PyMe₂tacn)(CF₃SO₃)₂] **14, H₂¹⁸O and H₂¹⁸O₂ and the observation of {[Fe^{III}(C₆H₁₀(¹⁸O)(¹⁸OH))(4Me-PyMe₂tacn)](CF₃SO₃)⁺, **35****



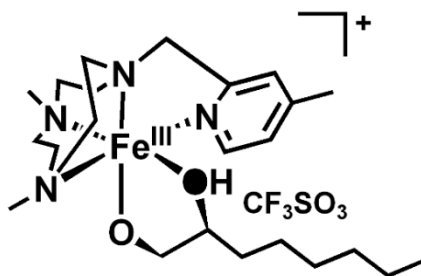
[Fe(4Me-PyMe₂tacn)(CF₃SO₃)₂] **31** (0.5 mg, 8 × 10⁻⁴ mmol) was dissolved in MeCN (~ 7 ml) and the solution cooled to 4 °C. A solution of H₂¹⁸O₂ (10 mM on 10 ml MeCN) was made up and also cooled to 4 °C. The solution of **31** (300 μl) was added to a vial that was cooled in a dry ice/MeCN bath and H₂¹⁸O (15 μl, 0.83 mmol) added. To this stirring solution H₂¹⁸O₂ (300 μl, 3 × 10⁻³ mmol) and cyclooctene (10 μl, 0.08 mmol) were added and the solution injected directly into the mass spectrometer (ESI-MS). The spectrum was collected for 2 mins. MS (ESI-MS) *m/z* 464.2 [M]⁺, 614.2 [M+H+CF₃SO₃]⁺.

4.3.4.19 Sample preparations of the dihydroxylation of 1-octene with [Fe(4Me-PyMe₂tacn)(CF₃SO₃)₂] **14, H₂¹⁶O and H₂¹⁶O₂ and the observation of {[Fe^{III}(C₈H₁₆(O)(OH))(4Me-PyMe₂tacn)](CF₃SO₃)⁺, **36****



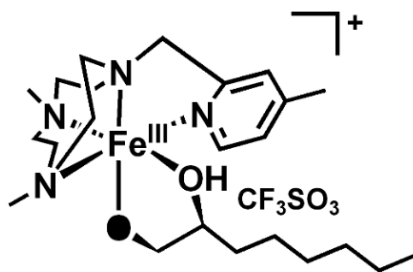
[Fe(4Me-PyMe₂tacn)(CF₃SO₃)₂] **31** (0.5 mg, 8 × 10⁻⁴ mmol) was dissolved in MeCN (~ 7 ml) and the solution cooled to 4 °C. A solution of H₂O₂ (10 mM on 10 ml MeCN) was made up and also cooled to 4 °C. The solution of **31** (300 μl) was added to a vial that was cooled in a dry ice/MeCN bath and H₂¹⁶O (15 μl, 0.83 mmol) added. To this stirring solution H₂¹⁶O₂ (300 μl, 3 × 10⁻³ mmol) and 1-octene (10 μl, 0.08 mmol) were added and the solution injected directly into the mass spectrometer (ESI-MS). The spectrum was collected for 2 mins. MS (ESI-MS) *m/z* 462.2 [M]⁺, 612.2 [M+H+CF₃SO₃]⁺.

4.3.4.20 Sample preparations of the dihydroxylation of 1-octene with [Fe(4Me-PyMe₂tacn)(CF₃SO₃)₂] **14, H₂¹⁸O and H₂¹⁶O₂ and the observation of {[Fe^{III}(C₈H₁₆(O)(¹⁸OH))(4Me-PyMe₂tacn)](CF₃SO₃)⁺, **37****



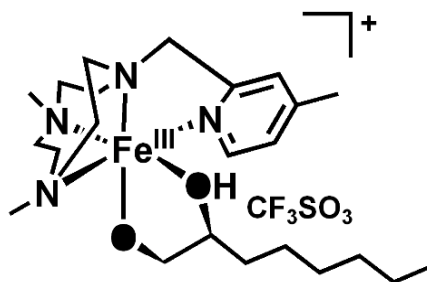
[Fe(4Me-PyMe₂tacn)(CF₃SO₃)₂] **31** (0.5 mg, 8 x 10⁻⁴ mmol) was dissolved in MeCN (~ 7 ml) and the solution cooled to 4 °C. A solution of H₂O₂ (10 mM on 10 ml MeCN) was made up and also cooled to 4 °C. The solution of **31** (300 μl) was added to a vial that was cooled in a dry ice/MeCN bath and H₂¹⁸O (15 μl, 0.83 mmol) added. To this stirring solution H₂¹⁶O₂ (300 μl, 3 x 10⁻³ mmol) and 1-octene (10 μl, 0.08 mmol) were added and the solution injected directly into the mass spectrometer (ESI-MS). The spectrum was collected for 2 mins. MS (ESI-MS) *m/z* 464.2 [M]⁺, 614.2 [M+H+CF₃SO₃]⁺.

4.3.4.21 Sample preparations of the dihydroxylation of 1-octene with [Fe(4Me-PyMe₂tacn)(CF₃SO₃)₂] **14, H₂¹⁶O and H₂¹⁸O₂ and the observation of {[Fe^{III}(C₈H₁₆(¹⁸O)(OH))(4Me-PyMe₂tacn)](CF₃SO₃)⁺, **38****



[Fe(4Me-PyMe₂tacn)(CF₃SO₃)₂] **31** (0.5 mg, 8 × 10⁻⁴ mmol) was dissolved in MeCN (~ 7 ml) and the solution cooled to 4 °C. A solution of H₂¹⁸O₂ (10 mM on 10 ml MeCN) was made up and also cooled to 4 °C. The solution of **31** (300 μl) was added to a vial that was cooled in a dry ice/MeCN bath and H₂¹⁶O (15 μl, 0.83 mmol) added. To this stirring solution H₂¹⁸O₂ (300 μl, 3 × 10⁻³ mmol) and cyclooctene (10 μl, 0.08 mmol) were added and the solution injected directly into the mass spectrometer (ESI-MS). The spectrum was collected for 2 mins. MS (ESI-MS) *m/z* 464.2 [M]⁺, 614.2 [M+H+CF₃SO₃]⁺.

4.3.4.22 Sample preparations of the dihydroxylation of 1-octene with [Fe(4Me-PyMe₂tacn)(CF₃SO₃)₂] **14, H₂¹⁸O and H₂¹⁸O₂ and the observation of {[Fe^{III}(C₈H₁₆(¹⁸O)(¹⁸OH))(4Me-PyMe₂tacn)](CF₃SO₃)⁺ **39****



[Fe(4Me-PyMe₂tacn)(CF₃SO₃)₂] **31** (0.5 mg, 8 × 10⁻⁴ mmol) was dissolved in MeCN (~ 7 ml) and the solution cooled to 4 °C. A solution of H₂¹⁸O₂ (10 mM on 10 ml MeCN) was made up and also cooled to 4 °C. The solution of **31** (300 μl) was added to a vial that was cooled in a dry ice/MeCN bath and H₂¹⁸O (15 μl, 0.83 mmol) added. To this stirring solution H₂¹⁸O₂ (300 μl, 3 × 10⁻³ mmol) and 1-octene (10 μl, 0.08 mmol) were added and the solution injected directly into the mass spectrometer (ESI-MS). The spectrum was collected for 2 mins. MS (ESI-MS) *m/z* 466.2 [M]⁺, 616.2 [M+H+CF₃SO₃]⁺.

5 VALIDATING ANION BINDING USING ELECTROSPRAY MASS SPECTROMETRY

The quantitative analysis of anion binders has been studied in great detail using NMR techniques such as the continuous method of variation (Job plot) and NMR titration experiments.^{48,49,125-127} Mass spectrometry has been used in this field to give qualitative analysis of the species present in solution^{128,129} but never before has been used to give both quantitative and qualitative results. This research will show Job plots using both NMR and MS techniques and will compare them to show that mass spectrometry can be used as a tool in the quantitative and qualitative analysis of coordination compounds.

The Job plot method was named after P. Job, who first introduced the methodology in 1928.¹³⁰ A Job plot (also known as the Method of Continuous Variation) is used to determine the stoichiometry of a binding event of two species in solution. The total molar concentration of the two binding partners is held constant but their mole fraction is varied (where the mole fraction is the $[Host]/([Host]+[Guest])$) and plotted against an observed parameter such as the peak shift in ¹H NMR or an absorption signal. The maximum (or minimum) on the plot then corresponds to the stoichiometry of the two species.

In the past, mass spectroscopy was used as a tool to provide qualitative analysis of a complex or molecule but has not been utilised as a tool for providing Job plots (Job plots were mostly obtained from NMR techniques). By transferring the skills used to perform Job plots in the NMR to the MS it was found that the change in intensity of the coordination species of relevance could be used to give the same Job plot as found in NMR and so from this data quantitative and qualitative data could be acquired.

For an anion binder to be successful the design of a receptor, that is, the geometrical arrangement of the binding sites and the structural flexibility of the backbone have great importance. The design of the receptor must take into account the shape of the anion that will be coordinated but also have enough flexibility to adapt if needed to.

A number of ligands such as urea and amides have been used for anion binding. The first amide based anion binder synthesised was by Pascal *et al* where a fluoride anion was bound to (1,3,5)-cyclophane containing three amide moieties.¹³¹ Such anion binders work by utilising amide functions where the NH group allows hydrogen bonding to a electronegative anion due to its electron deficient state. Amide containing receptors have a wide diversity over other types of anion binders. They can utilise either solely hydrogen-bonding or a combination of both hydrogen-bonding and electrostatic interactions. The amide moieties can also be pre-organised to act cooperatively within convergent architectures.¹³²

The receptor that was examined in this work was the ligand *cis,cis*-1,3,5-tris-acetylamino-cyclohexane **40**. As the aim of the research was to evaluate the use of mass spectrometry as a quantitative analytical tool the ligand was designed to be simple and also able to bind spherical anions such as chloride, bromide and iodide. The receptor **40** was synthesised from a ligand that has been extensively studied, *cis,cis*-triaminocyclohexane (*cis*-tach) **2**,^{26,133,134} and acetic anhydride (see Figure 82).

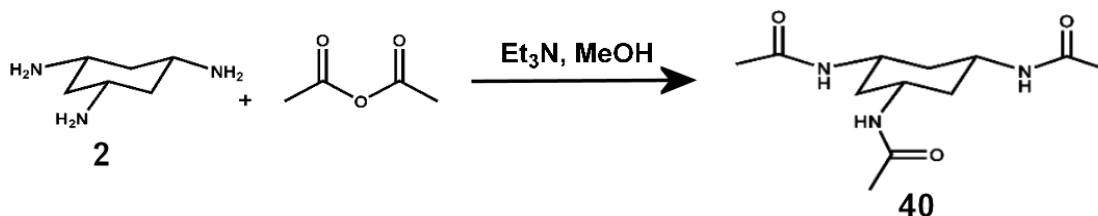


Figure 82. Synthesis of simple tripodal *cis*-tach anion receptor *cis,cis*-1,3,5-tris-acetylamino-cyclohexane **40**.

Ligand **40** contains three amide moieties allowing for anion binding through hydrogen bonding. The cyclohexane backbone is in the chair conformation with the three amide functionalities in the sterically favoured equatorial positions. As no crystal structure was obtained the binding motif in Figure 83 was proposed. It is also thought that the receptor is in the trisequatorial configuration due to steric effects, as in the tris-axial state the large amide groups would repel each other.

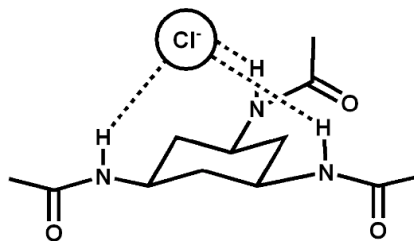


Figure 83. Proposed structure of *cis,cis*-1,3,5-tris-acetylamino-cyclohexane **40 when reacted with a chloride anion.**

Firstly, NMR experiments were carried out at 30 °C to obtain the correct stoichiometry of the coordination complex in solution by obtaining a Job plot. This was carried out by making up equimolar solutions (0.02 M) for both the receptor **40** and the anion, potassium salts in this instance, in d^6 -DMSO. Aliquots of each solution were taken and mixed together in differing ratios using a method where the final concentrations of each solution are the same.¹²⁷ ^1H NMR was then used to show the shift in ppm when different stoichiometries of the receptor to anion were present in solution.

Using ^1H NMR techniques, the complexation of the receptor **40** to the Cl^- anion was studied. It was observed that the NH chemical shifts of the receptor shifted upfield in the presence of the anionic guest, indicating that complexation had occurred (see Figure 84).

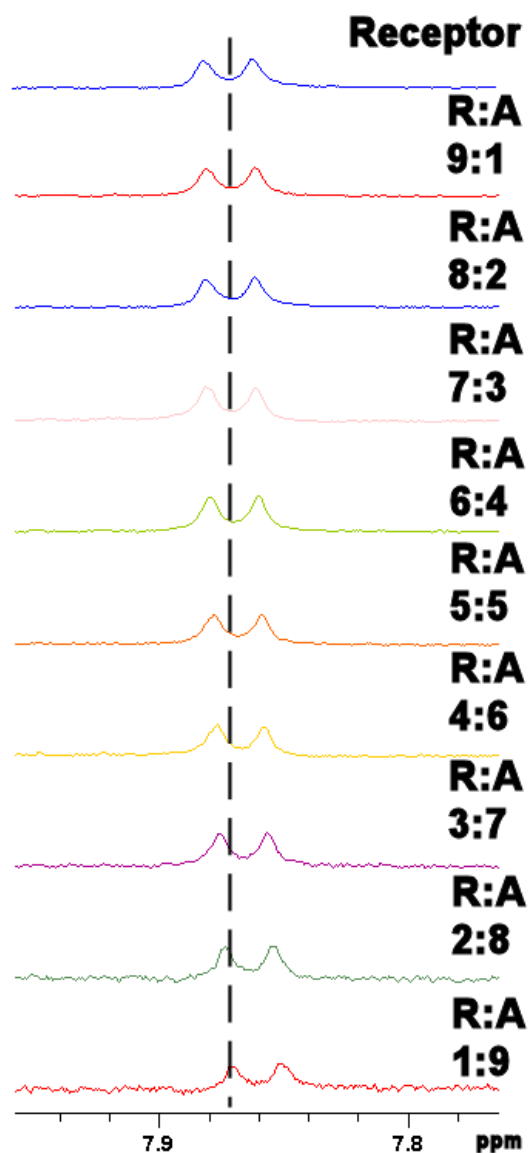
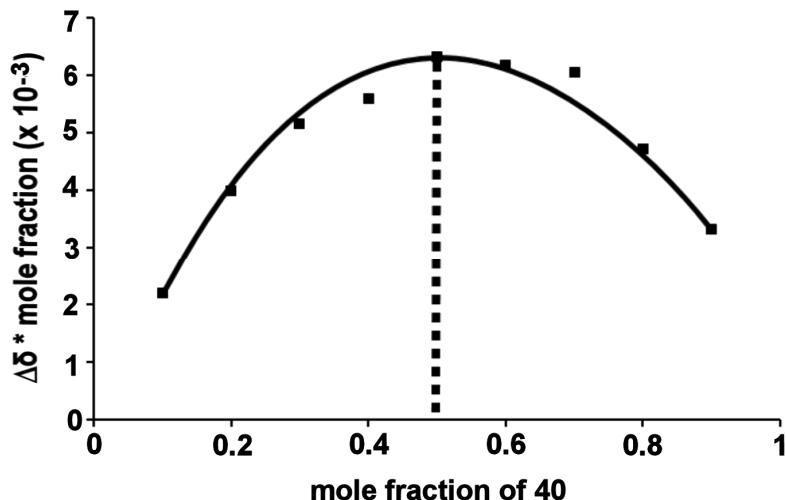


Figure 84. ^1H NMR (d^6 -DMSO) showing the shift of the amide NH when hydrogen bonding to chloride occurs (R is receptor 40, A is chloride).

The Job plot was then produced by plotting the signal of the N-H peaks of the receptor multiplied by the mole fraction (where the mole fraction is the $[\text{receptor}]/([\text{receptor}]+[\text{anion}])$) against the mole fraction (see Figure 85). The highest plot on the graph represented the mole fraction 0.5 which corresponded to a stoichiometry of 1:1 (40:Cl⁻)



Mole fraction	Shift/ppm	$\Delta\delta$	$\Delta\delta$ * mole fraction
receptor	7.89785	-	
0.1	7.87590	0.02195	0.002195
0.2	7.87790	0.01995	0.003990
0.3	7.88065	0.01720	0.00516
0.4	7.88385	0.01400	0.005600
0.5	7.88520	0.01265	0.006325
0.6	7.88755	0.01030	0.006180
0.7	7.88920	0.00865	0.006055
0.8	7.89195	0.00590	0.004720
0.9	7.89415	0.00370	0.003330

Figure 85. ^1H NMR (d^6 -DMSO) job plot of R + Cl showing a 1:1 (40:Cl⁻) stoichiometry and tabulated NMR data of 40 + KCl showing the actual shift (ppm) of the NH peak, $\Delta\delta$ (where $\Delta\delta$ = the shift of the receptor - (shift of the receptor + guest)) and $\Delta\delta$ * mole fraction.

The receptor **40** was reacted with three different potassium salts, potassium chloride, potassium bromide and potassium iodide. 18-crown-6 was also added to each solution to remove any unwanted cations from the starting material that could also bind with the receptor. From the Job plot it can be seen that the highest peak comes at a mole fraction of 0.5, this corresponds to a R:A stoichiometry of 1:1.

The ^1H NMR and MS studies were undertaken in two different solvents. Due to proton exchange in ^1H NMR experiments d^6 -DMSO had to be used to observe the amide shift, whilst methanol was used in the mass spectrometry studies. DMSO could not be used in the mass spectrometer as it has a high viscosity and interacts with the tubing in the instrument. d^6 -DMSO was the NMR solvent of choice, even though it is a polar aprotic solvent and therefore a good hydrogen acceptor, due to its ability to solvate both the neutral receptor and the negatively charged anion. The hydrogen bonding ability of the d^6 -DMSO was comparable for all the experiments carried out and so was used in these experiments. Methanol was used to solvate the receptor and anion in the mass spectrometry experiments as the solvent will be evaporated prior to entering the capillary and so would not interfere with the results.

Previously mass spectrometry has been used as a quantitative tool e.g. in pharmacokinetics but an internal standard has to be included. From this work it was found that mass spectrometric techniques can be used quantitatively to analyse solutions by varying the molar ratio and found that the intensity for the species $[\text{C}_6\text{H}_{12}\text{N}_3(\text{C}_2\text{H}_3\text{O})_3\text{Cl}]^-$ at 290.1 m/z would change in correspondence to the changing concentrations of R:A.

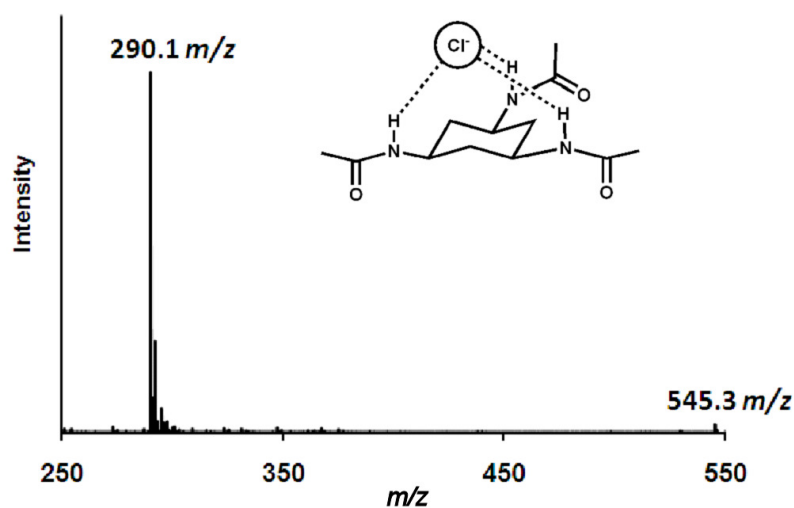
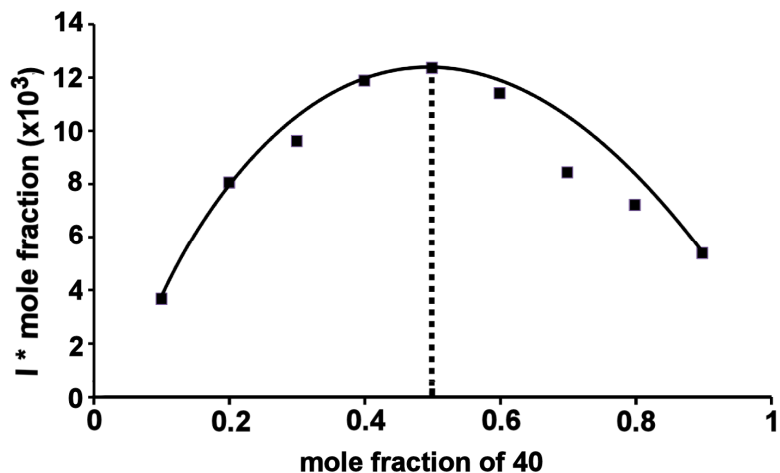


Figure 86. Mass spectrum at $30\text{ }^\circ\text{C}$ of the receptor **40** reacted with KCl giving the species $[\text{C}_6\text{H}_{12}\text{N}_3(\text{C}_2\text{H}_3\text{O})_3\text{Cl}]^-$ (290.1 m/z) and $[(\text{C}_6\text{H}_{12}\text{N}_3(\text{C}_2\text{H}_3\text{O})_3)_2\text{Cl}]^-$ (545.3 m/z).

It can be seen from Figure 86 that two species correlating to the receptor anion coordination species exists, one being $[\text{C}_6\text{H}_{12}\text{N}_3(\text{C}_2\text{H}_3\text{O})_3\text{Cl}]^-$ (290.1 m/z) and the other

$[(\text{C}_6\text{H}_{12}\text{N}_3(\text{C}_2\text{H}_3\text{O})_3)_2\text{Cl}]^-$ (545.3 m/z) but from quantitative studies using Job plots it was observed that the true stoichiometry of the solution is that of 1:1 (**40**:Cl⁻) (see Figure 86).

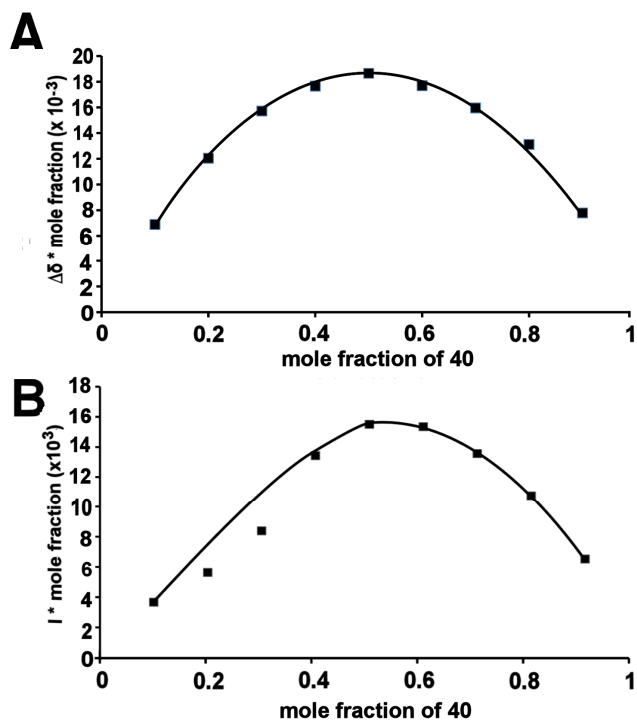
This change in intensity was multiplied by the mole fraction, as with the NMR studies, and this value plotted against the mole fraction of **40** to give a Job plot analogous to that produced for the NMR studies. From the Job plot (see Figure 87) a stoichiometry of 1:1 was observed for **40**:Cl⁻.



Mole fraction	Intensity	I * mole fraction
0.1	36721	3672
0.2	40305	8061
0.3	32062	9619
0.4	29719	11888
0.5	24742	12371
0.6	19025	11415
0.7	12064	8445
0.8	9020	7216
0.9	5983	5385

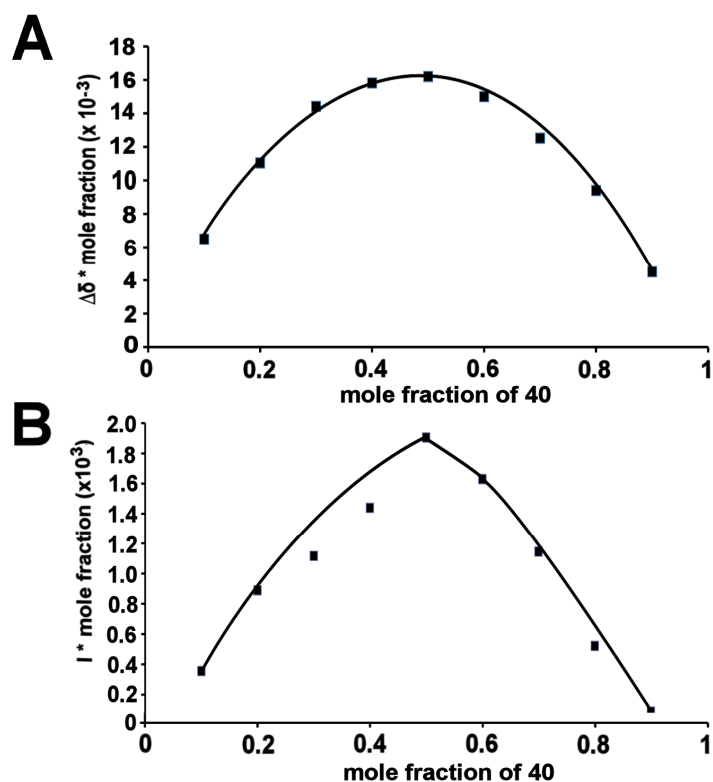
Figure 87. MS (CH₃OH) job plot of R + Cl showing a 1:1 (40:Cl⁻) stoichiometry and tabulated MS data of 40 + KCl showing the intensity of the [C₆H₁₂N₃(C₂H₃O)₃Cl]⁻ (290.1 *m/z*) peak and intensity * mole fraction

Further analysis using KBr and KI as the anion source also showed a correlation between NMR and MS with both giving a stoichiometry of 1:1 (R:A) respectively (see Figure 88 and Figure 89).



Mole fraction	Shift/ppm	$\Delta\delta$	$\Delta\delta^*$ mole fraction	Intensity	I * mole fraction
receptor	7.89665	-	-	-	-
0.1	7.82770	0.06895	0.006895	36699	3670
0.2	7.83640	0.06025	0.012050	28179	5636
0.3	7.84425	0.05240	0.015720	27950	8385
0.4	7.85250	0.04415	0.017660	33559	13424
0.5	7.85935	0.03730	0.018650	31006	15503
0.6	7.86715	0.02950	0.017700	25583	15350
0.7	7.87385	0.02280	0.015960	19380	13566
0.8	7.88025	0.01640	0.013120	13445	10756
0.9	7.88800	0.00865	0.007850	7242	6518

Figure 88. A. ^1H NMR (d^6 -DMSO) job plot of R + Br showing a 1:1 (40:Br $^-$) stoichiometry; B. MS (methanol) job plot of R + Br showing a 1:1 (40:Br $^-$) stoichiometry; tabulated data from NMR and MS experiments.



Mole fraction	Shift/ppm	$\Delta\delta$	$\Delta\delta^*$ mole fraction	Intensity	I^* mole fraction
receptor	7.88545	-	-	-	-
0.1	7.82055	0.06490	0.006490	3557	356
0.2	7.83020	0.05525	0.011050	4446	890
0.3	7.83740	0.04805	0.014415	3723	1117
0.4	7.84590	0.03955	0.015820	3599	1440
0.5	7.85305	0.03240	0.016200	3810	1905
0.6	7.86045	0.02500	0.015000	2717	1630
0.7	7.86755	0.01790	0.012530	1636	1145
0.8	7.87370	0.01175	0.009400	652	522
0.9	7.88045	0.00500	0.004500	98	88

Figure 89. A. ^1H NMR (d^6 -DMSO) job plot of L + I showing a 1:1 (40:I) stoichiometry; B. MS (methanol) job plot of L + I showing a 1:1 (40:I) stoichiometry; tabulated data from NMR and MS experiments.

High temperature studies (80 °C) were also carried out to examine the effect on the binding stoichiometries i.e. did the increasing temperature cause the receptor to change conformation and hence stoichiometry. The ^1H NMR studies showed an erratic shift in the amide NH peak and it can therefore be concluded that increasing the temperature of the complex causes the hydrogen bonds to break and so the complex falls apart. An experiment with the ligand and KCl using CD_3OH as the NMR solvent was also carried out. This gave a job plot where the highest mole fraction reading corresponds to a 1:1 (40:Cl) stoichiometry therefore supporting the claims made above.

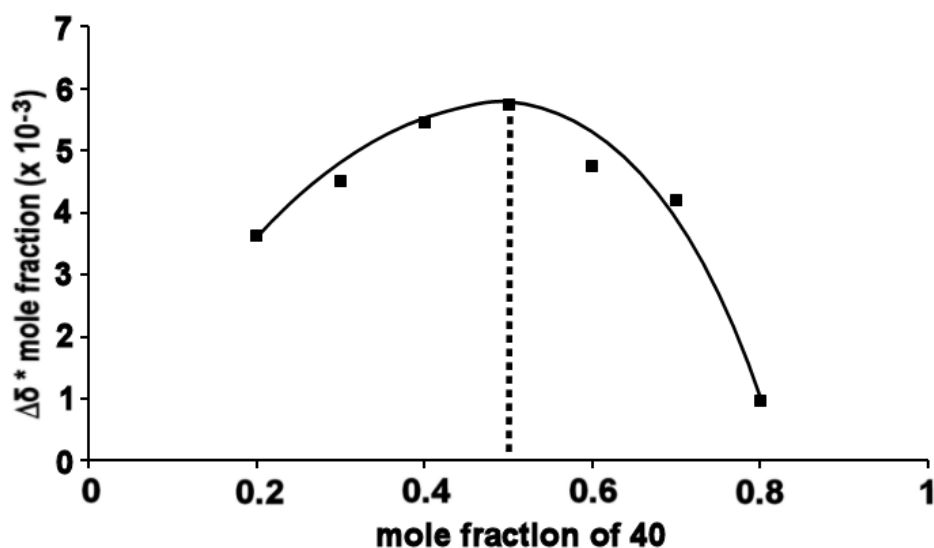


Figure 90. ^1H NMR ($\text{d}^3\text{-CD}_3\text{OH}$) job plot of R + KCl showing a 1:1 (40:Cl) stoichiometry

A NOESY NMR was carried out to confirm **40** had been synthesised. From Figure 91 it can be seen that the amide NH_e is correlated to H_d therefore providing evidence that the amide is bonded to the cyclohexane backbone. The NMR also showed no correlation between the receptor signals and the signals of attributed to 18-crown-6 providing evidence that 18-crown-6 plays no part in the complexation of an anion to the receptor.

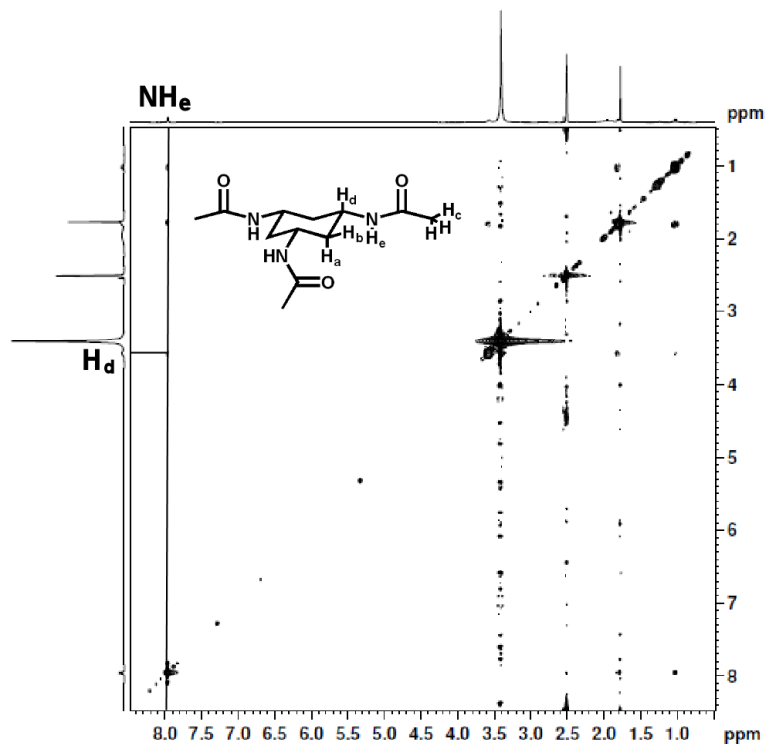


Figure 91. NOESY NMR (d^6 -DMSO) of 40 reacted with KCl.

This research has shown that mass spectrometry can be used as both a qualitative and quantitative analytical tool. It can be used to show binding stoichiometries through not just observation of a species, but also through quantitative means. This new technique may allow for the further development of mass spectrometry as a quantitative analytical tool as the need for expensive solvents like those used in 1H NMR studies are not needed with the observed data being more unambiguous than with 1H NMR.

5.1 Conclusions

ESI-MS has predominately been used as a qualitative tool in the analysis of chemical compounds and molecules. It has, however, not been used as a quantitative tool, with such analysis being carried out using ^1H NMR techniques. The aim of this research was to push the boundaries of mass spectrometry to show that the ESI-MS technique can be used as both a qualitative and quantitative analysis tool.

Standard Job plots were obtained to give the anion to receptor stoichiometry when the anion receptor **40** was reacted with potassium chloride, potassium bromide and potassium iodide. For the ^1H NMR measurements nine solutions of differing mole fraction ratios of ligand to receptor in d^6 -DMSO were measured and plotted against the shift of the host+ guest NH peak compared to that of the free ligand multiplied by the mole fraction. The highest point at 0.5 mole fraction gave a stoichiometry of 1:1 (R:A). The same experiment was carried out using ESI-MS in methanol to give a Job plot comparable to that produced using the conventional ^1H NMR methods and also giving a stoichiometry of 1:1 (R:A) (see Figure 92).

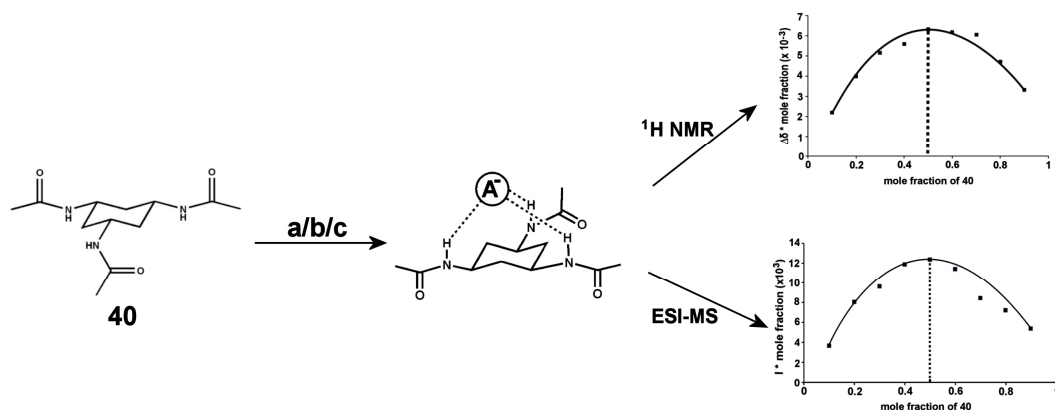
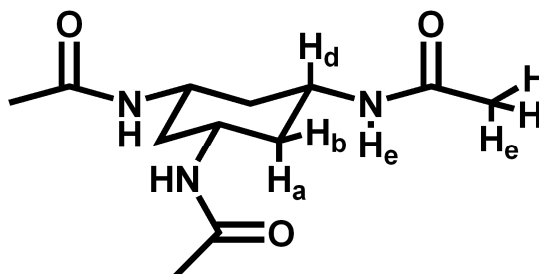


Figure 92. Overview of the Job plot data for the validation of anion binding using both ^1H NMR and ESI-MS where $a= \text{KCl}$, $b= \text{KBr}$ and $c= \text{KI}$. (Note that the Job plots are from the data produced using KCl).

The next step will be to validate this work by carrying out the same experimental procedure on a system that will change its receptor to anion stoichiometry when the solvent/anion is changed and provide evidence for this using ^1H NMR and ESI-MS.

5.2 Experimental

5.2.1 Synthesis of cis,cis-1,3,5-tris-acetylamino-cyclohexane, **40**



Cis-tach (100 mg, 0.77 mmol) was dissolved in MeOH (20ml) and to this triethylamine (545 mg, 5.39 mmol) was added. Acetic anhydride (236 mg, 2.31 mmol) was then added and the reaction refluxed for 24 hrs. The resulting solution was then vacuumed down to give a white precipitate. The excess triethylamine was then removed by redissolving the precipitate in water and then vacuuming to dryness. ^1H NMR (d^6 -DMSO): δ/ppm 1.02 (ddd, 3H, J 11.6, 11.7, 11.4 Hz, H_a), 1.78 (s, 9H, CH_3), 1.93 (ddd, 3H, H_b), 3.58 (ddd, 3H, H_d), 7.92 (d, NH, J 7.1 Hz); ^{13}C NMR (D_2O): δ/ppm 23.2 (CH_3), 36.3 (CH_2), 45.3 (CH), 181.5 (C=O); 1 $[\text{M}-\text{H}]^-$. IR (Golden Gate) ν/cm^{-1} 3410(w) (N-H stretch), 3279(m) (N-H stretch), 3063(w), 2939(w) (C-H stretch), 2854(w) (C-H stretch), 1635(m) (C=O), 1597(m), 1543(s) (C-H bend), 1373(s) ($-\text{CH}_3$), 1296(m), 1172(w), 1134(w), 1064(w), 1018(w), 972(w), 925(w), 802(w), 709(s), 671(s), 640(s). MS (ESI-MS) m/z 254.

5.2.2 Job plot analysis in ESI-MS

Standard solutions (0.02 M) of **40** and the salt (KCl/KBr/KI) were made up in methanol and 18-crown-6 (2 g, 7.56 mmol) dissolved in each solution. Varying ratios of each solution were then taken and mixed together (with the overall concentration remaining the same) e.g. 1 ml of **40** solution mixed with 9 ml of the salt solution, 2 ml of **40** solution mixed with 8 ml of the salt solution, 3ml of **40** solution mixed with 7 ml of the salt solution....9ml of **40** solution mixed with 1 ml of the salt solution. ESI-MS of the

reaction mixtures were then observed and the intensity of the corresponding peak recorded. The recorded change in intensity * mole fraction ($[Host]/[Host]+[Guest]$) was then plotted against mole fraction to give a maximum value at 0.5 mole fraction and therefore a stoichiometry of 1:1 (**36**:A). ESI-MS (-ve) **36**:Cl 290.1 m/z , **36**:Br 334.1 m/z , **36**:I 382.1 m/z .

5.2.3 Job plot analysis in 1H NMR

Standard solutions (0.02 M) of **40** and the salt (KCl/KBr/KI) were made up in d^6 -DMSO. Varying ratios of each solution were then taken and mixed together (with the overall concentration remaining the same) e.g. 1 ml of **40** solution mixed with 9 ml of the salt solution, 2 ml of **40** solution mixed with 2 ml of the salt solution, 3ml of **40** solution mixed with 7 ml of the salt solution....9ml of **40** solution mixed with 1 ml of the salt solution. 1H NMR experiments were carried out for each of the mixtures and the free receptor. A plot of $\Delta\delta$ * mole fraction was then plotted against mole fraction.

6 MASS SPECTROMETRIC STUDIES OF INORGANIC COMPLEXES

6.1 Mass spectrometric studies of chiral cyanide-bridged $\{\text{Ni}_6\text{Fe}_4\}$ cages

The study of polynuclear transition metal clusters is an area of great interest due to such complexes displaying properties, such as catalysis, which can be applied to modern technological challenges. The physical properties of such complexes are controlled by the metal ions present and the way in which they interact with the ligands linking them. One way to control such a complex is to utilise a ligand system that provides both rigidity, to minimise structural variability, and multidenticity to allow the coordination of multiple metal ions.

Mass spectrometric studies of chiral cyanide-bridged $\{\text{Ni}_6\text{Fe}_4\}$ cages were carried out to observe what effect the tetraethylammonium ion has on the formation of the complex. The chiral $\{\text{Ni}_6\text{Fe}_4\}$ decanuclear complex $(\text{Et}_4\text{N})[\text{Ni}(\text{L}^{\text{R}})_2]_6[\text{Fe}(\text{CN})_6]_4(\text{PF}_6)\cdot 22\text{H}_2\text{O}\cdot 26\text{CH}_3\text{OH}$ (where $\text{L}^{\text{R}} = \text{N}$ -(2-pyridylmethylene)-(R)-1-phenylethylamine) (**42**) was synthesised by Oshio *et al*¹⁷ from a chiral nickel precursor $[\text{Ni}(\text{L}^{\text{R}})_2\text{Cl}_2]$ (**41**) and a templating tetraethylammonium cation $(\text{Et}_4\text{N})_3[\text{Fe}(\text{CN})_6]$ in methanol. The polypyridyl ligand was used in the synthesis due to the three coordination sites available for binding and the structural rigidity that the ligand allows.

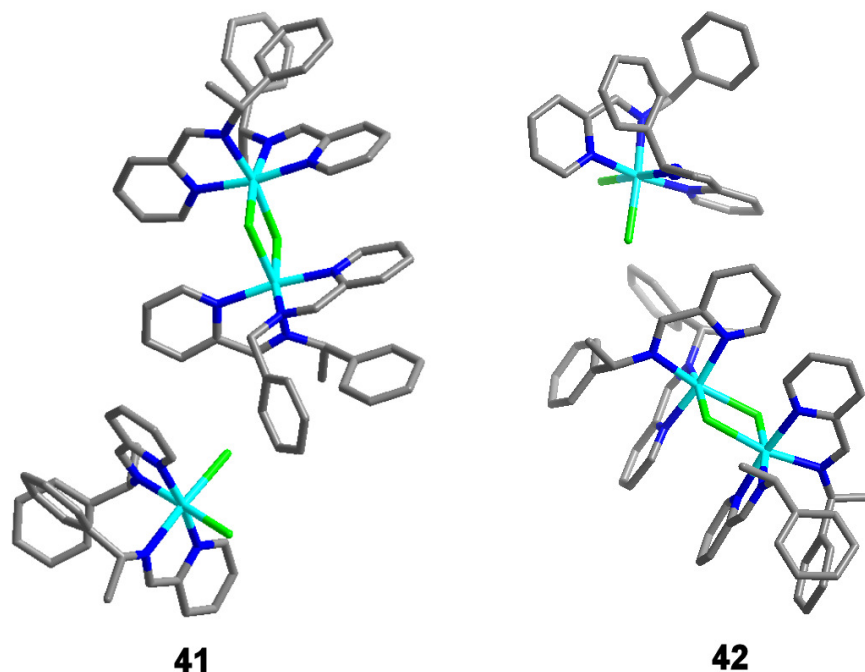


Figure 93. Structure of $[\text{Ni}_2\text{Cl}_2(\text{L}^{\text{R}})_4][\text{NiCl}_2(\text{L}^{\text{R}})_2]\text{Cl}_2 \cdot 3\text{MeOH}$ **41** and $[\text{Ni}_2\text{Cl}_2(\text{L}^{\text{S}})_4][\text{NiCl}_2(\text{L}^{\text{S}})_2]\text{Cl}_2 \cdot 3\text{MeOH}$ **42**¹⁷

Compound **41** is made up of a dinuclear and mononuclear unit and can be described as $[\text{Ni}_2\text{Cl}_2(\text{L}^{\text{R}})_4][\text{NiCl}_2(\text{L}^{\text{R}})_2]\text{Cl}_2 \cdot 3\text{MeOH}$. The nickel(II) metal centres in **41** are octahedral, with each being coordinated to four nitrogens from two bidentate L^{R} ligands and two chloride ions. π - π stacking interactions are present between the pyridyl and phenyl rings of the two chiral ligands and so gives the nickel ions a Λ -type coordination geometry. When L^{S} was used the homo-chiral complex **42** with a Δ -type configuration was obtained (see Figure 93).

Compound **43** was synthesised from the homochiral precursor **41** where $[\text{Ni}_2\text{Cl}_2(\text{L}^{\text{R}})_4][\text{NiCl}_2(\text{L}^{\text{R}})_2]\text{Cl}_2 \cdot 3\text{MeOH}$ was reacted with NH_4PF_6 and $(\text{Et}_4\text{N})_3[\text{Fe}(\text{CN})_6]$ to give brown hexagonal plates of $(\text{Et}_4\text{N})[\text{Ni}(\text{L}^{\text{R}})_2]_6[\text{Fe}(\text{CN})_6]_4(\text{PF}_6)_4 \cdot 22\text{H}_2\text{O}$ **43**. Four nitrogen atoms from two ligands and the nitrogen atoms from two cyano groups coordinate to the nickel ions to give an octahedral coordination sphere. The $[\text{Ni}(\text{L}^{\text{R}})_2]$ units are connected to the $[\text{Fe}(\text{CN})_6]^{3-}$ units through the nitrogen atoms of the CN ligands where each nickel centre is coordinated to two iron centres with each iron centre in turn being coordinated to three nickel centres. The six $[\text{Ni}(\text{L}^{\text{R}})_2]^{2+}$ and four $[\text{Fe}(\text{CN})_6]^{3-}$ units come together to form a

neutral decanuclear cyanide-bridged cage that is analogous to an adamantane-like structure.¹³⁵⁻¹³⁷ One tetraethylammonium cation can be found inside the cage and is thought to act as a template, with the counterion being one hexafluorophosphate ion. The π - π stacking of the $[\text{Ni}(\text{L}^{\text{R}})\text{Cl}_2]$ **41** ligands forces the six nickel ions to retain the Λ -type absolute configuration (see Figure 94).

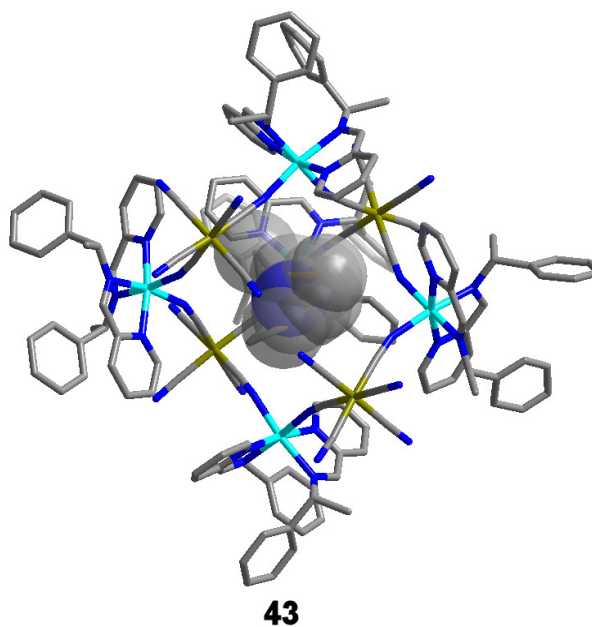
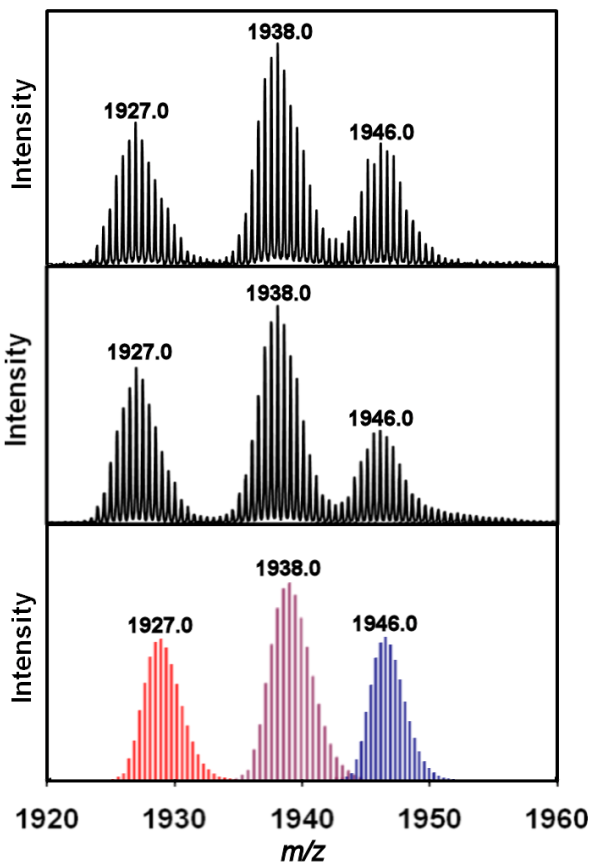


Figure 94. Structure of $(\text{Et}_4\text{N})[\text{Ni}(\text{L}^{\text{R}})_2]_6[\text{Fe}(\text{CN})_6]_4(\text{PF}_6)\cdot 22\text{H}_2\text{O}\cdot 26\text{CH}_3\text{OH}$ **43**

Compound **44** was synthesised from the homochiral precursor **42** to give a chiral cage complex analogous to **43** but with a Δ -type configuration.

Cryospray mass spectrometric studies were carried out to show if the tetraethylammonium cation acted as a template in the formation of the cage complex. From Figure 95 it can be seen that the dication $[(\text{Et}_4\text{N})\text{H}[\text{Ni}(\text{L}^{\text{S}})_2]_6[\text{Fe}(\text{CN})_6]_4]^{2+}$ was present in solution where the structural incarceration of the templating tetraethylammonium is observed. Other species observed were that of $[(\text{Et}_4\text{N})\text{Na}[\text{Ni}(\text{L}^{\text{S}})_2]_6[\text{Fe}(\text{CN})_6]_4]^{2+}$ and $[(\text{Et}_4\text{N})\text{K}[\text{Ni}(\text{L}^{\text{S}})_2]_6[\text{Fe}(\text{CN})_6]_4]^{2+}$ where it was thought that the potassium and sodium ions were sequestered from either the glassware used or slight contamination from previous samples. The CSI-MS measurement of complex **44** gave an identical spectrum to provide further evidence of the templating action of the tetraethylammonium cation.



<i>m/z</i>	Formula
1927.0	$[(\text{Et}_4\text{N})\text{H}[\text{Ni}(\text{L}^{\text{R/S}})_2]_6[\text{Fe}(\text{CN})_6]_4]^{2+}$
1938.0	$[(\text{Et}_4\text{N})\text{Na}[\text{Ni}(\text{L}^{\text{R/S}})_2]_6[\text{Fe}(\text{CN})_6]_4]^{2+}$
1946.0	$[(\text{Et}_4\text{N})\text{K}[\text{Ni}(\text{L}^{\text{R/S}})_2]_6[\text{Fe}(\text{CN})_6]_4]^{2+}$

Figure 95. CSI-MS of **42** (top) and **44** (middle) and the simulated spectrum (bottom)

CSI-MS measurements proved the existence of the chiral cage complexes **42** and **44** and the presence of the templating tetraethylammonium cation. Further work on this project is to use *in-situ* mass spectrometry to follow the formation of the cage complexes and show what effect changing the templating cation has on the structure formed.

6.2 Mass spectrometric studies of the self-assembly of heterometallic clusters

The heterometallic clusters $[\text{Fe}^{\text{III}}_2\text{Co}^{\text{II}}_5(\text{H}_2\text{L})_6\text{O}_6(\text{H}_2\text{O})_6](\text{BF}_4)_4$, **45**, and $[\text{Fe}^{\text{II}}_4\text{Fe}^{\text{III}}\text{Co}^{\text{II}}_4(\text{H}_2\text{L})_6(\text{OH})_{12}(\text{H}_2\text{O})_6](\text{BF}_4)_7$, **46**, (where $\text{H}_2\text{L} = 2,6\text{-bis}[5\text{-(2-pyridinyl)-1H-pyrazole-3-yl]pyridine}$) were synthesised by Oshio *et al.*¹³⁸ The helical complex **45** was obtained from the reaction of $\text{Fe}(\text{BF}_4)_2 \cdot 6\text{H}_2\text{O}$ and $\text{Co}(\text{BF}_4)_2 \cdot 6\text{H}_2\text{O}$ in a 1:8 ratio, with H_2L and triethylamine in a 2:1 mixture of MeOH/MeCN at room temperature. The grid complex **46** was obtained by the same procedure as used for synthesising **45** but a 1:1 Fe:Co ratio was used.

Complex $[\text{Fe}^{\text{III}}_2\text{Co}^{\text{II}}_5(\text{H}_2\text{L})_6\text{O}_6(\text{H}_2\text{O})_6](\text{BF}_4)_4$, **45**, has a helical structure and consists of six ligands which are coordinated to two iron(III) and five cobalt(II) ions. The core is made up of a pentanuclear structure in which three cobalt(II) centres in a planar triangular arrangement are capped by two $[\text{Fe}^{\text{III}}\text{O}_3(\text{OH})_2]^{3-}$ units, from which the oxo ligands act as μ_2 bridges between adjacent Co^{II} centres. The two iron centres have an octahedral geometry with the coordination sphere being completed by three oxide ions and three water molecules. The cobalt ions in the core are coordinated by two bidentate binding sites and two oxo ions giving an octahedral coordination geometry with the tridentate sites remaining uncoordinated. The two cobalt ions found at the edges of the complex are coordinated to three ligands through three bidentate binding sites forming an octahedral coordination sphere (see Figure 96).

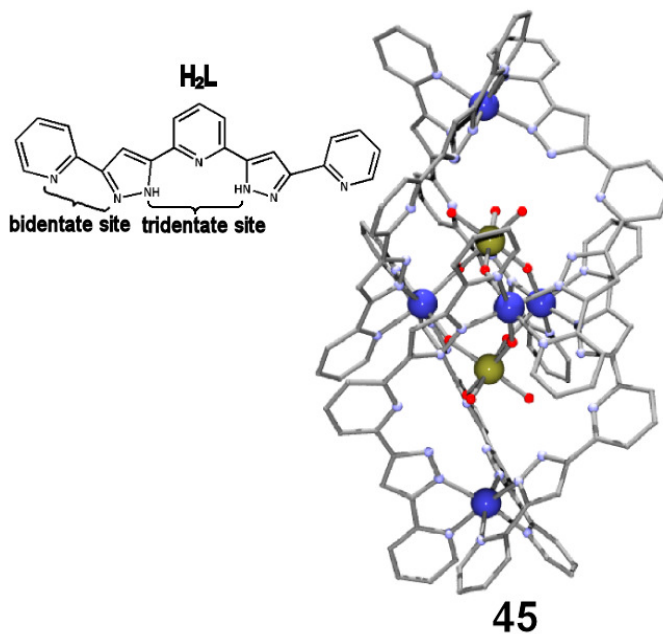
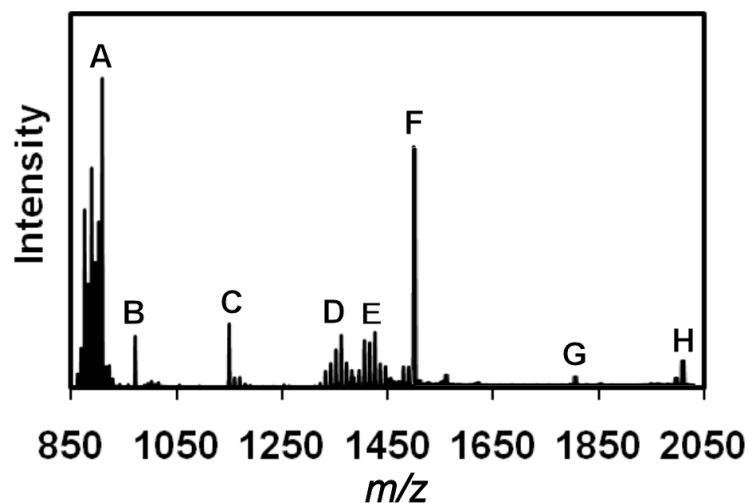


Figure 96. Crystal structure of **45** (complementary of the Oshio group) and the ligand H_2L showing the two bidentate and one tridentate binding sites.¹³⁸

The ESI-MS of **45** (see Figure 97) showed the crystals dissolved in a 2:1 methanol/acetonitrile solution formed a number of species in solution but all of which contain the $Fe_2Co_5(H_2L)_6$ core. These mass spectrometry results conclude that the helix structure is present and that the backbone of the complex remains intact in solution.



Label	m/z	Formula
A	908.5	$[\text{Fe}^{\text{III}}_2\text{Co}^{\text{II}}_5(\text{H}_2\text{L})_6\text{O}_6(\text{CH}_3\text{O})]^{3+}$
B	971.2	$[\text{Fe}^{\text{III}}_2\text{Co}^{\text{II}}_5(\text{H}_2\text{L})_6\text{O}_6(\text{H}_2\text{O})_2(\text{CH}_3\text{OH})_3(\text{BF}_4)]^{3+}$
C	1149.7	$[\text{Fe}^{\text{III}}_2\text{Co}^{\text{II}}_4(\text{H}_2\text{L})_4(\text{HL})\text{O}_4(\text{CH}_3\text{O})_2]^{2+}$
D	1382.2	$[\text{Fe}^{\text{III}}_2\text{Co}^{\text{II}}_5(\text{H}_2\text{L})_6\text{O}_6(\text{OH})_2(\text{H}_2\text{O})_2]^{2+}$
E	1426.3	$[\text{Fe}^{\text{III}}_2\text{Co}^{\text{II}}_5(\text{H}_2\text{L})_6\text{O}_6(\text{OH})(\text{H}_2\text{O})_3(\text{BF}_4)]^{3+}$
F	1500.3	$[\text{Fe}^{\text{III}}_2\text{Co}^{\text{II}}_5(\text{H}_2\text{L})_6\text{O}_6(\text{H}_2\text{O})_2(\text{CH}_3\text{OH})_3(\text{BF}_4)_2]^{2+}$
G	1817.5	$[(\text{Fe}^{\text{III}}_2\text{Co}^{\text{II}}_5(\text{H}_2\text{L})_6\text{O}_6(\text{BF}_4)_2)_3(\text{H}_2\text{O})_8(\text{CH}_3\text{OH})_4(\text{CH}_3\text{CN})_2(\text{BF}_4)]^{5+}$
H	2029.4	$[(\text{Fe}^{\text{III}}_2\text{Co}^{\text{II}}_5(\text{H}_2\text{L})_6\text{O}_6(\text{BF}_4)_2)_2(\text{H}_2\text{O})_4(\text{CH}_3\text{OH})_6(\text{BF}_4)]^{3+}$

Figure 97. ESI-MS assignments of a dissolved crystal of **45**.

Complex $[\text{Fe}^{\text{II}}_4\text{Fe}^{\text{III}}\text{Co}^{\text{II}}_4(\text{H}_2\text{L})_6(\text{OH})_{12}(\text{H}_2\text{O})_6](\text{BF}_4)_7$, **46**, was synthesised from the same synthetic procedure used for the synthesis of $[\text{Fe}^{\text{III}}_2\text{Co}^{\text{II}}_5(\text{H}_2\text{L})_6\text{O}_6(\text{H}_2\text{O})_6](\text{BF}_4)_4$, **45**, but a 1:1 Fe:Co ratio was used. The complex has a grid-type structure and is composed of six ligands that are coordinated together by five iron(III) and four cobalt(II) ions. The central iron(III) ion has octahedral coordination geometry consisting of four bridging hydroxo ligands and two water molecules with the four iron(III) centres found at the corners of the grid displaying distorted octahedral geometry to two bidentate ligand sets and two hydroxide ions completing the coordination sphere. The four edge cobalt(II) centres also have octahedral coordination geometries where they are coordinated to one bidentate ligand site, three μ_2 -hydroxyl groups and one water molecule (see Figure 98).

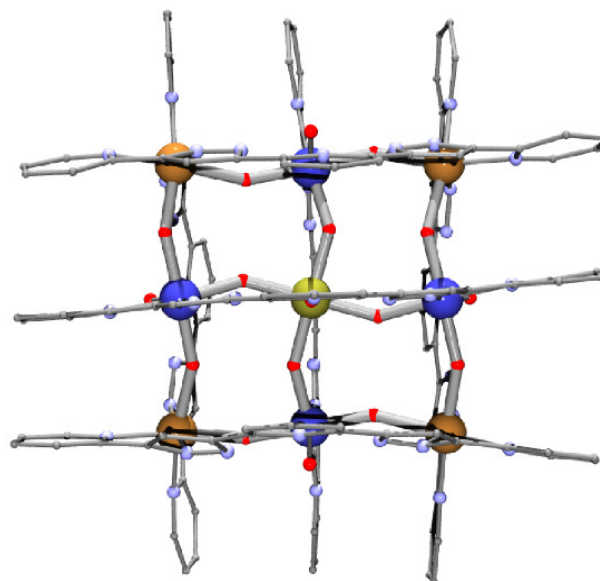
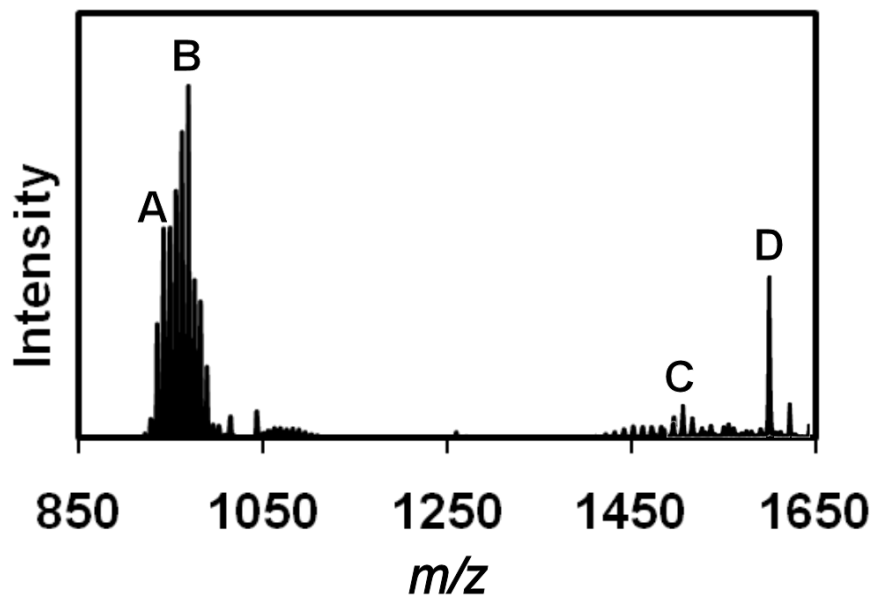
**46**

Figure 98. Crystal structure of 46 (complementary of the Oshio group) and the ligand H₂L showing the two bidentate and one tridentate binding sites.

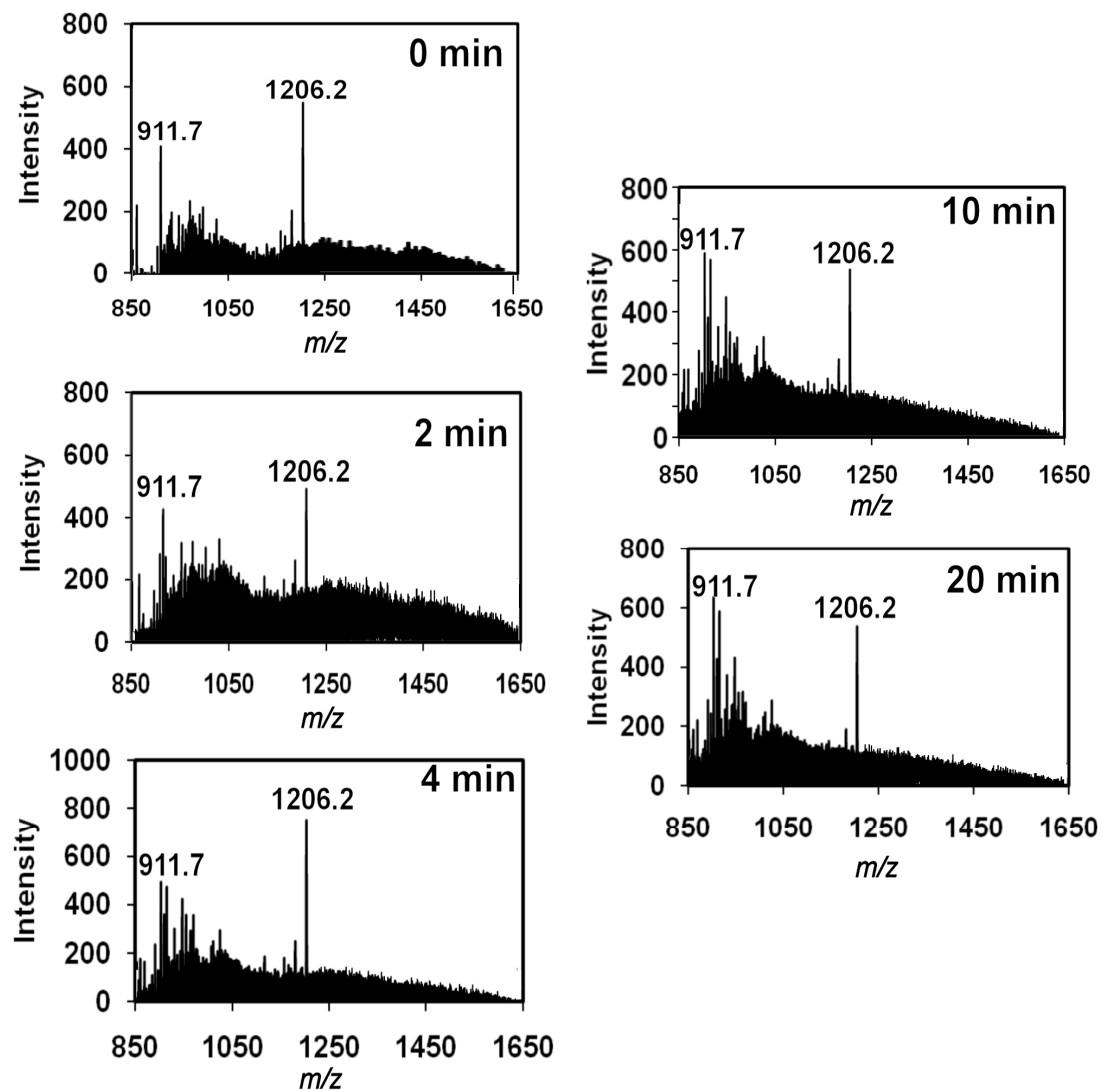
The ESI-MS of **46** (see Figure 99) showed the dissolved crystal forms a number of species in solution, some of were identified to contain the Fe₅Co₄(H₂L)₆ core. These mass spectrometry results conclude that the grid structure is present and that the backbone of the complex can be seen using ESI-MS.



Label	m/z	Formula
A	948.4	$[\text{Fe}^{\text{III}}_5\text{Co}^{\text{II}}_4(\text{H}_2\text{L})_5(\text{OH})_{13}(\text{H}_2\text{O})_6(\text{BF}_4)_2]^{3+}$
B	968.5	$[\text{Fe}^{\text{III}}_5\text{Co}^{\text{II}}_5(\text{H}_2\text{L})_6\text{O}_6(\text{OH})_6]^{3+}$
C	1515.7	$[\text{Fe}^{\text{II}}_3\text{Fe}^{\text{III}}_2\text{Co}^{\text{II}}_4(\text{H}_2\text{L})_6(\text{H}_2\text{O})(\text{OH})_{18}]^{2+}$
D	1607.7	$[\text{Fe}^{\text{III}}_5\text{Co}^{\text{II}}_4(\text{H}_2\text{L})_6(\text{OH})_{12}(\text{H}_2\text{O})_2(\text{CH}_3\text{O})_2(\text{CH}_3\text{OH})(\text{BF}_4)_2]^{2+}$

Figure 99. ESI-MS assignments of dissolved crystal of 46.

To gain an insight into the formation of complexes **45** and **46** time-resolved ESI-MS measurements were conducted. As the synthetic approach to **45** and **46** was almost identical but gave rise to two different structural motifs time resolved mass spectrometry at 180 °C was carried out on the reaction mixture in a MeCN/MeOH (2:1) solution to investigate the self-assembly process. A sample of the reaction mixture was taken directly after mixing of the reagents then every 2 mins after that for 30 mins. From the observed MS data the formation of the helix **45** could be seen directly after mixing but the most abundant species remained unchanged over time.(see Figure 100).

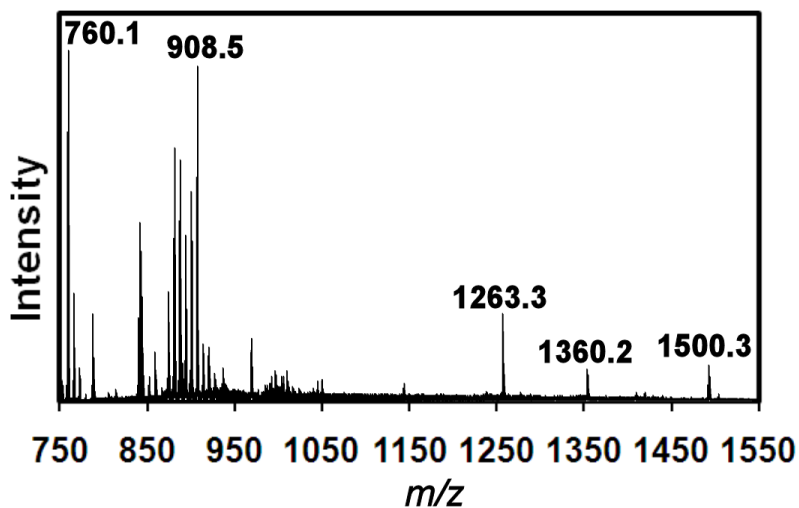


m/z	Formula
911.7	$[\text{Fe}^{\text{III}}\text{Co}^{\text{II}}_3(\text{H}_2\text{L})_4\text{O}(\text{OH})_3(\text{CH}_3\text{O})_2]^{2+}$
1206.2	$[\text{Fe}^{\text{III}}_2\text{Co}^{\text{II}}_4\text{Co}^{\text{III}}(\text{H}_2\text{L})_5\text{O}_6(\text{OH})_3(\text{CH}_3\text{OH})]^{2+}$

Figure 100. Time resolved ESI-MS of **45** measured at time 0, 2, 4, 10 and 20 mins showing that the helix spectrum with the most abundant species remaining unchanged over time.

The time resolved ESI-MS investigation of the self-assembly process involved in the formation of the grid complex **46** showed the gradual growth of building blocks over time. At time = 0 mins the spectrum showed a number of peaks representing generally simple

clusters such as $[\text{Fe}^{\text{II}}_2\text{Co}^{\text{II}}_3(\text{H}_2\text{L})_5\text{O}_2(\text{OH})_3(\text{H}_2\text{O})(\text{CH}_3\text{OH})_2]^{3+}$ (760.1 m/z), $[\text{Co}^{\text{III}}\text{Co}^{\text{II}}(\text{H}_2\text{L})\text{O}(\text{OH})_2]^+$ (1263.3 m/z) and $[\text{Fe}^{\text{III}}\text{Fe}^{\text{II}}\text{Co}^{\text{II}}(\text{H}_2\text{L})_3\text{O}_2(\text{CH}_3\text{O})_2]^+$ (1360.0 m/z). Also observed in the initial spectrum were peaks at 908.5 m/z and 1500.3 m/z which were assigned to the species $[\text{Fe}^{\text{III}}_2\text{Co}^{\text{II}}_5(\text{H}_2\text{L})_6\text{O}_6(\text{CH}_3\text{O})]^{3+}$ and $[\text{Fe}^{\text{III}}_2\text{Co}^{\text{II}}_5(\text{H}_2\text{L})_6\text{O}_6(\text{BF}_4)_2(\text{H}_2\text{O})_2(\text{CH}_3\text{OH})_3]^{2+}$ respectively, these species being attributed to the formation of the intact complex **45**. This suggested that the helical complex **45** may be an intermediate of the grid complex **46** (see Figure 101).



m/z	Formula
760.1	$[\text{Fe}^{\text{II}}_2\text{Co}^{\text{II}}_3(\text{H}_2\text{L})_5\text{O}_2(\text{OH})_3(\text{H}_2\text{O})(\text{CH}_3\text{OH})_2]^{3+}$
908.5	$[\text{Fe}^{\text{III}}_2\text{Co}^{\text{II}}_5(\text{H}_2\text{L})_6\text{O}_6(\text{CH}_3\text{O})]^{3+}$
1263.3	$[\text{Co}^{\text{III}}\text{Co}^{\text{II}}(\text{H}_2\text{L})\text{O}(\text{OH})_2]^+$
1360.0	$[\text{Fe}^{\text{III}}\text{Fe}^{\text{II}}\text{Co}^{\text{II}}(\text{H}_2\text{L})_3\text{O}_2(\text{CH}_3\text{O})_2]^+$
1500.3	$[\text{Fe}^{\text{III}}_2\text{Co}^{\text{II}}_5(\text{H}_2\text{L})_6\text{O}_6(\text{BF}_4)_2(\text{H}_2\text{O})_2(\text{CH}_3\text{OH})_3]^{2+}$

Figure 101. Time resolved ESI-MS of complex **46** at time 0 and its tabulated data showing a number of species present that could be assigned to the building blocks of the complex.

After two minutes the spectrum had changed to show the most abundant peak to be at 1240.1 m/z which was assigned to the species $[\text{Fe}^{\text{II}}_2\text{Fe}^{\text{III}}\text{Co}^{\text{II}}_2(\text{H}_2\text{L})_2(\text{OH})_{12}(\text{H}_2\text{O})_3]^+$, this being a building block of complex **46**. At four to six minutes numerous peaks that can be attributed to a range of oxidation and solvation species being formed were observed. At

eight minutes the peak at 1240.1 m/z was still visible but a new peak at 1482.1 m/z had appeared. This peak was analysed as the species $[\text{Fe}^{\text{III}}_2\text{Fe}^{\text{II}}\text{Co}^{\text{II}}_3(\text{H}_2\text{L})_2\text{O}_3(\text{OH})_7(\text{H}_2\text{O})_8(\text{CH}_3\text{OH})_3]^+$, another structural building block of complex **46** (see Figure 102).

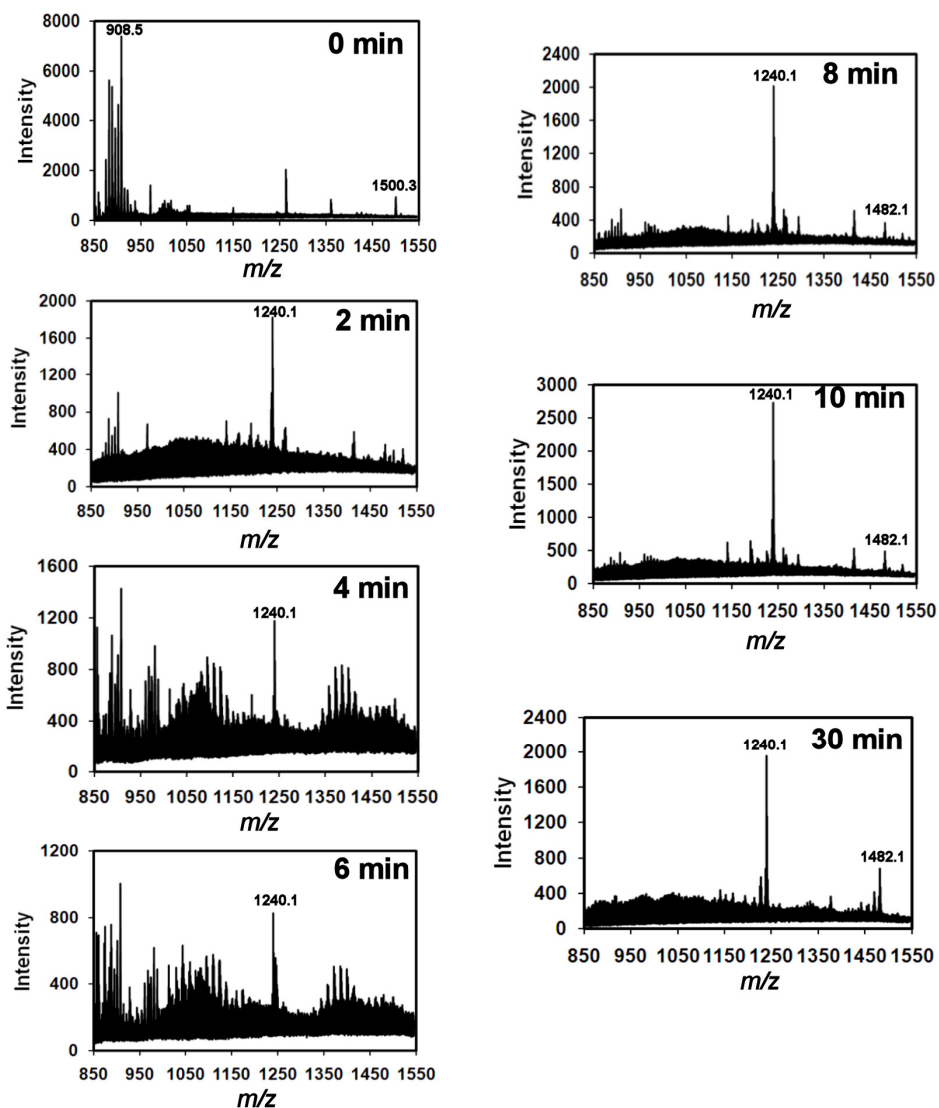
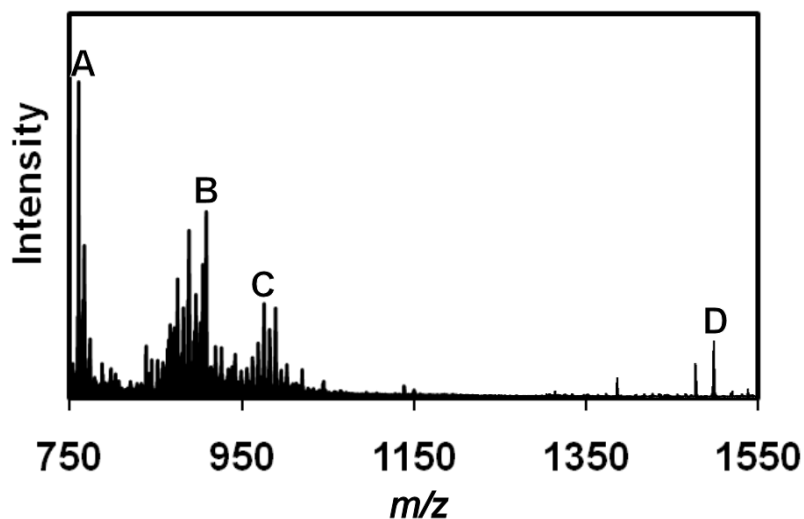


Figure 102. Time resolved ESI-MS of **46** measured at time 0, 2, 4, 6, 8, 10 and 30 mins.

Solutions of the grid reactants were left to react for 7 days. From Figure 103 it was observed that after one week species attributed to both the helix and grid can be seen

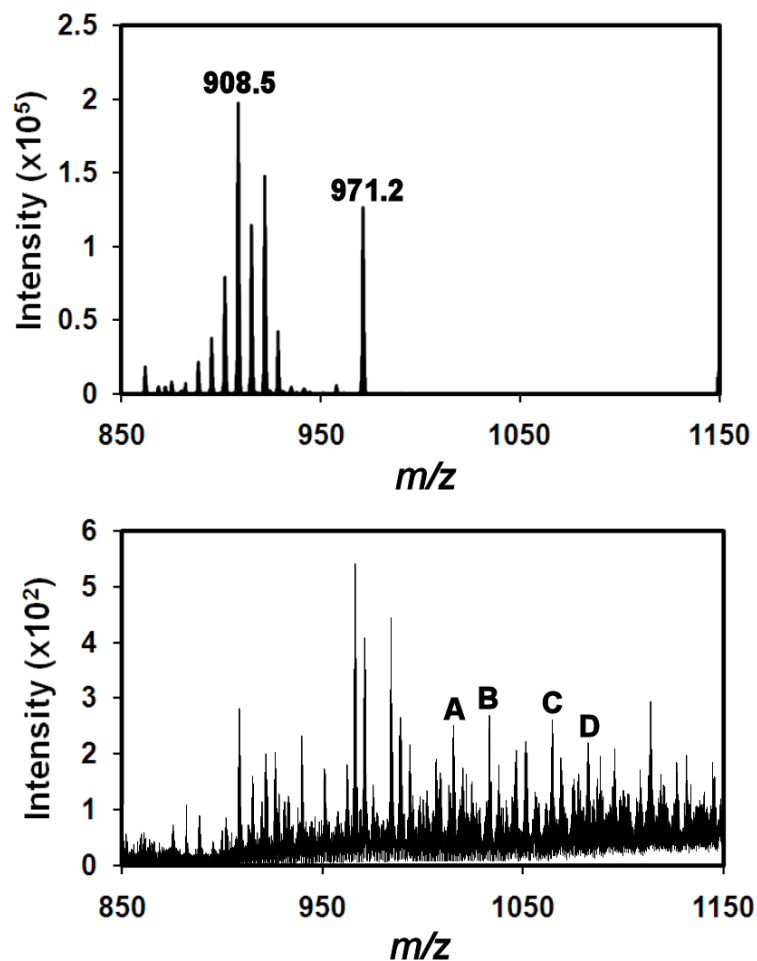
therefore confirming the theory that the helix complex **45** is an intermediate in the formation of the grid complex **46**.



Label	<i>m/z</i>	Formula
A	760.1	$[\text{Fe}^{\text{II}}_2\text{Co}^{\text{II}}_3(\text{H}_2\text{L})_5\text{O}_2(\text{OH})_3(\text{H}_2\text{O})(\text{CH}_3\text{OH})_2]^{3+}$
B	908.5	$[\text{Fe}^{\text{III}}_2\text{Co}^{\text{II}}_5(\text{H}_2\text{L})_6\text{O}_6(\text{CH}_3\text{O})]^{3+}$
C	975.7	$[\text{Fe}^{\text{II}}_3\text{Fe}^{\text{III}}_2\text{Co}^{\text{II}}_4(\text{H}_2\text{L})_6\text{O}_5(\text{OH})_7]^{3+}$
D	1500.3	$[\text{Fe}^{\text{III}}_2\text{Co}^{\text{II}}_5(\text{H}_2\text{L})_6\text{O}_6(\text{BF}_4)_2(\text{H}_2\text{O})_2(\text{CH}_3\text{OH})_3]^{2+}$

Figure 103. Time-resolved ESI-MS spectrum of **46** after 7 days showing the presence of both species attributed to the helix **45** (B and D) and the formation of the grid **46** (A and C).

For further evidence that the helical complex **45** was an intermediate in the formation of complex **46** an experiment was undertaken where the crystals of **45** were dissolved in a 2:1 mixture of MeOH/MeCN and to this solution an excess of $\text{Fe}(\text{BF}_4)_2 \cdot 6\text{H}_2\text{O}$ was added. The resultant spectrum showed many additional peaks compared to the spectrum of the crystal, and significantly, appeared to show peaks that corresponded to the grid complex **46** (see Figure 104).



Label	<i>m/z</i>	Formula
A	1015.7	$[\text{Fe}^{\text{II}}_5\text{Co}_4(\text{H}_2\text{L})_6(\text{OH})_{20}]^{3+}$
B	1033.8	$[\text{Fe}^{\text{II}}_2\text{Fe}^{\text{III}}_3\text{Co}_4(\text{H}_2\text{L})_6(\text{OH})_{17}(\text{H}_2\text{O})(\text{BF}_4)]^{3+}$
C	1065.1	$[\text{Fe}^{\text{II}}_5\text{Co}_4(\text{H}_2\text{L})_6(\text{OH})_{14}(\text{H}_2\text{O})_5(\text{BF}_4)(\text{CH}_3\text{OH})(\text{CH}_3\text{CN})]^{3+}$
D	1083.1	$[\text{Fe}^{\text{II}}_3\text{Fe}^{\text{III}}_2\text{Co}_4(\text{H}_2\text{L})_6(\text{OH})_{15}(\text{H}_2\text{O})_4(\text{BF}_4)_2(\text{CH}_3\text{CN})]^{3+}$

Figure 104. Top: ESI-MS spectrum of dissolved crystals of **45** between 850 and 1150 *m/z* showing the expected species $[\text{Fe}^{\text{III}}_2\text{Co}^{\text{II}}_5(\text{H}_2\text{L})_6\text{O}_6(\text{CH}_3\text{O})]^{3+}$ (908.5 *m/z*); bottom: ESI-MS of sample after the addition of excess $\text{Fe}(\text{BF}_4)_2 \cdot 6\text{H}_2\text{O}$ showing the formation of new species which are assigned in the table.

Through the use of time-resolved mass spectrometry and crystallography it can be concluded that a decreased ratio of metal centres to ligand will give the helix structure **45**. When the metal ratio is increased a grid type structure is formed, but with the helical

structure being observed as an intermediate (see Figure 105). Additional experiments, where an excess of $\text{Fe}(\text{BF}_4)_2$ was added to a crystal of **45**, showed the formation of the grid complex **46** therefore confirming its role as a stable intermediate in the synthesis of **46**.

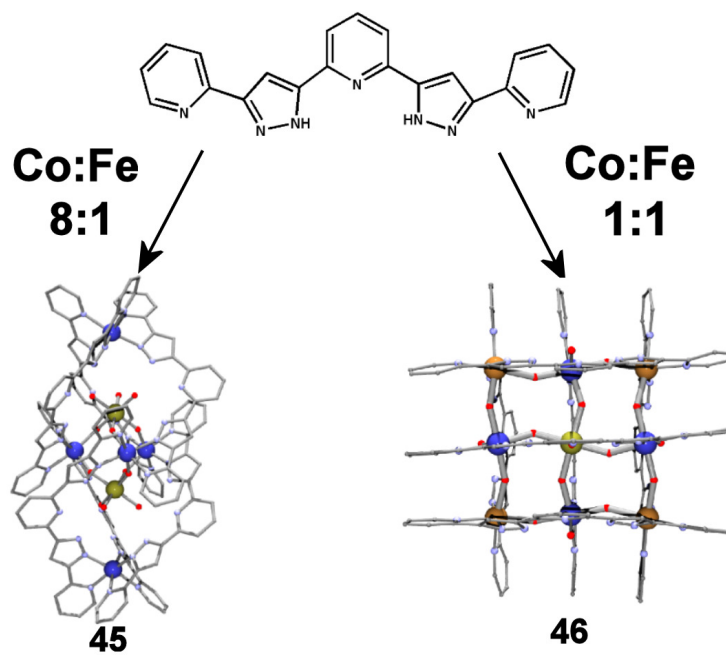


Figure 105. Representation of the different metal to ligand ratios giving different structures.

6.3 Other CSI-MS measurements of heterometallic structures

$\text{Ni}_6(\text{C}_{15}\text{H}_9\text{O}_4)_4(\text{CH}_3\text{OH})$ **47** and **48** $[\text{Mn}_8\text{O}_4(\text{C}_{15}\text{H}_9\text{N}_2\text{O}_2)_4(\text{CH}_3\text{O})_4(\text{CH}_3\text{OH})_8]\text{CH}_3\text{OH} \cdot \text{H}_2\text{O}$ that were synthesised by Oshio *et al* were also analysed by mass spectrometry to obtain knowledge of their structure. The ligand 3-hydroxy-1,3-bis(2-hydroxy-phenyl)-propenone was used to synthesise complex **47** with the complex being synthesised by the reaction of the ligand with triethylamine and $\text{NiCl}_2 \cdot 6\text{H}_2\text{O}$ to give a Ni_6L_4 complex. Each ligand is complexed to two nickel centres through coordination to three of the four oxygens from the ligand, with the hydroxyl group from one phenol group being left uncoordinated. Each nickel in turn is then coordinated to another nickel centre through a bridging μ_3 oxygen that is provided by a methanol or acetate ligand to give an octahedral coordination geometry. The coordinating oxygen of the phenol group also coordinates to a nickel centre

from a neighbouring ligand giving a discrete molecule containing four ligands and six metal centres (see Figure 106).

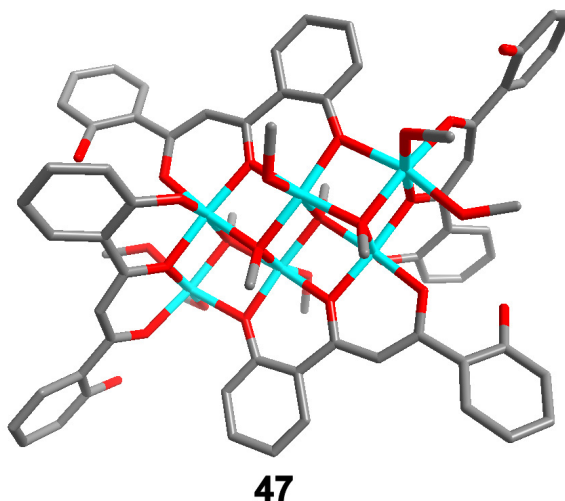
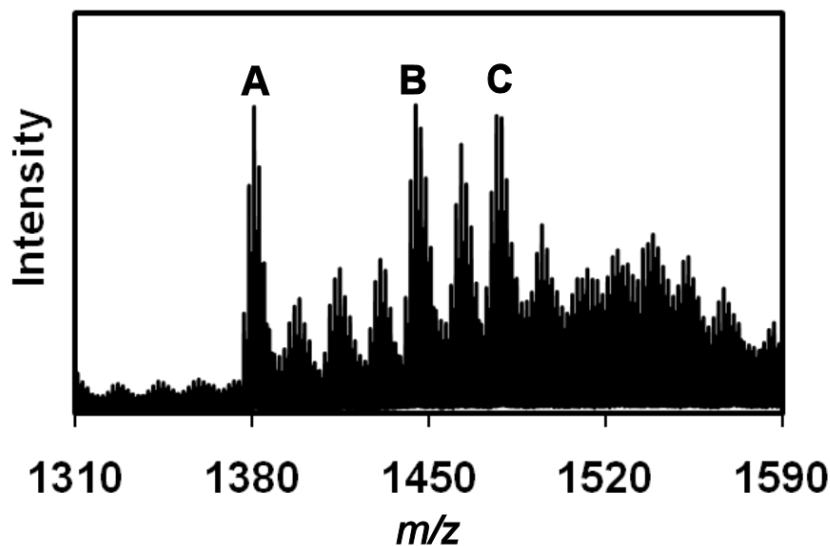


Figure 106. Structure of **47** showing four $C_{15}H_9O_4$ ligands coordinated together through six nickel centres.

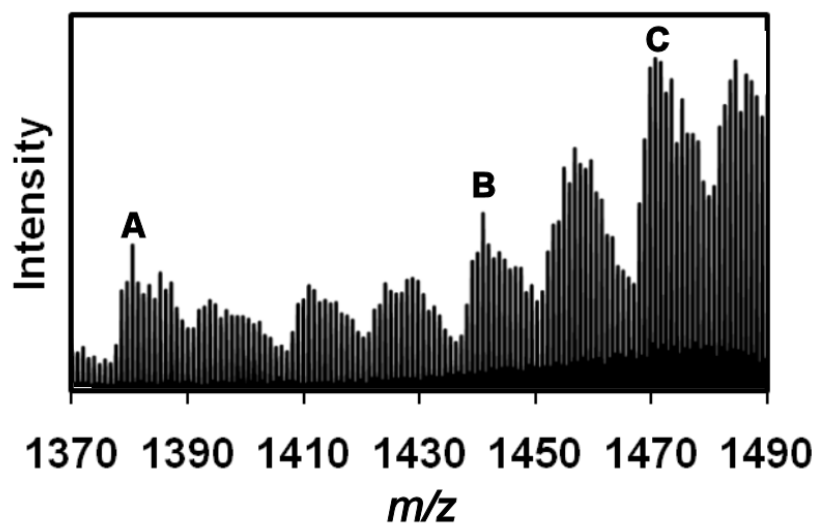
CSI-MS measurements of **47** showed a mixture of species present therefore giving a complicated spectrum. From Figure 107 it can be seen that the Ni_6 complex is present in solution and therefore confirms the stability of the structure in solution and gas phases. CSI-MS Analysis of the Ni_3Co_3 analogue, also synthesised by Oshio *et al*, where 50 % of the $NiCl_2 \cdot 6H_2O$ used to synthesise **47** was replaced with $CoCl_2 \cdot 6H_2O$, gave a complex spectrum that contained a mixture of different species with very similar m/z values.



Label	m/z	Formula
A	1380.8	$[\text{Ni}_6(\text{C}_{15}\text{H}_9\text{O}_4)_4(\text{OH})]^-$
B	1444.9	$[\text{Ni}_6(\text{C}_{15}\text{H}_9\text{O}_4)_4(\text{OH})(\text{CH}_3\text{OH})_2]^-$
C	1476.9	$[\text{Ni}_6(\text{C}_{15}\text{H}_9\text{O}_4)_4(\text{OH})(\text{CH}_3\text{OH})_3]^-$

Figure 107. Selected m/z range of the CSI-MS of 47 (Ni_6) and its tabulated data

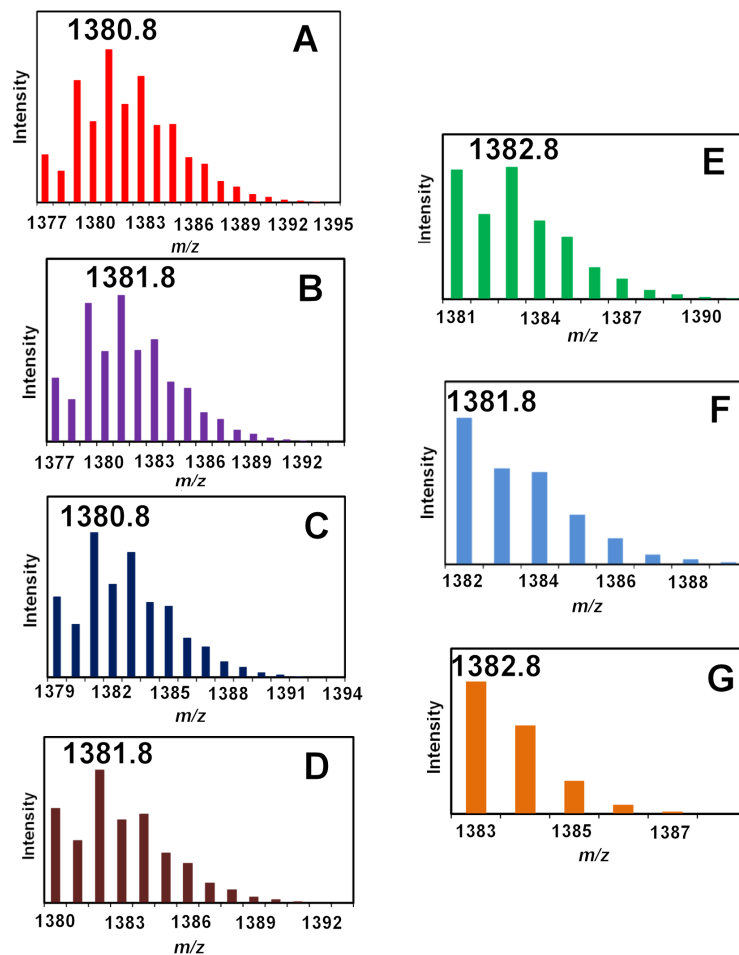
Figure 108 illustrates that the $[\text{Ni}_3\text{Co}_3(\text{C}_{15}\text{H}_9\text{O}_4)_4(\text{OH})]^-$ analogue of 47 can be seen using CSI-MS but analysis of the spectrum showed species from Ni_6 , Ni_5Co , Ni_4Co_2 to Co_6 being present. This could either be due to a number of differing crystal types being produced or that the structure is fairly labile and will fall apart and recombine in the mass spectrometry experiment. This sort of phenomena was observed by Cronin *et al* in 2009 where interchangeability between nickel and cobalt centers in solution lead to large envelope distribution.¹³⁹



Label	<i>m/z</i>	Species present in envelope
A	1380.8	$[\text{Ni}_6(\text{C}_{15}\text{H}_9\text{O}_4)_4(\text{OH})]^-$
	1381.8	$[\text{Ni}_5\text{Co}(\text{C}_{15}\text{H}_9\text{O}_4)_4(\text{OH})]^-$
	1380.8	$[\text{Ni}_4\text{Co}_2(\text{C}_{15}\text{H}_9\text{O}_4)_4(\text{OH})]^-$
	1381.8	$[\text{Ni}_3\text{Co}_3(\text{C}_{15}\text{H}_9\text{O}_4)_4(\text{OH})]^-$
	1382.8	$[\text{Ni}_2\text{Co}_4(\text{C}_{15}\text{H}_9\text{O}_4)_4(\text{OH})]^-$
	1381.8	$[\text{NiCo}_5(\text{C}_{15}\text{H}_9\text{O}_4)_4(\text{OH})]^-$
	1382.8	$[\text{Co}_6(\text{C}_{15}\text{H}_9\text{O}_4)_4(\text{OH})]^-$
B	1444.9	$[\text{Ni}_6(\text{C}_{15}\text{H}_9\text{O}_4)_4(\text{OH})(\text{CH}_3\text{OH})_2]^-$
	1445.9	$[\text{Ni}_5\text{Co}(\text{C}_{15}\text{H}_9\text{O}_4)_4(\text{OH})(\text{CH}_3\text{OH})_2]^-$
	1444.9	$[\text{Ni}_4\text{Co}_2(\text{C}_{15}\text{H}_9\text{O}_4)_4(\text{OH})(\text{CH}_3\text{OH})_2]^-$
	1445.9	$[\text{Ni}_3\text{Co}_3(\text{C}_{15}\text{H}_9\text{O}_4)_4(\text{OH})(\text{CH}_3\text{OH})_2]^-$
	1446.9	$[\text{Ni}_2\text{Co}_4(\text{C}_{15}\text{H}_9\text{O}_4)_4(\text{OH})(\text{CH}_3\text{OH})_2]^-$
	1445.9	$[\text{NiCo}_5(\text{C}_{15}\text{H}_9\text{O}_4)_4(\text{OH})(\text{CH}_3\text{OH})_2]^-$
	1446.9	$[\text{Co}_6(\text{C}_{15}\text{H}_9\text{O}_4)_4(\text{OH})(\text{CH}_3\text{OH})_2]^-$
C	1476.9	$[\text{Ni}_6(\text{C}_{15}\text{H}_9\text{O}_4)_4(\text{OH})(\text{CH}_3\text{OH})_2]^-$
	1477.9	$[\text{Ni}_5\text{Co}(\text{C}_{15}\text{H}_9\text{O}_4)_4(\text{OH})(\text{CH}_3\text{OH})_2]^-$
	1476.9	$[\text{Ni}_4\text{Co}_2(\text{C}_{15}\text{H}_9\text{O}_4)_4(\text{OH})(\text{CH}_3\text{OH})_2]^-$
	1477.9	$[\text{Ni}_3\text{Co}_3(\text{C}_{15}\text{H}_9\text{O}_4)_4(\text{OH})(\text{CH}_3\text{OH})_2]^-$
	1478.9	$[\text{Ni}_2\text{Co}_4(\text{C}_{15}\text{H}_9\text{O}_4)_4(\text{OH})(\text{CH}_3\text{OH})_2]^-$
	1477.9	$[\text{NiCo}_5(\text{C}_{15}\text{H}_9\text{O}_4)_4(\text{OH})(\text{CH}_3\text{OH})_2]^-$
	1478.9	$[\text{Co}_6(\text{C}_{15}\text{H}_9\text{O}_4)_4(\text{OH})(\text{CH}_3\text{OH})_2]^-$

Figure 108. Selected *m/z* range of the CSI-MS of Ni_3Co_3 analogue of 47 and its tabulated data showing the mixture of Ni/Co species present.

Figure 109 represents the individual isotopic envelopes that are present in envelope A at 1381.8 m/z (Figure 108). Each of these envelopes are overlaid on each other to form the isotope pattern shown in Figure 108. This can also be applied to peaks B and C.



Label	m/z	Species present in envelope
A	1380.8	$[\text{Ni}_6(\text{C}_{15}\text{H}_9\text{O}_4)_4(\text{OH})]$
B	1381.8	$[\text{Ni}_5\text{Co}(\text{C}_{15}\text{H}_9\text{O}_4)_4(\text{OH})]^-$
C	1380.8	$[\text{Ni}_4\text{Co}_2(\text{C}_{15}\text{H}_9\text{O}_4)_4(\text{OH})]^-$
D	1381.8	$[\text{Ni}_3\text{Co}_3(\text{C}_{15}\text{H}_9\text{O}_4)_4(\text{OH})]^-$
E	1382.8	$[\text{Ni}_2\text{Co}_4(\text{C}_{15}\text{H}_9\text{O}_4)_4(\text{OH})]^-$
F	1381.8	$[\text{NiCo}_5(\text{C}_{15}\text{H}_9\text{O}_4)_4(\text{OH})]^-$
G	1382.8	$[\text{Co}_6(\text{C}_{15}\text{H}_9\text{O}_4)_4(\text{OH})]^-$

Figure 109. Calculated spectra of the different species present in envelope A (m/z of 1381.8) of Figure 108.

Complex $[\text{Mn}_8\text{O}_4(\text{C}_{15}\text{H}_9\text{N}_2\text{O}_2)_4(\text{CH}_3\text{O})_4(\text{CH}_3\text{OH})_8]\cdot\text{CH}_3\text{OH}\cdot\text{H}_2\text{O}$ **48** was synthesised by the reaction of 3,5-diphenolpyrazole with $\text{MnCl}_2\cdot 4\text{H}_2\text{O}$ and $\text{NiCl}_2\cdot 6\text{H}_2\text{O}$. CSI-MS measurements of the crystals gave species corresponding to $[\text{Mn}_5\text{Ni}_3\text{C}_{15}\text{H}_9\text{O}_2\text{N}_2)_4\text{O}_4(\text{CH}_3\text{O})_2]^-$ (1572.8 m/z) and $[\text{Mn}_5\text{Ni}_3\text{C}_{15}\text{H}_9\text{O}_2\text{N}_2)_4\text{O}_4(\text{CH}_3\text{O})_2(\text{CH}_3\text{OH})]^-$ (1604.8 m/z). Each ligand complexed two manganese centres, with one centre being complexed to one nitrogen from the pyrazole and the oxygen from the phenol group. The second manganese centre complexed to the phenol group was also coordinated to a phenol group from the neighbouring ligand to give a complex containing four ligands with eight metal centres. The crystal structure of complex **48** showed only the incorporation of manganese in the structure but the synthetic method included the use of $\text{NiCl}_2\cdot 6\text{H}_2\text{O}$. The mass spectrometry measurements have shown the incorporation of nickel in the structure, providing evidence of more than one crystalline product; a mixture of pure manganese, pure nickel and a structure containing different ratios of nickel and manganese centres.

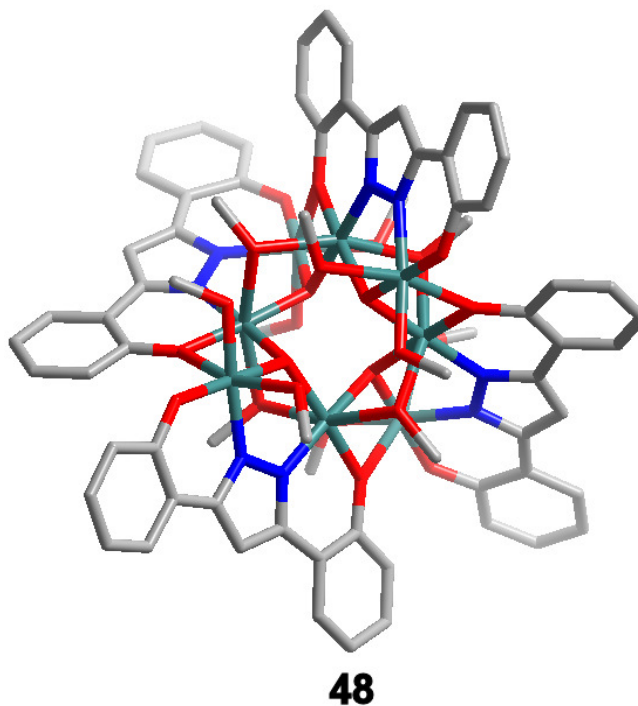
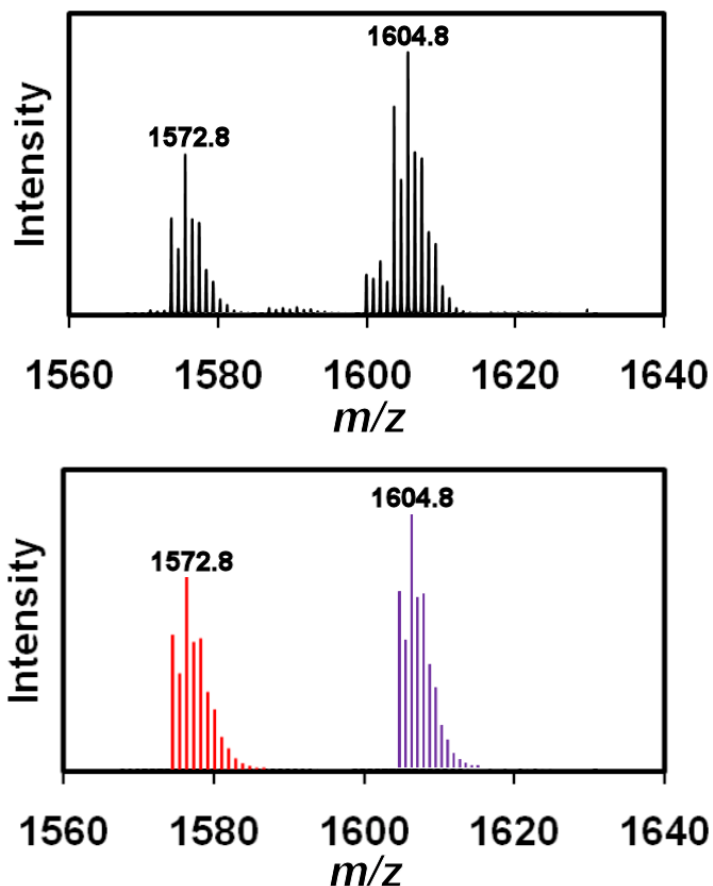


Figure 110. Structure of **48** showing the coordination of four $\text{C}_{15}\text{H}_9\text{O}_2\text{N}_2$ ligands to eight manganese ions.



<i>m/z</i>	Formula
1572.8	$[\text{Mn}_5\text{Ni}_3(\text{C}_{15}\text{H}_9\text{O}_2\text{N}_2)_4\text{O}_4(\text{CH}_3\text{O})_2]^-$
1604.8	$[\text{Mn}_5\text{Ni}_3(\text{C}_{15}\text{H}_9\text{O}_2\text{N}_2)_4\text{O}_4(\text{CH}_3\text{O})_2(\text{CH}_3\text{OH})]^-$

Figure 111. CSI-MS measurement of **48** showing the presence of nickel in the structure

The synthesis and mass spectrometry results demonstrate the inclusion of $\text{NiCl}_2 \cdot 6\text{H}_2\text{O}$ in the formation of the Mn_8 structure but the crystal structure does not incorporate any nickel. It was thought that the crystal used for the crystal structure diffraction of **48** was one of many different crystals obtained in the reaction mixture. This result can be compared to the reaction of nickel chloride and cobalt chloride to form a heterometallic structure like that shown in Figure 106. When CSI-MS measurements were carried out on this complex many new species were formed due to the breaking apart and reforming of species. This phenomenon could also have occurred with the Mn_8 structure, where the nickel could be

incorporated in the solid state structure but lost when introduced into the mass spectrometer. Further research is needed to gain a full insight into whether the structure is rearranging in the mass spectrometer or whether multiple forms of crystals are synthesised in this reaction.

6.4 Conclusions

6.4.1 Mass spectrometric studies of inorganic complexes

6.4.2 Mass spectrometric studies of chiral cyanide-bridged {Ni₆Fe₄} cages

ESI-MS studies were carried out on the chiral cages complexes (Et₄N)[Ni(L^R)₂]₆[Fe(CN)₆]₄(PF₆).22H₂O.26CH₃OH, **43**, and (Et₄N)[Ni(L^S)₂]₆[Fe(CN)₆]₄(PF₆).22H₂O.26CH₃OH, **44**, synthesised by Oshio *et al* from a chiral nickel precursor [Ni(L^{R/S})₂Cl₂], **41**, and a templating tetraethylammonium cation (Et₄N)₃[Fe(CN)₆]. ESI-MS measurements gave three peaks corresponding to the species [(Et₄N)H[Ni(L^{S/R})₂]₆[Fe(CN)₆]₄]²⁺ (1927.0 *m/z*), [(Et₄N)Na[Ni(L^{S/R})₂]₆[Fe(CN)₆]₄]²⁺ (1938.0 *m/z*) and [(Et₄N)K[Ni(L^{S/R})₂]₆[Fe(CN)₆]₄]²⁺ (1946.0 *m/z*), providing evidence of the structural incarceration of the tetraethylammonium cation (see Figure 112). Further studies will probe the formation of the cage complex in solution work using in-situ mass spectrometry and what effect changing the templating cation has on the structure formed.

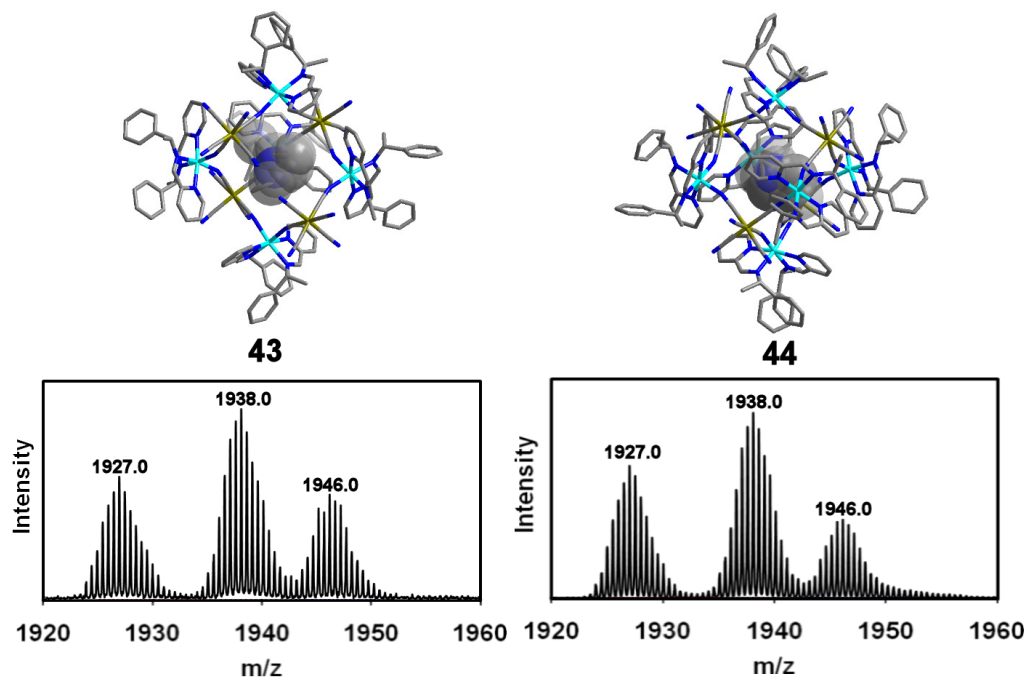


Figure 112. Structure of $(\text{Et}_4\text{N})[\text{Ni}(\text{L}^{\text{R}})_2]_6[\text{Fe}(\text{CN})_6]_4(\text{PF}_6) \cdot 22\text{H}_2\text{O} \cdot 26\text{CH}_3\text{OH}$, **43**, and $(\text{Et}_4\text{N})[\text{Ni}(\text{L}^{\text{S}})_2]_6[\text{Fe}(\text{CN})_6]_4(\text{PF}_6) \cdot 22\text{H}_2\text{O} \cdot 26\text{CH}_3\text{OH}$, **44**, and their corresponding CSI-MS spectra.

6.4.3 Mass Spectrometric Studies of the Self-Assembly of Heterometallic Clusters

The heterometallic ligands $[\text{Fe}^{\text{III}}_2\text{Co}^{\text{II}}_5(\text{H}_2\text{L})_6\text{O}_6(\text{H}_2\text{O})_6](\text{BF}_4)_4$, **45**, and $[\text{Fe}^{\text{II}}_4\text{Fe}^{\text{III}}\text{Co}^{\text{II}}_4(\text{H}_2\text{L})_6(\text{OH})_{12}(\text{H}_2\text{O})_6](\text{BF}_4)_7$, **46**, by Oshio *et al*, synthesised from almost identical experimental procedures apart from the metal to ligand ratio used, were analysed using ESI-MS. Analysis of the ESI-MS crystal structure of $[\text{Fe}^{\text{III}}_2\text{Co}^{\text{II}}_5(\text{H}_2\text{L})_6\text{O}_6(\text{H}_2\text{O})_6](\text{BF}_4)_4$, **45**, showed that the crystal formed a number of species in solution, all of which containing the $\text{Fe}_2\text{Co}_5(\text{H}_2\text{L})_6$ core, with speciation also present in the mass spectrometry data for $[\text{Fe}^{\text{II}}_4\text{Fe}^{\text{III}}\text{Co}^{\text{II}}_4(\text{H}_2\text{L})_6(\text{OH})_{12}(\text{H}_2\text{O})_6](\text{BF}_4)_7$, **46**.

Time-resolved mass spectrometry was used to follow the formation of complexes **45** and **46**. Solutions of the reagents were measured every 2 mins for 30 mins and also every 24 hours for one week to provide evidence of structural building blocks. For complex **45** the observed MS data showed the formation of the helix directly after mixing

but remained unchanged after this time. With complex **46** however, directly after mixing a number of species were observed that represented the building blocks in the formation of the grid complex but species could also be seen that were attributed to the formation of complex **45** (see Figure 113). Further studies were undertaken where an excess of $\text{Fe}(\text{BF}_4)_2 \cdot 6\text{H}_2\text{O}$ was added to a solution of **45** and ESI-MS measurements taken. The results showed peaks that corresponded to complex **46**.

It can be concluded from this work that a decreased metal to ligand ratio will produce complex **45** as the main product but an increased metal to ligand ratio will produce complex **46**, but with the helical structure being observed an intermediate in the synthetic process.

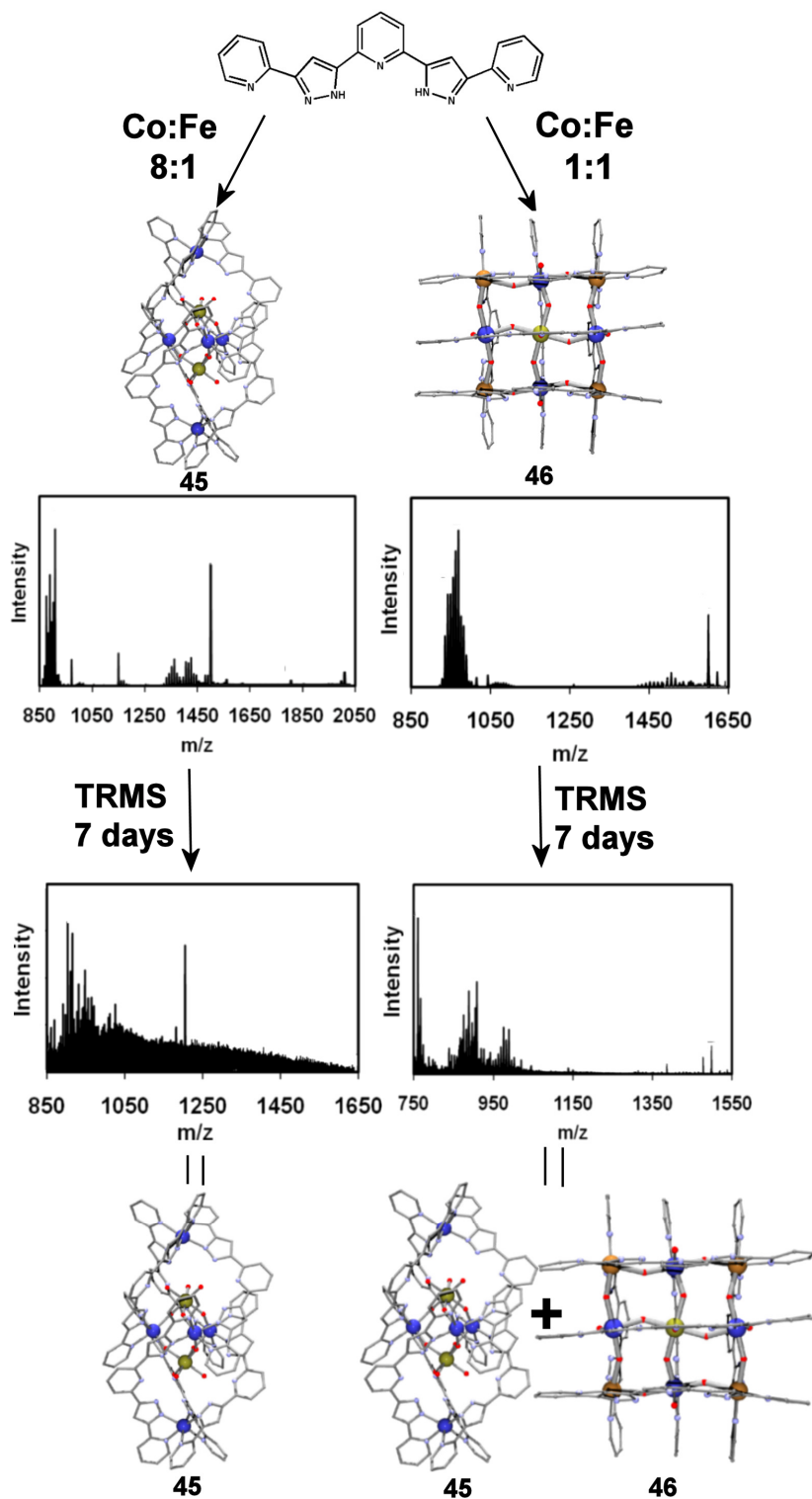


Figure 113. Overview of the experimental process undertaken to show the formation process of complex the helix complex 45 and the grid complex 46 from different metal to ligand ratios and their corresponding ESI-MS results.

6.4.4 Other CSI-MS measurements of heterometallic structures

Further to the work above mass spectrometry experiments were carried out on the Ni_6L_4 complex **47** synthesised from the ligand 3-hydroxy-1,3-bis(2-hydroxy-phenyl)propanone and $\text{NiCl}_2 \cdot 6\text{H}_2\text{O}$. CSI-MS measurements of the crystal gave a complicated spectrum due to a mixture of species with similar m/z values being present but the main peak at 1380.8 m/z was credited to the species $[\text{Ni}_6(\text{C}_{15}\text{H}_9\text{O}_4)_4(\text{OH})]^-$ therefore confirming the existence of the Ni_6L_4 complex (see Figure 114).

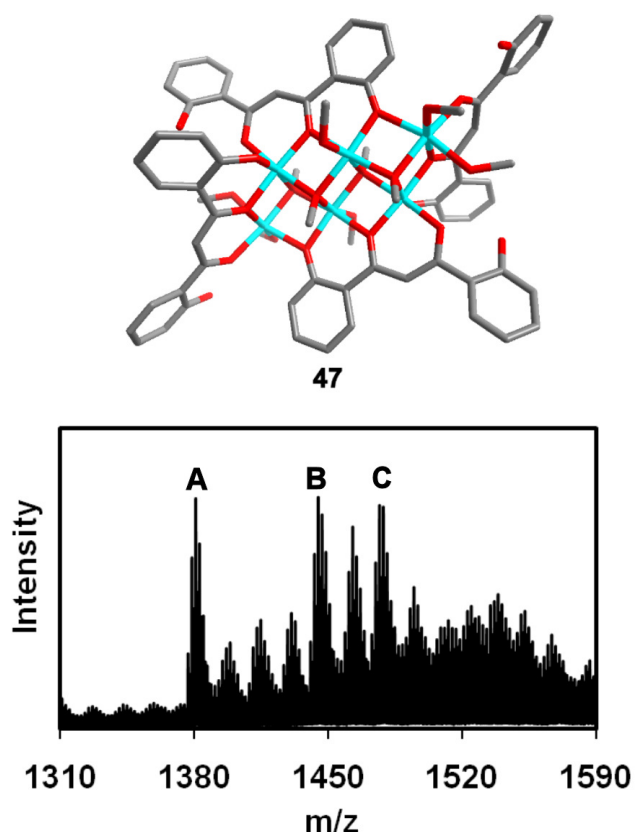


Figure 114. Structure of the Ni_6L_4 complex **47** and its corresponding CSI-MS spectrum.

An analogous $\text{Ni}_3\text{Co}_3\text{L}_4$ complex synthesised by Oshio *et al* was also analysed by CSI-MS. Analysis of the spectrum showed species from Ni_6L_4 , Ni_5CoL_4 , to Co_6L_4 being present, this being attributed to the labile nature of the complex which will easily fall apart and then recombine into new species in the mass spectrometer.

The Mn_8L_4 complex **48** was synthesised from 3,5-diphenolpyrazole and $\text{MnCl}_2 \cdot 4\text{H}_2\text{O}$ and $\text{NiCl}_2 \cdot 6\text{H}_2\text{O}$. CSI-MS measurements were carried out to observe what role the nickel has in the formation of the structure. From the spectrum it could be seen that both nickel and manganese were incorporated in the species found at 1572.8 m/z ($[\text{Mn}_5\text{Ni}_3(\text{C}_{15}\text{H}_9\text{O}_2\text{N}_2)_4\text{O}_4(\text{CH}_3\text{O})_2]^-$) but nickel was not found in the crystal structure. Further work will be carried out where time-resolved mass spectrometry will be used to follow the formation of the Mn_8L_4 complex **48** and provide evidence for the presence of $\text{NiCl}_2 \cdot 4\text{H}_2\text{O}$ in the synthesis of the complex.

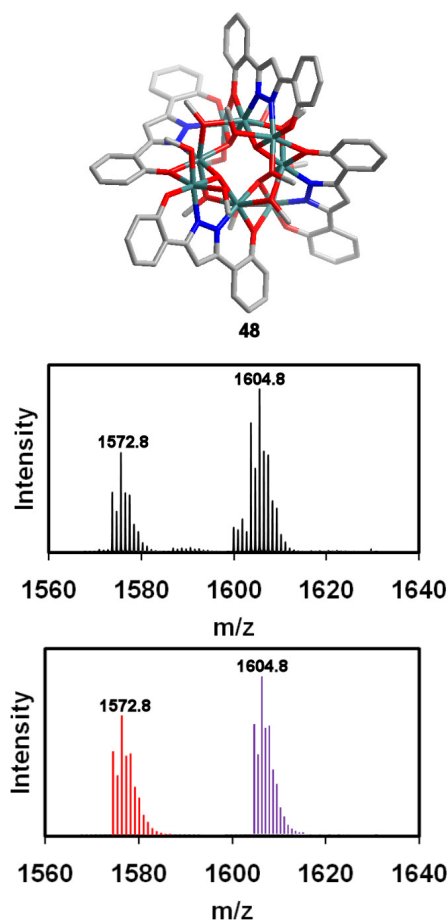


Figure 115. Structure of the Mn_8L_4 ligand **48 and its corresponding CSI-MS data.**

Mass spectrometry has been used as not only a tool in the analysis of supramolecular complexes but has been used to provide an insight into the self-assembly process in the formation of a number of complexes. CSI-MS has also been utilised as a tool in the trapping of unstable reaction intermediates that have never before been observed.

6.5 Experimental

6.5.1 Mass spectrometric studies of inorganic complexes

6.5.2 Mass spectrometric studies of chiral cyanide-bridged {Ni₆Fe₄} cages

Cryospray measurements at -20 °C were carried out at concentrations of the complex in the region of 10⁻⁵ mol L⁻¹ in methanol using a Bruker microTOFQ instrument. Data was collected in positive ion mode and the spectrometer was previously calibrated with the standard tune mix to give a precision of ca. 1.5 ppm in the region of 500-3000 m/z. The standard parameters for a medium mass data acquisition were used, the end plate voltage was set to -500 V and the capillary to +4500 V.

The synthesis of **41**, **42**, **43** and **44** were carried out by Oshio *et al.*¹⁷ [NiCl₂(L^R)₂] (**41**): NiCl₂·6H₂O (3.56 g, 15 mmol) in methanol (25 ml) was added to 2-pyridine carbaldehyde (3.21 g, 30 mmol) and *R*-phenyl ethyl amine (3.64 g, 30 mmol) in methanol (50 ml). The resulting light green solution was allowed to evaporate and crystalline green solid [NiCl₂(L^R)₂] (**41**) formed. Yield 8.434 g (92%). Since the resulting green precipitate was deliquescent, the dried precipitate was used for the following syntheses of **43**. Light green square plates were recrystallized from methanol by ether diffusion. Anal. calcd. (found) for (C₈₄H₁₀₄N₁₂Cl₆Ni₃O₁₀): C, 55.11 (55.36); H, 5.73 (5.71); N, 9.18 (9.10).

[[NiCl₂(L^S)₂] (**42**): **42** was obtained by the same synthetic approach as **41** with L^S in place of L^R. Yield 8.711 g (92%). Anal. calcd. (found) for (C₈₄H₁₁₀Cl₆N₁₂Ni₃O₁₃): C, 53.53 (53.34); H, 5.88 (5.76); N, 8.92 (8.90).

(Et₄N)[Ni(L^R)₂]₆[Fe(CN)₆]₄(PF₆)·22H₂O·26CH₃OH (**43**): A methanol-H₂O mixed solution (20 ml) of **41** (55 mg) and NH₄PF₆ (64 mg, 0.4 mmol) was diffused into (Et₄N)₃[Fe(CN)₆] (60 mg, 0.1 mmol) in methanol (20 ml) at 5 °C and light-brown hexagonal plates of (Et₄N)[Ni(L^R)₂]₆[Fe(CN)₆]₄(PF₆)·22H₂O (**42**) were obtained. Yield ca. 90%. Anal. calcd. (found) for C₂₀₀H₁₇₆N₄₉F₆P₁Fe₄Ni₆·22(H₂O): C, 54.81 (54.18); H, 5.06 (5.10); N, 15.66 (15.85); MS (ESI-MS) *m/z* 1926.9 [M+H]²⁺.

(Et₄N)[Ni(L^S)₂]₆[Fe(CN)₆]₄(PF₆)₄·22H₂O·28CH₃OH (**44**): Obtained by the same synthetic approach as **43**, but using **42** instead of **41**. Yield *ca.* 90%. Anal. calcd. (found) for C₂₀₀H₁₇₆N₄₉F₆P₁Fe₄Ni₆·22(H₂O): C, 54.81 (54.54); H, 5.06 (5.01); N, 15.66 (16.02); MS (ESI-MS) *m/z* 1926.9 [M+H]²⁺.

6.5.3 Mass spectrometric studies of the Self-Assembly of Heterometallic Clusters

Electrospray measurements at 20 °C were carried out at concentrations of the complex in the region of 10–5 mol L⁻¹ in methanol using a Bruker microTOFQ instrument. Data was collected in positive ion mode and the spectrometer was previously calibrated with the standard tune mix to give a precision of *ca.* 1.5 ppm in the region of 50–3000 *m/z*. The standard parameters for a medium mass data acquisition were used, the end plate voltage was set to –500 V and the capillary to +4500 V.

6.5.4 Synthesis of heterometallic helix, **45**, and grid, **46**, clusters

The synthesis of **45** and **46** were carried out by Oshio *et al.*¹³⁸

Synthesis of **45**: To a mixture of H₂L (= 2,6-bis[5-(2-pyridinyl)-1H-pyrazole-3-yl]pyridine) (87.6 mg, 0.24 mmol) and triethylamine (66 μL, 0.48 mmol) in methanol (10 ml) was added a solution of Fe(BF₄)₂·6 H₂O (33.8 mg, 0.1 mmol) and Co(BF₄)₂·6 H₂O (272.5 mg, 0.8 mmol) in methanol (15 ml). The mixture was stirred for several minutes after addition acetonitrile (13 ml). The resulting red-brown solution was allowed to stand for few days at room temperature to give orange-red plate crystals of, [Fe₂Co₅(H₂L)₆O₆(H₂O)₆](BF₄)₄·5(H₂O)·7(MeCN)·6(MeOH)(1·5(H₂O)·7(MeCN)·6(MeOH)). Anal. calcd. (found) for C₁₂₆H₁₁₂B₄Co₅F₁₆Fe₂N₄₂O₁₇ (1·5H₂O): C, 46.71 (46.38); H, 3.48 (3.14); N, 18.16 (18.20). ICP calcd. (found): Fe 2.00 (2.03); Co, 5.00 (4.97); MS (ESI-MS) *m/z* 1500.3 [Fe^{III}₂Co^{II}₅(H₂L)₆O₆(H₂O)₂(BF₄)₂(MeOH)₃]²⁺.

Synthesis of **46**: To a mixture of H₂L (109.6 mg, 0.3 mmol) and triethylamine (83.5 ml, 0.6 mmol) in MeOH/MeCN (v/v = 2/1, 20 ml) was added a solution of Fe(BF₄)₂·6 H₂O (151.9 mg, 0.45 mmol) and Co(BF₄)₂·6 H₂O (153.3 mg, 0.45 mmol) in MeOH / MeCN (v/v = 2/1, 20 ml). The mixture was stirred for several minutes. The resulting dark red-brown solution was allowed to stand for few days at room temperature to give yellow plate crystals of [Fe₅Co₄(H₂L)₆(OH)₁₂(H₂O)₆](BF₄)₇·3(H₂O)·4(MeCN)·2(MeOH) (2·3(H₂O)·4(MeCN)·2(MeOH)). Anal. calcd. (found) for C₁₂₆H₁₂₀N₄₂B₇Co₄F₂₈F₅O₂₁ (2·3H₂O): C, 41.08 (41.92); H, 3.28 (3.10); N, 15.97 (16.05). ICP calcd. (found): Fe, 5.00 (5.08); Co, 4.00 (3.92); MS (ESI-MS) *m/z* 968.4 [Fe^{II}₂Fe^{III}₃Co^{II}₄L₆O₆(OH)₆]³⁺.

6.5.4.1 Time resolved ESI-MS measurements of the synthesis of **45** (helix)

H₂L (7.5 mg, 0.02 mmol) was dissolved in MeOH/MeCN (2:1) (5ml) and to this triethylamine (4 mg, 0.04 mmol) was added. A second solution was made up where Fe(BF₄)₂·6H₂O (2 mg, 0.006 mmol) was dissolved in MeOH/MeCN (2:1) (5ml) and to this Co(BF₄)₂·6H₂O (18 mg, 0.05 mmol) was added. The two solutions were slowly added together and one drop of the resulting solution further diluted in MeOH/MeCN (2:1) (5ml). This was then injected into the mass spectrometer at 20 °C and collected at 0 mins then every 2 mins for 20 mins. This procedure was repeated by collecting a spectrum once every day for 7 days. MS (ESI-MS) *m/z* 1206.2 [Fe^{III}₂Co^{II}₄Co^{III}₁(H₂L)₅O₆(OH)₃(CH₃OH)]²⁺.

6.5.4.2 Time-resolved ESI-MS investigation of synthesis of **46** (grid)

H₂L (7.5 mg, 0.02 mmol) was dissolved in MeOH/MeCN (2:1) (5ml) and to this triethylamine (4 mg, 0.04 mmol) was added. A second solution was made up where Fe(BF₄)₂·6H₂O (10 mg, 0.03 mmol) was dissolved in MeOH/MeCN (2:1) (5ml) and to this Co(BF₄)₂·6H₂O (10 mg, 0.03 mmol) was added. The two solutions were slowly added together and one drop of the resulting solution further diluted in MeOH/MeCN (2:1) (5ml). This was then injected into the mass spectrometer at 20 °C and collected at 0 mins then every 2 mins for 20 mins. This procedure was repeated by collecting a spectrum once

every day for 7 days. MS (ESI-MS) at time 0 min - m/z 760.1 $[\text{Fe}^{\text{II}}_2\text{Co}^{\text{II}}_3(\text{H}_2\text{L})_5\text{O}_2(\text{OH})_3(\text{H}_2\text{O})(\text{CH}_3\text{OH})_2]^{3+}$, m/z 1263.3 $[\text{Co}^{\text{III}}\text{Co}^{\text{II}}(\text{H}_2\text{L})_3(\text{OH})_2\text{O}]^+$, m/z 1360.2 $[\text{Fe}^{\text{III}}\text{Fe}^{\text{II}}\text{Co}(\text{H}_2\text{L})_3\text{O}_2(\text{CH}_3\text{O})_2]^+$, m/z 908.5 $[\text{Fe}^{\text{III}}_2\text{Co}^{\text{II}}_5(\text{H}_2\text{L})_6\text{O}_6(\text{CH}_3\text{O})]^{3+}$, m/z 1500.3 $[\text{Fe}^{\text{III}}_2\text{Co}^{\text{II}}_5(\text{H}_2\text{L})_6\text{O}_6(\text{BF}_4)_2(\text{H}_2\text{O})_2(\text{CH}_3\text{OH})_3]^{2+}$; after 14 mins - m/z 1240.1 $[\text{Fe}^{\text{II}}_2\text{Fe}^{\text{III}}\text{Co}^{\text{II}}_2(\text{H}_2\text{L})_2(\text{OH})_{12}(\text{H}_2\text{O})_3]^+$, m/z 1482.1 $[\text{Fe}^{\text{III}}_2\text{Fe}^{\text{II}}\text{Co}^{\text{II}}_3(\text{H}_2\text{L})_2\text{O}_3(\text{OH})_7(\text{H}_2\text{O})_8(\text{CH}_3\text{OH})_3]^+$, m/z 1625.1 $[\text{Fe}^{\text{III}}_2\text{Co}^{\text{II}}_3(\text{H}_2\text{L})_3(\text{OH})_{11}(\text{H}_2\text{O})_3]^+$. The synthesis of **40** appears to show the gradual growth of structural building blocks (Figure 2). The spectrum after 0 mins showed that amongst the most prominent peaks were those representing generally simple clusters such as $[\text{Fe}^{\text{II}}_2\text{Co}^{\text{II}}_3(\text{H}_2\text{L})_5\text{O}_2(\text{OH})_3(\text{H}_2\text{O})(\text{CH}_3\text{OH})_2]^{3+}$ at 760.1 (760.1) m/z , $[\text{Co}^{\text{III}}\text{Co}^{\text{II}}(\text{H}_2\text{L})_3(\text{OH})_2\text{O}]^+$ at 1263.3 (1263.3) m/z and $[\text{Fe}^{\text{III}}\text{Fe}^{\text{II}}\text{Co}(\text{H}_2\text{L})_3\text{O}_2(\text{CH}_3\text{O})_2]^+$ at 1360.2 (1360.2) m/z . After 7 days the complete cluster **2** could still not be observed, however further, higher nuclearity, species had developed.

7 CRYSTALLOGRAPHY

9 single-crystal X-ray diffraction datasets are presented in this thesis. This section contains only the refinement details of each structure. For full bonding distances and angles the reader is referred to the supplementary data which is deposited with this thesis and can be obtained from the University of Glasgow. Structures were solved using Patterson or Direct methods with SHELXS-97¹⁴⁰ or SIR-92¹⁴¹ using WinGX routines.¹⁴² Refinement was accomplished by full matrix least-squares on F^2 via SHELXL-97. All non-hydrogen atoms were refined anisotropically unless stated otherwise. Hydrogen atom positions were calculated using standard geometric criteria and refined using a riding model. All data manipulation and presentation steps were performed using WinGX. Details of interest about the structure refinement are given in the tables. The following quantities are given in the information for each structure and were calculated as follows:

$$\text{Goodness-of-fit (GooF)} = \left(\sqrt{\frac{\sum w(F_0^2 - F_c^2)^2}{(n - p)}} \right)$$

$$\text{Weighting scheme } w = \frac{1}{[\sigma^2(F_0)^2 + (AP)^2 + (BP)]}$$

$$\text{With } P = \frac{[\max(I_{obs,O}) + 2F_c^2]}{3}$$

and p : number of parameters; n : number of data; A, B: weighting scheme parameters

$$R1 = \frac{\sum |F_0| - |F_c|}{\sum |F_0|}$$

$$wR2 = \sqrt{\frac{\sum [w(F_0^2 - F_c^2)^2]}{\sum w(F_0^2)^2}}$$

$$R(\text{int}) = \frac{\sum |F_0^2 - F_c^2(\text{mean})|}{\sum |F_0^2|}$$

where both summation involve reflections for which more than one symmetry equivalent is averaged.

7.1 [Cu(ttop)Cl]Cl(CH₃OH)₂, 5

Empirical formula	C ₂₆ H ₃₂ Cl ₂ CuN ₆ O ₂
Formula weight	595.02
Temperature	150(2) K
Wavelength	0.71073 Å
Crystal system, space group	triclinic, <i>P</i> -1
Unit cell dimensions	$a = 7.5983(2)$ Å $\alpha = 73.601(4)$ ° $b = 11.5797(5)$ Å $\beta = 89.339(3)$ ° $c = 16.5965(7)$ Å $\gamma = 84.940(3)$ °
Volume	1395.26(9) Å ³
Z, Calculated density	2 Mg/m ³
Absorption coefficient	1.009 mm ⁻¹
F(000)	618
Crystal size	0.37 x 0.29 x 0.04 mm
Theta range for data collection	3.12 to 25.50°
Limiting indices	-9 ≤ h ≤ 9, -12 ≤ k ≤ 12, -20 ≤ l ≤ 19
Reflections collected / unique	9129 / 4474 [R(int) = 0.0191]
Completeness to theta = 22.67	99.2 %
Absorption correction	Analytical
Max. and min. transmission	1.000 and 0.980
Refinement method	Full-matrix least-squares on F ²
Data / restraints / parameters	4474 / 0 / 338
Goodness-of-fit on F ²	1.006
Final R indices [I > 2σ(I)]	R1 = 0.0275, wR2 = 0.0611
R indices (all data)	R1 = 0.0390, wR2 = 0.0631
Largest diff. peak and hole	0.32 and -0.32 e.Å ⁻³

7.2 [Cu₂(ttop)Cl₄](CH₃OH), 6

Empirical formula	C ₂₅ H ₂₈ Cl ₄ Cu ₂ N ₆ O
Formula weight	697.41
Temperature	150(2) K
Wavelength	0.71073 Å
Crystal system, space group	Monoclinic <i>Pc</i>
Unit cell dimensions	$a = 9.1119(4)$ Å $\alpha = 90^\circ$ $b = 8.8875(5)$ Å $\beta = 99.019(4)^\circ$ $c = 17.8313(7)$ Å $\gamma = 90^\circ$
Volume	1426.16(12) Å ³
Z, Calculated density	2 Mg/m ³
Absorption coefficient	1.897 mm ⁻¹
F(000)	708
Crystal size	0.18 x 0.09 x 0.06 mm
Theta range for data collection	3.22 to 28.45 °
Limiting indices	-11 ≤ h ≤ 11, -10 ≤ k ≤ 10, -21 ≤ l ≤ 21
Reflections collected / unique	6892 / 4393 [R(int) = 0.0428]
Completeness to theta = 26.32	98.3 %
Absorption correction	Analytical
Max. and min. transmission	0.9580 and 0.907
Refinement method	Full-matrix least-squares on F ²
Data / restraints / parameters	4393 / 2 / 345
Goodness-of-fit on F ²	0.891
Final R indices [I > 2σ(I)]	R1 = 0.0288, wR2 = 0.0470
R indices (all data)	R1 = 0.0423, wR2 = 0.0494
Largest diff. peak and hole	0.31 and -0.25 e.Å ⁻³

7.3 [Cu(H(*trans*-1-amino-*cis*-3,5-*N'*,*N''*-2-imidopyridine))(H₂O)Cl]Cl₂, 7

Empirical formula	C ₁₈ H ₂₈ Cl ₃ CuN ₅ O ₃	
Formula weight	532.34	
Temperature	150(2) K	
Wavelength	0.71073 Å	
Crystal system, space group	triclinic, <i>P</i> -1	
Unit cell dimensions	$a = 7.4342(5) \text{ \AA}$	$\alpha = 95.409(3)^\circ$
	$b = 11.5628(6) \text{ \AA}$	$\beta = 94.561(3)^\circ$
	$c = 14.1665(8) \text{ \AA}$	$\gamma = 106.415(3)^\circ$
Volume	1155.71(12) Å ³	
Z, Calculated density	2 Mg/m ³	
Absorption coefficient	1.321 mm ⁻¹	
F(000)	550	
Crystal size	0.26 x 0.13 x 0.06 mm	
Theta range for data collection	1.85 to 25.42°	
Limiting indices	-8 ≤ h ≤ 8, -13 ≤ k ≤ 13, 0 ≤ l ≤ 17	
Reflections collected / unique	14110 / 4218 [R(int) = 0.0707]	
Completeness to theta = 25.42	99.4 %	
Absorption correction	Gaussian	
Max. and min. transmission	0.9249 and 0.7251	
Refinement method	Full-matrix least-squares on F ²	
Data / restraints / parameters	4218 / 4 / 289	
Goodness-of-fit on F ²	1.028	
Final R indices [I > 2σ(I)]	R1 = 0.0490, wR2 = 0.0914	
R indices (all data)	R1 = 0.0899, wR2 = 0.1024	
Largest diff. peak and hole	0.66 and -0.37 e.Å ⁻³	

7.4 $\{[\text{Cu}_2(\text{cis-3-amino-cis,trans-}N',N''\text{-2-imidopyridine})_2]\}_2(\text{NO}_3)_4$, **8**

Empirical formula	$\text{C}_{39}\text{H}_{54}\text{Cu}_2\text{N}_{14}\text{O}_{15}$
Formula weight	1086.04
Temperature	150(2) K
Wavelength	0.71073 Å
Crystal system, space group	monoclinic, $P2_1/n$
Unit cell dimensions	$a = 11.8957(3)$ Å $\alpha = 90^\circ$ $b = 26.6195(8)$ Å $\beta = 110.442(1)^\circ$ $c = 15.8896(3)$ Å $\gamma = 90^\circ$
Volume	4714.7(2) Å ³
Z, Calculated density	4 Mg/m ³
Absorption coefficient	0.985 mm ⁻¹
F(000)	2256
Crystal size	0.44 x 0.12 x 0.06 mm
Theta range for data collection	1.15 to 25.35 °
Limiting indices	$-14 \leq h \leq 13$, $0 \leq k \leq 31$, $0 \leq l \leq 18$
Reflections collected / unique	30755 / 8258 [R(int) = 0.0615]
Completeness to theta = 25.00	99.6 %
Absorption correction	Gaussian
Max. and min. transmission	0.6712 and 0.9433
Refinement method	Full-matrix least-squares on F ²
Data / restraints / parameters	8258 / 13 / 645
Goodness-of-fit on F ²	1.116
Final R indices [I > 2σ(I)]	R1 = 0.0751, wR2 = 0.1770
R indices (all data)	R1 = 0.0972, wR2 = 0.1860
Largest diff. peak and hole	1.40 and -0.63 e.Å ⁻³

7.5 $\{[\text{Cu}_2(\text{ttop})\text{Cl}_3]\text{Cl}\}_2$, **9**

Empirical formula	$\text{C}_{26}\text{H}_{32}\text{Cl}_4\text{Cu}_2\text{N}_6\text{O}_2$
Formula weight	729.46
Temperature	150(2) K
Wavelength	0.71073 Å
Crystal system, space group	triclinic, <i>P</i> -1
Unit cell dimensions	$a = 9.7929(3)$ Å $\alpha = 88.942(2)^\circ$ $b = 12.8175(5)$ Å $\beta = 78.430(2)^\circ$ $c = 13.9117(7)$ Å $\gamma = 69.323(2)^\circ$
Volume	1597.91(11) Å ³
Z, Calculated density	2 Mg/m ³
Absorption coefficient	1.699 mm ⁻¹
F(000)	744
Crystal size	0.20 x 0.20 x 0.12 mm
Theta range for data collection	1.70 to 25.00°
Limiting indices	$-11 \leq h \leq 11$, $-15 \leq k \leq 15$, $0 \leq l \leq 16$
Reflections collected / unique	21121 / 5623 [R(int) = 0.0546]
Completeness to theta = 25.00	99.7 %
Absorption correction	Gaussian
Max. and min. transmission	0.8221 and 0.7275
Refinement method	Full-matrix least-squares on F ²
Data / restraints / parameters	5623 / 0 / 370
Goodness-of-fit on F ²	1.119
Final R indices [I > 2σ(I)]	R1 = 0.0659, wR2 = 0.1666
R indices (all data)	R1 = 0.0909, wR2 = 0.1781
Largest diff. peak and hole	0.91 and -0.58 e.Å ⁻³

7.6 [Zn(ttop)Cl]Cl(H₂O)₂, 10

Empirical formula	C ₂₆ H ₃₂ Cl ₂ N ₆ O ₂ Zn	
Formula weight	596.85	
Temperature	150(2) K	
Wavelength	1.54184 Å	
Crystal system, space group	triclinic, <i>P</i> -1	
Unit cell dimensions	$a = 7.6032(4)$ Å	$\alpha = 105.988(5)$ °
	$b = 11.7730(7)$ Å	$\beta = 90.218(5)$ °
	$c = 16.6154(9)$ Å	$\gamma = 96.367(5)$ °
Volume	1420.02(14) Å ³	
Z, Calculated density	2 Mg/m ³	
Absorption coefficient	3.208 mm ⁻¹	
F(000)	620	
Crystal size	0.16 x 0.13 x 0.05 mm	
Theta range for data collection	3.93 to 61.60 °	
Limiting indices	-7 ≤ h ≤ 8, -10 ≤ k ≤ 12, -17 ≤ l ≤ 16	
Reflections collected / unique	10264 / 3654 [R(int) = 0.0232]	
Completeness to theta = 56.00	98.7 %	
Absorption correction	Analytical	
Max. and min. transmission	0.867 and 0.704	
Refinement method	Full-matrix least-squares on F ²	
Data / restraints / parameters	3654 / 0 / 326	
Goodness-of-fit on F ²	1.056	
Final R indices [I > 2σ(I)]	R1 = 0.0308, wR2 = 0.0814	
R indices (all data)	R1 = 0.0324, wR2 = 0.0828	
Largest diff. peak and hole	0.46 and -0.62 e.Å ⁻³	

7.7 [Zn(ttop)I]I(CH₃OH), 11

Empirical formula	C ₂₇ H ₃₆ N ₆ ZnI ₂ O ₃
Formula weight	811.79
Temperature	100(2) K
Wavelength	0.71073 Å
Crystal system, space group	monoclinic, <i>P</i> ₂ ₁ / <i>c</i>
Unit cell dimensions	<i>a</i> = 7 8.9983(2) Å $\alpha = 90^\circ$ <i>b</i> = 15.7615(4) Å $\beta = 97.013(2)^\circ$ <i>c</i> = 21.9243(6) Å $\gamma = 90^\circ$
Volume	3086.19(13) Å ³
Z, Calculated density	4 Mg/m ³
Absorption coefficient	2.834 mm ⁻¹
F(000)	1600
Crystal size	0.15 x 0.11 x 0.07 mm
Theta range for data collection	1.60 to 25.73 °
Limiting indices	-9 ≤ <i>h</i> ≤ 10, -19 ≤ <i>k</i> ≤ 19, -26 ≤ <i>l</i> ≤ 26
Reflections collected / unique	10264 / 3654 [R(int) = 0.0232]
Completeness to theta = 25.73	98.1 %
Absorption correction	Empirical
Max. and min. transmission	1.000 and 0.8233
Refinement method	Full-matrix least-squares on F ²
Data / restraints / parameters	5760 / 0 / 357
Goodness-of-fit on F ²	1.089
Final R indices [I > 2σ(I)]	R1 = 0.0323, wR2 = 0.0818
R indices (all data)	R1 = 0.0380, wR2 = 0.0854
Largest diff. peak and hole	1.22 and -0.75 e.Å ⁻³

7.8 $[\text{Co}_2(\text{ttop})(\text{NO}_3)_3(\text{H}_2\text{O})_2](\text{NO}_3)(\text{CH}_3\text{CN})_2$, 12

Empirical formula	$\text{C}_{28}\text{H}_{34}\text{Co}_2\text{N}_{12}\text{O}_{14}$
Formula weight	880.53
Temperature	150(2) K
Wavelength	0.71073 Å
Crystal system, space group	triclinic, $P-1$
Unit cell dimensions	$a = 10.2222(4)$ Å $\alpha = 95.925(4)^\circ$ $b = 13.4558(6)$ Å $\beta = 109.869(4)^\circ$ $c = 14.0885(6)$ Å $\gamma = 97.529(4)^\circ$
Volume	1783.94(13) Å ³
Z, Calculated density	2 Mg/m ³
Absorption coefficient	1.015 mm ⁻¹
F(000)	904
Crystal size	0.30 x 0.15 x 0.07 mm
Theta range for data collection	3.44 to 26.02 °
Limiting indices	$-12 \leq h \leq 12, -16 \leq k \leq 16, -17 \leq l \leq 17$
Reflections collected / unique	12622 / 6756 [R(int) = 0.0470]
Completeness to theta = 26.02	96.0 %
Absorption correction	Analytical
Max. and min. transmission	0.944 and 0.835
Refinement method	Full-matrix least-squares on F ²
Data / restraints / parameters	6756 / 4 / 519
Goodness-of-fit on F ²	1.027
Final R indices [I > 2σ(I)]	R1 = 0.0460, wR2 = 0.1011
R indices (all data)	R1 = 0.0734, wR2 = 0.1162
Largest diff. peak and hole	0.77 and -0.47 e.Å ⁻³

7.9 $[\text{Cu}_2(\text{ttop})(\text{NO}_3)_4(\text{NO}_3)_4(\text{H}_2\text{O})](\text{CH}_3\text{OH})$, 13

Empirical formula	$\text{C}_{24}\text{H}_{28}\text{Cu}_2\text{N}_{10}\text{O}_{14}$
Formula weight	807.64
Temperature	150(2) K
Wavelength	1.54184 Å
Crystal system, space group	triclinic, $P-1$
Unit cell dimensions	$a = 7.4673(10)$ Å $\alpha = 84.770(10)^\circ$ $b = 8.8676(11)$ Å $\beta = 83.694(11)^\circ$ $c = 25.520(3)$ Å $\gamma = 65.964(13)^\circ$
Volume	1532.0(3) Å ³
Z, Calculated density	2 Mg/m ³
Absorption coefficient	2.494 mm ⁻¹
F(000)	824
Crystal size	0.14 x 0.05 x 0.03 mm
Theta range for data collection	3.49 to 53.97 °
Limiting indices	$-7 \leq h \leq 7$ $-7 \leq k \leq 9$, $-26 \leq l \leq 26$
Reflections collected / unique	6491 / 3223 [R(int) = 0.0810]
Completeness to theta = 53.97	86.8 %
Absorption correction	Analytical
Max. and min. transmission	0.925 and 0.805
Refinement method	Full-matrix least-squares on F ²
Data / restraints / parameters	3223 / 6 / 463
Goodness-of-fit on F ²	1.023
Final R indices [I > 2σ(I)]	R1 = 0.0742, wR2 = 0.1891
R indices (all data)	R1 = 0.0944 wR2 = 0.2145
Largest diff. peak and hole	0.86 and -0.58 e.Å ⁻³

- (1) Lehn, J. M. *Angew. Chem. Int. Ed.* **1988**, 27, 89.
- (2) Fischer, E. *Ber. Dt. Chem. Ges* **1894**, 27, 2985.
- (3) Watson, J. D.; Crick, F. H. C. *Nature* **1953**, 171, 737.
- (4) Harada, A.; Li, J.; Kamachi, M. *Nature* **1992**, 356, 325.
- (5) Harada, A.; Li, J.; Kamachi, M. *Nature* **1994**, 370, 126.
- (6) Rebek, J. *Angew. Chem. Int. Ed.* **1990**, 29, 245.
- (7) Schweiger, M.; Seidel, S. R.; Arif, A. M.; Stang, P. J. *Inorg. Chem.* **2002**, 41, 2556.
- (8) Leininger, S.; Olenyuk, B.; Stang, P. J. *Chem. Rev.* **2000**, 100, 853.
- (9) Steed, J. W.; Atwood, J. L. *Supramolecular Chemistry*; John Wiley & Sons, Ltd: Chichester, **2000**.
- (10) Beer, P. D.; Gale, P. A.; Smith, D. K. *Supramolecular Chemistry*; Oxford University Press: Oxford, **2003**.
- (11) Huck, W. T. S.; Hulst, R.; Timmerman, P.; vanVeggel, F.; Reinhoudt, D. N. *Angew. Chem. Int. Ed.* **1997**, 36, 1006.
- (12) Hof, F.; Palmer, L. C.; Rebek, J. *J. Chem. Educ.* **2001**, 78, 1519.
- (13) Calhorda, M. J. *Chem. Commun.* **2000**, 801.
- (14) McGaughey, G. B.; Gagne, M.; Rappe, A. K. *J. Biol. Chem.* **1998**, 273, 15458.
- (15) Burley, S. K.; Petsko, G. A. *Science* **1985**, 229, 23.
- (16) Chandler, D. *Nature* **2005**, 437, 640.
- (17) Shiga, T.; Newton, G. N.; Mathieson, J. S.; Tetsuka, T.; Nihei, M.; Cronin, L.; Oshio, H. *Dalton Trans.* **2010**, 39, 4730.
- (18) Fujita, M. *Chem. Soc. Rev.* **1998**, 27, 417.
- (19) Orgel, L. E. *An Introduction to Transition-Metal Chemistry: Ligand-Field Theory*; Wiley, **1966**.
- (20) Jircitano, A. J.; Henry, R. F.; Hammond, R. R. *Acta Cryst. C* **1990**, 46, 1799.
- (21) M. Muller, I.; Rottgers, T. *Chem. Commun.* **1998**, 823.
- (22) Clifford, F.; Counihan, E.; Fitzgerald, W.; Seff, K.; Simmons, C.; Tyagi, S.; Hathaway, B. *Chem. Commun.* **1982**, 196.
- (23) Winter, M. J. *d-Block Chemistry*; Oxford Science Publications, **1994**.
- (24) Housecraft, C. E.; Sharpe, A. G. *Inorganic Chemistry*; Prentice Hall, **2001**.
- (25) Yang, J. Y.; Shores, M. P.; Sokol, J. J.; Long, J. R. *Inorg. Chem.* **2003**, 42, 1403.
- (26) Pickering, A. L.; Seeber, G.; Long, D.-L.; Cronin, L. *Chem. Commun.* **2004**, 136.
- (27) Bolognina, E.; Gatos, M.; Lucatello, L.; Mancin, F.; Moro, S.; Palumbo, M.; Sissi, C.; Tecilla, P.; Tonellato, U.; Zagotto, G. *J. Am. Chem. Soc.* **2004**, 126, 4543.
- (28) Seeber, G.; Cooper, G. J. T.; Newton, G. N.; Rosnes, M. H.; Long, D. L.; Kariuki, B. M.; Kogerler, P.; Cronin, L. *Chem. Sci.* **2010**, 1, 62.
- (29) Cooper, G. J. T.; Newton, G. N.; Kogerler, P.; Long, D. L.; Engelhardt, L.; Luban, M.; Cronin, L. *Angew. Chem. Int. Ed.* **2007**, 46, 1340.
- (30) Park, G.; Przyborowska, A. M.; Ye, N.; Tsoupas, N. M.; Bauer, C. B.; Broker, G. A.; Rogers, R. D.; Brechbiel, M. W.; Planalp, R. P. *Dalton Trans.* **2003**, 318.
- (31) Park, G.; Ye, N.; Rogers, R. D.; Brechbiel, M. W.; Planalp, R. P. *Polyhedron* **2000**, 19, 1155.
- (32) Suhr, D.; Lotscher, D.; Stoeckli-Evans, H.; von Zelewsky, A. *Inorg. Chim. Acta* **2002**, 341, 17.
- (33) Hilfiker, K. A.; Brechbiel, M. W.; Rogers, R. D.; Planalp, R. P. *Inorg. Chem.* **1997**, 36, 4600.
- (34) Park, G.; Lu, F. H.; Ye, N.; Brechbiel, M. W.; Torti, S. V.; Torti, F. M.; Planalp, R. P. *J. Biol. Inorg. Chem.* **1998**, 3, 449.
- (35) Park, G.; Dadachova, E.; Przyborowska, A.; Lai, S.-j.; Ma, D.; Broker, G.; Rogers, R. D.; Planalp, R. P.; Brechbiel, M. W. *Polyhedron* **2001**, 20, 3155.

-
- (36) Childers, M. L.; Su, F.; Przyborowska, A. M.; Bishwokarma, B.; Park, G.; Brechbiel, M. W.; Torti, S. V.; Torti, F. M.; Broker, G.; Alexander, J. S.; Rogers, R. D.; Ruhlandt-Senge, K.; Planalp, R. P. *Chem. Eur. J.* **2005**, *2005*, 3971.
- (37) Wang, Y.; Gu, M. *Anal. Chem.* **2010**, *82*, 7055.
- (38) Mallet, A. I.; Down, S. *Dictionary of Mass Spectrometry*; Wiley, **2009**.
- (39) Hoffmann, E. d.; Stroobant, V. *Mass Spectrometry, Principles and Applications*; Wiley, **2002**.
- (40) Henderson, W.; McIndoe, J. S. *Mass spectrometry of Inorganic and Organometallic Compounds*; Wiley, **2005**.
- (41) Miras, H. N.; Wilson, E. F.; Cronin, L. *Chem. Commun.* **2009**, 1297.
- (42) *micrOTOF-Q User Manual Version 1.0*; Bruker Daltonics, **2006**.
- (43) Gates, P. <http://www.chm.bris.ac.uk/ms/newversion/ionisation.htm> **2005**
- (44) Sakamoto, S.; Fujita, M.; Kim, K.; Yamaguchi, K. *Tetrahedron* **2000**, *56*, 955.
- (45) Abbas, H.; Pickering, A. L.; Long, D.-L.; Kögerler, P.; Cronin, L. *Chem. Eur. J.* **2005**, *11*, 1071.
- (46) Gale, P. A. *Coord. Chem. Rev.* **2003**, *240*, 191.
- (47) Beer, P. D.; Gale, P. A. *Angew. Chem. Int. Ed.* **2001**, *40*, 486.
- (48) Gale, P. A.; Gunnlaugsson, T. *Chem. Soc. Rev.* **2010**, *39*, 3595.
- (49) Berger, M.; Schmidtchen, F. P. *J. Am. Chem. Soc.* **1999**, *121*, 9986.
- (50) Simmons, H. E.; Park, C. H. *J. Am. Chem. Soc.* **1968**, *90*, 2428.
- (51) Kavallieratos, K.; de Gala, S. R.; Austin, D. J.; Crabtree, R. H. *J. Am. Chem. Soc.* **1997**, *119*, 2325.
- (52) Zielinski, T.; Jurczak, J. *Tetrahedron* **2005**, *61*, 4081.
- (53) Camiolo, S.; Gale, P. A.; Hursthouse, M. B.; Light, M. E. *Org. Biomol. Chem.* **2003**, *1*, 741.
- (54) Chmielewski, M. J.; Jurczak, J. *Chem. Eur. J.* **2005**, *11*, 6080.
- (55) Lee, J.-J.; Stanger, K. J.; Noll, B. C.; Gonzalez, C.; Marquez, M.; Smith, B. D. *J. Am. Chem. Soc.* **2005**, *127*, 4184.
- (56) Kang, S. O.; VanderVelde, D.; Powell, D.; Bowman-James, K. *J. Am. Chem. Soc.* **2004**, *126*, 12272.
- (57) Shriver, D. F.; Biallas, M. J. *J. Am. Chem. Soc.* **1967**, *89*, 1078.
- (58) Chen, T. S. S.; Chang, C.-J.; Floss, H. G. *J. Org. Chem.* **1981**, *46*, 2661.
- (59) Wedge, T. J.; Hawthorne, M. F. *Coord. Chem. Rev.* **2003**, *240*, 111.
- (60) Beer, P. D.; Hazlewood, C.; Heseck, D.; Hodacova, J.; Stokes, S. E. *J. Chem. Soc.-Dalton Trans.* **1993**, 1327.
- (61) Rudkevich, D. M.; Stauthamer, W.; Verboom, W.; Engbersen, J. F. J.; Harkema, S.; Reinhoudt, D. N. *J. Am. Chem. Soc.* **1992**, *114*, 9671.
- (62) Montellano, O. d. *Cytochrome P450: Structure, Mechanism and Biochemistry*; Kluwer Academic/Plenum Publishers, **2005**.
- (63) Ferraro, D. J.; Gakhar, L.; Ramaswamy, S. *Biochem. Biophys. Res. Commun.* **2005**, *338*, 175.
- (64) Solomon, E. I.; Brunold, T. C.; Davis, M. I.; Kemsley, J. N.; Lee, S.-K.; Lehnert, N.; Neese, F.; Skulan, A. J.; Yang, Y.-S.; Zhou, J. *J. Chem. Rev.* **1999**, *100*, 235.
- (65) Costas, M.; Mehn, M. P.; Jensen, M. P.; Que, L. *Chem. Rev.* **2004**, *104*, 939.
- (66) Abu-Omar, M. M.; Loaiza, A.; Hontzeas, N. *Chem. Rev.* **2005**, *105*, 2227.
- (67) Hegg, E. L.; Jr, L. Q. *Eur. J. Biochem.* **1997**, *250*, 625.
- (68) Koehntop, K. D.; Emerson, J. P.; Que, L. *J. Biol. Inorg. Chem.* **2005**, *10*, 87.
- (69) Karlsson, A.; Parales, J. V.; Parales, R. E.; Gibson, D. T.; Eklund, H.; Ramaswamy, S. *Science* **2003**, *299*, 1039.

-
- (70) Wolfe, M. D.; Altier, D. J.; Stubna, A.; Popescu, C. V.; Münck, E.; Lipscomb, J. D. *Biochemistry* **2002**, *41*, 9611.
- (71) Bassan, A.; Blomberg, M.; Siegbahn, P. *J. Biol. Inorg. Chem.* **2004**, *9*, 439.
- (72) Fridovich, I. *Science* **1978**, *201*, 875.
- (73) Han, S.; Eltis, L. D.; Timmis, K. N.; Muchmore, S. W.; Bolin, J. T. *Science* **1995**, *270*, 976.
- (74) Ford, P. C.; Fernandez, B. O.; Lim, M. D. *Chem. Res.* **2005**, *105*, 2439.
- (75) Haber, F.; Weiss, J. **1932**, *20*, 948.
- (76) Barton, D. H. R. *Tetrahedron* **1998**, *54*, 5805.
- (77) Barton, D. H. R.; Gastiger, M. J.; Motherwell, W. B. *Chem. Commun* **1983**, 41.
- (78) Kolb, H. C.; VanNieuwenhze, M. S.; Sharpless, K. B. *Chem. Rev.* **1994**, *94*, 2483.
- (79) Chen, K.; Costas, M.; Kim, J.; Tipton, A. K.; Que, L. *J. Am. Chem. Soc.* **2002**, *124*, 3026.
- (80) Costas, M.; Que, J. L. *Angew. Chem. Int. Ed.* **2002**, *41*, 2179.
- (81) De Vos, D. E.; de Wildeman, S.; Sels, B. F.; Grobet, P. J.; Jacobs, P. A. *Angew. Chem. Int. Ed.* **1999**, *38*, 980.
- (82) de Boer, J. W.; Brinksma, J.; Browne, W. R.; Meetsma, A.; Alsters, P. L.; Hage, R.; Feringa, B. L. *J. Am. Chem. Soc.* **2005**, *127*, 7990.
- (83) Kim, C.; Chen, K.; Kim, J.; Que, L. *J. Am. Chem. Soc.* **1997**, *119*, 5964.
- (84) Legros, J.; Bolm, C. *Angew. Chem. Int. Ed.* **2003**, *42*, 5487.
- (85) Legros, J.; Bolm, C. *Angew. Chem. Int. Ed.* **2004**, *43*, 4225.
- (86) Rose, E.; Ren, Q.-Z.; Andrioletti, B. *Chem. Eur. J.* **2004**, *10*, 224.
- (87) Gelalcha, F. G.; Bitterlich, B.; Anilkumar, G.; Tse, M. K.; Beller, M. *Angew. Chem. Int. Ed.* **2007**, *46*, 7293.
- (88) Oldenburg, P. D.; Shteinman, A. A.; Que, L. *J. Am. Chem. Soc.* **2005**, *127*, 15672.
- (89) Company, A.; Gómez, L.; Güell, M.; Ribas, X.; Luis, J. M.; Que, L.; Costas, M. *J. Am. Chem. Soc.* **2007**, *129*, 15766.
- (90) Company, A.; Feng, Y.; Güell, M.; Ribas, X.; Luis, J. M.; Que, L.; Costas, M. *Chem. Eur. J.* **2009**, *15*, 3359.
- (91) Company, A.; Gómez, L.; Fontrodona, X.; Ribas, X.; Costas, M. *Chem. Eur. J.* **2008**, *14*, 5727.
- (92) Chen, M. S.; White, M. C. *Science* **2007**, *318*, 783.
- (93) Arakawa, H.; Aresta, M.; Armor, J. N.; Barteau, M. A.; Beckman, E. J.; Bell, A. T.; Bercaw, J. E.; Creutz, C.; Dinjus, E.; Dixon, D. A.; Domen, K.; DuBois, D. L.; Eckert, J.; Fujita, E.; Gibson, D. H.; Goddard, W. A.; Goodman, D. W.; Keller, J.; Kubas, G. J.; Kung, H. H.; Lyons, J. E.; Manzer, L. E.; Marks, T. J.; Morokuma, K.; Nicholas, K. M.; Periana, R.; Que, L.; Rostrup-Nielson, J.; Sachtler, W. M. H.; Schmidt, L. D.; Sen, A.; Somorjai, G. A.; Stair, P. C.; Stults, B. R.; Tumas, W. *Chem. Rev.* **2001**, *101*, 953.
- (94) Punniyamurthy, T.; Velusamy, S.; Iqbal, J. *Chem. Rev.* **2005**, *105*, 2329.
- (95) Que, L.; Tolman, W. B. *Nature* **2008**, *455*, 333.
- (96) Denisov, I. G.; Makris, T. M.; Sligar, S. G.; Schlichting, I. *Chem. Rev.* **2005**, *105*, 2253.
- (97) Krebs, C.; Galonić Fujimori, D.; Walsh, C. T.; Bollinger, J. M. *Acc. Chem. Res.* **2007**, *40*, 484.
- (98) Andersson, K. K.; Froland, W. A.; Lee, S.-K.; Lipscomb, J. D. *New J. Chem.* **1991**, *15*, 411.
- (99) Wolfe, M. D.; Lipscomb, J. D. *J. Biol. Chem.* **2003**, *278*, 829.
- (100) Chen, K.; Costas, M.; Que, J. L. *Dalton Trans.* **2002**, 672.
- (101) Chen, K.; Que, L. *J. Am. Chem. Soc.* **2001**, *123*, 6327.

-
- (102) Chen, G.; Hoag, G. E.; Chedda, P.; Nadim, F.; Woody, B. A.; Dobbs, G. M. *J. Haz. Mat.* **2001**, *87*, 171.
- (103) Seeber, G.; Kogerler, P.; Kariuki, B. M.; Cronin, L. *Chem. Commun.* **2004**, 1580.
- (104) Alajarin, M.; Pastor, A.; Orenes, R.-A.; Goeta, A. E.; Steed, J. W. *Chem. Commun.* **2008**, 3992.
- (105) Gadzikwa, T.; Lu, G.; Stern, C. L.; Wilson, S. R.; Hupp, J. T.; Nguyen, S. T. *Chem. Commun.* **2008**, 5493.
- (106) Wilson, E. F.; Abbas, H.; Duncombe, B. J.; Streb, C.; Long, D.-L.; Cronin, L. *J. Am. Chem. Soc.* **2008**, *130*, 13876.
- (107) Yoshizawa, M.; Takeyama, Y.; Kusukawa, T.; Fujita, M. *Angew. Chem. Int. Ed.* **2002**, *41*, 1347.
- (108) Müller, A.; Beckmann, E.; Bögge, H.; Schmidtman, M.; Dress, A. *Angew. Chem. Int. Ed.* **2002**, *41*, 1162.
- (109) Seeber, G.; Long, D.-L.; Kariuki, B. M.; Cronin, L. *Dalton Trans.* **2003**, 4498.
- (110) Newton, G. N.; Geoffrey, J. T. C.; Long, D. L.; Kogerler, P.; Cronin, L. *J. Mol. Struct.* **2006**, *796*, 23.
- (111) Liu, C.-M.; Xiong, R.-G.; You, X.-Z.; Liu, Y.-J.; Cheung, K.-K. *Polyhedron* **1996**, *15*, 4565.
- (112) Mochizuki, K.; Miyashita, S. *Chem. Lett.* **1996**, 899.
- (113) Caira, M. R.; Nassimbeni, L. R.; Wooley, P. R. *Acta Crystallogr. Sect. B* **1975**, *31*, 1334.
- (114) Youngme, S.; Poopasit, K.; Fun, H.-K.; Chinnakali, K.; Razak, I. A.; Chantrapromma, S. *Acta Crystallogr. Sect. C* **1998**, *54*, 1221.
- (115) Xu, Z.; White, S.; Thompson, L. K.; Miller, D. O.; Ohba, M.; Okawa, H.; Wilson, C.; Howard, J. A. K. *Dalton Trans.* **2000**, 1751.
- (116) Sommerer, S. O.; Westcott, B. L.; Jircitano, A. J.; Abboud, K. A. *Inorg. Chim. Acta* **1995**, *238*, 149.
- (117) Atria, A. M.; Baggio, R. F.; Espinosa, N.; Garland, M. T.; Manzur, J.; Moreno, Y.; Spodine, E. *Acta Crystallogr. Sect. C* **1994**, *50*, 1066.
- (118) Tshuva, E. Y.; Lippard, S. J. *Chem. Rev.* **2004**, *104*, 987.
- (119) Chen, M. S.; White, M. C. *Science* **2010**, *327*, 566.
- (120) Adam, W.; Malisch, W.; Roschmann, K. J.; Saha-Möller, C. R.; Schenk, W. A. *J. Organomet. Chem.* **2002**, *661*, 3.
- (121) Markert, C.; Pfaltz, A. *Angew. Chem. Int. Ed.* **2004**, *43*, 2498.
- (122) Feichtinger, D.; Plattner, D. A. *Angew. Chem. Int. Ed.* **1997**, *36*, 1718.
- (123) Quiñonero, D.; Morokuma, K.; Musaev, D. G.; Mas-Ballesté, R.; Que, L. *J. Am. Chem. Soc.* **2005**, *127*, 6548.
- (124) Bassan, A.; Blomberg, M. R. A.; Siegbahn, P. E. M.; Que, L. *J. Am. Chem. Soc.* **2002**, *124*, 11056.
- (125) Kang, S. O.; Begum, R. A.; Bowman-James, K. *Angew. Chem. Int. Ed.* **2006**, *45*, 7882.
- (126) Gale, P. A.; Navakhun, K.; Camiolo, S.; Light, M. E.; Hursthouse, M. B. *J. Am. Chem. Soc.* **2002**, *124*, 11228.
- (127) Blanda, M. T.; Horner, J. H.; Newcomb, M. *J. Org. Chem.* **1989**, *54*, 4626.
- (128) Sarwar, M. G.; Dragisic, B.; Sagoo, S.; Taylor, M. S. *Angew. Chem. Int. Ed.* **2010**, *49*, 1674.
- (129) Becherer, T.; Meshcheryakov, D.; Springer, A.; Böhmer, V.; Schalley, C. A. *J. Mass. Spectrom.* **2009**, *44*, 1338.
- (130) Job, P. *Ann. di. Chim. Appl.* **1928**, 113.
- (131) Pascal, R. A.; Spergel, J.; Van Engen, D. *Org. Lett.* **1986**, *27*, 4099.

-
- (132) Bondy, C. R.; Loeb, S. J. *Coord. Chem. Rev.* **2003**, *240*, 77.
- (133) Pickering, A. L.; Cooper, G. J. T.; Long, D.-L.; Cronin, L. *Polyhedron* **2004**, *23*, 2075.
- (134) Camphausen, K.; Sproull, M.; Tantama, S.; Sankineni, S.; Scott, T.; Menard, C.; Coleman, C. N.; Brechbiel, M. W. *Bioorg. Med. Chem.* **2003**, *11*, 4287.
- (135) Li, D.; Clérac, R.; Roubeau, O.; Harté, E.; Mathonière, C.; Le Bris, R.; Holmes, S. M. *J. Am. Chem. Soc.* **2007**, *130*, 252.
- (136) Herrera, J. M.; Marvaud, V.; Verdaguer, M.; Marrot, J.; Kalisz, M.; Mathonière, C. *Angew. Chem. Int. Ed.* **2004**, *43*, 5468.
- (137) Heinrich, J. L.; Berseth, P. A.; Long, J. R. *Chem. Commun.* **1998**, 1231.
- (138) Newton, G. N.; Onuki, T.; Shiga, T.; Noguchi, M.; Matsumoto, T.; Mathieson, J. S.; Nihei, M.; Nakano, M.; Cronin, L.; Oshio, H. *Angew. Chem. Int. Ed.* **2011**, *123*, 4946.
- (139) Cooper, G. J. T.; Newton, G. N.; Long, D.-L.; Kögerler, P.; Rosnes, M. H.; Keller, M.; Cronin, L. *Inorg. Chem.* **2009**, *48*, 1097.
- (140) Sheldrick, G. M. *Acta Crystallogr A* **2008**, *64*, 112.
- (141) Altomare, A.; Cascarano, G.; Giacovazzo, C.; Guagliardi, A. **1993**, *26*, 343.
- (142) Farrugia, L. J. *J. Appl. Cryst.* **1999**, *32*, 837.